Systematic Study to Improve the Performance of 2D Materials based Photodetectors

THESIS

Submitted in partial fulfillment
of the requirements for the degree of

DOCTOR OF PHILOSOPHY

by

Venkatarao Selamneni

ID No. 2018PHXF0429H

Under the Supervision of

Dr. Parikshit Sahatiya

BITS Pilani
Pilani | Dubai | Goa | Hyderabad

BIRLA INSTITUTE OF TECHNOLOGY AND SCIENCE, PILANI

2023

BIRLA INSTITUTE OF TECHNOLOGY AND SCIENCE, PILANI

CERTIFICATE

This is to certify that the thesis entitled Development of a "**Systematic Study to Improve the Performance of 2D Materials based Photodetectors"** and submitted by **Venkatarao Selamneni**, ID. No. **2018PHXF0429H** for award of Ph.D. of the Institute embodies original work done by him under my supervision.

Name of the Supervisor- **Dr. Parikshit Sahatiya**

Designation- Assistant Professor

Department of Electrical and Electronics

Birla Institute of Technology and Science-Pilani

Date:

DECLARATION

This is to certify that the thesis titled "**Systematic Study to Improve the Performance of 2D Materials based Photodetectors"** is based on my own research work and has been carried out under the guidance and supervision of Dr. Parikshit Sahatiya, Assistant Professor, Dept of Electrical Engineering, BITS Pilani, Hyderabad Campus, Hyderabad, India.

The data and information which I have used from various sources have been duly acknowledged. I declare that this work has not been previously submitted by me to any other university/Institute for the award of any other degree or diploma.

Date:
Place: Hyderabad

Name:**Venkatarao Selamneni**
ID No: **2018PHXF0429H**

Acknowledgment

First and foremost, I would like to express my sincere gratitude to my advisor Dr. Parikshit Sahatiya for his invaluable guidance and motivation throughout my PhD. I deeply appreciate my advisor for giving me countless advises, and always being very patient to teach and answer me, even for very fundamental questions. I also express my sincere thanks to my Doctoral Committee members Prof. Sanket Goel, and Dr. Himanshu Aggarwal for their insightful comments, encouragement and support that helped improve the quality of my thesis. Special thanks goes to our FAWND lab colleagues Naveen Bokka, Vivek Adepu, and MNNE lab students who greatly contributed to my professional and personal development at BITS Pilani Hyderabad Campus. I also acknowledge the help of graduate students and postgraduate students at BITS Pilani Hyderabad campus. I also extend my thanks to the Central Analytical Laboratory (CAL), BITS Pilani Hyderabad Campus for providing characterization facilities. I would like thank our collaborator Professor Andres De Luna Bugallo from UNAM, Mexico and Indian Nanoelectronics User Program (INUP), CenSE, IISC and IITBNF for the characterization and cleanroom fabrication facilities.

My sincere thanks to Prof. Subhendu Kumar Sahoo, current Head of Department (HOD), and Prof. Sanket Goel, Prof. Alivelu Manga Parimi former HODs, Department of Electrical and Electronics Engineering, BITS Pilani, Hyderabad Campus for allowing me to carry out my research work and equipping the facilities in the department. During the course of this PhD I have met many good people at BITS Pilani, Hyderabad and I would like to thank P Shambu Prasad, and Dr. Chandra Sekhar Reddy Kolli, who become good friends and with whom I shared many moments inside and outside BITS.

Lastly, I am extremely grateful to my family, especially my wife Bhavya Chennupati, Geethika Sriya (daughter), and Surya Karthikeya (son) for their support over the last couple of years.

Abstract

Photodetectors are one of the key components in many optoelectronic applications. Right now, photodetectors have reached the level of a mature technology and been used in many applications including remote sensing, imaging, fiber-optic communications, environmental monitoring and so on. But still there is a need for new photodetector systems outperforming the existing state-of-art technology in terms of performance or cost or less complex fabrication with some additional features such as wearability or flexibility or transparency or transiency. In particular, due to rapid development of technology in human life, the demand for new generation flexible and wearable optoelectronic devices has increased tremendously. According to Precedence Research, by 2030 the global flexible/wearable electronics market size is projected to be worth approximately $61 billion. 2D materials are considered as a promising candidate for a next generation of flexible optoelectronics due to their exceptional electronic, mechanical and optoelectronic properties. Out of the big family of 2D materials, semiconducting TMDs have gained significant attention of research community due to their unique electronic and optoelectronic properties. Atomic thin, tunable bandgap and extraordinary optoelectronic properties of TMDs are unique features than can be explored and applied in novel photodetector applications.

This thesis presents the development of high-performance and broadband photodetectors based on 2D materials and their hybrids. The first part of the thesis delas with fabrication of high responsivity flexible photodetectors based on 2D TMDs materials. Various techniques including plasmonic photodetection, piezo-phototronic photodetection and use of transport layer were employed to fabricate the high-performance photodetectors. The first chapter deals with fabrication of high-performance photodetectors by integrating transport layer. Transport layer assists in the effective separation of photogenerated electron-hole pairs. In the recent years the research on semi-metal MXenes based electronics increased tremendously due to its high conductivity, high mobility, unique electronic and optoelectronic properties. Solution processed MXene ($Ti_3C_2T_X$) was used as transport layer and solution processed ReS_2 was used as photoactive layer. Significant improvement in the photodetection performance was observed with the integration of $Ti_3C_2T_X$ transport layer.

The next chapter deals with development of plasmonic photodetectors based on 2D materials (MoS_2 and ReS_2) by integrating metal nanoparticles (NPs) and also detailed plasmonic photodetection mechanism was discussed. Significant change in the photodetection performance was observed after integrating metal NPs compared to the pristine materials due to the plasmonic effect of metal NPs. The next chapter deals with the development of p-n heterostructure based photodetector with piezo-phototronic effect for the enhancement of photoresponsivity. Flexible PET sheet was used as substrate. Solution-processed p-type SnS and n-type MoS_2 were used to fabricate p-n heterostructure. It is well known that odd layer MoS_2 shows the piezotronic effect. By applying external strain on the fabricated device, the change in the photodetection performance of the device was investigated. Also, detailed piezo-phototronic effect based photodetection mechanism was discussed.

In recent years, significant research has been done by the scientific community to enhance the responsivity of a photodetector. Despite the continuous development and responsivity improvement of photodetectors, the key factor limiting the performance of the photodetectors is the limited spectral range in the electromagnetic spectrum. Next part of the thesis focuses on the development of a fabrication technique which not only enhances the photoresponsivity but also extends the spectral range of the 2D materials based photodetectors. Use of pristine 2D TMDs has disadvantages like limited spectral absorption due to the bandgap. In order to increase the absorption and spectral range, mixed-dimensional 0D/2D vdW heterostructure method was used. 0D quantum dots (QDs) (MoS_2 QDs, SnS_2-QDs, WS_2-QDs) are decorated on the layered 2D material (MoS_2, SnS) were used to fabricate 0D/2D vdW heterostructures. This compelling synergy combines strong and size-tunable light absorption of QDs, efficient charge separation at the QD/TMDs interface and fast carrier transport through the 2D channel. Also, the detailed photodetection mechanism of mixed-dimensional vdW heterostructure was discussed.

CONTENTS

List of Tables

List of Figures

List of Abbreviations

0D – Zero Dimension

2D – Two Dimension

3D – Three Dimension

ICs – Integrated circuits

Si – Silicon

Ge – Germanium

TMDs – Transition Metal Dichalcogenides

QDs –Quantum Dots

MoS_2 – Molybdnum disulfide

WS_2 – Tungsten Disulfide

SnS_2 – Tin Disulfide

ReS_2 – Rhenium disulfide

$MoSe_2$ – Molybdenum diselenide

GaN – Gallium Nitride

CdS – Cadmium Sulfide

SnS – Tin Sulfide

$Ti_3C_2T_x$ – Titanium Carbide

HRTEM – High Resolution Transmission Electron Microscopy

FESEM – Field Emission Scanning Electron Microscopy

PL – Photoluminescence

XPS – X-ray Photoelectron Spectroscopy

UPS – Ultraviolet Photoelectron Spectroscopy

DI – Deionized

FETs – Field Effect Transistors

SAED – Selective Area Electron Diffraction

Pt – Platinum

Pd – Palladium

Ag – Silver

W – Tungsten

Mo – Molybdenum

XRD – X-ray Diffraction

LED – Light Emitting Diode

CVD – Chemical Vapor Deposition

SiO_2 – Silicon Dioxide

ITO – Indium Tin Oxide

UV – Ultraviolet

Vis – Visble

NIR – Near InfraRed

CBM – Conduction Band Minima

VBM – Valence Band Maxima

DOS – Density of States

NPs – Nano Particles

e-h – Electron-Hole

PET – Polyethylene Terephthalate

MILD – Minimally Intensive Layer Delamination

B.E. – Binding Energy

MOSFET – Metal Oxide Semiconductor Field Effect Transistor

LMI – Light Matter Interaction

LSPR – Localized Surface Plasmon Resonance

FTIR – Fourier Transform IR spectroscopy

FDTD – Finite Difference Time Domain

NEP – Noise Equivalent Power

EQE – External Quantum Efficiency

SNR– Signal to Noise Ratio

IQE – Internal Quantum Efficiency

CHAPTER 1

2D Materials based Photodetectors

1.1 Introduction

Sensing elements are critical components in many electronic applications. Among them, optoelectronic sensors have gained significant attraction from research community in many fields due to their wide applications. Photodetectors are optoelectronic devices which can convert a light signals into quantifiable electric signals. In the recent years, significant research has been carried out on the fabrication of photodetectors due to their possible applications in a wide variety of areas like optical communication, image sensing, fire detection, environmental monitoring, and surveillance. Right now, photodetectors have reached the level of a mature technology and been used in many applications including remote sensing, imaging, fiber-optic communications, environmental monitoring and so on [1–5]. But still there is a need for new photodetector systems outperforming the existing state-of-art technology in terms of performance or cost or less complex fabrication with some additional features such as wearability or flexibility or transparency or transiency. In particular, due to rapid development of technology in human life, the demand for new generation flexible and wearable optoelectronic devices has increased tremendously. According to Precedence Research, by 2030 the global flexible/wearable electronics market size is projected to be worth approximately $61 billion[6].

Currently, the photodetection market is predominantly controlled by bulk Si based products. These devices are efficient in detecting in light across Vis to NIR region. In addition, photodetectors developed using other 3D materials such as III-V semiconductor alloys (e.g., InGaAs) or Si/Ge heterostructures can operate beyond the absorption limit of Si at 1100 nm. These photodetectors typically fabricated on rigid substrates. However, 3D materials based photodetectors suffers from some drawbacks such as high-cost and complex fabrication process, and stringent operating environment. These limitations hinder their usage in flexible and wearable electronic applications. In contrast, devices fabricated on flexible substrates offers several advantages, which can meet with growing demands of future generation optoelectronic applications including better portability, integration on human body, excellent implantability, low manufacturing cost. Due to

their flexible, thing as well as remarkable mechanical and optoelectronic properties, 2D materials are emerged as a potential candidate for future generation of flexible optoelectronic applications [7–11].

1.2 The rise of 2D materials

During the lecture "There's Plenty of Room at the Bottom" in 1959, Richard P. Feynman inspired the scientific community to explore layered materials with his questions "What would the properties of materials be if we could really arrange the atoms the way we want them?", "what could we do with layered structures with controlled layers?"[12]. Feynman questions ignited the research community. After several years, graphene (sp^2-hybridized single atomic layer carbon) was discovered in 2004 by Novoselov, Geim, and their co-workers, which is an inspirational material. The discovery of graphene fuelled a new era of atomic thin 2D layered materials [9,10]. 2D materials are described as nanomaterials, with sheet-like morphology, showing a lateral size in the range of tens of nm to tens of μm or further higher and thickness in the range of a few Å to a few nm [11]. 2D materials have gained attention due to their fascinating electronic, optoelectronic, physical, and mechanical properties [7–11]. In 2D materials, the layers are connected by weak van der Waals (vdW) interactions, and the atoms of the same plane are connected by covalent bonds [10]. In 2D materials, quantum confinement effect is very prominent due to the nanoscale dimensions. The big family of 2D materials comprises TMDs, transition metal nitrides (MXenes), chalcogenides, mono-elemental 2D atomic crystals such as graphene, tellurene, and phosphorene, and so forth [13], as displayed in Figure 1.1.

Typical representation of TMDs is MX_2, wherein M is a transition metal such as Mo or W or Ta, and X represent a chalcogen such as S or Te or Se. Among different 2D materials, TMDs exhibits unique properties such as layer dependent electronic band structures and changes from direct to indirect when changes monolayer to bulk form, the density of charge carriers can be tuned and suitable to exfoliate and develop a wide variety of van der Waals (vdW) heterostructures due to the weak vdW interactions within the layers without lattice mismatching [14]. The vdW interactions do not rely on one-to-one chemical bonds or chemical processing; therefore, choice of materials is not necessary to have similar lattice structures or processing compatibility. These vdW heterostructures provide better performance compared to pristine 2D layered materials [9,15]. Because of their outstanding features, 2D TMDs have a lot of potential in various applications in all most in all fields of applied electronics and engineering such as

electronic and optoelectronic applications [16–20], transistors [21–23], energy storage [24–26], biological and chemical sensors [27,28], breath or respiration sensor[29][30], drug delivery [31,32], memory devices [33–36], pressure sensor [29][37], strain sensor[38], nanogenerators [39–41] and so forth. Other inherent benefit of 2D materials over conventional Si technology is atomic thickness of the material and 2D materials could provide thin channel thickness for the development of faster and smaller field-effect-transistors (FETs) in digital circuit applications. In the last two decades, several top-down and bottom-up techniques have been demonstrated for the synthesis of 2D layered TMDs materials, such as mechanical exfoliation [42,43], electrochemical exfoliation [44,45], liquid phase exfoliation [46,47], atomic layer deposition [48,49], chemical vapor deposition [50–53], magnetron sputtering [54–56], solution process method [57,58], and so forth.

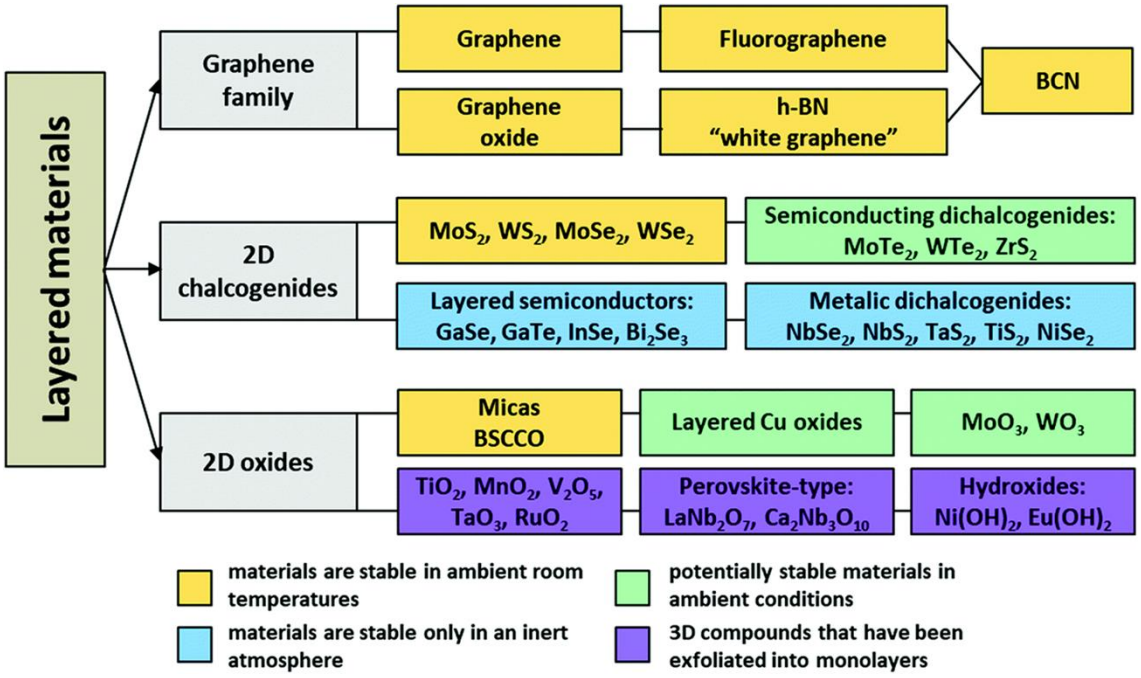

Figure 1.1: Classification of 2D layered materials [59].

1.3 Photodetectors based on 2D materials

Photodetectors convert illuminated photons into electrical signal, and these are one of the widely used optoelectronic devices. Presently, applications of photodetectors in real life are increasing rapidly. Photodetector is a fundamental component in many technologies and is widely utilized in various applications in military, industry, agricultural and daily life. For instance, infrared (IR) light detection is utilized for remote control, night vision,

optical communications, fire alarming, navigational aids, precision strike, fire alarms, etc.; visible (Vis) light detection devices are utilized for e-eyes, digital camera, displays, optoelectronic storage, etc.; Ultraviolet (UV) light sensitive devices are utilized for military reconnaissance, environmental monitoring, sterilization, space science, etc. Due to these wide varieties of applications, there has been a significant increase in demand for high-performance broadband photodetectors in recent times.

Typically, the electromagnetic wavelength spectrum is classified as follows: terahertz (30 μm – 3 mm), infrared (IR) (750 nm – 30 μm), visible (400 – 750 nm), ultraviolet (10-400 nm). Furthermore, IR wavelength range is separated in five segments: very long-wave IR (12 – 30 μm), long-wave IR (LWIR) (8 – 12 μm), mid-wave IR (MWIR) (3 – 5 μm), short-wave IR (SWIR) (1 – 3 μm) and near-IR (NIR) (750 nm – 1.1 μm). Similarly, UV wavelength is separated into three regions: UV A (320 – 400 nm), UV B (290 – 320 nm), and UV C (200 – 290 nm). Conventional materials that have been used for photodetection include Si for visible to NIR (400 – 1100 nm), GaN for UV (< 400 nm), InGaAs for NIR to mid-IR (MIR) (1-5 μm) [60,61]. The photodetection range of various 2D materials and the corresponding energy bandgap values are depicted in Figure 1.2. Fabrication of broadband photodetector using conventional materials requires the integration of multiple photodetectors of various materials, which makes it very complex for practical applications and also increase the cost of the system. Also, conventional materials suffer from low flexibility, high-temperature processing, and miniaturization problem by Moore's law.

Due to the superior properties including high in-plane carrier mobility, layer dependent bandgap, excellent optoelectronic properties, high dielectric constant, and quantum confinement, 2D TMDs have emerged has a promising candidates for photodetection and interest is growing exponentially in both industrial and academic communities [62,63]. But however, 2D materials based photodetectors also face some challenges such as limited light absorption due to atomic thickness and limited spectral range due to their optical bandgap. Various methods have been developed to overcome this issue, such as integrating with strong light absorption materials [64], bandgap engineering [64–66], doping of the material [67–69], mixed-dimensional heterostructure [70,71], defect engineering [72,73].

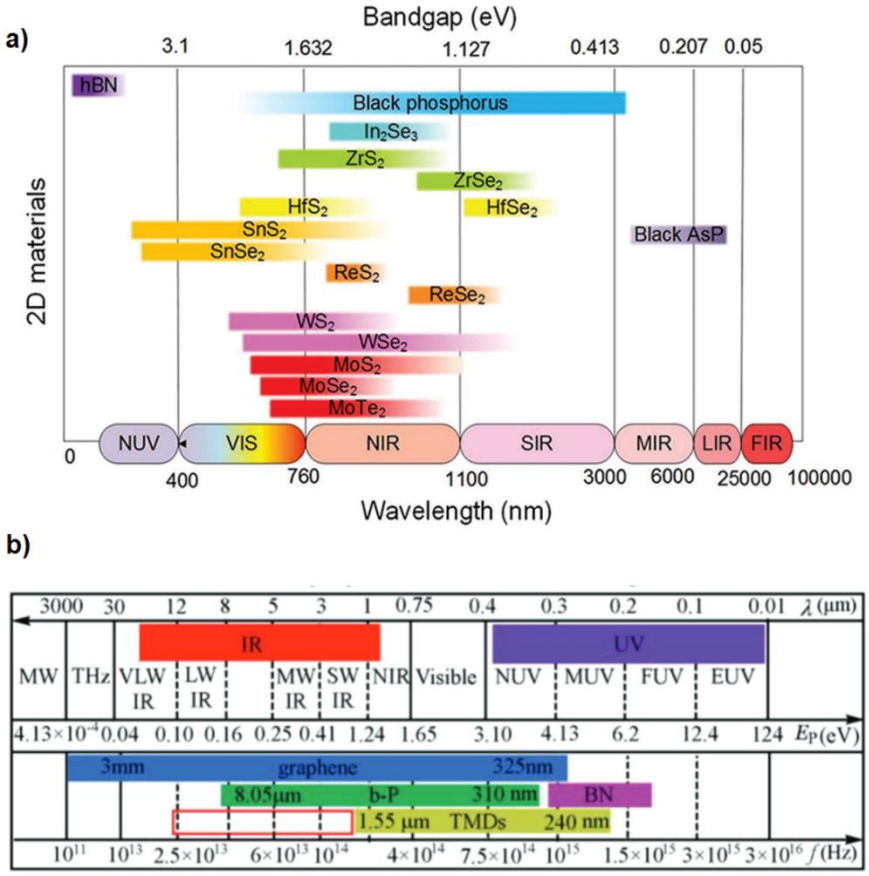

Figure 1.2: a) List of few 2D materials with detection range and band gap values, b) electromagnetic spectrum from ultraviolet to terahertz [60].

1.4 Fundamentals of Photodetectors

1.4.1 Classification of Photodetectors

Generally, semiconductor based photodetectors are classified into three types that are photoconductors, photodiodes, and phototransistors.

i. Photoconductors

Under light illumination, the number of charge carriers in the photoconductor changes and thus detects the light. Two metal ohmic contacts are made on the two ends of the photoconductor to collect the photoexcited electron-hole (e-h) pairs, as illustrated in Figure 1.3a. The photogenerated e-h pairs are collected at electrodes by external bias. Photoconductor is equivalent to the photosensitive resistor, and the values of the resistance changes with light incident. Photogenerated charge carriers recirculate through the external circuit before recombination happens. The photoconductive gain (G) is described as the ratio between life time ($\tau_{lifetime}$) and transit time ($\tau_{transit}$). Sensitizing

centers or trap states of semiconductor capture one of the charge carriers and effectively prolong the lifetime of carrier, leads to multiple carriers per single photon and results in ultra-high photoresponsivity. It is important note that increase in carrier lifetime degrades the response time of the photoconductor and thus bandwidth of the photoconductor is lower than the other category of photodetectors. Hence, while designing photoconductors for particular applications, trade-off between response time and photoconductive gain need to be considered.

ii. Photodiodes

Photodiode consists of semiconductor junction (p-n, p-i-n) or metal/semiconductor junction. Photodiode type photodetector operates under reverse bias and when the light is illuminated, photoexcited e-h pairs move to opposite direction due to the internal-electric field formed at the interface of the junction. The response time is described by the following equation: $\tau_{transit} = L^2/\mu V_{bias}$, wherein V_{bias} is bias voltage, μ mobility of the charge carriers, and L is the length of channel. As the charge carrier transmission is short, hence response time of photodiode is usually quicker than the photoconductors [74,75]. In p-i-n photodiodes, p and n semiconductor regions are isolated by an intrinsic region and width of the depletion layer increase up to the width of intrinsic region under reverse bias condition. In avalanche photodiode carrier multiplication effect happens and 2D materials, for example InSe, MoS_2 based avalanche photodiodes exhibited a carrier multiplication of 100-1000 [76–78].

iii. Phototransistors

The techniques used to enhance the performance of the photodetector should not only increase the gain of the detector but also suppress the noise in the photodetector. Low-resistance or Ohmic contacts in photoconductors result in large dark current, which leads to higher flicker (1/f) noise or shot noise. On the other hand, in high-quality photodiodes under photovoltaic mode, low-noise can be achieved, but the absence of gain limits the response. To rectify the noise issue, the concept of phototransistors has emerged. Phototransistor is similar to photoconductors with a gate terminal that is electrically separated from channel by a dielectric layer, as shown in Figure 1.3c. Charge density and dark current of the channel can be modulated with the gate voltage. Thus, both low noise and high photoconductive gain could be obtained resulting in high responsivity and gain-bandwidth product. For example, single-layer MoS_2 exhibits high gate-tunable

conductivity with I_{on}/I_{off} ratio of more than 10^8 [79] and showed a detectivity of 10^{11}-10^{12} Jones and high responsivity of ~ 1000 A/W [75,79,80].

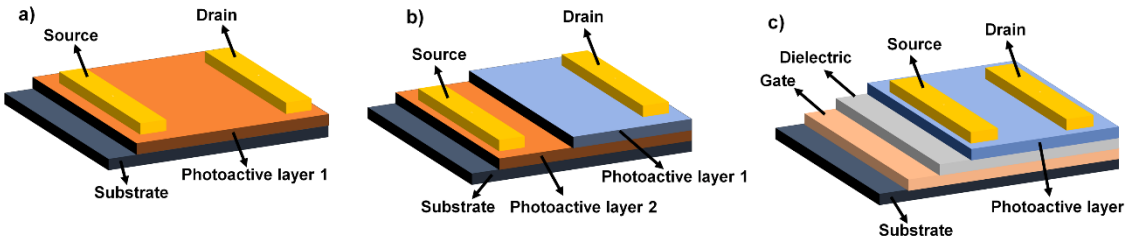

Figure 1.3: Schematic representation of types of photodetectors: a) photoconductor b) photodiode c) phototransistor.

1.4.2 Photodetection mechanism

Photocurrent generation mechanism typically classified into two types: one is related to generation charge carriers due to light illumination including photoconductive effect, photogating effect, and photovoltaic effect. The second one is due to the thermal effect including photobolometric effect and photothermoelectric effect.

i. Photoconductive effect

In photoinductive effect, photogenerated excess charge carriers increase the concentration of free charge carriers which reduces the resistance of the photoconductor. The excess charge carriers generated under light illumination are collected by applying external bias (V_{bias}), leads to change in the device current which is called photocurrent (I_{ph}). A small amount of current flow through the device without light illumination, it is called as dark current (I_{dark}) of device. Photocurrent is expressed as $I_{ph} = I_{light}-I_{dark}$. When the illuminated photon energy is greater than band gap of the semiconductor, then the absorbed photon generates e-h pairs which are segregated and collected by the external voltage results the current $I_{light,}$ which is much higher than the $I_{dark.}$ Figure 1.4a-b displays the illustration of photoconductive effect mechanism. It should be noted that the in photoconductive effect, photocurrent can be obtained only with an external bias, unlike the photovoltaic effect.

ii. Photogating effect

The photogating effect is a special case of the photoconductive effect. Extra e-h pairs are generated under light illumination and if the electrons or holes are captured by the trap states of semiconductor then life time of captured carrier is more than the transit time of

the other charge carrier. With the trapped carrier the semiconductor conductivity can be modulated [81]. The graphic illustration of the photogating effect is displayed in Figure 1.4c-d. If the holes are trapped, then trapped charges acts as a localized gate electrode and control the conductivity of the channel effectively. Thus, conductivity of the channel can be tuned with photogating effect. As detrapping process is time taking, thus lifetime of free carrier increases, which leads to high gain. Normally, photodetectors having photogating effect exhibits a higher gain than photoconductors but the response time is low.

iii. Photovoltaic effect

In photovoltaic effect, the photoexcited e-h pairs are segregated by the internal electric field formed at p-n junction or Schottky junction (metal/semiconductor interface). For instance, in p-n junction, due to the concentration gradient charge carriers move in the opposite direction and eventually form an internal electric field. The photocurrent flow depends on the electric field direction, as shown in Figure 1.4e-f. When the light is irradiated, e-h pairs are generated and separated by the internal in-built potential, thus creating short circuit current (I_{SC}). Under open circuit, the photogenerated e-h pairs accumulate at terminals of the device, resulting in an open circuit voltage (V_{OC}). I_{SC} and V_{OC} Due to the built-in potential, photovoltaic effect based photodetectors can work at reverse or zero bias.

iv. Photothermoelectric effect

Thermal effect induced by light illuminated is the root cause of photothermoelectric effect. When the spot size of the laser used is less than the device dimensions, then temperature gradient occurs at the channel and results in a temperature difference (ΔT) between the two ends of the semiconductor, as illustrated in Figure 1.4g. This temperature difference generates a photo-thermoelectric voltage (ΔV) and drives the current without an external bias. Typically, the magnitude of photo-thermoelectric voltage is in the range of tens of μV to mV. Hence, a good Ohmic contact is needed at the metal/semiconductor interface.

v. Photobolometric effect

The photobolometric effect is related to the resistivity change in the channel due to the temperature variations caused by the light heating induced by absorption of photons. Depending on the material property the channel resistance could be increased or

decreased under thermal irradiation. Thus, due to the photobolometric effect, the current in the system may increase or decrease under external bias. It should be noted that the photocurrent caused by bolometric effect changes proportionally with the applied bias. Photothermoelectric effect based devices are self-powered like photovoltaic devices, and in Photobolometric effect based devices photocurrent can be observed without external bias.

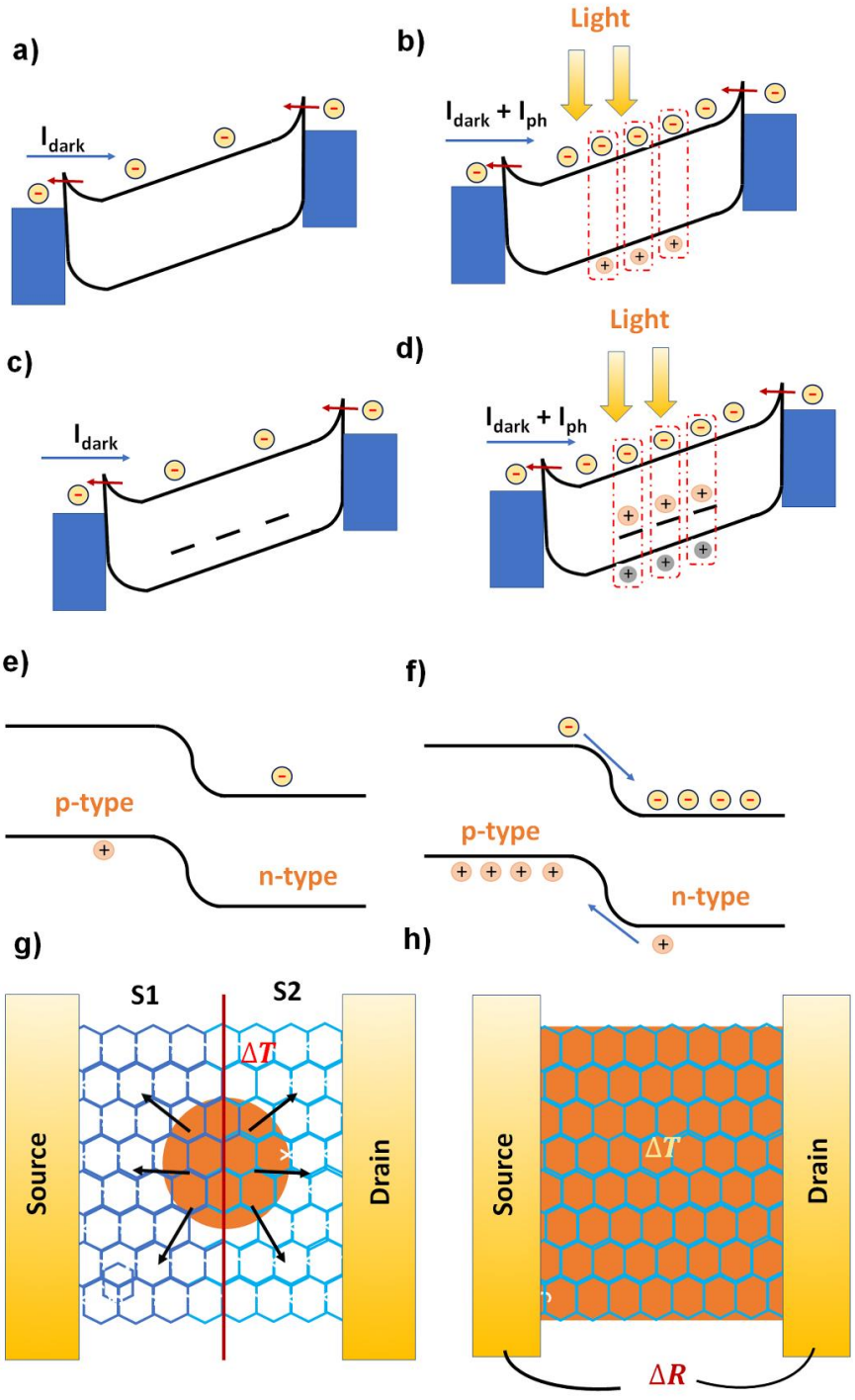

Figure 1.4: Schematic representing various types of photodetection mechanism a-b) photoconductive effect c-d) photogating effect e-f) photovoltaic effect g) photothermoelectric effect h) photobolometric effect.

1.5 Performance parameters of Photodetectors

Several key performance parameters are needed to evaluate a photodetector performance. Usually, responsivity (R), photoconductive gain (G), response time, detectivity (D*), Noise equivalent power (NEP), external quantum efficiency (EQE), signal to noise (SNR), etc., are measured for a photodetector. In this section, a brief introduction about these important performance parameters is given.

i. Responsivity

Responsivity (R) indicates the efficiency of photoelectric conversion of a photodetector. Responsivity is described as the ratio of photocurrent to illuminated light power density. Responsivity can be expressed by the following equation:

$$R = \frac{I_{light} - I_{dark}}{P_{in}A} = \frac{I_{ph}}{P_{in}A}$$

Where, I_{dark} is the dark current, I_{light} is the output current in the presence of light, A is device area, and P_{in} is the power density of input light.

ii. External quantum efficiency (EQE)

EQE indicates the number of e-h pairs generated per the number of photons incident and gives the conversion efficiency of the detector. EQE is determined using the following equation:

$$EQE = R\,\frac{hc}{q}$$

wherein c, q, and h represent the light speed, electron charge, and, Planck's constant, respectively.

iii. Internal quantum efficiency (IQE)

IQE is similar to EQE, except that number of photons absorbed is considered in IQE. IQE is the ratio between the number of generated e-h pairs to number of absorbed

Figure 1.4: Schematic representing various types of photodetection mechanism a-b) photoconductive effect c-d) photogating effect e-f) photovoltaic effect g) photothermoelectric effect h) photobolometric effect.

photons. IQE is given by the following equation:

$$IQE = R\frac{hc}{qA_{abs}}$$

wherein A_{abs} is the ratio of the absorbed to incident light power at a particular wavelength.

iv. Response speed

Response speed contains rise time (τ_r) and decay time or fall time (τ_f), describes the response speed of the photodetector for input light upon turning on and off the laser source. Response of the photodetector mainly depend on the charge carriers separation, transportation and collection in the channel. Rise time and fall time of the detector is determined by calculating the time difference between 10% to 90% and 90% to 10% of the device current.

v. Photoconductive gain (G)

Photoconductive gain (G) gives the number of charge carriers flowing through the device per the number of photons incident. It is determined according to the following equation:

$$G = \frac{\tau_{life}}{\tau_{transit}} = \frac{\tau_{life}}{L^2/\mu V_{bias}}$$

Where $\tau_{transit}$ and τ_{life} are the transit time of the charge carriers and the lifetime of the charge carriers, respectively, V_{bias} is the applied bias, μ is the mobility of the carrier, and L is the length of the channel.

Photoconductive gain mainly depends on the lifetime of the charge carriers, and it increases with an increase in carrier life time (τ_{life}). Conversely, the response time of the device decreases with a prolonged carrier lifetime, which results in a trade-off between response time and gain. However, developing a photodetector with ultrahigh responsivity and very short response time is not possible in practice.

vi. Noise equivalent power

Noise equivalent power (NEP) is described as the minimum detectable illumination power to deliver unity signal to noise ratio at a bandwidth of 1 Hz and it gives the detection capability of the device. NEP is expressed as:

$$NEP = \frac{\sqrt{\overline{i_n^2}}}{R}$$

Where $\sqrt{\overline{i_n^2}}$ (A $Hz^{-1/2}$) is the mean-square noise current at 1 Hz of the bandwidth of under darkness. Thus, a high responsivity and a small dark current are beneficial to obtain a low NEP.

vii. Specific detectivity (D*)

Detectivity of the photodetector indicates the sensitivity of the detector. The equation of the detectivity is given below:

$$D^* = \frac{\sqrt{A.\Delta f}}{NEP}$$

Where A is an effective area of a device, Δf is electrical bandwidth, and NEP is the noise equivalent power. When shot noise dominates then detectivity could be simplified as follows:

$$D^* = \frac{R}{\sqrt{2qJ_d}}$$

Wherein J_d represents dark current density. The unit is cm $Hz^{1/2}/W$ or Jones.

viii. I_{on}/I_{off} ratio

The I_{on}/I_{off} is the ratio between the device current under light illumination to device current without light illumination. Photodetectors with high light absorption and very low dark current exhibit high on/off ratio. For practical applications photodetectors with higher on/off ratio is needed to detect low-intensity signals.

ix. Signal to noise ratio (SNR)

The noise of the photodetector effects the accuracy. SNR is described as the ratio between input signal power to noise power. It is always necessary to have a SNR greater than 1 so that input signal can be differentiated from noise signal.

1.6 Types of heterojunctions/band diagrams

Once, Nobel laureate Herbert Kromer said, "The interface is the device" in his Nobel lecture. The interface plays a vital role in the vdW heterostructure based optoelectronic devices [82,83]. The behavior of the heterostructure such as spectrum absorption range, in-built electric field, and generation-separation-transportation of photogenerated e-h pairs, primarily depends on the energy band alignment at the interface of the materials used. Hence it is crucial to choose the materials properly for the design of vdW heterostructures. Depending on the band alignment of two semiconductors interface, the energy band structure of the heterostructure can be classified into three types: type-I (symmetric/straddling-gap), type-II (staggered-gap), and type-III (broken-gap).

In type-I band structure, the conduction band minimum (E_C) of semiconductor-2 is at lower energy level than the E_C of semiconductor-1 and the valence band maximum (E_V) of semiconductor-2 is at higher energy level than that of semiconductor-1; thus band

diagram of the semiconductor-2 is completely lie between the E_C and E_V levels of semiconductor-1, as shown in Figure 1.5a. Hence, the in type-I interface both electrons and holes are transferred from semiconductor-1 to semiconductor-2. In type-II (staggered-gap) band alignment, both E_C and E_V of one material are higher than the other one, as shown in Figure 1.5b, which results in the transfer and separation of photoexcited e-h pairs at the heterostructure interface. Type-II heterostructure band alignment is widely used in the design of high-performance optoelectronic devices such as photodetectors and photovoltaics [71,84–86]. For example, type-II band alignment will be created, when n-type and p-type semiconductors are in contact and have a various application of in the field of optoelectronics, especially in self-powered photodetectors. When n-type and p-type semiconductors are in contact, charge carriers move from higher carrier concentration to lower carrier concentration and a depletion region is formed across the junction. A strong internal electric field is formed across the junction due to the positive charge region on n-type side and the negative charge region on the p-type side. The built-in electric field helps in the efficient segregation of photogenerated e-h pairs when light is illuminated on p-n junction.

In type-III (broken-gap) band alignment, E_V of one semiconductor is at higher energy level than the E_C of second semiconductor and there is no overlapping in the band structure of the two semiconductors, as illustrated in Figure 1.5c. Thus, band-to-band tunnelling occurs in type-III, which results in fast transportation of the carriers compared to type-II heterostructure. Type-III band alignment has prominent applications in low power consumption, tunnel field-effect transistors, high-speed switching [87–89]. Some of the reported type-III heterostructures are $SnSe_2/MoTe_2$ [90], WTe_2/HfS_2 [91].

Apart from these three types, there is another vital band alignment between metal and a semiconductor that is Schottky contact. When a semiconductor and metal are in contact, to attain the equilibrium charge carriers move from one section to another and it causes a charge build-up at the interface of metal-semiconductor, which causes band structure deformation. This deformation continues till Fermi energy level in semiconductor attains equilibrium with metal. The band bending creates a barrier potential (Schottky barrier) at the interface of metal-semiconductor. It is important to note that the condition for Schottky barrier formation at metal-semiconductor interface depends on the semiconductor type (p-type or n-type), as illustrated in Figure 1.5d-e. In case of metal-semiconductor (n-type) interface, Schottky barrier is formed when metal work function (φ_M) is greater than that of the semiconductor (φ_S), i.e., $\varphi_M > \varphi_S$, otherwise ohmic contact

is formed. On the other hand, in case of metal-semiconductor (p-type) interface, Schottky barrier is formed when φ_M is less than the work function of the semiconductor (φ_S), i.e., $\varphi_M < \varphi_S$, otherwise Ohmic contact is formed. The Schottky barrier height (SBH) is described as the difference between the metal Fermi energy level and band edge where the majority carriers are available and this barrier height for electrons moving from metal to semiconductor. In a metal and n-type semiconductor interface, SBH (φ_B) is the difference between metal work function (φ_M) and conduction band edge (which is electron affinity) of the semiconductor (χ), $\varphi_B = \varphi_M - \chi$. Similarly, for metal-semiconductor (p-type) interface, the Schottky barrier height is the difference between valence band edge ($E_g + \chi$) and the metal work function (φ_M), $\varphi_B = E_g + \chi + \varphi_M$. On the contrary, the energy needed for the charge carriers to move from semiconductor to metal is termed as built-in barrier potential (V_{built}) on the semiconductor side. The built-in barrier potential in metal-semiconductor is the difference between the work function of the semiconductor and metal, $V_{built} = \varphi_M - \varphi_S$.

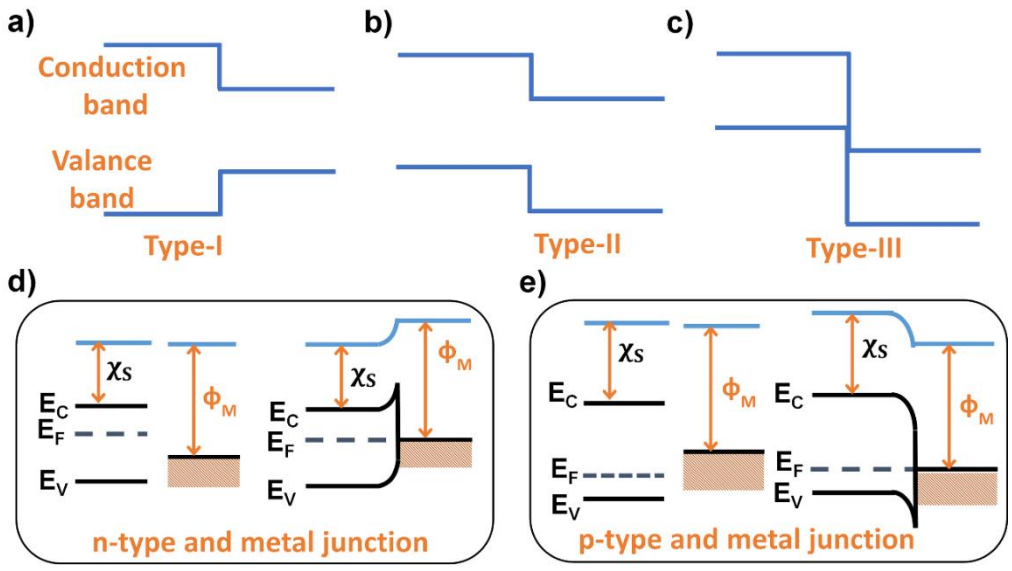

Figure 1.5: Schematic illustrating various types of band alignment: a-) type-I, b) type-II, c) type-III, d-e) Schottky contact between n-type semiconductor and metal, and p-type semiconductor and metal.

1.7 Research gaps/Thesis objectives

To develop a high-performance flexible photodetector, further work is needed to optimize the fabrication techniques and the device design to improve the performance. To enhance the light absorption of the devices and for effective separation of

photogenerated e-h pairs techniques such as integration of plasmonic technologies, strain engineering (using piezo-phototronic effect), using of transport layer can be employed. By using a p-n junction or Schottky barriers dark current of the device can be reduced. Further, high photoconductive gain can be realized by using graphene or MXene as the fast transfer channel for charge carriers.

The overall aim of the thesis is the development of high performance and broadband photodetectors based on 2D materials and their hybrids with other low-dimensional materials.

Integration of a transport layer to improve the performance of 2D materials based photodetectors

Research on the fabrication of semiconductor/transport layer based heterostructures has been increased significantly because in semiconductor/transport-layer heterostructural stacking the whole transport layer area can be used as a junction and the photoexcited charge carriers in 2D semiconductor transported to transport layer followed by the quick collection at the electrodes. Due to ultra-high mobility, graphene is most widely used as charge carrier transport layer. Recently, a new family of 2D transitional metal carbides, nitirdes called as MXene has attracted significant attention in the research community as a transport layer due to its high electrical conductivity, easy tunable structure, and MXene can be an efficient 2D alternative to graphene. The research on using MXene as a transport layer in fabricating flexible photodetectors is very limited. Hence there is a need to study the effect of MXene as a transport layer in improving the performance of flexible 2D material based broadband photodetectors. The goal of the work is to fabricate a high-performance photodetector based on 2D/MXene heterostructure.

To improve the performance of 2D materials based photodetectors using plasmonic effect by integrating metal nanoparticles

Another technique to enhance the performance of a 2D materials based photdetectors is use of plasmonic effect by integrating metal nanostructures. In 2D materials, most light will still transmit through the thin layers of the material. To make the 2D materials viable for practical photodetector applications, it is much need to improve the light-matter interaction of the material. One effective method to improve the light-matter interaction

of the 2D materials is integration of plasmonic metal NPs on 2D materials. This can be achieved by either decorating/patterning plasmonic NPs on top of 2D materials and it can increase the light absorption at certain wavelengths. In addition, direct contact between 2D material and metal NPs facilitates hot-electron injection over Schottky barriers.

To improve the performance of a photodetector by external strain modulation

Semiconductor heterostructures and their modulation plays a vital role in the fabrication of optoelectronics. The properties of the vdW heterostructure can be modulated by various techniques such as bandgap engineering, doping, piezotronics effect and so forth. Recently, rapid progress in the dominant fields of piezo-phototronics and piezotronics has been observed. The significance of the *piezo-phototronic* devices is to use the inherent piezoelectric polarization to tune the charge generation, separation, and transport and/or recombination process at the interface for enhancing optoelectronic processes. Upon external strain, piezotronic effect induces polarization charges which can effectively modify the energy band structure of p-n junction or metal-semiconductor interface and thus modulate the separation, transport/migration, and recombination processes of photoexcited charge carriers. Further, p-n junction based heterostructures gained special attention as they provide basic building block for various modern optoelectronics applications such as photodetectors, light-emitting diodes, solar cells, ultrafast lasers, and many more. Over the last few years, number of p-n junction photodetectors were demonstrated utilizing piezotronic effect based on non-centro symmetrical wurtzite-structured semiconductors such as ZnO nanowires, CdS, GaN, MoS_2, etc... The majority of them have disadvantages, including complex fabrication, high costs, and a tight operating environment. Hence there is a need for the development of cost-effective, flexible p-n junction based piezotronic photodetectors. The objective of this work is to fabricate a high-performance broadband photodetector based on 2D materials with piezo-phototronic effect.

To fabricate the high performance and broadband photodetectors using mixed-dimensional 0D/2D vdW heterostructures

Use of 2D materials in photodetectors have some drawbacks such has limited spectral absorption due to the bandgap and limited absorption efficiency. The objective of this

work is to overcome the limited spectral range problem of the pristine 2D materials based photodetectors. This can be achieved through the implementation of mixed-dimensional 0D/2D vdW heterostructure method. The incorporation of 0D QDs on 2D materials, with their tunable absorption through control over their size expands the spectral selectivity and also improves the devices absorption efficiency. In addition, the high mobility of TMDs facilitates the effective charge transport, thereby enabling the potential for large photoconductive gain.

1.8 Thesis outline

The thesis is organized as follows:

Chapter 2 focusses on the development of ReS_2 based high performance photodetectors using MXene ($Ti_3C_2T_X$) as a transport layer.

Chapter 3 focusses on the fabrication of plasmonic photodetectors based on Metal-NPs/MoS_2 and Metal-NPs/ReS_2 heterostructures.

Chapter 4 focusses on the development of high-performance photodetectors employing piezo-phototronic effect based on SnS/MoS_2 heterostructure.

Chapter 5 focusses on the development of mixed-dimensional 0D/2D heterostructure based broadband photodetectors using MoS_2-QDs/MoS_2, WS_2-QDs/SnS, and SnS_2-QDs/MoS_2 heterostructures.

Chapter 6 gives the summary of the work done and future prospectives.

CHAPTER 2

Ultra-high responsivity and enhanced trap assisted charge transfer by utilizing Ti_3C_2Tx(MXene) as a transport layer for ReS_2 based flexible broadband photodetector

Even though there are many reports on low-cost flexible broadband photodetector the main issue is the low value of the responsivity due to non-uniformity of the substrate. The reason is the lack of suitable transport material. Graphene has proven to be the best till date, but, on unconventional substrates such as biodegradable paper, responsivity values still remain an unresolved issue. This work demonstrates the use of $Ti_3C_2T_X$(MXene) as transport layer, utilizing 2D ReS_2 as active material on paper substrate as broadband photodetector and further compared its performance with graphene. Responsivity values calculated for ReS_2/MXene and ReS_2/graphene under visible and NIR illumination are 40.8 AW^{-1}, 26.9 AW^{-1}, and 26.5 AW^{-1}, 17.5 AW^{-1}, respectively, which suggests that MXene as transport layer largely enhances performance. To understand the phenomena, detailed mechanisms studies are presented in terms of density of surface states and energy band diagram. Surface states density was found to be larger in MXene compared to graphene structure, suggests that the lifetime of the carrier is high with MXene as transport layer compared to Graphene due to trap assisted charge transfer. This ReS_2/MXene heterostructure based environment friendly photodetector can find potential applications in future flexible optoelectronics.

2.1 Introduction

Photodetectors are devices that quantify light by converting photons to electrical signals. Two-dimensional (2D) Material based photodetectors have gained enormous interest from researchers due to their unique electronic and optical properties compared to conventional bulk materials [64][92][93][65]. However, improving the responsivity of the flexible 2D material based photodetectors fabricated on unconventional substrates such as biodegradable paper is still challenging. Photoconductive gain (G) of a photodetector is ($G = \tau_{lifetime}/\tau_{transit}$) the ratio of charge carrier lifetime and transit time. Transmit time of charge carries is defined as $\tau_{transit} = L^2/\mu V_{bias}$ [94].Thus, photocurrent gain is inversely proportional to the square of the channel length (L) and proportional to the

mobility of the carrier (μ), carrier life time ($\tau_{lifetime}$) and applied bias voltage. Current research reveals that mobility of 2D materials other than graphene are lower compared to conventional materials such as Si, GaAs, etc. [95,96]. To enhance the optoelectronic properties 2D TMDs based heterostructures have been developed [64][92] because heterostructures configuration suppresses the dark current, enables quick carrier transport, improves the band alignment, and enhances the charge carrier lifetime and reduces the recombination rate, etc. [64][92] [65][97]. Recently research on the fabrication of semiconductor/transport layer based heterostructures has been increased significantly because in semiconductor/transport-layer heterostructural stacking the whole transport layer area can be used as a junction and the photoexcited charge carriers in 2D semiconductor transported to transport layer followed by the quick collection at the electrodes [92][93]. Graphene was first discovered in 2004, and it has been widely used as a transport layer to improve the performance of a photodetector due to its high mobility [98–100]. Recently, a new family of 2D transitional metal carbides, nitirdes called as MXene has attracted significant attention in the research community as a transport layer due to its high electrical conductivity, easy tunable structure, and MXene is an efficient 2D alternative to graphene [101–105]. The research on using MXene as a transport layer in fabricating flexible photodetectors is very limited. Hence there is an urgent need to study the effect of MXene as a transport layer in improving the performance of flexible 2D material based broadband photodetectors.

Research is currently underway on one of the most recently discovered next-generation TMDs materials, rhenium disulfide (ReS_2). The ReS_2 maintains a direct bandgap of around 1.4 eV) [112–114] and also unlike other TMDs which have a layer tunable bandgap and exhibit direct bandgap only in the monolayer state, ReS_2 maintains a direct bandgap irrespective of the number of layers due to low symmetry and weak interlayer coupling [113,115,116]. This eliminates the need for monolayer fabrication, which is relatively more difficult than multilayer synthesis. The direct bandgap also means a higher density of states which, coupled with enhanced light absorption due to anisotropic in-plane optical properties, makes ReS_2 an ideal candidate for the photosensitive layer. However, existing reports on ReS_2 photodetectors show that the low mobility of ReS_2 is a limiting factor in the performance of these devices [114,117,118]. Hence there is a need for integration in the form of a heterostructure to improve the charge transport in such a device. $Ti_3C_2T_X$ is one of the MXenes with high metallic conductivity ~ 10^4 $S.cm^{-1}$ [119] and has shown

excellent contact performance with TMDs like $MoS_2/Ti_3C_2T_X$and $WSe_2/Ti_3C_2T_X$ (barrier heights of about 0.19 eV and 0.23 eV, respectively)[120–122]. Further, unlike graphene, there is no post-synthesis reduction process to fabricate highly conductive MXene films, making them a more facile alternative.

Since their discovery, MXenes have found a multitude of applications as Schottky contacts, transparent electrodes, charge transfer layers, and more in devices for energy storage and conversion, gas and pressure sensors, and optoelectronic devices like light-emitting diodes (LEDs) and photodetectors [101,105,123][124]. MXenes have a general chemical formula of $M_{n+1}X_nT_x$, in which M is an early transition metal, X is carbon or nitrogen or both, and Tx is a surface functional group, such as -OH, -O, -F, or -Cl, and n = 1, 2, or 3 [123] . Aside from their excellent metallic conductivity, they have a tunable work function that can be engineered to be [125,126]. Out of 20-30 MXenes discovered to date, $Ti_3C_2T_X$ is by far the most thoroughly studied. It has shown remarkable electromechanical properties when coated on flexible substrates, in addition to showing promise as a conductive film. While it has been explored as transparent electrodes that can potentially replace the existing expensive gold electrodes, [103] and reports on $Ti_3C_2T_X$ as a carrier transport layer are scarce. The few existing reports on photodetectors with MXene as transport layer show that the high metallic conductivity of MXenes aids electron transport, resulting in a larger photocurrent and a faster photoresponse [104,127]. Hence, it would be interesting to study ReS_2/MXene heterostructure based photodetector performance.

ReS_2 was synthesized using facile hydrothermal method and MXene($Ti_3C_2T_X$) was prepared by minimally intensive layer delamination (MILD) method from the commercially obtained T_3AlC_2 MAX phase. Highly scalable vacuum filtration technique was used to deposit synthesized $Ti_3C_2T_X$ on a paper substrate, and contacts were created on MXene using thermal evaporation technique. Later, ReS_2/MXene device was fabricated by drop-casting ReS_2 on MXene/paper. The Schottky barrier created at the interface of the ReS_2 and MXene assists in effective separation on photoexcited electron-hole pairs and MXene layer allowed for efficient charge transport, which enhances the photoresponsivity of the device significantly. Responsivity of the fabricated ReS_2/MXene photodetector was found to be 40.8 A/W and 26.9 A/W under visible and NIR regions, respectively. Furthermore, ReS_2/graphene based photodetector was fabricated to compare the performance with ReS_2/MXene photodetector. Responsivity of ReS_2/graphene device in visible and NIR illumination was 26.5 AW^{-1} and 17.5 AW^{-1},

respectively. It was observed that performance of photodetector with MXene ($Ti_3C_2T_X$) transport layer is better compared to graphene transport layer based photodetector.

The enhancement in ReS_2/MXene compared to ReS_2/Gr structure is attributed to the large density of states and band alignment at the interface. Due to surface terminations (dangling bonds) MXene has a large number of surface states compared to graphene. In order to understand the phenomena, detailed mechanisms studies are presented in terms of density of surface states and energy band diagram. The successful demonstration of highly responsive flexible and biodegradable photodetector on paper substrate projects potential applications in future optoelectronics field.

2.2 Experimental Section

Synthesis Procedure of ReS_2

ReS_2 was synthesized using the hydrothermal technique [128], wherein 0.149 g of NH_4ReO_4, 0.209 gm of CH_4N_2S, and 0.0936 gm of $NH_2OH.HCl$ was added to DI water (30 mL quantity) and later transferred to a 50 mL Teflon container. Further, the Teflon container was placed in stainless steel autoclave and held for 36 hours at 220^oC. Consequently, the final solution was centrifuged with IPA, DI water multiple times to remove unwanted residues. The conventional synthesis procedure of the ReS_2 is illustrated in Figure 2.1a, shown below.

Synthesis Procedure of $Ti_3C_2T_x$

$Ti_3C_2T_x$ was synthesized from Ti_3AlC_2 utilizing the MILD method [129]. In brief, initially, 0.8 g of LiF was added to 10 mL of 6M of HCl kept for 5 minutes of stirring. Subsequently, 0.5 g of Ti_3AlC_2 was added to the above mixture and kept for 36 hrs of uninterrupted stirring at room temperature. Later, the resultant solution obtained was subjected to centrifugal filtration numerous times till the pH reaches ~ 6-7. Further, the filtered $Ti_3C_2T_x$ solution was ultrasonicated for one hour in an ice bath. The conventional synthesis of the $Ti_3C_2T_x$ solution is illustrated in Figure 2.1b below.

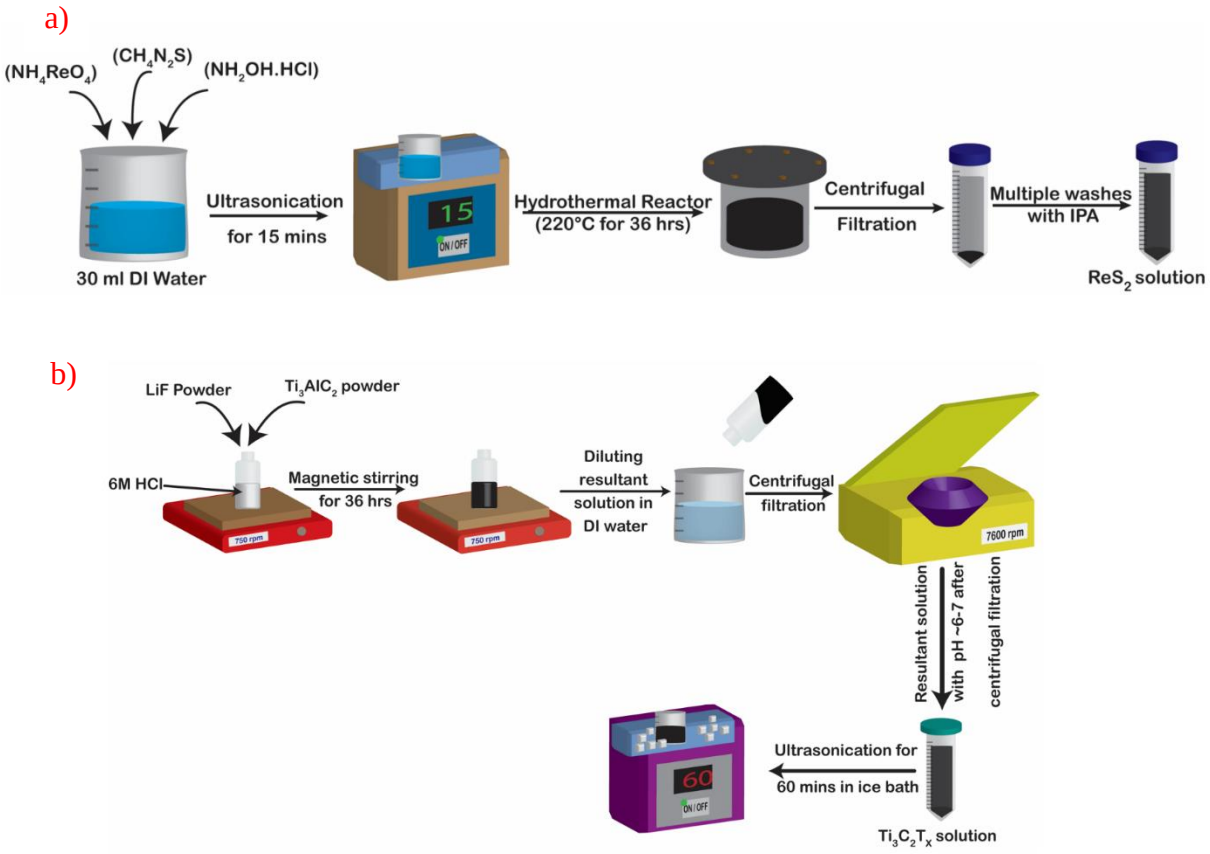

Figure 2.1: a) Synthesis procedure of the ReS_2 using a hydrothermal technique b) Synthesis of Ti3C2Tx utilizing the MILD technique.

Fabrication of the device

Synthesized $Ti_3C_2T_X$ was coated on a paper substrate of dimension (2 cm × 2 cm) using a highly scalable vacuum filtration method. Later, silver (Ag) lines of width 2 mm separated by 300 µm channel gap were deposited on $Ti_3C_2T_X$ coated paper substrate using thermal evaporation technique. MXene/paper with Ag contacts was cut into the required dimensions. Subsequently, synthesized ReS_2 solution was carefully drop-casted on MXene/paper with contacts and dried in hot air oven at 70 ^oC for 30 minutes. Figure 2.2 illustrates the complete fabrication process. Also, ReS_2/Graphene device was prepared by depositing graphene on paper substrate using dip-coating method and followed by drop-casting of synthesized ReS_2. Furthermore, FESEM image of ReS_2/Graphene can be found in Figure S1, Appendix A.

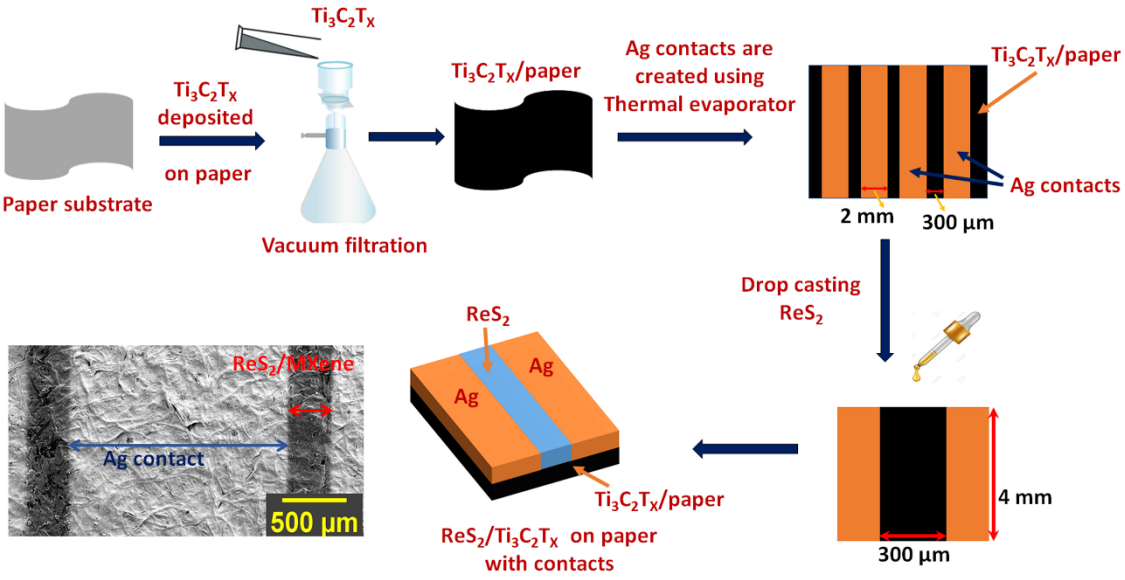

Figure 2.2: Schematic illustrating the fabrication of $ReS_2/Ti_3C_2T_X$ heterostructure on paper substrate.

2.3 Results and discussions

Characterization details of synthesized pristine ReS_2 and MXene ($Ti_3C_2T_X$) are included in Appendix A as Figure S2 and Figure S3, respectively. Figure 2.3a displays the XRD spectra for $ReS_2/Ti_3C_2T_x$ thin film. The XRD spectra validate the successful deposition of $ReS_2/Ti_3C_2T_x$ thin film, wherein the attained XRD spectra of $ReS_2/Ti_3C_2T_x$ was accredited to diffraction peaks at 6.51°(0 0 2), 14.50°(1 0 0), 16.52°(1 1 0), 22.69° (2 0 0), 27.07° (0 0 6), 32.61° (-1 2 0), 32.70° (0 0 2), 41.60° (1 0 5), 42.92° (-1 2 1), 56.95°(0 -2 4), 57.80° (-1 2 2), 60.56° (1 1 0), respectively. The inhibition of peak at 39.04° and the shift of peak pattern to 5.51° from 9.52° peak implies the successful exfoliation of Al from Ti_3AlC_2 with JCPDS number 52-0875 to form resultant $Ti_3C_2T_x$ along with -OH, -F, -O terminal groups by using the MILD method, and the presence of ReS_2 with JCPDS number 82-1379 in the resultant $ReS_2/Ti_3C_2T_x$ thin film was confirmed. The existence of peaks at 16.52° (1 1 0), and 22.69° (2 0 0) are attained with JCPDS number 03-0226 in the final XRD spectra was from cellulose paper substrate. In particular, uneven XRD profile from the planes (-1 2 0), (0 -1 3), and (0 -2 4) of ReS_2 is a characteristic signature of TMDs that are in thin-layered form and also attributed to the Warren effect of its corresponding TMDs layered structure crystal lattice. The achieved XRD results are found reliable with the existing literature [130,131].

Figure 2.3b depicts the XPS survey spectra of $ReS_2/Ti_3C_2T_x$ thin film deposited on cellulose paper with binding energy (B.E.) ranging between 0-800 eV. Figure 2.3c exhibits the Re 4f deconvoluted XPS spectra, which discloses the peaks $4f_{7/2}$, $4f_{5/2}$ at binding energies 41.86 eV, 44.24 eV, respectively. Figure 2.3d displays element S 2p deconvoluted XPS spectra and obtained peaks S $2p_{3/2}$, S $2p_{1/2}$ at B.E. 162.41 eV, 163.61 eV. Figure 2.3e depicts the Ti 2p deconvoluted XPS spectra and shown that the pair $2p_{1/2}$ at 461.3 eV and $2p_{3/2}$ at 454.58 eV assigned to Ti-C, Ti^{3+} oxide at B.E. 462.59 eV and 456.88 eV and Ti-O oxide at B.E. 464.41 eV, 459.32 eV. Moreover, Ti^{2+} oxide at $2p_{3/2}$ and Ti-O-F at $2p_{1/2}$ were obtained at B.E. 455.58 and 465.71 eV, respectively. Figure 2.3f illustrates the C 1s deconvoluted XPS spectra, wherein C-O, C-Ti-T_x (I, II, III or IV), graphitic C-C and C-O are prominent C 1s peaks, observed at B.E. 288.54, 285.03, and 281.83 eV. Figure 2.3g reveals the F 1s deconvoluted spectra, wherein the major contribution is designated to C-Ti-F groups at B.E. 685.04 eV. Furthermore, the F atoms associated with the unidentified fluorinated phase is found at 686.82 eV. Also, contributions owing to CF_{2+X} were obtained at 689.21 eV. Figure 2.3h exhibits the O 1s deconvoluted XPS spectra, wherein contributions from C-Ti-$(OH)_x$, C-Ti-O_x, and TiO_2, are obtained at 532.47, 530.59, and 529.58 eV. Further, the XPS spectra for each element deliberated above were found reliable with the reported literature [130,132,133]. Owing to $ReS_2/Ti_3C_2T_x$, thin film deposition was performed in open atmospheric conditions on cellulose paper substrate, the minimal oxidation observed in the spectra.

Figure 2.3i depicts the Raman spectra of $ReS_2/Ti_3C_2T_x$. However, the typical peaks obtained at 205, 311, and 420 cm^{-1} Raman shifts can be assigned to E_{1g} (first order in-plane vibrations), A_{2g} (second order out-of-plane vibrations), and A_{1g} (out-of-plane first order vibrations), corresponding to ReS_2. Furthermore, the typical peak found at 203 cm^{-1} assigned to A_{1g} (out-of-plane first-order vibrations related to Ti, C), and peak acquired at 403, 630 cm^{-1} assigned to shear mode (in-plane) vibrations of Ti, C corresponding $Ti_3C_2T_x$ of $ReS_2/Ti_3C_2T_x$ thin film [134–136]. Further, the existence of few layered structure of $ReS_2/Ti_3C_2T_x$ nanohybrid based photodetector was corroborated from the distinctive peaks realized in Raman spectra due to in-plane/out-of-plane vibrations explained above. Figure 2.3j displays the FESEM images of $ReS_2/Ti_3C_2T_x$ thin film at high magnification which was deposited on cellulose paper. In particular, from surface morphology images, it is evident that ReS_2 nanosheets are deposited on the $Ti_3C_2T_x$ deposited cellulose paper. It is important to note that that there will be alteration in the microstructure of $Ti_3C_2T_x$ by increasing the dwell time for the synthesis process as it was synthesized using

chemical etching (MILD) technique, but resultant $Ti_3C_2T_x$ was successfully synthesized at 36 hrs dwell in LiF + HCl etchant which was clearly proven by using XRD spectra of pristine $Ti_3C_2T_x$ displayed below in Figure S3a of supplementary information. However, post chemical etching process there is a process called delamination, can be done by ice bath sonication method to tune the interplanar spacing of layered $Ti_3C_2T_x$. In conclusion, the microstructure of attained $Ti_3C_2T_x$ can be tuned by increasing the ice bath sonication time instead of varying the chemical etching time for synthesizing $Ti_3C_2T_x$ from Ti_3AlC_2. Furthermore, the chemical etching can be done utilizing other acids such as HF which will result in different microstructure [137], but extensive usage of HF hinders the electrical conductivity of the resultant $Ti_3C_2T_x$ which in turn show effect on the device performance of as fabricated $ReS_2/Ti_3C_2T_x$ photodetector.

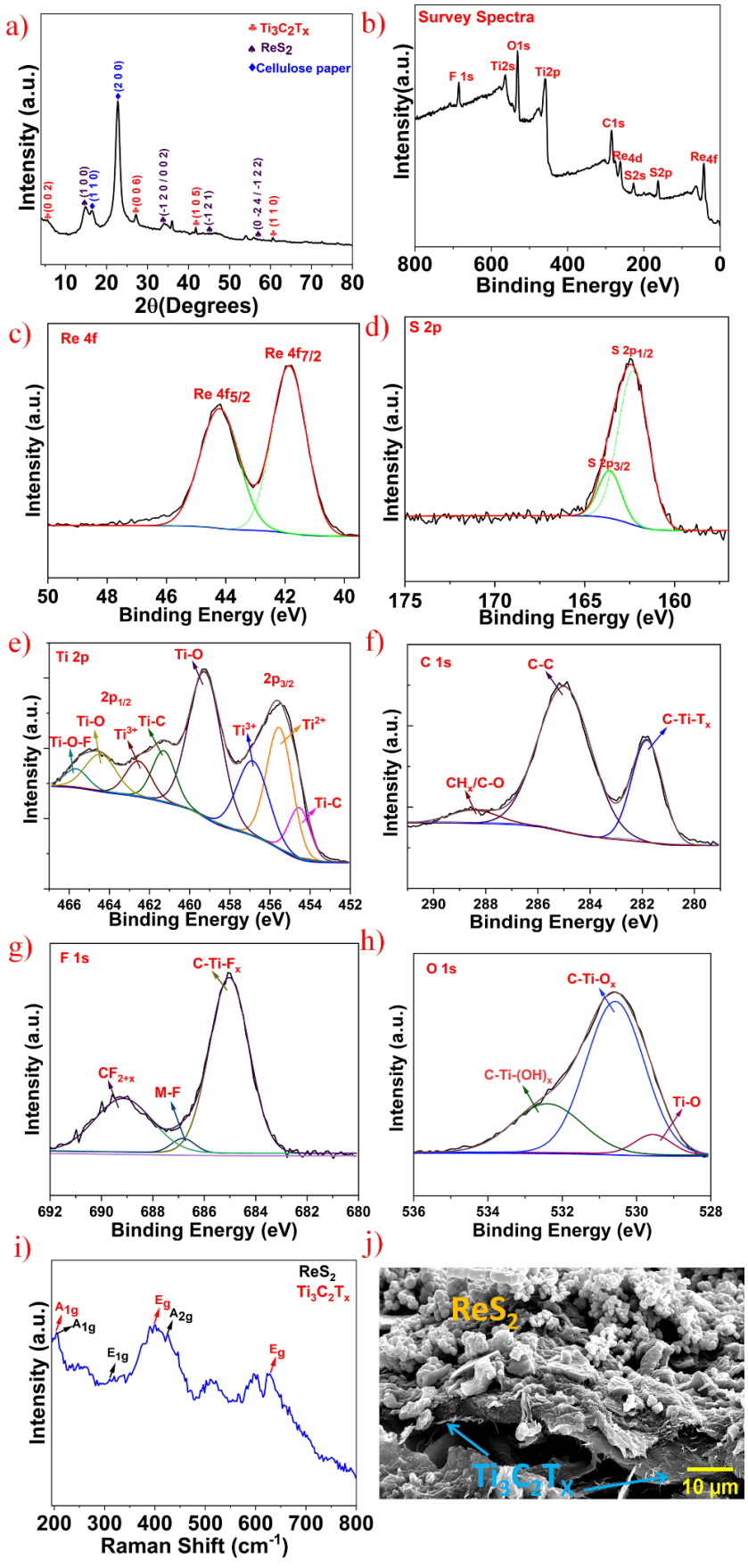
a)
Ti3C2Tx
ReS2
Cellulose paper
Intensity (a.u.)
2θ(Degrees)
b)
Survey Spectra
Intensity(a.u.)
Binding Energy (eV)
c)
Re 4f
Re 4f5/2
Re 4f7/2
Intensity (a.u.)
Binding Energy (eV)
d)
S 2p
S 2p1/2
S 2p3/2
Intensity (a.u.)
Binding Energy (eV)
e)
Ti 2p
Ti-O
2p3/2
2p1/2
Ti-O
Ti3+
Ti-C
Ti-O-F
Ti3+
Ti2+
Ti-C
Intensity (a.u.)
Binding Energy (eV)
f)
C 1s
C-C
C-Ti-Tx
CHx/C-O
Intensity (a.u.)
Binding Energy (eV)
g)
F 1s
C-Ti-Fx
CF2+x
M-F
Intensity (a.u.)
Binding Energy (eV)
h)
O 1s
C-Ti-Ox
C-Ti-(OH)x
Ti-O
Intensity (a.u.)
Binding Energy (eV)
i)
ReS2
Ti3C2Tx
A1g
A1g
E1g
Eg
A2g
Eg
Intensity (a.u.)
Raman Shift (cm-1)
j)
ReS2
Ti3C2Tx
10 μm

Figure 2.3: a) ReS_2/MXene XRD Spectra b) ReS_2/MXene Survey Spectra, c-h) Deconvoluted XPS Spectra of individual elements, i.e., Re 4f, S 2p, Ti 2p, C 1s, F 1s, and O 1s, i) Raman spectra of ReS_2/MXene, j) FESEM image of ReS_2/MXene at high magnification.

Photodetection measurements:

Figure 2.4a illustrates the schematic of the fabricated ReS_2/MXene device (0.3 mm × 4 mm). Various lab-based experiments were performed to verify the photodetection capability of the fabricated ReS_2/MXene photodetector. Current-voltage (I-V) curves for the fabricated ReS_2/MXene device are shown in Figure 2.4b, with the measurements conducted in the dark, and at different visible light illuminations. The linear I-V characteristics confirm the ohmic contact. Under NIR light illumination, similar measurements were performed, and the I-V characteristics are shown in Figure 2.4c. With constant visible and NIR illuminations, the switching stability of the photodetector was investigated. The results are depicted in Figure 2.4d and 2.4e, respectively, where the light intensity applied is 0.25 mW/cm^2. As evident by the UV-visible spectra depicted in Figure S2f, Appendix A, the change in photocurrent is greater under visible light illumination than under NIR light illumination. Figure 2.4f shows the temporal response at different visible light intensities from 0.25 to 12.73 mW/cm^2 at a bias voltage of 2 V; when the light intensity increases, an increase in photocurrent was noticed, which is in line with I-V curves. The increase in device current under light illumination is ascribed to the generation of huge number of excitons in ReS_2. Additionally, the device response v/s time is plotted in Figure 2.4g under different NIR light illumination, and the similar pattern of increased current has been observed with an increase in intensity.

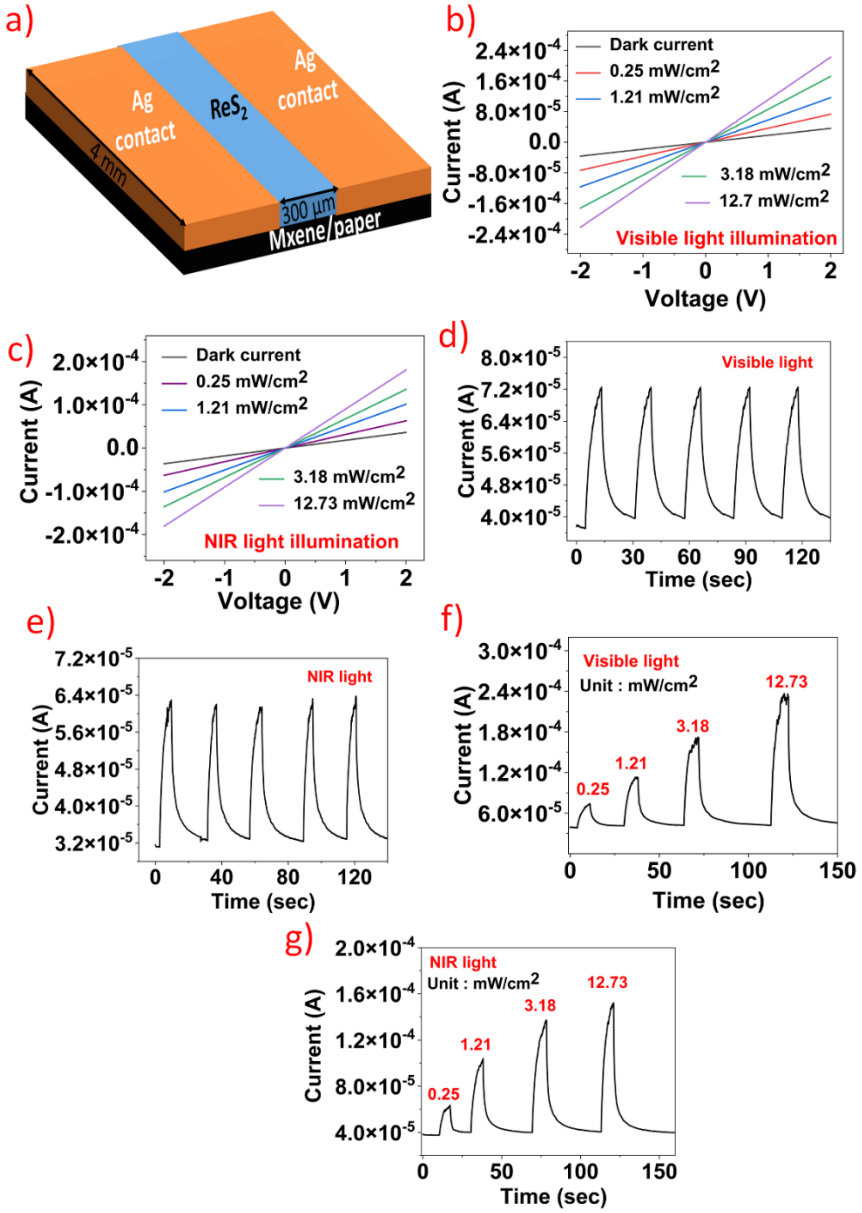

Figure 2.4: a) Illustration of fabricated ReS_2/MXene b,c) I-V characteristics of ReS_2/MXene device under visible and NIR regions d,e) Temporal response under constant light illumination of visible and NIR light, 0.25 mW/cm^2 f,g) device current vs. time plot under various visible and NIR illuminations.

Three widely accepted measures for photodetectors are responsivity (R), external quantum efficiency (EQE), and detectivity (D*). R represents the photocurrent produced per unit area by the illumination of light. The ability to distinguish weak signals from noise is represented by the detectivity of the photodetector. EQE refers to the number of charge carriers that are collected by the photodetector to the number of photons. R, EQE, and D* can be stated as follows:

$$R = I_{ph}/(P \times A)$$

$$EQE = hc \times (R/e\lambda) \times 100$$

$$D^* = (R \times \sqrt{A})/\sqrt{2 \times I_d \times q}$$

wherein, I_d, A, P, I_{ph}, *and* q represent device current in dark, active area of the photodetector, illuminated light intensity, charge of electron. Active area (A) of the fabricated sensor is 1.2 mm^2.

Responsivity of the photodetector for visible and NIR light illumination was calculated to be ~ 40.8 $AW^{-1}$and ~ 26.9 AW^{-1} at 0.25 mW/cm^2, as depicted in Figure 2.5a and 2.5b. The responsivity graph shows that the ReS_2/MXene photodetector has a higher responsivity for visible light compared to NIR, due to the high absorption of prepared ReS_2 in the visible range, as depicted in absorption spectrum shown in Figure S2f, Appendix A. Responsivity of the device declines as intensity increases, which is in line with published reports [138,139]. This phenomenon can be related to the trap states present in ReS_2. During low light illuminations, photogenerated electrons are mostly captured by trap states near the conduction band, which minimizes the amount of electron-hole pairs recombination. As intensity is increased, a smaller proportion of the photo-generated electrons will be trapped because of the limited number of available trap states. As a result, the fabricated device becomes more sensitive to low light illuminations. Furthermore, responsivity of the fabricated ReS_2/graphene based photodetector for visible and NIR illumination was found to be 26.5 AW^{-1} and 17.5 AW^{-1}, respectively, as illustrated in Figure 2.5a and 2.5b. Further wavelength dependence of the fabricated $ReS_2/Ti_3C_2T_X$ photodetector was investigated and the corresponding response spectrum can be found in the Appendix A, Figure S4.

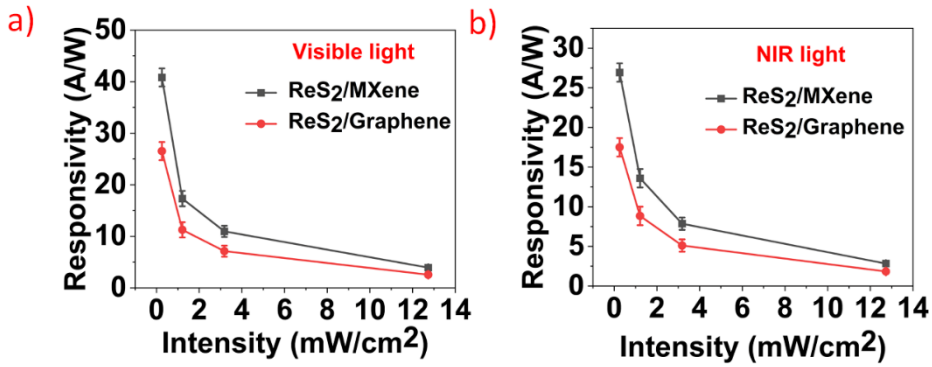

Figure 2.5: a,b) Responsivity of fabricated ReS_2/MXene and ReS_2/Graphene under visible and NIR light illumination.

Density of Surface States Calculation for MXene and Graphene:

The better performance of ReS_2/MXene compared to ReS_2/Gr can be understood by calculating the density of surface states. I-V measurement of $Ti_3C_2T_X$/Ag and graphene/Ag reveal Schottky characteristics and the graphs for the same are given in Figure S5, Appendix A. Further, thermionic emission theory was used to understand the transport mechanism, and current (I) can be expressed as [140]:

$$I = I_0 \exp\left((q(V - IR)/\eta KT\right)$$

$$I_0 = aA^*T^2 \exp\left(-q\Phi_B/KT\right)$$

$$A^* = (4\pi q m^* K^2)/h^3$$

$$\eta = q/KT \; \frac{dV}{d(\ln I)}$$

Where K, η, R, and q represent Boltzmann constant, ideality factor, series resistance electronic charge, respectively. Ideality factor (η) indicates the deviation of I-V curve from ideal characteristics. A* is Richardson constant, a is junction area, and T is absolute temperature. Φ_B is barrier height, h is planks constant and I_0 is reverse saturation current. The ideality factor of the $Ti_3C_2T_X$/Ag and Gr/Ag were calculated to be 1.49 and 1.3, respectively, by a linear fit of semilog graph of current vs. voltage. The deviation of the ideality factor from the ideal value of 1 is ascribed to the presence of surface defect states. Further, density of surface states (N_{SS}) of $Ti_3C_2T_X$/Ag and Gr/Ag structures were calculated. Assuming the equilibrium state, N_{SS} was calculated using the voltage dependence η using the following equation [140]:

$$N_{SS} = (\eta - 1)\frac{\varepsilon_i}{q\delta} - \frac{\varepsilon_{sc}}{qW}$$

Where δ and ε_i are thickness and relative dielectric constant, respectively. ε_i is assumed to be permittivity of air, as the device is exposed to air, and thickness is considered as 5 A^o. W and ε_{sc} are width and relative dielectric constant, respectively. Width (W) was considered as 160 nm, and ε_{sc} for $Ti_3C_2T_X$/Ag and graphene/Ag interface was considered as $370\varepsilon_0$ [141] and $8\varepsilon_0$ [142], respectively.

$$E_c - E = \Phi_B - qV$$

Graph plotted between E_c-E and density of surface states and it was observed that density of surface states increases towards the bottom of the conduction band and the number of surface states in graphene are less than that of $Ti_3C_2T_X$, as shown in Figure 2.6a and 2.6b. Large number of surface states in MXene ($Ti_3C_2T_X$) are attributed to the surface

terminations (O, F, and OH) and dangling bonds, which is evident from the FTIR spectra of pristine $Ti_3C_2T_X$, Figure S3g, Appendix A. The number of surface states can be related to the trap states. Since the number of trap states are more in MXene, the lifetime of the photogenerated carriers is increased, which leads to enhanced responsivity when compared to Graphene as a transport layer.

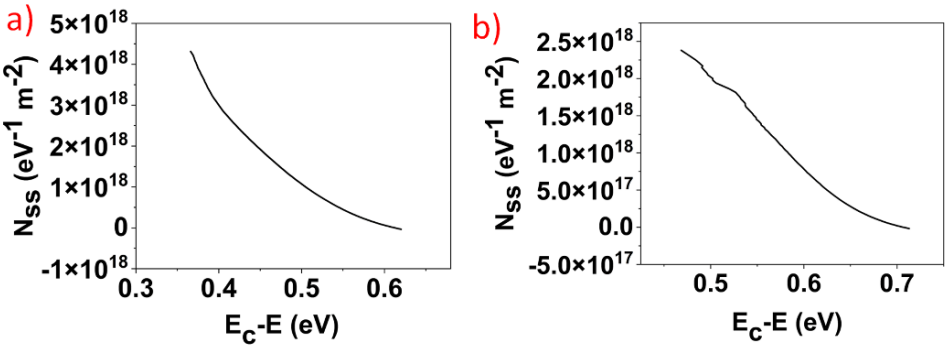

Figure 2.6: a, b) Density of surface states (N_{SS}) as a function of $E_c - E$ of MXene ($Ti_3C_2T_X$) and Graphene.

The EQE of the device was drawn against the intensity of the light, as depicted in Figure 2.7a. For visible and NIR light illuminations, the EQE of the constructed ReS_2/MXene photodetector was calculated to be ~ 91.36 × 10^2 % and ~ 42.8 × 10^2 %, respectively. As EQE is proportional to photodetector responsivity, EQE plot shows a similar trend where EQE values decline with increasing light intensity. Detectivity (D*) of the device in visible and NIR regions was ~ 1.07 × 10^{12} Jones and ~ 7.08× 10^{11} Jones, respectively, as illustrated in Figure 2.7b. One of the essential factors to consider when evaluating the performance of a photodetector is response time (or rise time). Rise time is the time interval between $0.9I_{peak}$ and $0.1I_{peak}$ points on the device current, wherein I_{peak} represents the device current peak value. For visible and NIR light irradiation, the rise time of the fabricated photodetector was ~ 3.7 sec and ~ 3.85 sec, respectively, as seen in Figure 2.7c and 2.7d. Transmit time of charge carries is defined as $\tau_r = L^2/V_{bias}(\mu)$. Transit time is inversely proportional to the mobility of the carrier (μ). The slow response time of the fabricated photodetector is attributed to the existence of impurity states or defect states in synthesized ReS_2 using solution processed method, and the rough surface of the paper substrate impedes charge carrier movement. In addition, the photodetector bendability was verified by 500 continuous bending cycles. While performing the bending test, a 2% strain was applied to the device and it was returned to its original position, and later

photodetector studies were performed. As seen in Figure 2.7e, the responsivity remained unchanged after 500 continuous bending cycles, showing the device robustness.

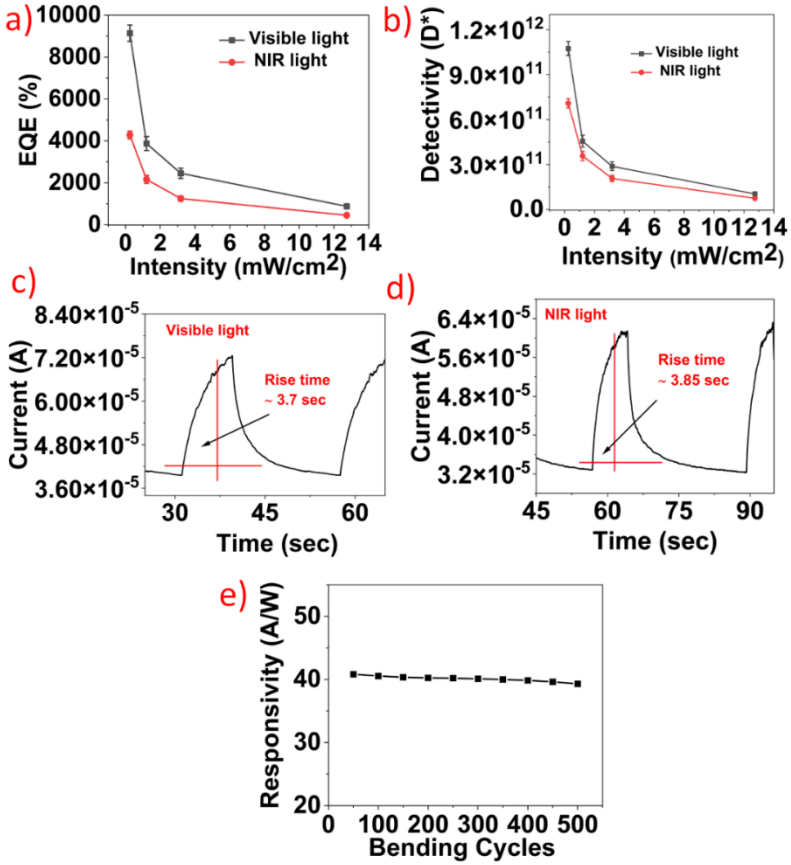

Figure 2.7: a,b) EQE and detectivity of the fabricated ReS_2/MXene photodetector c,d) Rise time of the fabricated ReS_2/MXene device under visible and NIR light illuminations e) Graph illustrating the responsivity vs. number of bending cycles of fabricated ReS_2/MXene device.

2.3.1 Photodetection mechanism

Photodetection phenomenon of the ReS_2/MXene($Ti_3C_2T_X$) device is understood using the band energy diagram of the heterostructure. Work function of synthesized ReS_2 and $Ti_3C_2T_X$ were determined using ultraviolet photoelectron spectroscopy (UPS) spectra. The measured secondary electron cutoff energy of ReS_2 was around 16.12 eV as shown in Figure 2.8a. Work function was calculated to be 5.1 eV by subtracting the cutoff energy from excitation energy (He I, 21.22 eV). Similarly, for $Ti_3C_2T_X$ cutoff energy was found to be 15.5 eV as shown in Figure 2.8b and the work function was calculated to be 5.72 eV. For ReS_2, the valence band maximum with respect to Fermi level was found to be 1.04 eV. The energy band diagram of interface was drawn by utilizing calculated work function and bandgap values, as shown in Figure 2.8c and 2.8d.

Thus, discretely distributed Schottky barriers are formed at the interface of $ReS_2/Ti_3C_2T_X$ heterojunction, and the band energy diagram of the $ReS_2/Ti_3C_2T_X$ under nonequilibrium state upon light illumination is illustrated in Figure 2.8d. It shows a band bending at the interface of ReS_2 and $Ti_3C_2T_X$ due to the work function difference, creating a strong built-in electric field at the interface pointing from ReS_2 to $Ti_3C_2T_X$. When light is illuminated on $ReS_2/Ti_3C_2T_X$ heterostructure, electron-hole pairs would be generated in ReS_2. Photogenerated electron-hole pairs in pristine ReS_2 have a high tendency to recombine because of the lack of internal electric field. Hence the need of transport layer arises which not only generates internal electric field and also assists in quick collection of generated charge carriers at the electrodes. The photogenerated electron/hole pairs in ReS_2 are promptly and effectively separated due to internal electric filed created at $ReS_2/Ti_3C_2T_X$ interface. This charge separation is favourable in reducing the recombination electrons and holes, which enhances the photocurrent. As the work function of MXene is less than conduction band of the ReS_2 the photogenerated carriers are transported to MXene. Due to high mobility of MXene, accumulated charge carriers in MXene could be captured by the electrodes immediately under the external bias, resulting in a high photocurrent. Photoconductive gain is expressed as $G = \tau_{lifetime}/\tau_{transit}$ where $\tau_{lifetime}$ represents lifetime and $t_{transit}$ is transit time of the photogenerated carriers [94]

In photoconductor, transit time is defined as $\tau_{transit} = L^2/(\mu V_{bias})$, where V_{bias} is applied bias voltage, L is the length of the channel, and μ is the mobility of the charge carriers. Hence, the gain of photoconductor is directly proportional to charge carriers lifetime ($\tau_{lifetime}$). The trap states in a semiconductor photoconductor play an important role in increasing the life time of photoexcited carriers [143][144][145][94]. The trap states available at ReS_2/MXene interface and reduces the recombination rate, which leads to the increment in the lifetime ($\tau_{lifetime}$) charge carriers significantly. The increase in lifetime ($\tau_{lifetime}$) leads to high photoconductive gain/responsivity of the fabricated photodetector. Furthermore, energy band diagram of ReS_2/Graphene under light illumination is illustrated in Figure S6, Appendix A.

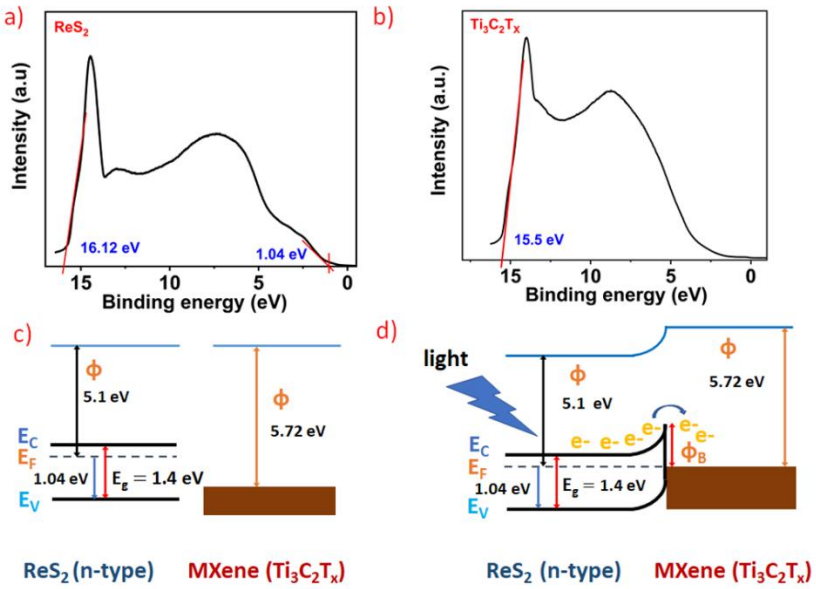

Figure 2.8: a-b) UPS spectra (measured by He I source, hν = 21.22 eV) of pristine ReS_2 and pristine $Ti_3C_2T_X$. Illustration of the energy band diagram of ReS_2/MXene ($Ti_3C_2T_X$): c) before contact d) Schottky junction upon light illumination. φ, E_C, E_F, and E_V represent work function, conduction band, Fermi level, and valence band.

The performance of the fabricated flexible photodetector is compared with recently reported photodetectors, as listed in Table 2.1, indicating that the fabricated device highly competitive. *Kwak et al.* developed a high-performance hybrid photodetector using InP-QDs and black phosphorous (BP), wherein BP was used as a transport layer [93]. High performance of InP-QDs/BP based photodetector was ascribed to the transfer of photogenerated electrons to BP layer. *Wang et al.* highly photosensitive $CsPbBr_3$ QDs based photodetector using ZnO nanorods as electron transport layer [146]. *Abid et al.* demonstrated a wearable UV light sensitive photodetector based on WS_2-QDs/RGO heterostructure, wherein p-type RGO was utilized as a carrier transport medium[98]. *Zhang et al.* demonstrated a hybrid photodetector by stacking graphene on MoS_2 layer [92]. Enhancement of responsivity in MoS_2/Graphene device is attributed to graphene transport layer, wherein photogenerated electrons in MoS_2 are transferred to graphene. *Luo et al.* constructed a UV photodetector using ZnO nanorod array/CuSCN/rGO, and CuSCN/rGO was utilized as a hole transport layer [147]. Most of the above reports used high temperature and expensive fabrication techniques. In this work, ReS_2/$Ti_3C_2T_X$ based

visible-NIR photodetector was fabricated on a flexible and biodegradable paper substrate, wherein MXene($Ti_3C_2T_X$) was used as a transport layer, using facile, simple, clean room free and low temperature hydrothermal and vacuum filtration method.

Material	Substrate	Fabrication techniques	Photodetection Range	Responsivity (A/W)	Ref.
WS_2/ReS_2	SiO_2/Si	Exfoliation	Visible	0.0018	[148]
WSe_2/ReS_2	SiO_2/Si	Exfoliation	Visible	3	[149]
MoS_2/ReS_2	SiO_2/Si	CVD	Visible-NIR	42.61	[150]
$MoTe_2/ReS_2$	Glass	Exfoliation	Visible-NIR	0.54	[151]
ReS_2/Graphene/ WSe_2	SiO_2/Si	Exfoliation	Visible to infrared	1.02	[152]
1D Se/2D ReS_2	SiO_2/Si	CVD	UV	36	[153]
n-ReS_2/p-Si	Si	Exfoliation	Visible	33.47	[154]
$CsPbBr_3$ QDs/ ZnO	ITO	Pulse laser deposition	UV-Visible	0.14	[146]
WS_2-QDs/RGO	Textile cloth	Hummers' and solvothermal method	UV	5.22×10^{-3}	[98]
ZnO NR/CuSCN/ rGO	FTO glass	Hydrothermal	UV	18.65×10^{-3}	[147]
SnS_2/Gr	Paper	Hydrothermal	Visible-NIR	6.98×10^{-3}, 3.67×10^{-3}	[99]
ReS_2/ $Ti_3C_2T_X$	**Paper**	**Solution process method, etching method**	**Visible-NIR**	**40.8, 26.9**	**This work**

Table 2.1: Performance evaluation of the fabricated photodetector.

2.4 Conclusion

In summary, flexible, biodegradable, and high-performance ReS_2/MXene($Ti_3C_2T_X$) based visible-NIR photodetector on paper substrate was fabricated using facile and simple hydrothermal and vacuum filtration method. It is observed that integration of ReS_2 and $Ti_3C_2T_X$ creates a sufficient Schottky junction induced built-in electric field, which rapidly separates photogenerated electron-hole carriers. Further, contacts were taken from MXene ($Ti_3C_2T_X$) to avoid the trapping of carriers in ReS_2. Responsivity of the fabricated ReS_2/MXene photodetector was calculated to be 40.8 A/W and 26.9 A/W under visible and NIR illuminations, respectively. Also, it was found that MXene can be

a better alternative to graphene as a transport layer in the fabrication of 2D materials based flexible photodetectors due to the creation of more surface states, thereby creating more trap states. Even after 500 continuous bending cycles, the developed ReS_2/MXene photodetector performance was unchanged, suggesting that the device is quite robust. It is believed that due to excellent performance of the fabricated photodetector, this is a promising study for future flexible and biodegradable nanoelectronics applications of optoelectronics field.

CHAPTER 3

Fabrication of high performance photodetectors using plasmonic effect

Another technique to enhance the performance of a 2D materials based photdetectors is plasmonic effect by integrating metal nanostructures. It is known to us that 2D material can have remarkably high single-pass absorption. However, most light will still transmit through the thin layers of the material. Therefore, the light-matter interactions must be further enhanced before it can be used in practical applications, especially for light detection. The combinations of plasmonic metal nanostructures with 2D materials can enhance light-matter interactions. Either decorating/patterning plasmonic nanostructures on top of 2D materials or stacking 2D materials on top of those plasmonic nanostructures can increase the light absorption at certain wavelengths. On the other hand, a direct contact between 2D materials and metals enables hot electron injection over Schottky barriers.

3.1 MoS_2/paper Decorated with Metal Nanoparticles (Au, Pt and Pd) Based Plasmonic-Enhanced Broadband (Visible-NIR) Flexible Photodetectors

Even though there are reports on flexible photodetectors, one of the main issues that still need to be resolved is the lower values of responsivity arising due to the use of non-conventional substrates such as polymers, cellulose paper, etc. There are ways to improve the responsivity such as piezotronics and surface plasmonic resonance but studies on utilizing the same for flexible substrates remain limited. Further, comparative performance of different nanoparticles remains unexplored. This work demonstrates the fabrication of flexible visible/near-infrared (NIR) photodetectors by functionalizing MoS_2 grown on paper substrate with various noble metal nanoparticles (NPs) such as gold (Au), platinum (Pt), and palladium (Pd) for enhanced photoresponse. The metal NPs-MoS_2 (Au, Pt, Pd-NPs-MoS_2) based photodetector showed a prominent improvement in the photoresponse characteristics when compared to pristine MoS_2. Enhancement in the photodetector performance is mainly due to the localized surface plasmon resonance (LSPR) of prepared metal NPs and increase in incident light

scattering. Out of the fabricated metal NPs-MoS_2 photodetectors, Au-NPs/MoS_2 showed maximum responsivity of 99.3 mA W^{-1} and 46.03 mA W^{-1} under visible and NIR region, respectively which is ~ 8 times higher than pristine MoS_2.

3.1.1 Introduction

The increasing demand for wearable, foldable, portable electronics, especially in the biomedical field, has led to an exploration of flexible substrate photodetectors. In the recent years, outstanding achievements have been achieved in the development of flexible electronics, especially in the biomedical field, has led to an exploration of flexible substrate photodetectors[155][156]. These devices are far more compact and cost-effective compared to the conventional bulk substrate devices and reduce the expenditure on material as well as fabrication [157] Still several issues need to be addressed [158]. Some of the issues are: Surface roughness, thermal stability and cleanroom compatibility. Almost of the flexible substrates utilized (polymers, paper, textile, etc.) have rough surface which not only affects the charge carrier mobility but also increases the recombination rate. Further, the rise time is also affected which affects the gain of the photodetector. The second is thermal stability i.e. most of the flexible substrates cannot withstand high temperatures and hence performing high temperature processes is not possible which restricts limited fabrication methodologies[159]. Lastly, the flexible substrates are not cleanroom compatible and novel methodologies needs to be developed for integrating novel functional nanomaterials onto the flexible substrates. Novel functional materials ranging from 0D to 2D, and hybrids (0D-1D, 0D-2D, 1D-2D) based on these materials have been explored for this purpose [160][106][161][162]. Piezotronics is another means to improve the responsivity upon application of external strain which modulates the depletion region width and increases the electric field and thereby the responsivity. But the issue with piezotronics is that, the application of strain leads to permanent damage in the device, thereby decreasing the reliability of the photodetector. Localized surface plasmon resonance (LSPR) is another means of increasing the absorption, and hence the responsivity and speed and is a widely researched domain for conventional rigid substrate devices with the decoration of noble nanoparticles [163][164]. However, reports on the use of metal nanoparticles for high performance flexible devices using LPSR are few. Moreover, the reports on the comparative performance of different nanoparticles also remain limited. Hence, there is a need to explore Plasmonic enhancement in flexible substrate devices.

Transition Metal Dichalcogenides (TMDs) are a popular class of 2D materials because of their outstanding optical and mechanical properties and tunable bandgap [165]. Of these, MoS_2 is of special interest due to its superior electrical properties, high mobility, suitable elastic modulus and bandgap that ranges from 1.2 - 1.8 eV depending on the number of layers [166–168]. On the other hand, light incident on the plasmonic nanoparticles makes the charge clouds in the NP oscillate. This collective oscillation of the charge clouds (surface plasmons) with the incident light is called LSPR. This helps improve the absorption of light through generation of hot carriers, near field enhancement and far field scattering. MoS_2 absorbs only in the visible and near IR range, and so combining plasmonic nanoparticles with MoS_2 can enhance its performance in the visible and NIR regions. Such a device would have potential applications in military and soft biomedical devices in the healthcare industry.

There are many reports on plasmonic enhancement in MoS_2 based rigid substrate photodetectors [169][170][171][172]. However, reports on plasmonic enhancement in MoS_2 based flexible substrate devices are scarce [173]. Further, while extensive research has been done using Ag and Au nanoparticles [173][174], reports on Pt and Pd nanoparticles are few [175]. Pd and Pt show promise because they exhibit strong catalytic activity over a broad spectral range, and strong absorption due to broad LSPR [176]. There are works comparing Au and Pt nanoparticles on N, F-Doped TiO [177] and Pt/Pd alternating nanodisk arrays with Ag [178]. However, to the best of the authors' knowledge, no work comparing individual Au, Pt and Pd nanoparticles for flexible MoS_2 photodetectors, exists. Hence, in addition to exploring the effect of plasmonic nanoparticles in MoS_2 based flexible photodetectors, a comparison between Au, Pt and Pd nanoparticles was studied.

Herein we demonstrate three novel, paper-based plasmonic photodetectors with Au/MoS_2, Pt/MoS_2 and Pd/MoS_2 heterojunctions, respectively. The heterojunction between the metal nanoparticle and MoS_2 allowed for an increase in absorption due to absorption and scattering by the metal nanoparticles and a phenomenon called LSPR. Among the fabricated metal NP-MoS_2 photodetectors, Au-NPs/MoS_2 showed maximum responsivity of 99.3 mA W^{-1} and 46.03 mA W^{-1} under visible and NIR region respectively. The Pt-NP/MoS_2 device demonstrated a responsivity of 51.4 mA W^{-1} and 42.3 mA W^{-1} in the visible and NIR region, respectively, and the Pd-NP/MoS_2 device performed with a responsivity of 46.03 mA W^{-1} and 34.7 mA W^{-1} in the visible and NIR

region respectively. Moreover, the device was constructed on cellulose paper making the fabricated device environment friendly and cost effective.

3.1.2 Experimental Section

Materials and characterizations:

All the chemicals used for the synthesis of MoS_2 and metal nanoparticels were procured from Sigma Aldrich, Molychem and have been used as received. Rigaku Smartlab X-ray diffraction (XRD) was used to study the Structural characterisation with Cu Kα radiation. Raman spectra analysis was carried out using LabRAM HR system with an excitation length of 532 nm. Optical properties of MoS_2 and metal nanoparticles were studied using UV-vis spectrometer, JASCO V-670. Source meter, Keithley 2450, was used for electrical measurements. Light sources of wavelength 554 nm (visible light) and 780 nm (NIR light) were used to carry out the photodetection experiments.

Direct growth of MoS_2 on paper substrate:

The direct growth of MoS_2 on paper substrate was carried out by a similar process repeated previously [179]. In brief, the growth process was carried out in two steps, seeding process followed by hydrothermal method. Seeding solution was prepared by dispersing $Na_2MoO_4.2H_2O$ (24 mg) and CH_4N_2S (15 mg) in 10 ml of DI water. The flexible paper substrate was immersed in the prepared seed solution for 60 min and later dried for 15 min at 65 ºC. Parallelly, a nutrient solution was prepared by mixing $Na_2MoO_4.2H_2O$ (362 mg) and CH_4N_2S (228 mg) in 30 ml of DI water. The well mixed nutrient solution and paper substrate which was seed coated were transferred to autoclave and kept in oven at 200ºC for 20 hr. The resultant black colour MoS_2 coated paper substrate was dried in hot air oven for 15 min at 65ºC.

Synthesis of Au, Pt, and Pd nanoparticles:

At room temperature, 1 mmol of gold chloride ($AuCl_3$), chloroplatinic acid (H_4PtCl_6) and palladium chloride ($PdCl_2$) each were dissolved separately in 1L of DI water followed by a sonication for 30 min. During the sonication HCl was added drop by drop to get stabilized and uniform NPs. These synthesized NPs were used for decoration of fabricated MoS_2/paper.

Fabrication of Device (drop casting Nano particles on MoS_2):

The prepared MoS_2/paper was cut into required dimension of 6 mm × 6 mm. Device was fabricated by drop casting synthesized metal nanoparticles (Au, Pt and Pd-NPs) on the

synthesized MoS_2 coated cellulose paper. Two electrodes were prepared using conductive and adhesive silver paste and for electrical measurement thin copper wires were bonded on silver paste. The detailed fabrication process is illustrated in Figure 3.1.

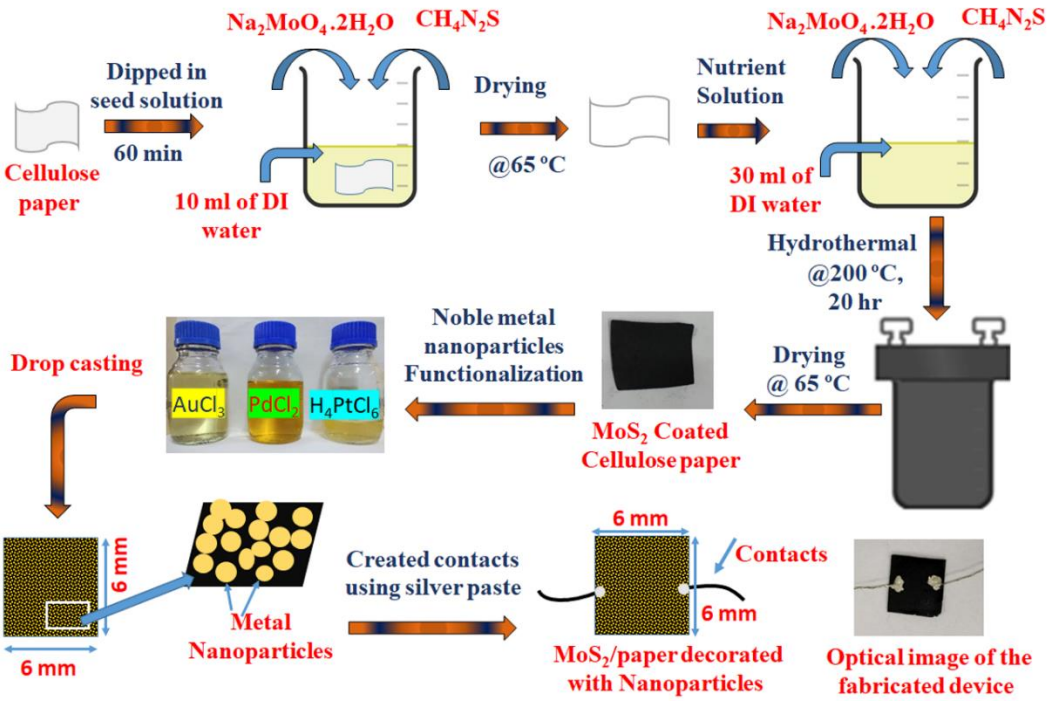

Figure 3.1: Schematic illustrating the fabrication procedure of Plasmatic Photodetector Au/Pt/Pd/MoS_2.

3.1.3 Results and Discussion

Surface morphology of MoS_2 grown on paper was analysed using FESEM study at different magnifications, as shown in Figure 3.2a-d. Low magnification FESEM image of MoS_2/paper is shown in Figure 3.2(a-b), wherein microfiber structure of cellulose paper was observed. As displayed in Figure 3.2c, high magnification FESEM images show the microflower morphology of the MoS_2, where individual MoS_2 nanoflakes aggregated. Figure 3.2d displays the highest magnification, 100 nm scale, FESEM image wherein individual nanoflakes of MoS_2 are clearly visible. Crystal structure of the MoS_2 grown on paper substrate was analysed using XRD. As seen in Figure 3.2e, XRD pattern of MoS_2 well matches with the JCPDS no: 37-1492 and it indicates the mixed phase of rhombohedral and hexagonal. The broadening peaks of (110) and (100) could be ascribed to the 200°C temperature of hydrothermal synthesis. Further, the formation of few layer MoS_2 can be confirmed by a small peak at ~ 14° [180][57]. Furthermore, Raman spectra analysis of pristine MoS_2 grown on cellulose paper was performed to confirm the number of layers and chemical composition. As displayed in Figure 3.2f, two prominent peaks

were observed at ~ 406 cm^{-1} and ~ 384 cm^{-1} which could be ascribed to A_{1g} (out-of-plane) and E_{1g} (in-plane). The E_{1g} and A_{1g} peaks were separated by ~ 22 cm^{-1} which suggests the formation of three-layer individual nanoflakes of MoS_2 [181][182]. Surface morphology of the MoS_2 functionalized with noble metal NPs is shown in Figure 3.2(g-h). Gold (Au) nanoparticles of size ~ 40 nm were discretely distributed over MoS_2 as seen in the high magnification FESEM image in Fig 2h. Pt nanoparticles with a dimension of ~ 55 nm on MoS_2 nanoflakes are clearly visible from the FESEM image shown in Figure 3.2 (i-j). Further, Palladium nanoparticles of size ~ 76 nm, comparatively larger, were observed on Pt NPs /MoS_2 paper substrate as seen in Figure 3.2(k-l). Further, to confirm the presence of metal nanoparticles over MoS_2/cellulose paper, elemental mapping of MoS_2/paper decorated with Au-NPs, Pt-NPs and Pd-NPs were performed. As expected, metal NPs were found to be discretely distributed on MoS_2/paper and it was also evident from FSEEM analysis. The elemental mapping of Au, Pt and Pd on MoS_2/paper can be found in the Appendix A (Figure S7-S9).

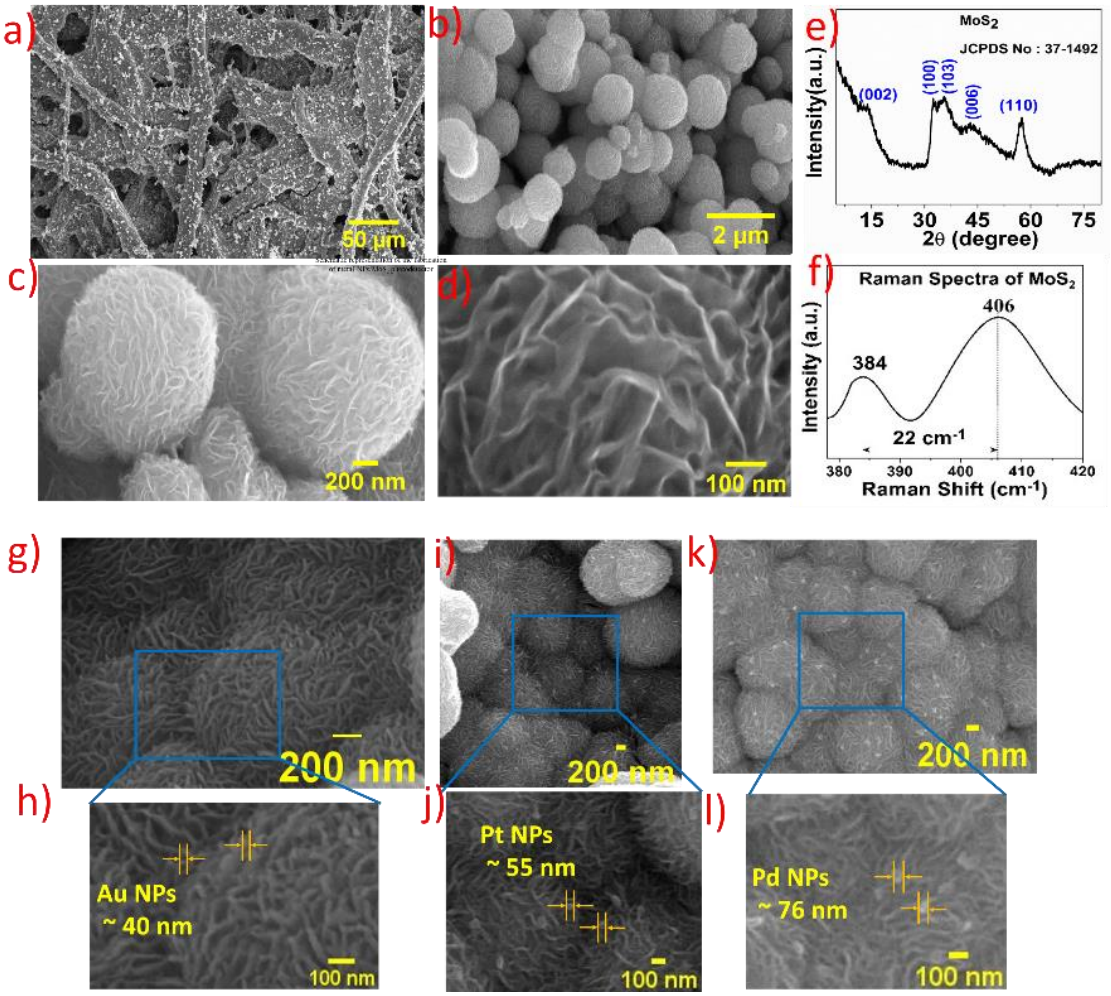

Figure 3.2: a-d) FESEM images of MoS_2 grown on paper substrate with low and high magnifications e) Graph showing XRD pattern of MoS_2/paper and f) Raman analysis of MoS_2/paper. FESEM images clearly showing the decorated NPs on MoS_2: g, h) Au NPs (~ 40 nm Au) i, j) ~55 nm Pt NPs k, l) ~76 nm Pd NPs.

To further study the elemental composition of synthesized pristine MoS_2, XPS measurements were performed. XPS survey spectra containing the prominent peaks representing Mo3d, S2p, C1s and O1s, shown in Figure S10 (Appendix A). Carbon peak is observed due to the stub used and oxygen peak is present due to partial exposure of MoS_2 to the atmosphere while carrying out the XPS experiments. As seen in Figure 3.3a, the deconvoluted high resolution spectra of Mo3d contains two signature peaks at 232.1eV and 228.7 eV which represents the Mo^{4+} $3d_{3/2}$ and Mo^{4+} $3d_{5/2}$ respectively [161] [58]. Also, a low intensity peak is observed around 235.3 eV, which indicated the +6 oxidation state of the Mo, which could be ascribed to the unreacted MoO_4^{2-} during hydrothermal synthesis of MoS_2. Another peak representing S 2s was observed at 225.2 eV. Figure 3.3b shows the high resolution spectra of S2p, which was deconvoluted to two characteristic peaks at 163.2 eV and 161.7 eV which indicates the $S2p_{1/2}$ and $S2p_{3/2}$ respectively and it confirms the S^{2-} oxidation state of sulfur in MoS_2 [39-40].

Further, XPS analysis was performed for MoS_2 functionalized with noble metal nanoparticles (Au, Pt, and Pd). The presence of Au, Pt, and Pd nanoparticles were confirmed from the wideband XPS spectra of Au/MoS_2, Pt/MoS_2 and Pd/MoS_2 as seen in Figure 3.3 (c-h), respectively. The high resolution spectra of Au 4f shown in Figure 3.3d**,** which was deconvoluted to two doublet peaks at 87.77 eV and 84.09 eV corresponding to Au $4f_{5/2}$ and Au $4f_{3/2}$ respectively. These two peaks are separated by ~ 3.67 eV, confirms the existence of Au NPs [183]. The shift in the binding energy towards higher energies when compared to the standard Au bulk values i.e. Au $4f_{7/2}$ at 83.9 eV and Au $4f_{5/2}$ at 87.6 eV, confirms the existence of Au NPs on the surface of MoS_2. As shown in Figure 3.3f, narrow band spectra of Pt NPs consist of two significant peaks at 75.59 eV and 72.29 eV indicating Pt $4f_{5/2}$ and Pt $4f_{7/2}$ respectively and two peaks are separated by ~3.3 eV. The peak positions authenticate the existence of Pt NPs on MoS_2 [184]. As seen in Figure 3.3h, doublet peaks located at 337.14 eV and 342.3 eV represent Pd $3d_{5/2}$ and Pd $3d_{3/2}$ and the difference between the peaks was found to be ~ 5.18 eV that confirms the existence of Pd NPs [185]. In high resolution XPS spectra of metal nanoparticles (Au 4f, Pt 4f and Pd 3d) isolated doublet peaks with no additional

component peaks indicate the presence of metal nanoparticles without any oxidation possibilities.

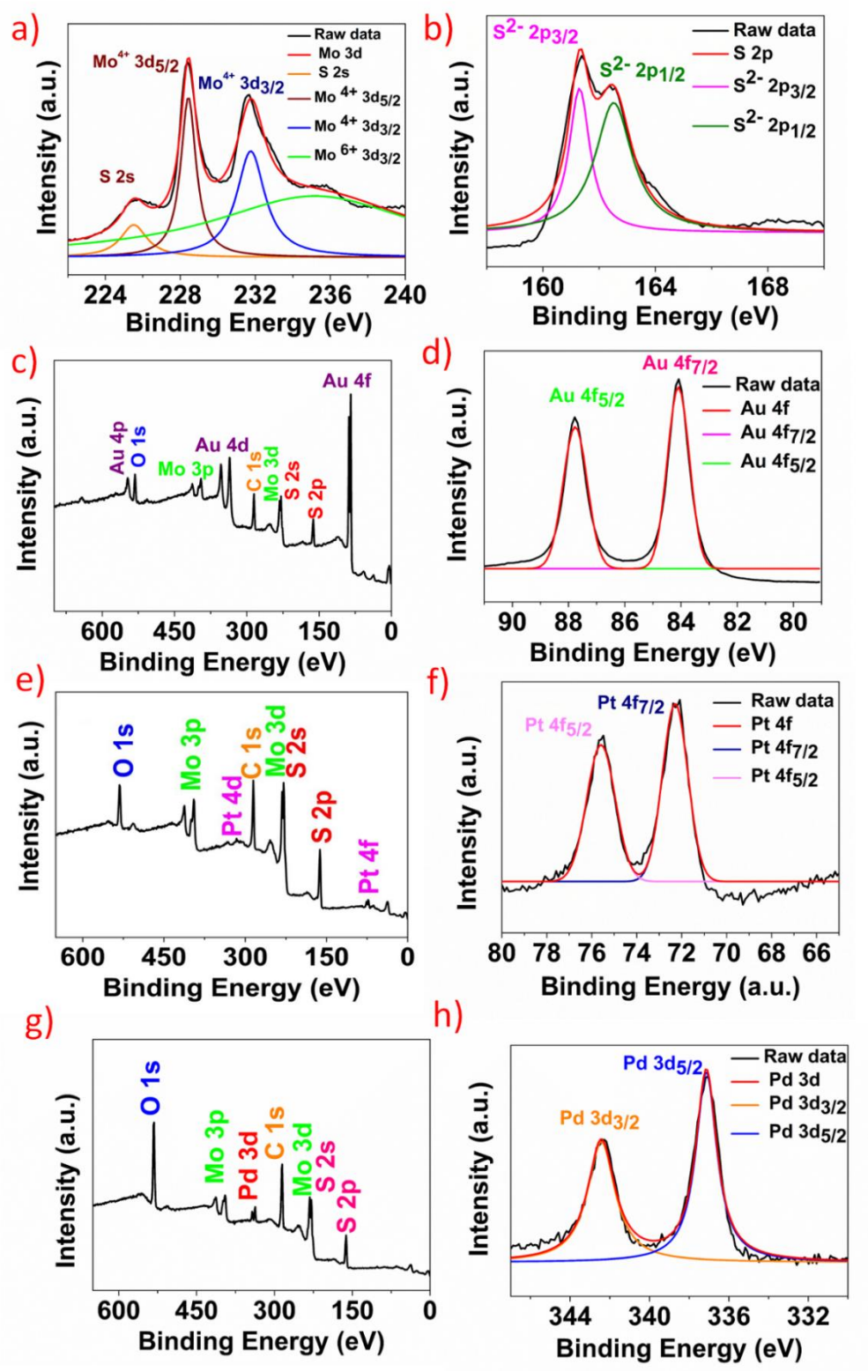

Figure 3.3: a,b) Narrowband XPS spectra of Mo3d and S2p, pristine MoS_2/paper. XPS survey spectra and high resolution scan of MoS_2 functionalized with: c, d) Au NPs e,f) Pt NPs g,h) Pd NPs.

The absorption spectrum of synthesized MoS_2 and metal nanoparticles was studied using UV-vis-NIR spectrometer, as shown in Figure 3.4a. MoS_2 showed absorption peaks in visible region and NIR region. From the Tauc plot, shown in the inset of Figure 3.4a, the bandgap of the synthesized MoS_2 was found to be ~ 1.53 eV. The absorption spectra of metal nanoparticles (Au, Pt, and Pd -NPs) is shown in Figure 3.4(b-d). It is a known fact that Au-NPs strongly absorb visible light [186]. As expected, the synthesized Au NPs showed stronger absorption peak in the visible region, shown in Figure 3.4b, which is ascribed to the surface plasmon resonance of Au -NPs that originated from the intraband excitation of 6sp electrons [186]. As shown in Figure 3.4c, Pt, NPs also showed considerable absorption in visible region. It is observed that the absorption of Au NPs was stronger when compared to the Pt NPs in the visible region. However, no such absorption peaks were observed for Pd NPs as shown in Figure 3.4d and an increase in the absorption was observed with a decrease in wavelength.

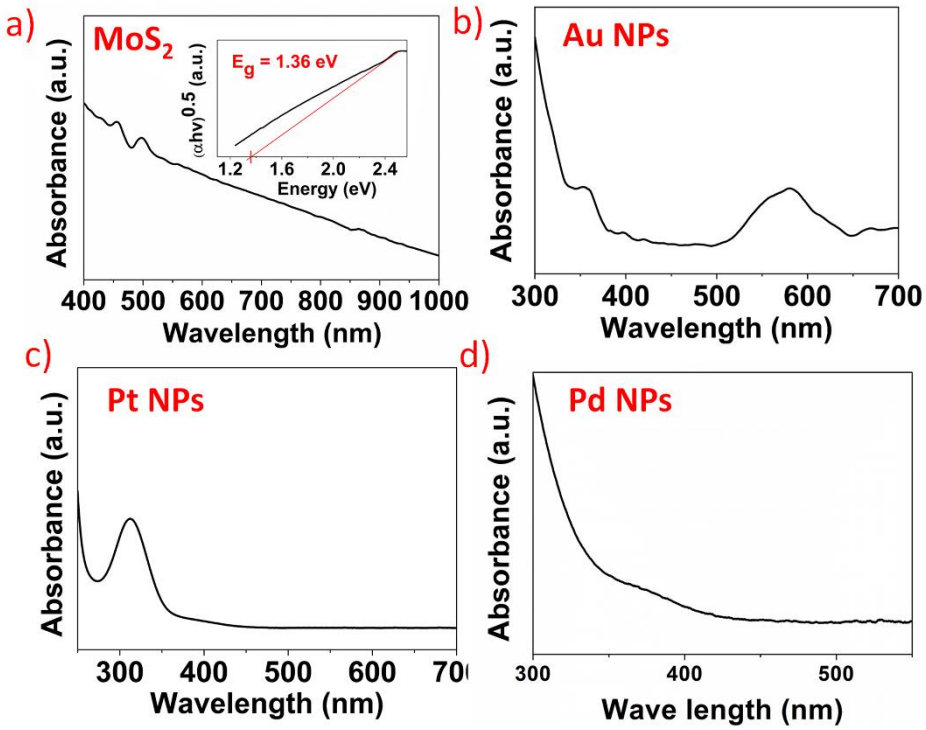

Figure 3.4: Absorption spectra of a) pristine MoS_2, inset showing the Tauc plot, where in the bandgap (Eg) synthesized MoS_2 was found to be ~ 1.53 eV b) Au NPs c) Pt NPs d) Pd NPs.

To investigate the photodetection properties of all the fabricated photodetectors (Au, Pt, Pd-NPs/MoS_2), serval in-depth experiments were performed. Figure 3.5a displays the

current v/s voltage (I-V) characteristics of fabricated Au-NPs/MoS_2 device on paper substrate for various visible light illumination intensities. Before performing the measurements, the device was kept in dark for a few hours. As seen in Figure 3.5a the fabricated Au-NPs/MoS_2 device showed ohmic behavior, and as intensity of light illuminated increases, an increase in the current level of the device was observed. Similarly, I-V measurements were performed for Pt-NPs/MoS_2 and Pd-NPs/MoS_2. As shown in Figure 3.5(b-c), the device exhibited ohmic behaviour and device current increased with increase in intensity. Figure 3.5(d-f) displays the temporal response of MoS_2/paper decorated with nanoparticles (Au, Pt and Pd) under constant visible light intensity of 1.21 mW/cm^2 and it was observed that the fabricated device was capable of detecting the light illumination and also displayed repeatability of the fabricated photodetectors. As compared to Pt and Pd nanoparticles, MoS_2 decorated with Au-NPs showed highest photocurrent, an increment of approximately ~ 93 %, under visible light intensity, which matches with absorption spectrum results shown in Figure 3.4 (b-d).

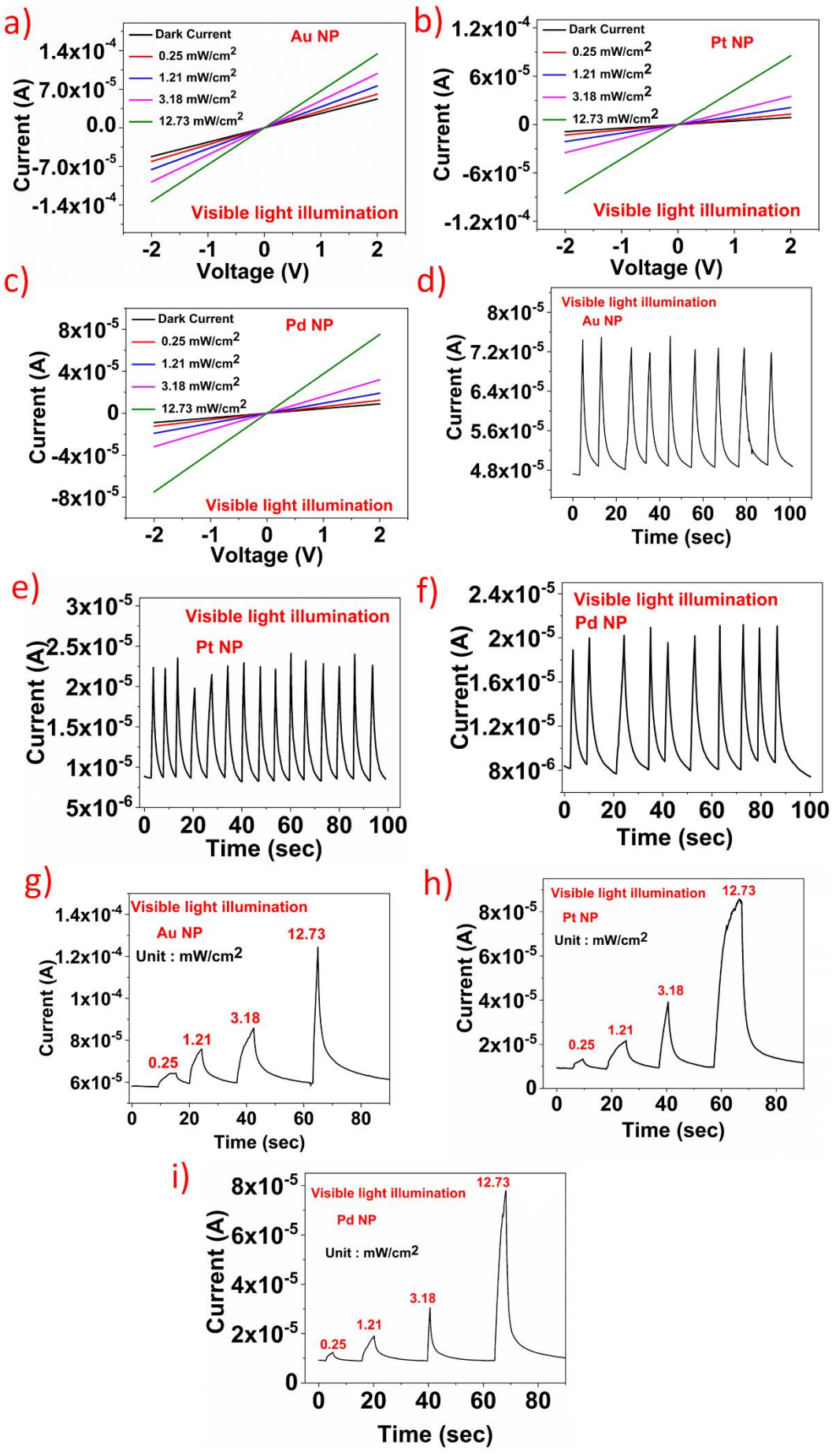
a)
Au NP
Dark Current
0.25 mW/cm2
1.21 mW/cm2
3.18 mW/cm2
12.73 mW/cm2
Visible light illumination
Current (A)
Voltage (V)
b)
Pt NP
Dark Current
0.25 mW/cm2
1.21 mW/cm2
3.18 mW/cm2
12.73 mW/cm2
Visible light illumination
Current (A)
Voltage (V)
c)
Pd NP
Dark Current
0.25 mW/cm2
1.21 mW/cm2
3.18 mW/cm2
12.73 mW/cm2
Visible light illumination
Current (A)
Voltage (V)
d)
Visible light illumination
Au NP
Current (A)
Time (sec)
e)
Visible light illumination
Pt NP
Current (A)
Time (sec)
f)
Visible light illumination
Pd NP
Current (A)
Time (sec)
g)
Visible light illumination
Au NP
Unit : mW/cm2
0.25
1.21
3.18
12.73
Current (A)
Time (sec)
h)
Visible light illumination
Pt NP
Unit : mW/cm2
0.25
1.21
3.18
12.73
Current (A)
Time (sec)
i)
Visible light illumination
Pd NP
Unit : mW/cm2
0.25
1.21
3.18
12.73
Current (A)
Time (sec)

Figure 3.5: a,b,c) Current (I) vs. Voltage (V) characteristics of MoS_2/paper decorated with metal nanoparticles (Au, Pt and Pd) d,e,f) Temporal responses of the fabricated devices under constant visible light intensity g,h,i) Graphs showing the temporal response with various visible light intensities, suggesting that device decorated with Au-NPs is more sensitive towards visible light.

Further, MoS_2 functionalized with Au, Pt and Pd nanoparticles based devices were tested under various visible intensities and the corresponding temporal responses are shown in Figure 3.5 (g-i). It was observed that current increases with increase in the illuminated light intensities, which are compatible with the current-voltage characteristics displayed in Figure 3.5 (a-c). The same experiments were repeated under NIR illuminations with the fabricated devices (Au, Pt, Pd-NPs/MoS_2). As shown in Figure 3.6(a-c), the I-V characteristics confirm the ohmic behavior of the fabricated devices. Figure 3.6(d-f) displays the temporal response of the devices under constant NIR light intensity. Furthermore, the fabricated photodetectors were tested under various NIR light intensities, an increase in current was observed as light intensity increases as seen in Figure 3.6(g-i), which agrees with I-V curves shown in Figure 3.6 (a-c).

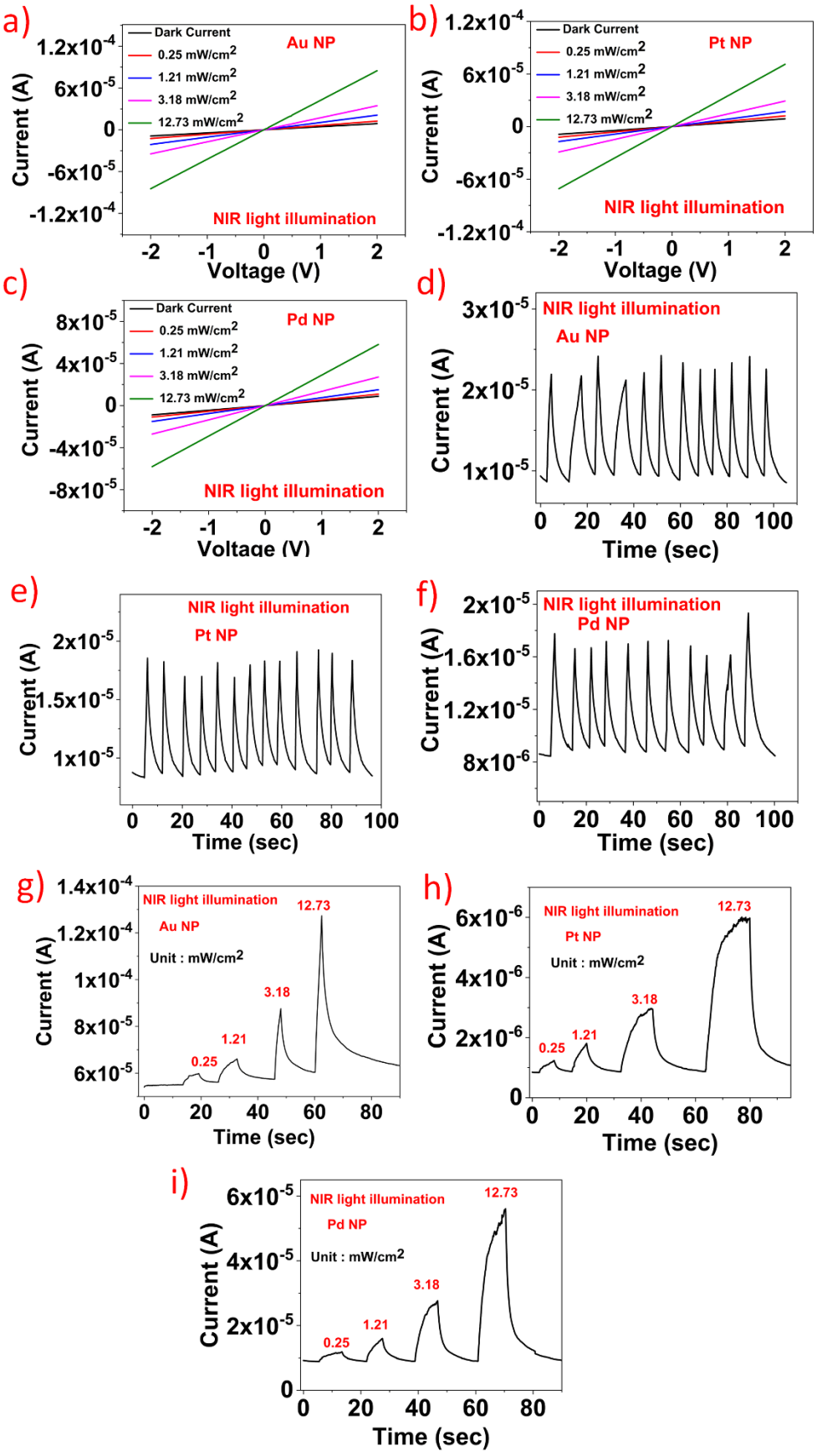
a)
Dark Current
0.25 mW/cm2
1.21 mW/cm2
3.18 mW/cm2
12.73 mW/cm2
Au NP
NIR light illumination
Current (A)
Voltage (V)
b)
Pt NP
c)
Pd NP
d)
NIR light illumination
Au NP
Time (sec)
e)
Pt NP
f)
Pd NP
g)
Unit : mW/cm2
0.25
1.21
3.18
12.73
h)
i)

Figure 3.6: a,b,c) Current (I) vs. Voltage (V) characteristics of MoS_2/paper decorated with metal nanoparticles (Au, Pt and Pd) under NIR light illuminations d,e,f) Temporal responses of the fabricated devices under constant NIR light intensity g,h,i) Graphs showing the temporal response with various NIR light intensities.

Responsivity (R_λ), detectivity (D*) and external quantum efficiency (EQE) are considered to be significant parameters to determine the quality of a photodetector. Responsivity of a photodetector is defined as photocurrent produced by light per unit area and detectivity is photodetectors ability to differentiate weak signals from noise. EQE is defined as the ratio of number of electron-hole pairs (charge carriers) collected to number of photons incident on the device. The equations defining R_λ, D*, and EQE are given as follows:

$$R_\lambda = I_\lambda/(P_\lambda \times A)$$

$$EQE = hc \times (R_\lambda / e_\lambda) \times 100$$

$$D^* = (R_\lambda \times A^{1/2})/(2 \times e \times I_{dark})^{1/2}$$

where A, I_{dark}, I_λ , P_λ *and* e are the area of the device, dark current, photocurrent and incident *power and electron charge.* The devices were fabricated with an active area of 36 mm^2. Responsivity of the fabricated devices under visible light illumination was calculated to be 99.3 mA W^{-1}, 51.4 mA W^{-1} and 46.03 mA W^{-1} for Au-NPs/MoS_2, Pt-NPs/MoS_2 and Pd-NPs/MoS_2 respectively under a visible light intensity of 0.25 mW/cm^2 as shown in Figure 3.7a. From the graph it is clear that MoS_2 decorated with Au –NPs exhibited highest responsivity when compared to other fabricated photodetectors (Pt and Pd-NPs/MoS_2), which matches with absorption spectrum results, shown in Figure 3.4 (b-d). Similarly, responsivity of the fabricated MoS_2/paper decorated with Au, Pt and Pd-NPs under NIR light intensity was found to be 61.13 mA W^{-1}, 42.3 mA W^{-1} and 34.7 mA W^{-1} respectively, displayed in Figure 3.7b. This further shows that fabricated devices are more sensitive to visible light illumination due to the fact that the active material MoS_2 exhibited strong absorption in visible region rather than NIR region, as shown in Figure 3.4a. The Responsivity graph shows that responsivity decreases with increasing intensity, which is consistent with the other photodetector reports [162][170].

Detectivity (D*) of the fabricated photodetectors (Au, Pt, Pd-NPs/MoS_2) under visible region was found to be 3.53×10^{10} Jones, 1.83×10^{10}Jones and 1.63×10^{10} Jones, respectively as shown in Figure 3.7c, similarly D* under NIR illuminations was

calculated to be 2.17×10^{10} Jones, 1.5×10^{10} Jones and 1.23×10^{10} Jones, as plotted in Figure 3.7d. Under visible light illumination, EQEs were found to be 22.23%, 11.5% and 10.3% for the device decorated with Au-NPs, Pt-NPs and Pd-NPs, respectively, as shown in Figure 3.7e. Similarly, EQE values under NIR illumination was calculated to be 9.71 %, 6.72% and 5.53 %, as seen in Figure 3.7f.

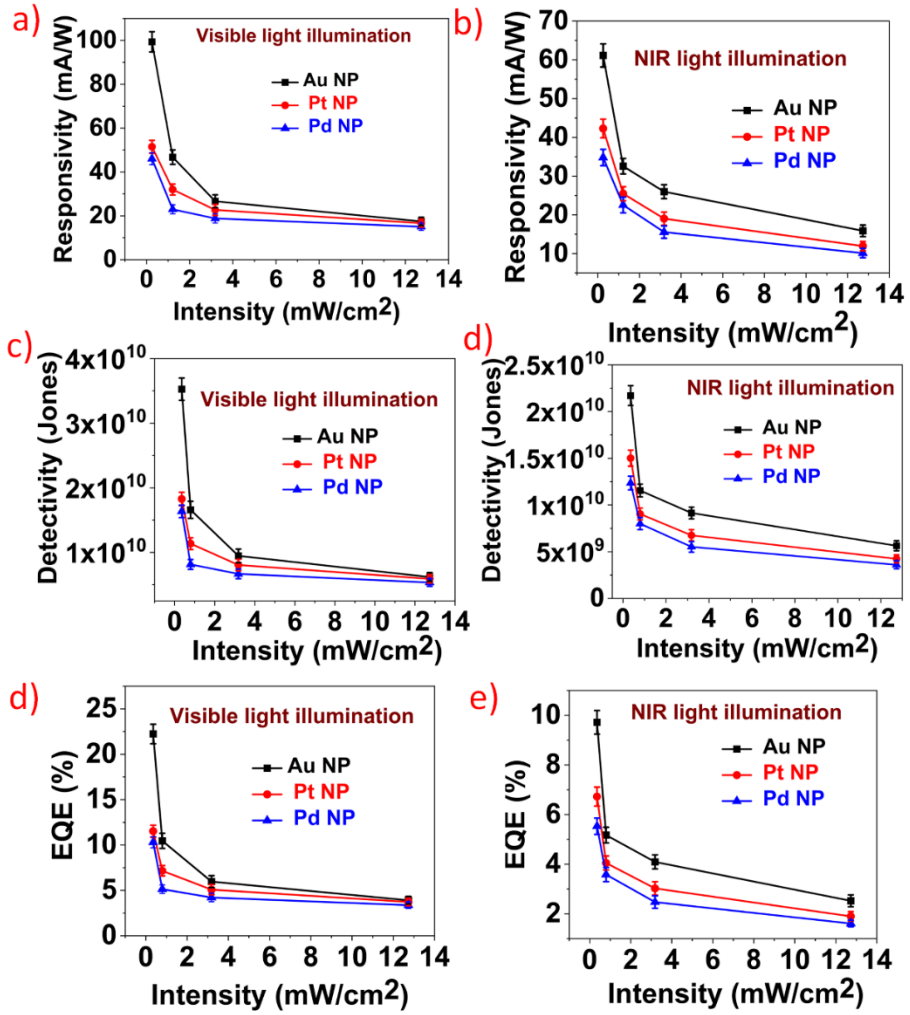

Figure 3.7: Responsivity of the fabricated photodetectors under a) Visible light illumination b) NIR light illumination, c,d) Graph showing the detectivity under visible and NIR regions e,f) EQE of the photodetectors under visible and NIR regions (N=3).

Signal to noise ratio (SNR) and energy consumption are critical parameters for a photodetector[187]. SNR is defined as $SNR = Signal\ power/Noise\ power$ and SNR of the fabricated device was found to be ~ 143 dB and detailed calculation procedure was included in the Appendix A. Further energy consumption of the fabricated photodetector was calculated to be ~ 151 μJ. Rise time is one of the key figures of merit to assess the

performance of the photodetectors. Rise time of the photodetector can be described as the time taken by the photocurrent to reach $0.9I_{max}$ from $0.1I_{max}$, where I_{max} in the maximum value of the photocurrent. As displayed in Figure 3.8(a-c), rise time of the fabricated photodetectors (Au, Pt, Pd-NPs/ MoS_2) was found to be ~ 0.9 s, ~ 1.19 s and ~ 1.2 s under visible light illumination respectively. Similarly rise time of MoS_2/paper decorated with metal NPs (Au, Pt, Pd) under NIR illumination were calculated and results are discussed in Appendix A, Figure S12. The slow response rate of the fabricated device is ascribed to the presence of charge impurity states or defect states, trap states. Defect states might be originated during the hydrothermal synthesis of MoS_2 on paper substrate. Furthermore, the mobility of the photogenerated carriers is affected by the rough surface of the paper substrate used. By smoothing/polishing the surface of paper substrate used the response time could be improved. The fabricated device was subjected to 500 bending cycles, where the sensor was bent by strain (~ 2 %) and bought back to original position and carried out the experiments. As shown in Figure 3.8d, a marginal change in the device performance was observed even after 500 bending cycles.

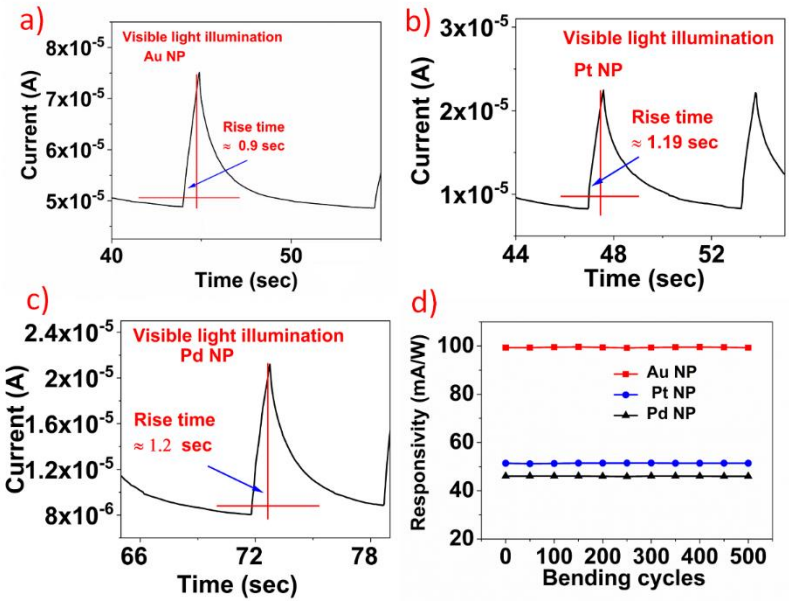

Figure 3.8: a,b,c) Graphs showing the response time of the fabricated photodetectors (Au, Pt, Pd-NPs/MoS_2) under visible light illumination d)Graph indicating the bending cycle stability, visible light illumination.

3.1.3.1 Plasmonic photodetection mechanism

The photoresponsivity of all the fabricated metal NPs-MoS_2 photodetectors were observed to be significantly higher than pristine MoS_2. In case of Au-NPs/MoS_2

photodetector, ~ 800 % increment in responsivity was observed in comparison with MoS_2 without Au NPs. The improved photocurrent of metal NPs-MoS_2 photodetectors is ascribed to the plasmonic effect of the NPs. When the light falls on the metal nanoparticles (Au, Pt, Pd-NPs), conductive electrons in the Metal NPs oscillate collectively due to the incident oscillating electromagnetic field of light, as illustrated in Figure S13, Appendix A. When the frequency of the oscillating charge clouds (plasmons) matches the frequency of the light used, a phenomenon called localized surface plasmon resonance occurs (LSPR) [188]. This collective oscillation dephases rapidly, releasing the plasmons energy predominantly in three ways, far-field scattering of light (radiatively), near-field enhancement of electromagnetic field (non-radiatively) and hot carriers generation. The light scattered by one nanoparticle is trapped by its neighbouring NPs, resulting in a strong coupling effect, thereby trapping the light in the plane of NPs. It is important to note that the fraction of light absorbed and light scattered depends heavily on the size (d) and shape of the nanoparticle. Based on size, there are two limits at which the behaviour of the NP changes (i) when the nanoparticle is large enough that the electric field is no longer uniform over the entire sphere, (ii) vanishingly small nanoparticles with d much lesser than the mean free path of the oscillating electrons [189]. Moreover, due to the large surface area and extensively exposed edges of MoS_2 microflowers as shown in Figure 3.2(c-d), the decorated nanoparticles (Au, Pt, and Pd) are trapped within microflowers and significantly increased the contact cross-section between the surface of MoS_2 and NPs as shown in high magnification FESEM images, Figure 3.2(g-l). This localization of enhanced field in the vicinity of NP, dramatically increases the overall absorption of MoS_2 and it leads to increase in photogenerated electron-hole pairs which consequently increases the photocurrent of detector. Since the metal contacts are taken from MoS_2, the generated electron-hole pairs get collected effectively. It is important to note that the electric field created at the interface of the NPs-MoS_2 due to the difference in Fermi levels, as illustrated in Figure 3.9, assists in efficiently separating the photogenerated electron-hole pairs. Further, the plasmon can dephase non-radiatively through a phenomenon called Landau damping. This occurs when there are electrons with the same velocity as the incident light. These electrons are accelerated, as they move with the incident wave, and hence they extract an energy of $\hbar\omega_{LSPR}$ (where $\hbar\omega_{LSPR}$ is the LSPR energy) from the incident wave. The electrons in the NPs are then excited from E_F to $E_F + \hbar\omega_{LSPR}$ generating hot electron-hole pairs. The hot electrons possessing enough energy to cross the Schottky barrier, contribute to the photocurrent [190].

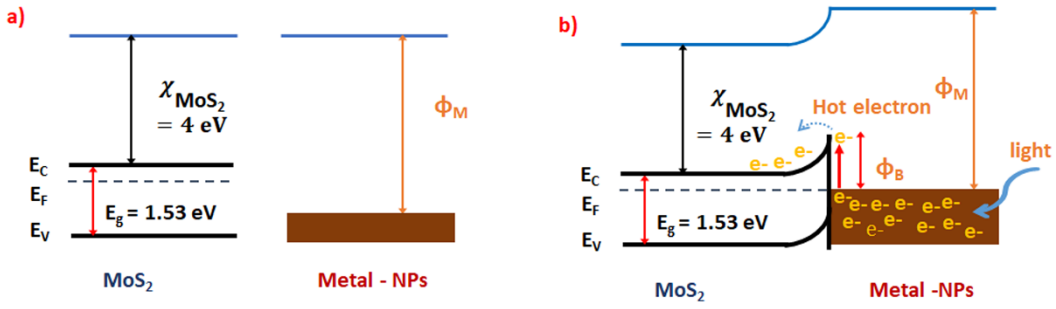

Figure 3.9: Schematic illustrating the Energy band diagram of a) MoS_2 (n) and metal Nanoparticles (Au, Pt, and Pd) b) Schottky barrier formation at the interface of MoS_2 and metal nanoparticles.

There are several reports wherein the photoresposne performance of 2D materials (MoS_2, ZnO, WS_2, etc.) [191][171][192][193][194][195]have been improved using the plasmonic effect through metal nanoparticles. *Rahmati et al.* demonstrated that the photocurrent of vertically aligned MoS_2 deposited on SiO_2/Si substrate was significantly enhanced by Au NPs [18]. *Park et al.* investigated the performance of NIR photodetector built from few-layer MoS_2 films functionalized with Ag nanocrystals [192]. *Sobhani et al.* enhanced the photocurrent of monolayer MoS_2 deposited on SiO_2/Si substrate by Au nanoshells [171]. *Rajan et al.* studied the enhancement of sol-gel derived ZnO film in the UV region after integrating different metal nanoparticles such as Au, Ag and Pt [193]. *Guo et al.* fabricated a UV photodetector based on ZnO/Pt NPs/ZnO films by magnetron sputtering method [194]. *Hsu et al.* fabricated a UV/visible photodetector based on NiO(p)/ZnO(n) decorated with Pd-NPs [195]. However, reports on flexible plasmonic photodetectors with comparative performance of different nanoparticles is very limited. Herein, photoresponse characteristics of MoS_2/paper decorated with metals nanoparticles (Au, Pt and Pd-NPs) were studied and cost-effective, highly-scalable fabrication techniques (hydrothermal synthesis and drop-casting) were used. Performance comparison of the various plasmonic photodetectors is provided in Table 3.1.

Material	Synthesis	Substrate	NPs	Range	Flexibility	Responsivity	Ref.
Vertical MoS_2	CVD	SiO_2/Si	Au NPs	Visible	No	24 mA W^{-1}	[191]
Multilayer MoS_2	Exfoliate	SiO_2/Si	Ag NPs	NIR	No	0.8 mA W^{-1}	[192]
Monolayer MoS_2	CVD	SiO_2/Si	Au nano shell	Visible, NIR	No	0.9 mA W^{-1}	[171]
ZnO	Magnetron sputtering	Quartz	Pt NPs	UV	No	0.4 A W^{-1}	[194]
NiO(p)/ ZnO(n)	Sol-Gel, Hydrothermal synthesis	Glass	Pd-NPs	UV, Visible	No	34.6 mA W^{-1}, 0.9 mA W^{-1}	[195]
MoS_2	CVD	SiO_2/Si	Au NPs	Visible	No	22.3 A W^{-1}	[196]
MoS_2	Scotch-tape method, Pulsed magnetron sputtering	SiO_2/Si	Au NPs	NIR	No	64 mA W^{-1}	[197]
Bilayer MoS_2	Focused ion Beam, Scotch tape method	SiO_2/Si	Pt nanostrips	UV, Visible, NIR	No	14 A W^{-1} (325 nm), 312.5 A W^{-1} (532 nm), 69.2 A W^{-1} (980 nm)	[175]
MoS_2	CVD, Atomic layer deposition	SiO_2/Si	Pd	Visible	No	5.04 A W^{-1}	[198]
MoS_2	DC magnetron sputtering	SiO_2/Si	Pd	UV, Visible, NIR	No	654 mA W^{-1}	[199]
MoS_2	Hydrothermal, Drop-casting	Cellulose paper	Au-NPs	Visible, NIR	Yes	99.3 mA W^{-1}, 61.13 mA W^{-1}	**This work**
MoS_2	Hydrothermal, Drop-casting	Cellulose paper	Pt-NPs	Visible, NIR	Yes	51.4 mA W^{-1}, 42.3 mA W^{-1}	**This work**
MoS_2	Hydrothermal, Drop-casting	Cellulose paper	Pd-NPs	NIR	Yes	46.03 mA W^{-1}, 34.7 mA W^{-1}	**This work**

Table 3.1: Performance comparison of fabricated plasmonic photodetector.

3.1.4 Conclusion

In conclusion, flexible, cost-effective plasmonic photodetector was fabricated based on MoS_2/paper functionalized with metal NPs (Au, Pt and Pd). MoS_2 was grown on paper substrate by a facile and highly scalable hydrothermal synthesis method. High responsivity of 99.3 mA W^{-1} and 46.03 mA W^{-1} was observed in Au-NPs/MoS_2 photodetector under visible and NIR region, respectively. The enhanced performance of photodetectors is ascribed to the electric field created by plasmonic effect and trapping of incident light by the decorated metal NPs (Au, Pt and Pd). This local electric field formed between NPs and MoS_2 efficient separation of photogenerated electro-hole pairs that in turn increase the photocurrent. The work reported herein promotes the fabrication of large-area paper-based plasmonic photodetector that finds several applications in the field of flexible electronics.

3.2 Plasmonic Au Nanoparticles Coated on ReS_2 Nanosheets for Visible-NIR Photodetector

Even though there are various reports on the fabrication of flexible photodetectors, still there is a need for the development of high-performance photodetectors. In recent years, plasmonic photodetection technique has emerged as one of the prominent solutions to enhance photodetection performance. In this work, flexible and high-performance broadband (visible-NIR) plasmonic photodetector is demonstrated by integrating gold (Au) nanoparticles (NPs) on 2D ReS_2 nanosheets. Fabricated Au-NPs/ReS_2 showed an approximately 15-fold enhancement in the photodetection performance compared to pristine ReS_2. Photoresponsivity of the fabricated Au-NPs/ReS_2 device under visible (Vis) and NIR regions is ~ 2.1 A W^{-1} and ~ 1.3 A W^{-1}, respectively. Significant enhancement in the photo-sensing performance of the device could be a combined effect of multiple factors, including localized surface plasmons resonance (LPSR) and effective charge transfer at the interface of Au-NPs and ReS_2. Response speed of the fabricated device is approximately 200 ms. Further, theoretical understanding of light interaction with Au-NPs is studied and also electromagnetic simulations are performed using Lumerical Finite difference time domain (FDTD) Multiphysics simulation to investigate the plasmon coupling effect of Au-NPs on 2D ReS_2 nanosheets. To further understand the photodetection mechanism energy band diagram of Au-NPs/ReS_2 interface is drawn using UPS measurements.

3.2.1 Introduction

In recent years, there is a huge surge in the development of flexible photodetectors due to the growing automotive, health care, and consumer electronics industry[170,200]. According to precedence research, by 2030 the global flexible electronics market size is projected to be worth approximately $61 billion[6]. Flexible photodetectors have become the key component of wearable optoelectronics technology for a plethora of applications such as sensors for portable and wearable health monitoring devices, soft robotics, high-speed optical communication, bioimaging, electronic skin, and so forth[201] While early research progress and various innovations have already been achieved, still fabricating cost-effective and large area high-performance photodetectors faces practical problems before they become part of daily life practical applications. Hence there is a need for the development of high-performance flexible photodetectors.

However, designing a flexible device requires materials with exceptional optical, electrical, and mechanical properties. Transition Metal Dichalcogenides (TMDs) are layered 2D materials which have consistently exhibited high responsivities due to their superior optoelectronic properties, mechanical durability, and a tunable bandgap[202–204]. In recent years, rhenium disulfide (ReS_2) emerged as the most prominent 2D TMDs material for optoelectronic applications due to its unique electronic and optical properties[205]. Because of weak interlayer coupling and low symmetry, ReS_2 has a direct bandgap irrespective of the number of layers, unlike tungsten and molybdenum based TMDs[113,115]. Multilayer synthesis is more difficult than monolayer synthesis, thus ReS_2 eliminates the necessity for monolayer synthesis. Additionally, the direct bandgap results in a higher density of states and enhanced light absorption as a result of the anisotropic in-plane optical properties. All these properties make ReS_2 a promising material for the photosensitive layer. On the other hand, published literature shows that the low mobility of ReS_2 hampers the performance of optoelectronic devices[71,206]. To date, various techniques have been proposed to improve the absorbance of TMDs photosensitive layer, such as heterostructure engineering[148,207], chemical doping [208], integration of metal nanoparticles[207,209], use of field-effect transistors[210,211], mixed-dimensional heterostructures[71,212,213], transport layer integration[205,214], and so forth. However, the embedment of plasmonic metal nanoparticles on TMDs is a superior approach to enhance the photo-sensing performance without changing the device area or 2D material thickness.

The use of metal nanoparticles prominently improves the interaction of light with the surrounding materials.[215] When the NPs integrated into a semiconductor material, these NPs produce an oscillation of charge clouds in the NPs under light illumination, creating a much stronger dipole/near-field electromagnetic field in the vicinity of the nanoparticle. Such a phenomenon occurs at a particular frequency of light, known as the surface plasmon resonance frequency. Also, the metal NPs increase the light scattering and increase optical path length. Thus, the light absorptance of the surrounding material could be significantly enhanced via an increase in optical path length and near-field electromagnetic field improvement [216]. Although, there are multiple high-performance ReS_2 based photodetectors are reported using various techniques such as exfoliation,[217] chemical vapor deposition,[114,211] and so forth. Till now the effect of NPs integration on the surface of ReS_2 microflowers synthesized by hydrothermal has not been explored.

In this work flexible, high-performance plasmonic broadband (Vis-NIR) photodetector was demonstrated by integrating Au-NPs on ReS_2 nanosheets. Hydrothermal synthesis technique was used to prepare ReS_2 and the synthesized ReS_2 was spin-coated on PET substrate. Subsequently, prepared Au-NPs were decorated on ReS_2 nanosheets using the drop-casting method. Photodetection measurements of fabricated Au-NPs/ReS_2 heterojunction show a significant improvement in the photo-sensing performance of the device when compared to pristine ReS_2 device. Fabricated Au-NPs/ReS_2 exhibited a 15-fold improvement in the photodetection performance compared to the pristine ReS_2. The plasmonic enhancement in the performance of Au-NPs/ReS_2 device is attributed to the following reasons: i) increased near-surface electromagnetic field, ii) increased optical path length due to multiple light trapping, which results in improved light-material interaction, iii) hot electron doping from Au-NPs to ReS_2 nanosheets. In addition, the internal electric field formed at the interface of Au-NP and ReS_2, due to the Schottky barrier, boost the effective segregation of photogenerated e-h pairs. The photoresponsivity of the fabricated Au-NPs/ReS_2 device was measured to be ~ 2.1 A W^{-1} and ~ 1.3 A W^{-1} under Vis and NIR light illumination, respectively. Photoresponsivity of the fabricated device is more under visible light compared to NIR, which is attributed to the higher absorption of ReS_2 in the visible region and the surface plasmon effect of decorated Au-NPs. Detectivity of the device was 1.12×10^{12} Jones and 7.27×10^{11} Jones at Vis and NIR light illumination, respectively. EQE of the device was 469.2% and 216.4%, respectively. Another critical parameter, the response speed of the device was estimated to be ~ 200 ms. This contribution may inspire the research community to develop flexible, cost-effective, highly scalable, plasmonic enhanced high-performance photodetectors for potential wearable optoelectronic applications.

3.2.2 Experimental Section

Materials and Characterization

X-Ray Diffraction (X'pert PRO) was utilized to do structural analysis. In order to determine the chemical composition and oxidation state of the samples, K-alpha XPS equipment was used. Helium source (He I, 21.22 eV) was utilized for UPS measurements. FEI Titan Themis 300kV was used for transmission electron microscopy analysis (TEM). Measurements of Raman spectra were made using the LabRAM HR Raman spectrometer. In order to obtain the ReS_2 UV-visible spectrum, JASCO V-670 UV-visible spectrophotometer was utilized. All electrical measurements were performed

utilizing a source meter (Keithley 2450). 554 nm and 780 nm are the wavelengths of the visible and NIR lights, respectively that are used. All chemicals utilized for the preparation of metal nanoparticles, ReS_2 and polyethylene terephthalate (PET) sheet were procured from Molychem and Sigma Aldrich, and they were utilized as received.

Synthesis of ReS_2

Hydrothermal method was used to synthesize ReS_2 as reported previously from our lab[218]. Briefly, NH_4ReO_4 (0.149 g), CH_4N_2S (0.209 g), and $NH_2OH.HCl$ (0.0936 g) were added to deionized (DI) water (30 ml) and vigorously stirred using a magnetic stirrer. After that, the solution was shifted to a Teflon container (50 ml) for hydrothermal reaction (220^{o}C, 36 h) in hot-air oven. Later, the final solution containing ReS_2 nanoparticles was cleaned several times utilizing ethanol and DI water to remove the residues. The resultant solution is dried in oven and the complete procedure is shown in Figure 3.10.

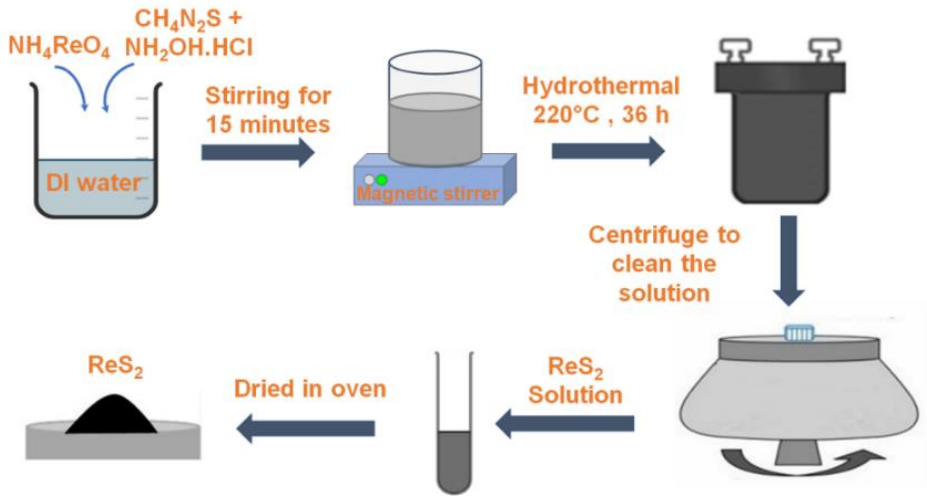

Figure 3.10: Schematic illustration of ReS_2 nanoparticle synthesis using hydrothermal method.

Synthesis of Au nanoparticles

1 mmol gold chloride ($AuCl_3$) was dissolved in 1L DI water at room temperature, followed by a 30 minutes sonication period. HCl was added drop by drop during the sonication process in order to obtain uniform and stabilized NPs. The synthesized Au-NPs were utilized to decorate the synthesized ReS_2.

Fabrication of the Au-NPs/ReS_2 device

Synthesized ReS_2 nanoparticles dissolved in dimethylformamide (DMF) were spin-coated on PET substrate. Later, silver (Ag) lines separated by 500 µm channel gap were made on fabricated ReS_2/PET film with shadow masking method by thermal evaporator

technique. After that, ReS_2/PET film was cut into the required dimension, and synthesized Au-NPs were drop-casted carefully on fabricated ReS_2/PET film. Figure 3.11 depicts the schematic representation of the fabrication procedure.

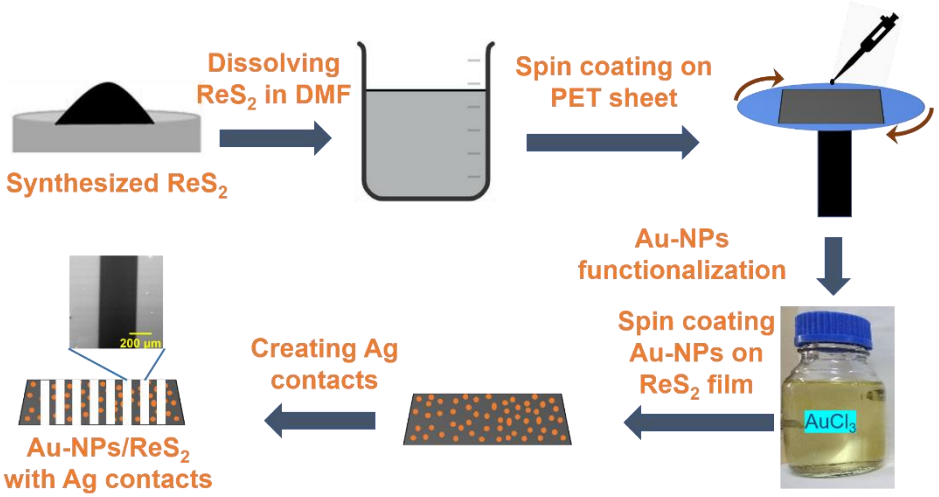

Figure 3.11: Schematic representation of Au-NPs/ReS_2 device fabrication.

3.2.3 Results and discussions

Figure 3.12a and 3.12b illustrate the FESEM images at low and high magnifications with spherical micro flower-like morphology, the assembly of individual ReS_2 nanosheets. Also, the ReS_2 layer has been uniformly coated on PET substrate, which can be seen in FESEM images. High magnification FESEM images (Figure 3.12b), reveal that the ReS_2 clusters are formed by many tube-like structures adhered together. Figure 3.12c shows the XRD pattern of pristine ReS_2. The observed diffraction peaks for ReS_2 match well with the JCPDS card number: 82-1379. The XRD pattern confirms the successful formation of ReS_2 having a triclinic crystal structure. To get further insight on the crystal symmetry, Raman Spectroscopy was performed. The Raman spectra of pristine ReS_2 is shown in Figure 3.12d. Many peaks exist from 100 to 400 cm^{-1}, thereby indicating that the as-synthesized ReS_2 exhibits low crystal symmetry. Also, the presence of several peaks in the above-mentioned region is attributed to the unique asymmetry in the distorted 1T structure of ReS_2[219]. The Raman peaks around 160 cm^{-1} and 200 cm^{-1} are the main characteristic peaks for ReS_2.

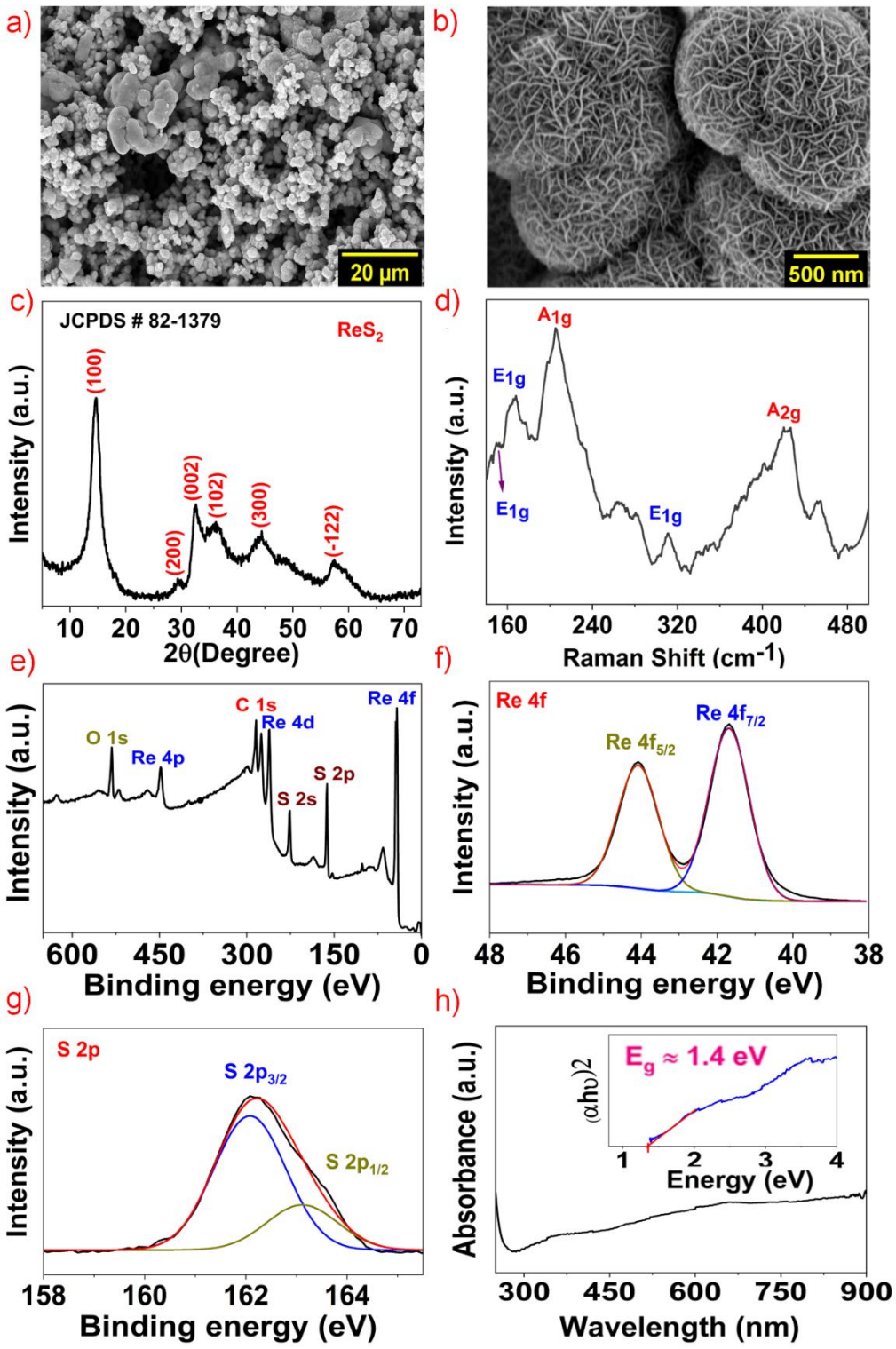

Figure 3.12: a-b) FESEM images of ReS_2 coated on PET substrate c) XRD spectrum of synthesized ReS_2 d) Raman spectrum of ReS_2 e) XPS survey spectra of ReS2 f, g) High-resolution spectra of Re 4f and S 2p h) UV-Visible spectroscopy of ReS_2 and inset displays the Tauc plot, where the bandgap was ~ 1.4 eV.

The in-plane E_g modes are observed around 160 cm^{-1} and 310 cm^{-1} whereas the out-of-plane A_{1g} mode is observed around 200 cm^{-1}. A peak at 423 cm^{-1} represents the A_{2g} mode[220]. To get the elemental composition of pristine ReS_2 and the Au NP-ReS_2, XPS was carried out. Figure 3.12e-g shows the XPS spectra of pristine ReS_2. The XPS survey spectra displayed in Figure 3.12e shows the presence of Re and S. The binding energy (BE) peaks at around 44 eV and 42 eV corresponds to the $4f_{5/2}$ and $4f_{7/2}$ core levels of Re as shown in Figure 3.12f. As shown in Figure 2g, the BE peaks at around 162 eV and 163 eV indicate the $2p_{3/2}$ and $2p_{1/2}$ levels of sulfur. Figure 3.12h depicts the UV-visible spectra of pristine ReS_2, and it is clear that ReS_2 exhibits strong absorption in the Vis and NIR region. The direct bandgap of ReS_2 was determined using the standard Tauc plot technique, as illustrated in the inset of Figure 3.12h, and it was found to be ~ 1.4 eV.

To get a detailed knowledge of the structure of the synthesized ReS_2 and Au NPs- ReS_2, FESEM analysis was performed. Figure 3.13a shows that the Au NPs have a spherical shape and are in deposited over the ReS_2 surface. The elemental mapping of the Au NPs-ReS_2, included in Figure S14 (Appendix A) confirms the presence of Re, S, and Au. Further, XPS analysis of Au-NPs/ReS_2 was performed. The XPS spectra of Au NP-ReS_2, shown in Figure 3b-e. The existence of Re, S and Au elements were confirmed from XPS survey spectra. Figure 3.13c and 3.13d display the high-resolution spectra of Re 4f and S 2p. As shown in Figure 3.13e, two important BE peaks for Au 4f core level, are $4f_{5/2}$ and $4f_{7/2}$ seen at around 87 eV and 83 eV, respectively. These two BE peak confirms the presence of elemental gold (Au^0)[221,222]. Figure 3.13f presents the UV-Vis spectra of Au NPs. Because of the surface plasmon resonance (SPR) effect, Au NPs exhibited strong absorption in the visible region as observed in UV-Vis spectra [221,222].

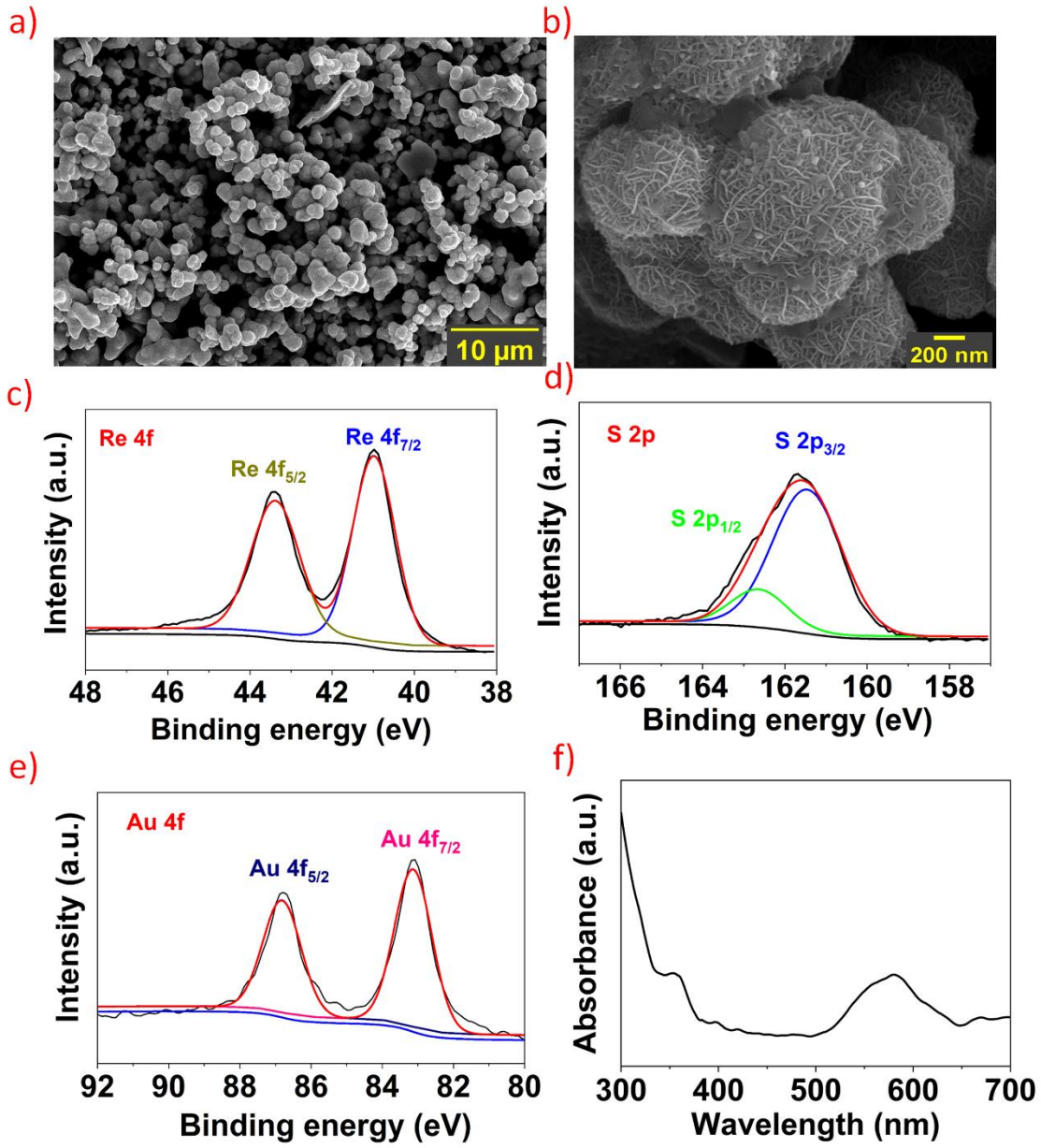

Figure 3.13: a,b) FESEM images of the Au-NPs decorated on ReS_2 at low and high magnifications c-e) high-resolution spectrum of Re 4f, S 2p, and Au 4f f) UV-visible spectrum of synthesized Au-NPs.

To further confirm the morphology of pristine ReS_2 and interface of Au-NPs/ReS_2, TEM analysis was carried out. Figure 3.14a-b shows the TEM images of pristine ReS_2. For TEM analysis, synthesized ReS_2 powder was dispersed in IPA solution followed by ultrasonication for more than 30 minutes and then drop casted on TEM grid. As displayed in Figure 3.14a, TEM image of pristine ReS_2 shows the presence of thin nano-petals. Figure 3.14b shows the HR-TEM image wherein the interplanar distance was found to be around 0.61 nm corresponding to (100) crystal plane of ReS_2[223], which is consistent

with XRD results of ReS_2. Selected area electron diffraction (SAED) pattern is displayed in the inset in Figure 3.14b and it confirms the polycrstaline nature of ReS_2. Figure 3.14c shows the TEM image of Au-NP/ReS_2 wherein it can be clearly seen the decorated hemispherical Au-NP on ReS_2 nano sheets. Furthermore, EDS measurements confirmed the presence of Re, S and Au elements, as displayed in Figure S15 (Appendix A). The presence of C and Cu in the spectrum is attributed to the carbon coated copper grid utilized for TEM measurements. Figure 3.14d shows the HR-TEM image of Au-NP/ReS_2 interface wherein the interplanar distance for ReS_2 was found to be approximately 0.61 nm which is corresponding to (100) crystal plane of ReS_2. The inset within Figure 3.14d illustrates the SAED pattern of Au-NPs/ReS_2.

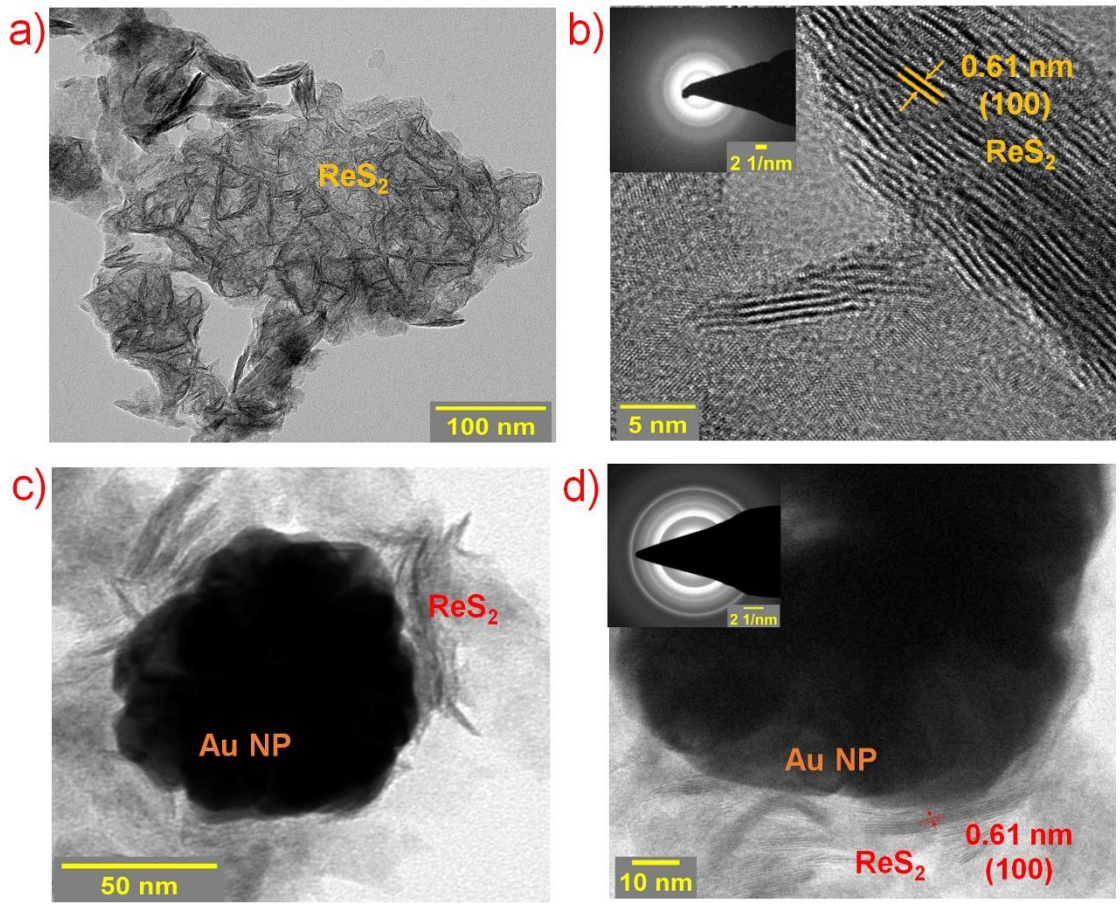

Figure 3.14: a) TEM image of pristine ReS_2 showing the nano-petal/sheets morphology b) HR-TEM image of ReS_2.The interlayer distance of ReS_2 nanosheets is around 0.61 nm and inset shows the SAED pattern c) TEM image showing the decorated Au-NPs on ReS_2 nanosheets d) HR-TEM image showing the interface between Au-NP and ReS_2 nanosheets; inset shows the SAED pattern of Au-NP/ReS_2 nanocomposite.

The fabricated Au-NPs/ReS_2 photodetector was subjected to a series of lab-based measurements to verify its photodetection capabilities. To study the device dependence on the light intensity, various light intensities are illuminated on the fabricated device and measured the current-voltage characteristics. Figure 3.15a and 3.15b show the I-V measurements of the fabricated Au-NPs/ReS_2 photodetector. The excitations were produced using wavelengths in both visible (Figure 3.15a) and NIR (Figure 3.15b) regions of the spectrum. The linear behaviour of the I-V curve confirms the Ohmic nature of the metal-semiconductor interface. The photocurrent is described as the difference between device currents with and without light illumination, $I_{ph} = I_{light} - I_{dark}$. It was observed that device photocurrent is significantly increased due to the incorporation Au-NPs because the integrated Au-NPs trigger the localization, redistribution, and improvement of the electromagnetic field and result in a significant increase of absorption of light surrounding ReS_2. Switching behaviour of the photodetector can be seen in Figure 3.15c and 3.15d, for illumination of Vis and NIR light, respectively. The intensity of light used in these studies was ~ 1.21 mW cm^{-2}. When light is turned on, the photocurrent increases rapidly and then stabilizes; later the photocurrent comes down to initial value when the light is turned off. The change in device current for visible light is higher than under NIR light because ReS_2 is more sensitive to visible light. Figure 3.15e shows the photo-sensing performance under visible light illumination with various light intensity values. As shown in the temporal response with increasing light intensity an increase in device photocurrent was observed, in line with current vs. voltage characteristics (Figure 5a). The increase in photocurrent can be ascribed to the higher generation of excitons under an increased light illumination. Figure 3.15b presents the temporal response of the fabricated Au-NPs/ReS_2 device when subjected to Vis and NIR illuminations and results are compatible with I-V characteristics, Figure 3.15b.

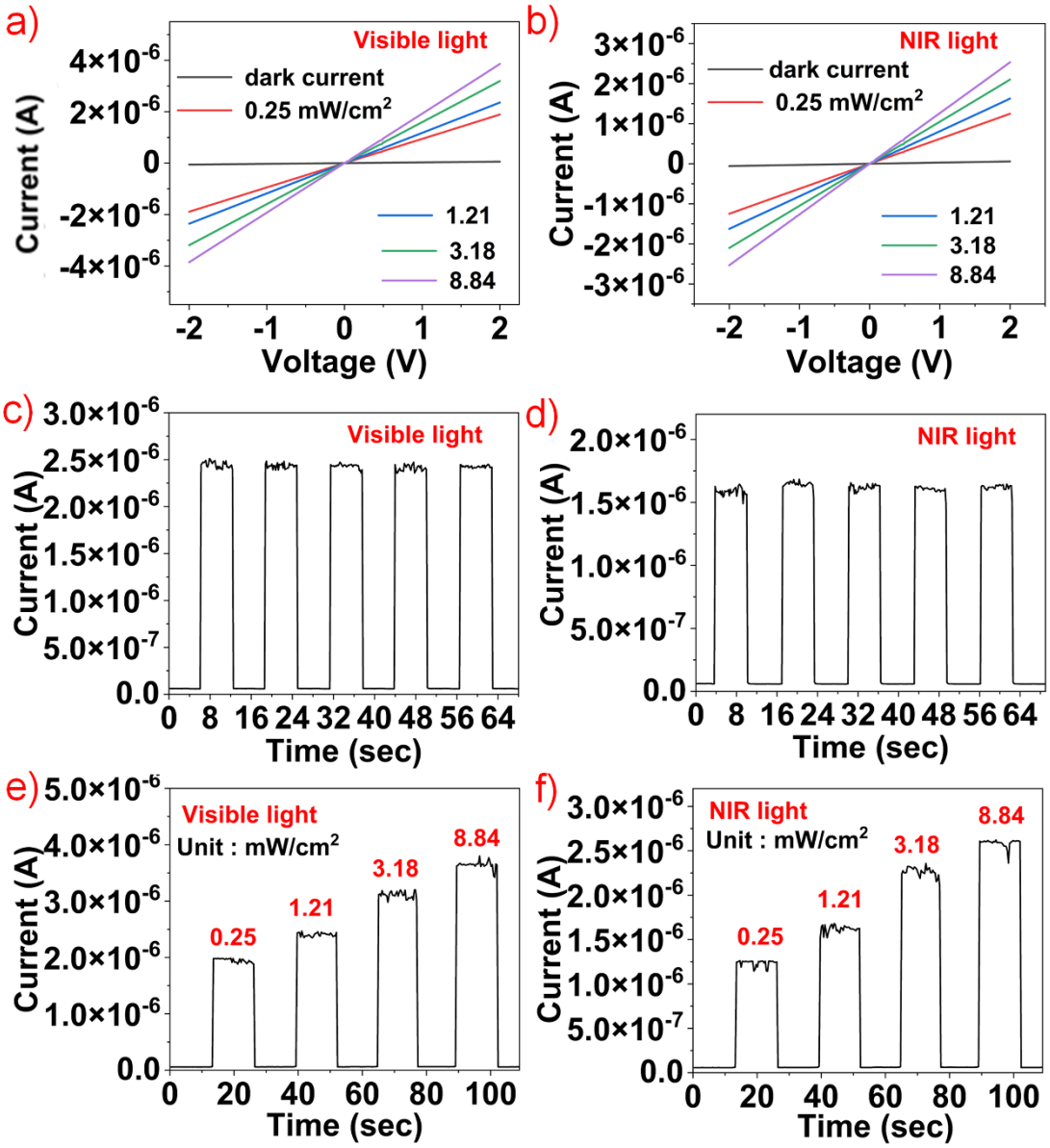

Figure 3.15: a-b) I-V characteristics of the fabrication Au-NPs/ReS_2 device for illumination of Vis and NIR light, c-d) switching characteristics of the device with light (Vis and NIR) turned on and off at a bias 1 V, e-f) time-dependent photoresponse of the device for Vis and NIR illuminations.

The ubiquitous metrics used to quantify the performance of a photodetector include Responsivity (R), specific detectivity (D*), and external quantum efficiency (EQE). The mathematical expressions for the given quantities are given below:

$$R = I_{ph}/(P_{in} \times S)$$

$$D^* = (R \times S^{1/2})/\sqrt{2 \times q \times I_{dark}}$$

$$EQE = hc \times (R/q\lambda) \times 100$$

where I_{dark}, P_{in}, h, $I_{ph,}$ $\boldsymbol{\lambda}$, q, S, and c are dark current, intensity of light illuminated, Planck's constant, photocurrent, the wavelength of light, charge of electron, active area of the device (0.0035 cm^2), and speed of light. Photoresponsivity (R) indicates the photocurrent generated per unit area under light illumination. Detectivity is a numerical measure of the device ability to discern weak signals from noise. Detectivity is measured in Jones, 1 Jones = 1 cm $Hz^{1/2}$ W^{-1}.

The calculated responsivity of the Au-NPs/ReS_2 device was determined to be ~ 2.1 A W^{-1} and ~ 1.3 A W^{-1} in the case of Visible (554 nm) and NIR (780 nm) light excitation, respectively, Figure 3.16a. Due to the plasmon-enhanced absorption, the fabricated Au-NPs/ReS_2 device showed significant improvement in photodetection performance. 15-fold enhancement in the photoresponsivity was observed in Au-NPs/ReS_2 device compared to pristine ReS_2. Photodetection results of pristine ReS_2 are included in Figure S16, Appendix A. The device responsivity decreased with increasing light intensity, as reported in the previous literature [70,71,218]. This trend is attributed to the ReS_2 trap states. Under low light intensities, the trap states capture the most of the photogenerated charge carriers and therefore reduce the recombination of e-h pairs. Due to the limited trap states, increasing the light intensity leads to a comparatively lower number of the photoexcited charge carriers to be captured. Thus, the fabricated device is more responsive for lower light intensities. Further, the detectivity under visible, and NIR light illumination was 1.12×10^{12} Jones and 7.27×10^{11} respectively, as shown in Figure 3.16b. On the other hand, EQE of the device was determined to be 469.2 % and 216.4 % for Vis and NIR light excitations, respectively as shown in Figure 3.16c. Response time or rise time, is an essential parameter to determine any detector performance. The conventional definition of rise time describes it as the time difference between $0.9I_{max}$ and $0.1I_{max}$ points in the photocurrent graph, wherein I_{max} is the maximum value. As displayed in Figure 3.16d, the response time of the fabricated photodetector was measured to be ~ 200 ms. The lower response time can be owed to the presence of trap states and impurity states in ReS_2 synthesized by hydrothermal method. In addition, to determine the flexibility of the fabricated device bending tests were performed by subjecting the device to more than 500 continuous bending cycles, as shown in Figure 3.16e. During this test, the device was subjected to external strain (~ 2 %) and returned to its original position, following which the photodetector experiments were conducted. The device exhibits a negligible change in performance, revealing the robustness of the device. Futhermore, reposne

spectrum of the fabricated device was displayed in Figure 3.16f and it was observed that resposne of the farbicated photodetector decreased significantly after 800 nm.

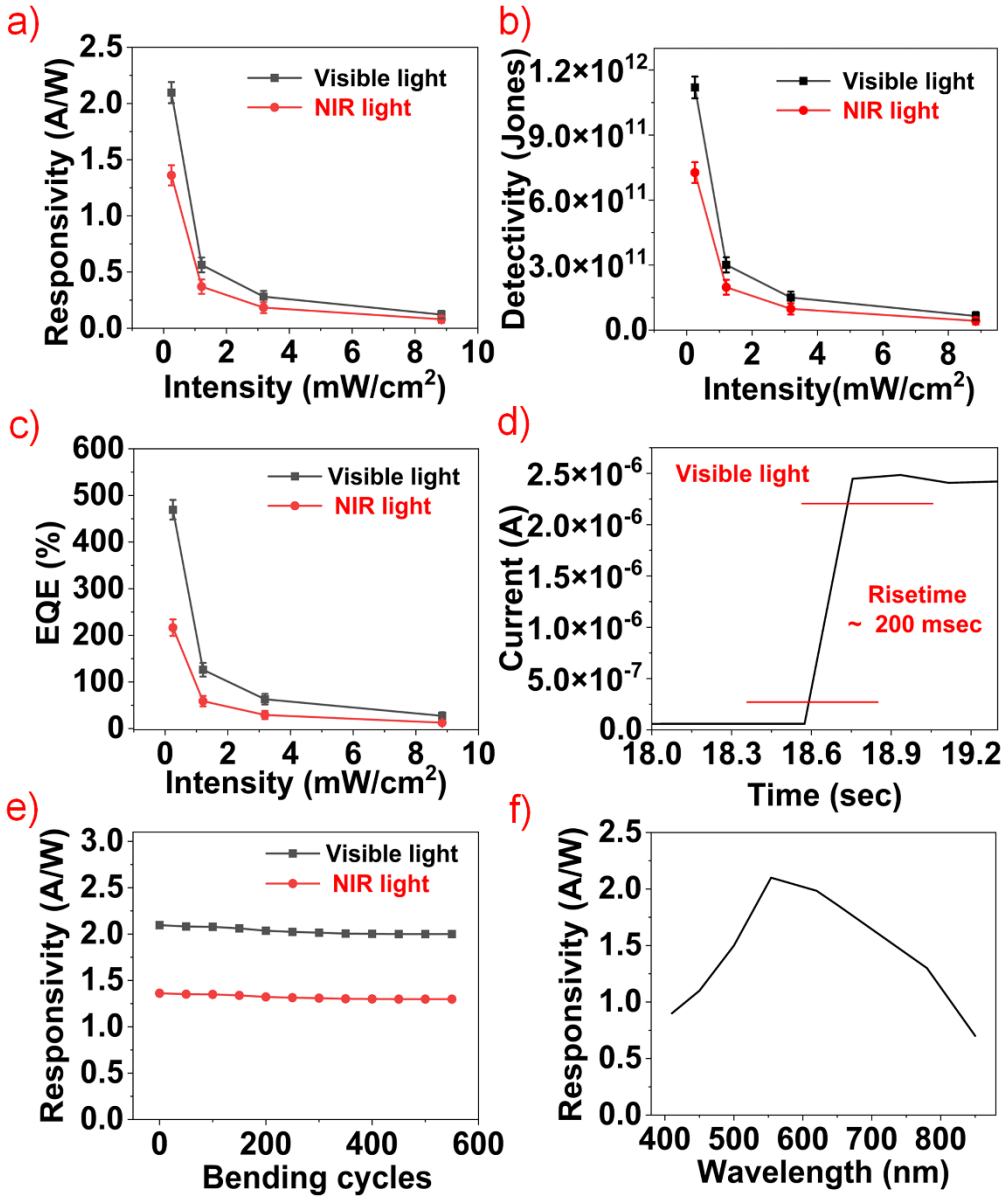

Figure 3.16: a) Graph displaying the photoresponsivity of the fabricated Au-NPs/ReS_2 photodetector under different light illuminations b) plot showing the detectivity of the device c) EQE vs. intensity plot under various light intensities d) graph displaying the response speed of the device and it was found to be ~ 200 ms, e) photoresponsivity of the fabricated device under more than 500 continuous bending cycles, f) response spectrum of the fabricated Au-NPs/ReS_2 device.

3.2.3.1 Photodetection mechanism

Figure 3.17a illustrates the Au-NPs/ReS_2 hybrid device. To understand the charge transfer mechanism across the Au-NPs/ReS_2 heterojunction and efficacy of Au-NPs in improving the performance of the device, an energy band diagram was drawn. Work function of synthesized ReS_2 was determined using UPS measurements. As displayed in Figure 3.17b, secondary electron cutoff energy was determined to be 16.12 eV. By substracting the secondary cutoff energy from 21.22 eV (excitation energy), the work function was calculated and it was found to be 5.1 eV. Furthermore, UPS measurements were carried out to examine the change in the work function of ReS_2 due to the integration of Au-NPs. As shown in Figure 3.17c, a shift in the secondary electron cutoff energy towards the higher energy levels was observed, which indicates the lower work function of Au-NPs/ReS_2 compared to pristine ReS_2 and reveals the n-doping of ReS_2. Due to this n-doping, Schottky barrier height at the interface of Au-NP and ReS_2 decreases which improves the charge carrier transfer from Au-NP to ReS_2 and helps in the enhancement of device performance.

Energy band diagram of synthesized ReS_2 is shown in Figure 3.17d. Due to the n-type nature of ReS_2, and the fact the work function of Au-NPs (~ 5.2 eV) [224,225] is greater than the work function of 5.1 eV, the nature of the contact is Schottky and hence a Schottky barrier is formed at the junction of Au-NP and ReS_2 , as depicted in Figure 3.17e. The amelioration in the fabricated Au-NPs/ReS_2 device photocurrent compared to the pristine ReS_2 photodetector is attributed to the plasmonic effect of Au-NPs decorated on ReS_2 nanosheets. The enhancement in fabricated device performance under light illumination is attributed to the two primary reasons. i) when the illuminated light is in resonance with the plasmonic frequency of the NPs decorated, a large number of higher energy electrons form oscillating electron clouds also known as hot electrons at Au-NPs surface, and the optical phenomenon is called localized surface plasmon resonance (LSPR)[191]. When plasmons couple with incident light, they can cause the light waves to get highly confined near the interface and result in enhanced near-field electromagnetic fields. The optical energy is collected by neighboring Au-NPs, resulting in a strong electric field within the device and boosting the absorption of illuminated light on ReS_2 microflowers. The increased light absorption of ReS_2 produces a large number of e-h pairs, which are further collected by the external bias and result in a significant increase in device photocurrent. ii) as previously mentioned, due to the LSPR effect, a large

number of higher energy electrons are generated at the surface of Au-NPs, which are called hot electrons. These hot electrons get sufficient energy to cross the Schottky barrier formed at the junction of Au-NPs/ReS_2 and transfer into the conduction band of ReS_2. The transfer of hot electrons makes the ReS_2 more n-doping and leads to increased charge density and photoresponsivity of the ReS_2.

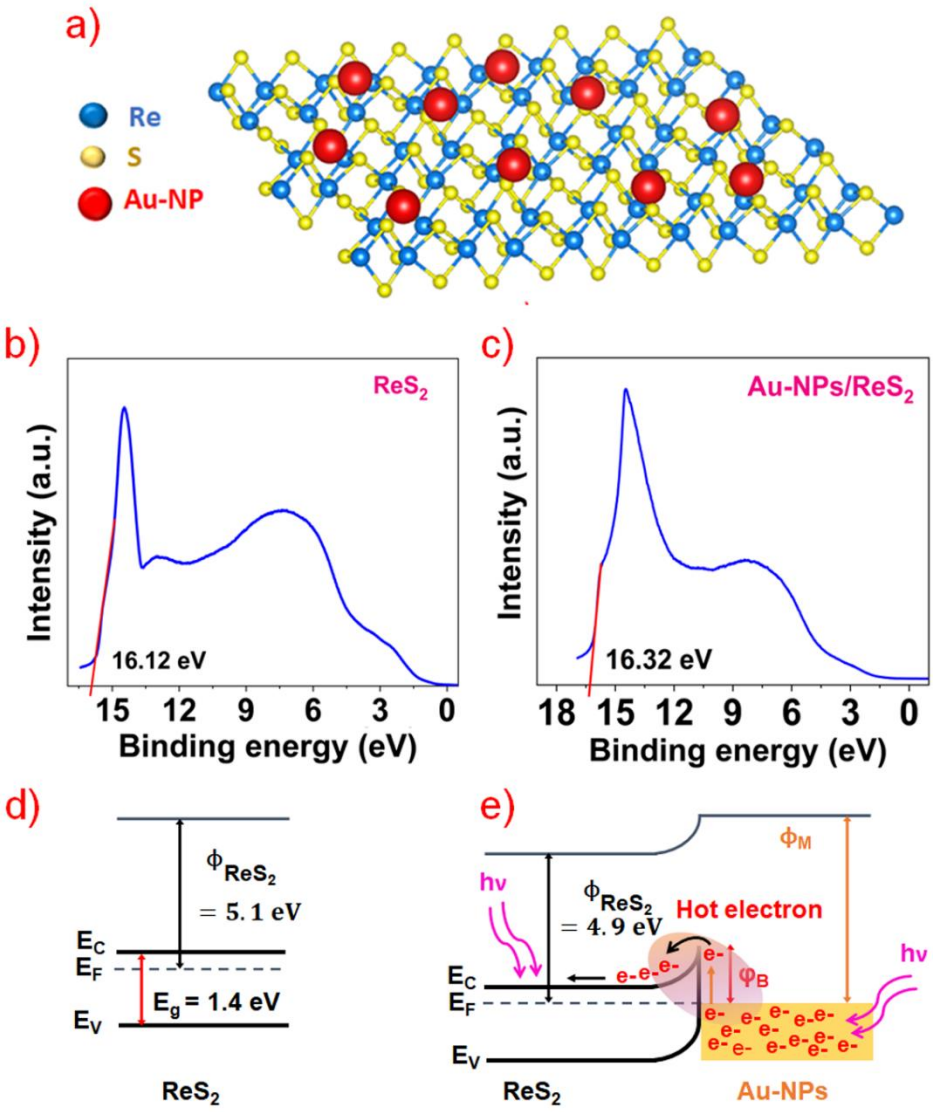

Figure 3.17: a) Schematic of the Au-NPs/ReS_2 heterostructure b-c) UPS spectra of pristine ReS_2 and ReS_2 decorated with Au-NPs d) band diagram of synthesized pristine ReS_2 e) schematic representing band diagram of Au-NP and ReS_2 heterojunction and the charge transport mechanism under light illumination.

Additionally, because of the large surface area and microflower surface morphology of synthesized ReS_2, decorated Au-NPs trap within ReS_2 microflowers and this trapping

causes the enhancement in light absorption due to multiple light scattering within the ReS_2 nanosheets. Furthermore, the internal electric field formed at the interface of Au-NPs and ReS_2 due to band bending aids in the effective segregation and transportation of photogenerated e-h pairs and also reduces the recombination rate of photoexcited e-h pairs. Thus, the overall device photocurrent of the fabricated Au-NPs/ReS_2 device increases significantly when light is illuminated. Also, in Au-NPs/ReS_2 heterostructure, ReS_2 acts as an electron acceptor and Au-NPs serve as the electron donor. The charge transfer leads to the absence of valence band holes in ReS_2, which suppresses the charge carriers recombination and helps in the improvement of device performance.

3.2.4 Plasmonic behavior explanation and simulation results

When a metallic nanoparticle is irradiated by light, their localized surface plasmons are excited. As a result, the light matter interaction (LMI) improves via light scattering and light absorption. As per classical theory, scattering dominates when diameter of NP is beyond 100 nm while absorption dominates for NP with a diameter less than 40 nm [226]. For NP with diameter within 40-100 nm, both scattering and absorption are present. Mathematically, the scattering (C_{SCA}) and absorption (C_{ABS}) cross-sectional area can be estimated using the following relations:[227]

$$C_{SCA}(\lambda) = \frac{8\pi^3}{3\lambda^4}|\beta(\lambda)|$$

$$C_{ABS}(\lambda) = \frac{2\pi}{\lambda}\mathrm{Im}\{\beta(\lambda)\}$$

where β denotes the polarizability of the nano-particle along the directional parallel to the electric field lines as illustrated in Figure 3.18. For spheroidal shaped nanoparticles, the polarizability can be calculated using the following relations.

$$\beta(\lambda) = \frac{(4\pi abc)(\tilde{\varepsilon}_1(\lambda) - \tilde{\varepsilon}_m(\lambda))}{3\tilde{\varepsilon}_m(\lambda) + 3L_j(\tilde{\varepsilon}_1(\lambda) - \tilde{\varepsilon}_m(\lambda))}$$

$$L_j = \frac{abc}{2}\int_0^\infty \frac{dq}{(l^2+q)\sqrt{(q+a^2)(q+b^2)(q+c^2)}}$$

Here, a, b, c are the radii of the spheroid axes; $\widetilde{\varepsilon_1}$and $\widetilde{\varepsilon_m}$ are the complex dielectric functions of the particle and surrounding medium respectively.

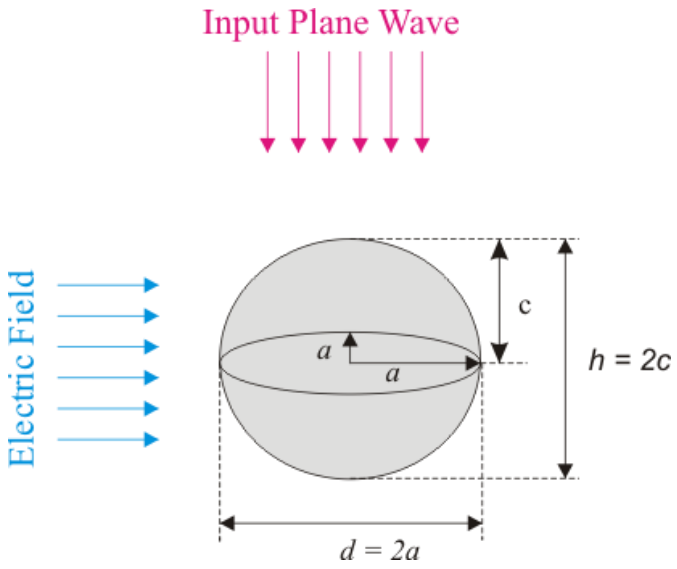

Figure 3.18: Schematic geometry of the nano-particle and light (input plane wave) interaction system.

The average size of Au-NPs particles used for the fabrication of device is approximately 40 nm, as a result light absorption is more compared to scattering. Further, FDTD based simulations were performed to calculate the optical cross-sectional areas using Mie theory for Au-NPs on ReS_2 thin layer. For simulation dimeter Au-NP considered is 40 nm while a plane wave is projected on the NP vertically and the surrounding medium is air. The wavelength of the plane-wave is varied between 400 nm to 800 nm. The obtained optical cross-sectional area (in terms of extinction, scattering and absorption cross-sectional area) is depicted in Figure 3.19a. The absorption and scattering cross-section to be approximately 6763.1 nm^2 and 1153.6 nm^2 respectively, at 554 nm. As a result, the extinction cross-sectional area has a high value (approximately 7916.4 nm^2) at 554 nm wavelength. Similarly, at 780 nm, the estimated value of scattering, absorption, and extinction cross-sectional area are 41.2 nm^2, 58.2 nm^2 and 99.4 nm^2, respectively. Thus, no significant role of Au NP is to be expected at 780 nm wavelength. From the simulation results, it is can be concluded that the Au NP on ReS_2 improves the total absorption by improving the absorption cross-sectional area at 554 nm wavelength while such an improvement is absent at 780 nm. Figure 3.19b and 3.19c presents the electric field intensity profiles for the excitation wavelengths of 554 and 780 nm. Because of localized surface plasmon resonance (LSPR), the oscillations of conductive electrons in Au nanoparticles trap the incoming light waves. This causes the electric field to be enhanced

around the nanosphere, as shown in Figure 3.19b and 3.19c, thus leading to strong absorption of ReS_2.

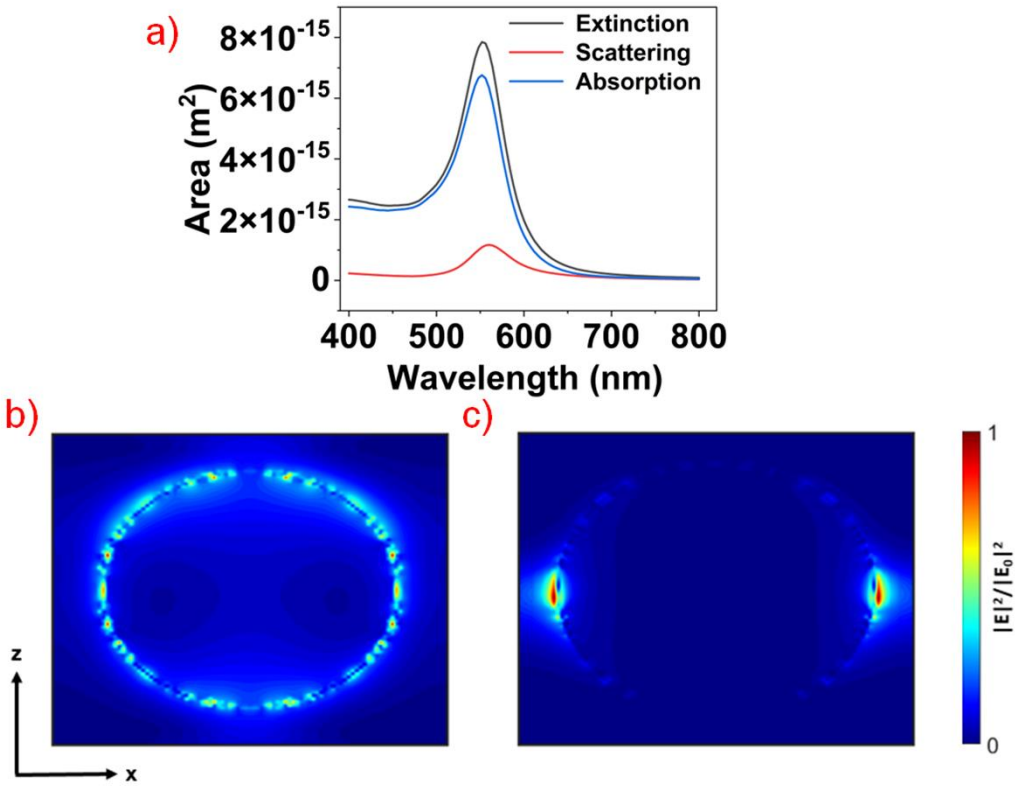

Figure 3.19: a) Simulation result of Mie Theory based optical cross-sections of Au nano-particles on ReS_2 film over 400 nm to 800 nm. Note that the absorption process is dominant at 554 nm resulting a high extinction cross-sectional area, b,c) E-field distribution around the interface of Au-NP and ReS_2 under excitation wavelength of 554 nm and 780 nm, respectively.

Table 3.2 shows a comparison of the fabricated plasmonic photodetector performance with that of other previously reported papers. *Rahamati et al.* reported that the device current of vertically grown MoS_2 could be improved by integrating with Au-NPs and reported the photoresponsivity of the Au-NPs/MoS_2 device increased 2.1 times compared to the pristine MoS_2 [191]. *Park et al.* fabricated a plasmonic NIR photodetector based on Ag NPs/MoS_2 heterostructures and a highest photoresponsivity of 0.881 mA W^{-1} at 980 nm was observed[190]. Recently, *Tang et al.* fabricated an isotropic-anisotropic vdWs heterostructure-based visible light photodetector using WS_2/ReS_2 and exhibited a photoresponsivity of 1.85 mA W^{-1} [148]. *Hafeez et al.* developed a visible light photodetector utilizing a bilayer ReS_2 film and it exhibited a photoresponsivity of 4 mA W^{-1} [219]. As displayed in Table 1, the fabricated plasmonic Au-NPs/ReS_2 photodetector

showed superior photo-sensing performance compared to other plasmonic photodetectors and vdWs heterojunction-based photodetectors reported earlier. Also, the fabrication technique used provides a reliable method for scalable production of high-performance broadband photodetectors. However, some improvements are needed to attain the desired response such as adjusting the size of Au-NPs and minimizing the distance between the electrodes, etc...

Table 3.2: Comparison of the fabricated Au-NPs/ReS_2 based plasmonic photodetector performance with other TMDs based photodetectors reported.

Device	**Fabrication method**	**Detection Range**	**Responsivity (mA W^{-1})**	**Response time**	**Ref.**
Au-NPs/ vertical MoS_2	CVD	Visible	24	> 100 ms	[191]
Ag-NPs/Multilayer MoS_2	Exfoliation	NIR	0.88	~ 10 s	[190]
Ag NPs/Few layer Graphene	Liquid-phase exfoliation	Visible	~ 28	-	[228]
Ag-NPs/ZnSe nanowire	Vapor-liquid-solid process	visible	184.8	-	[229]
WS_2/ReS_2	Exfoliation, dry transfer method	Visible	1.85	1.3 ms	[148]
Au-NP/MoS_2	PVD	Visible	1.5×10^3	-	[230]
ReS_2 bilayer film	CVD	Visible	4	1 s	[219]
Au-NPs/ReS_2	**Hydrothermal, Spin coating**	**Visible-NIR**	**2.1×10^3, 1.3×10^3**	**~ 200 ms**	**This work**

3.2.5 Conclusion

In summary, flexible Vis-NIR plasmonic photodetector was demonstrated by integrating Au-NPs with 2D ReS_2 nanosheets. Hydrothermal synthesis technique was used to synthesize ReS_2 and later it was deposited on flexible PET substrate using the spin coating method. Au-NPs were decorated on ReS_2 by the drop-casting technique.

Photosensing performance of the Au-NPs/ReS_2 device is 15-fold enhanced compared to pristine ReS_2. The improvement in photodetection performance is attributed to the LSPR generated by Au NPs, increased light absorption of ReS_2 due to light trapping, hot electron transfer to the conduction band of ReS_2, reduced e-h recombination, and effective charge transfer at Au-NPs/ReS_2 interface. The photoresponsivity of the developed Au-NPs/ReS_2 device for Vis and NIR light illumination was determined to be ~ 2.1 A W^{-1} and ~ 1.3 A W^{-1}, respectively. The response speed of the fabricated photodetector was measured to be ~ 200 ms. Further, the strong near-field improvement in the vicinity of Au-NPs under light illumination and the optical properties of Au-NPs/ReS_2 heterojunction were verified using the Lumerical FDTD Multiphysics simulation tool. This work may inspire future research on the fabrication of flexible, high-performance plasmonic photodetectors based on 2D TMDs for next-generation/future optoelectronic applications.

CHAPTER 4

Performance enhancement of highly flexible SnS(p)/MoS_2(n) heterostructure based broadband photodetector by piezo-phototronic effect

This work demonstrates the fabrication of a flexible p-SnS/n-MoS_2 heterostructure based piezo-phototronic photodetector and understanding the detailed charge transport mechanism. Electrical measurement of fabricated heterojunction shows excellent rectification behavior with an ideality factor of ~ 2.06. When the external strain is applied on the device, due to non-centrosymmetric structure of MoS_2, piezo-potential gets induced in MoS_2, which modulates the band structure and increases the width of the depletion region across the junction. The increase in depletion region results in a strong built-in electric field, which promotes the separation of photogenerated electron-hole (e-h) pairs more effectively and improves photogenerated charge carrier transport across the p-SnS/n-MoS_2 interface. The photoresponsivity of the device is increased by ~ 97 % at ~ 2% strain by piezo-phototronic effect compared to strain-free conditions. Energy band structure drawn by the values extracted from real-time ultraviolet photoelectron spectroscopy (UPS) measurements are used to explain the physical working mechanism behind the enhancement of photoresponsivity. The fabricated SnS/MoS_2 heterostructure showed a higher photoresponsivity in visible region compared to NIR region due to higher absorption in the visible region. This work demonstrates the cost-effective approach for the development of high performance photodetectors by using piezotronic interface engineering and paves the way for future flexible and wearable optoelectronics.

4.1 Introduction

Over the last decade, significant research has been conducted to enhance the performance of photodetectors. Piezo-phototronic effect is one of the prominent methods used to tune the performance of flexible optoelectronic devices and also attracted significant attention in the last decade [231,232]. The study of coupling between piezoelectric, semiconductor, and photoexcitation characteristics form the field of piezo-phototronics [231,233]. Upon external strain, piezotronic effect induces polarization charges which can effectively modify the energy band structure of p-n junction or metal-semiconductor interface and

thus modulate the separation, transport/migration, and recombination processes of photoexcited charge carriers [231]. Further, p-n junction based heterostructures gained special attention as they provide basic building block for various modern optoelectronics applications such as photodetectors, light-emitting diodes, solar cells, ultrafast lasers, and many more [234–237]. Over the last few years, number of p-n junction photodetectors were demonstrated utilizing piezotronic effect based on non-centrosymmetrical wurtzite-structured semiconductors such as ZnO nanowires, CdS, GaN, MoS_2, etc... [235,238–241]. The majority of them have disadvantages, including complicated fabrication, high costs, and a tight operating environment. Hence there is a need for the development of cost-effective, flexible p-n junction based piezotronic photodetectors.

TMDs such as MoS_2, $MoTe_2$, etc... simultaneously possess both piezoelectric and semiconducting properties due to non-central symmetric crystal structure, which produces piezo-potential when strained [235,238,240]. In addition, distinct optoelectronic and mechanical properties, which significantly surpass bulk and even some one-dimensional (1D) nanowires, promote utilizing of 2D materials in the fabrication of piezo-phototronic devices. Among 2D materials, MoS_2 has sparked a lot of interest in fabricating piezotronic devices for nanorobotics, human-machine interfacing, and wearable applications due to unique optoelectronic, semiconducting and piezoelectric properties [170,242,243]. Recently, piezoelectric effect in odd-numbered layered MoS_2 was reported in which the height of Schottky barrier was modulated with applied strain [244,245]. There are various reports on the fabrication of heterojunction of MoS_2 with CuO, WSe_2, GaN, SnS for various applications such as photodetectors, energy storage, sensors, etc.. [235,246,247].

As a member of group IV-VI semiconductor, tin sulfide is p-type 2D metal chalcogenide (MC). SnS had received a lot of attention as a result of its superior electronic and mechanical properties, non-toxic in nature, inexpensive, and abundant in nature [248–250]. These properties enable SnS as a suitable p-type semiconductor for the fabrication of p-n heterojunction based photodetector, solar cells, etc.. [250–252]. Until now, very few reports are available on the fabrication of TMDs-MC heterostructure based piezotronic devices for photodetector applications. Hence, there is a need for the study and development of TMDs-MC heterostructure based piezotronics devices for next-generation optoelectronic applications. There are several techniques for synthesizing MoS_2 and SnS, for example mechanical exfoliation, chemical vapor deposition, ALD, etc… [170,240,250,253]. All the above-mentioned methods are expensive, require high temperature and cleanroom facilities. Alternatively, hydrothermal synthesis method is

capable of preparing 2D materials at low-temperature, low-cost and with various surface morphologies.

In this work, highly flexible p-SnS/n-MoS_2 (TMDs-MC) heterostructure based visible-NIR photodetector was fabricated on PET substrate using hydrothermal spin-coating techniques. Further, demonstrated the significant enhancement in the fabricated photodetector performance under strain by piezo-phototronic effect. Here in p-SnS/n-MoS_2 heterostructure, SnS exhibits nonpiezoelectric properties due to the higher layer thickness [254] and odd number layered MoS_2 shows piezoelectric properties [244,255] . When a specific strain is applied on the fabricated device, polarization ions get generated in MoS_2 and lead to generation piezo-potential, which modulated the band structure at the junction. This modulation of band structure leads to effective photoexcited electron-hole pair separation and transportation at the interface. The responsivity of the fabricated p-SnS/n-MoS_2 heterostructure was increased by ~ 97 % at 2 % strain under visible (Vis) light illumination. Maximum photoresponsivity of the device at Vis and NIR light irradiation at a strain of ~ 2 % and light intensity of 0.44 mW/cm^2 is ~ 211 mA/W and ~133 mA/W, respectively. Furthermore, detectivity of the device in Vis and NIR region was ~ 3.18 × 10^{11} Jones and ~ 2.04 × 10^{11} Jones, respectively. Response time of the fabricated photodetector was found to be ~ 120 msec. To understand the enhancement in the photodetection performance, the energy band structure of p-SnS/n-MoS_2 is plotted, and the corresponding working mechanism is discussed. This work provides the understanding of piezo-phototronic effect in p-SnS/n-MoS_2 heterostructure and also demonstrates the low-cost and unconventional path to fabricate high performance flexible visible and NIR photodetectors.

4.2 Experimental Section

Materials and Characterization:

All the chemicals utilized were procured from Sigma-Aldrich. A Thermo Scientific K-alpha X-ray photoelectron spectroscopy (XPS) equipment was used for XPS analysis. Ultraviolet photoelectron spectroscopy (UPS) measurements were conducted using a helium source emitting at 21.22 eV in an ultrahigh vacuum chamber. LabRAM HR system, 532 nm laser with 10 mW was used for Raman measurements. UV-visible spectrophotometer (JASCO V-670) was utilized to analyze absorption spectra. Wavelengths of visible and NIR light used are 554 nm and 780 nm, respectively. Polyethylene terephthalate (PET) sheet procured from Sigma-Aldrich was used as a

flexible substrate for the fabrication of the device. Source meter, Keithley 2450, was used to complete all the electrical measurements.

Synthesis of SnS:

As reported previously from our group, SnS was synthesized using solvothermal method [97]. Figure 4.1a shows the schematic representation of SnS synthesis. Briefly, a nutrient solution was prepared by mixing $SnCl_2.2H_2O$ (1 mmol) and $Na_2S.9H_2O$ (2.5 mmol) in 30 ml ethylene glycol. For 30 minutes, prepared solution was stirred until it turned yellow. After thoroughly mixing the solution, it was transferred to a Teflon container (50 mL) and maintained at 180°C for 24 hours in a hot-air oven. The resultant solution was washed multiple times using centrifugal filtration to remove the residues.

Synthesis of MoS_2:

MoS_2 was synthesized using hydrothermal method. A nutrient solution was made by mixing CH_4N_2S (228 mg) and $Na_2MoO_4.2H_2O$ (362 mg) in DI water (30 ml). The well-mixed was moved to Teflon container (50 ml) and kept in oven for 20 hr at 200ºC. The final solution containing MoS_2 was used for the fabrication of the device. Figure 4.1b shows the schematic representation of MoS_2 synthesis.

Fabrication of device:

The fabrication procedure of the p-SnS/n-MoS_2 heterostructure is illustrated in Figure 4.1c. Synthesized MoS_2 solution was spin coated on a flexible PET sheet, Aluminum (Al) foil and polyimide (PI) tape were used to mask specific area. Later, MoS_2 coated PET sheet was dried at 100ºC for few minutes. Further, some portion of the MoS_2 coated PET sheet was masked with PI tape Al foil. To form the p-n junction with MoS_2, synthesized SnS solution was spin coated on the unmasked portion and dried at 100ºC for a few minutes. Finally, the silver (Ag) contacts were made on two sides of the p-SnS/n-MoS_2 heterostructure using thermal evaporator deposition technique.

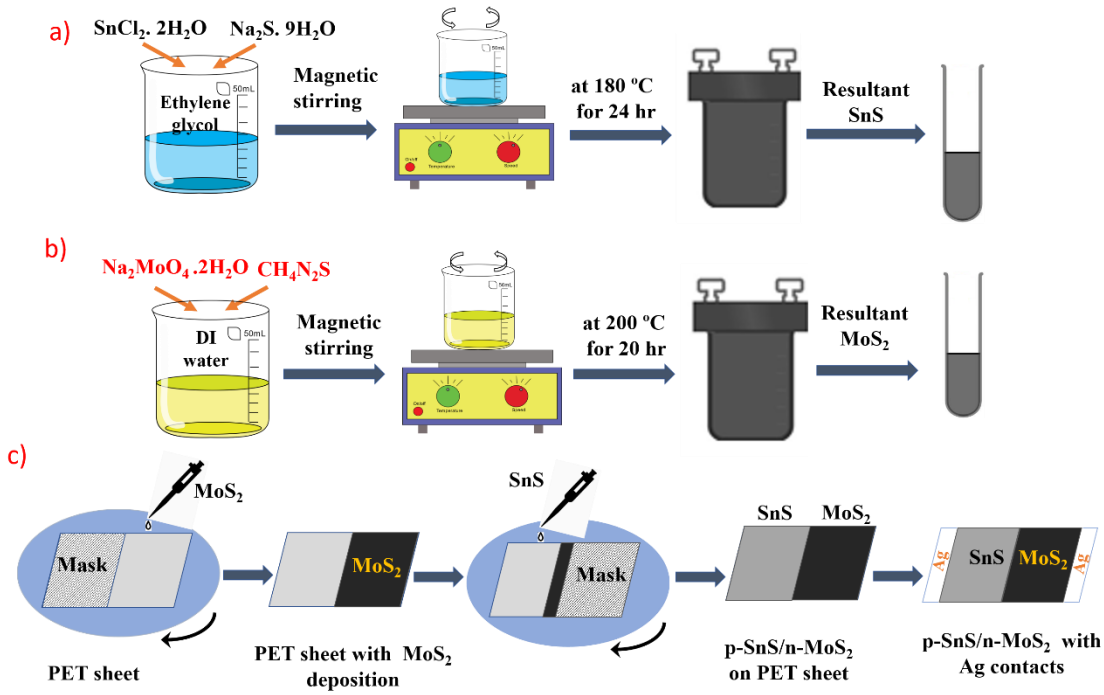

Figure 4.1: Schematic representing the synthesis procedure of a) SnS, b) MoS_2 using hydrothermal method. c) illustration of fabrication procedure of p-SnS/n-MoS_2 heterostrucutre on PET sheet using spin coating technique.

4.3 Results and Discussions

Surface morphology of the SnS deposited on PET sheet was observed by FESEM analysis. Figure 4.2a showcases the low-magnification FESEM images of SnS, confirms the uniform deposition on the substrate. Figure 4.2b shows a high-magnification FESEM image of SnS that reveals nonuniform microbelt-like features. Elemental mapping images of synthesized SnS are included in Appendix A, Figure S17. XRD spectrum analysis was used to examine the crystallinity and crystal structure of as prepared SnS. As shown in Figure 4.2c, XRD pattern of SnS contains peaks at 66.7°, 64.3°, 56.8°, 53.31°, 51.45°, 48.68°, 45.62°, 42.68°, 39.17°, 31.73°,30.65°, 27.6°, 26.16°, and 22.16°. These XRD diffraction peaks can be indexed to (171), (212), (042), (231), (112), (211), (002), (210), (131), (111), (101), (021), (120), and (110) orientations respectively, which are consistent with orthorhombic structures of SnS, JCPDS # 39-0354 [256,257].

Further XPS measurements were carried out. The presence of Sn, S elements are observed in the XPS survey spectra, Figure 4.2d. Additionally, due to the partial oxidation of SnS, oxygen is present and also, due to the stub used carbon is present in the survey spectrum. High resolution Sn 3d XPS spectrum is depicted in Figure 4.2e,

contains two characteristic peaks centered at binding energies 495.2 eV and 486.5 eV, which could be attributed to Sn^{2+} $3d_{3/2}$ and Sn^{2+} $3d_{5/2}$, respectively. Sn^{4+} peaks are not detected in the spectrum. As depicted in Figure 4.2f, high resolution spectrum of S2p contains two prominent peaks centered at 161.2 eV and 160.1 eV, which can be assigned to S^{2-} $2p_{1/2}$ and S^{2-} $2p_{3/2}$. Damping in XPS spectrum is attributed to the surface roughness of the fabricated sample because non-ideal surface topography strongly influences number of signal electrons in photoelectron spectroscopy [258]. The characterization results are well matched with the reported literature of SnS [259]. Furthermore, structural phases of prepared SnS were studied by Raman spectrum analysis. As shown in Figure 4.2g, Raman modes are observed at 214 cm^{-1}, 184.7 cm^{-1}, 156.6 cm^{-1}, 95 cm^{-1}, and 64 cm^{-1} corresponding to the different optical phonon modes of SnS [260,261]. Peak at 95 cm^{-1} represents to A_g transverse optical (TO) mode and the peaks noticed at 214 cm^{-1} and 184.7 cm^{-1} are corresponding to A_g longitudinal optical (LO) mode. The peak noticed at 156.6 cm^{-1} is assigned to B_{3g} mode and peak observed at 64 cm^{-1} represents the combinations B_{2g} and A_g modes of SnS. [262]. Raman spectrum analysis confirms that there are no impurity phases of SnS such as SnS_2, Sn_2S_3, which usually show prominent peaks at 312 cm^{-1} and 308 cm^{-1} [260]. UV-vis spectroscopy was used to study the optical absorption spectra of SnS nanoflakes. As depicted in Figure 4.2h, synthesized SnS showed higher absorption in visible region rather than NIR and UV regions. The indirect bandgap of synthesized SnS was estimated using well known Tauc plot technique, and the bandgap of the synthesized SnS was determined to be ~ 1.2 eV, as seen in the inset of Figure 4.2h.

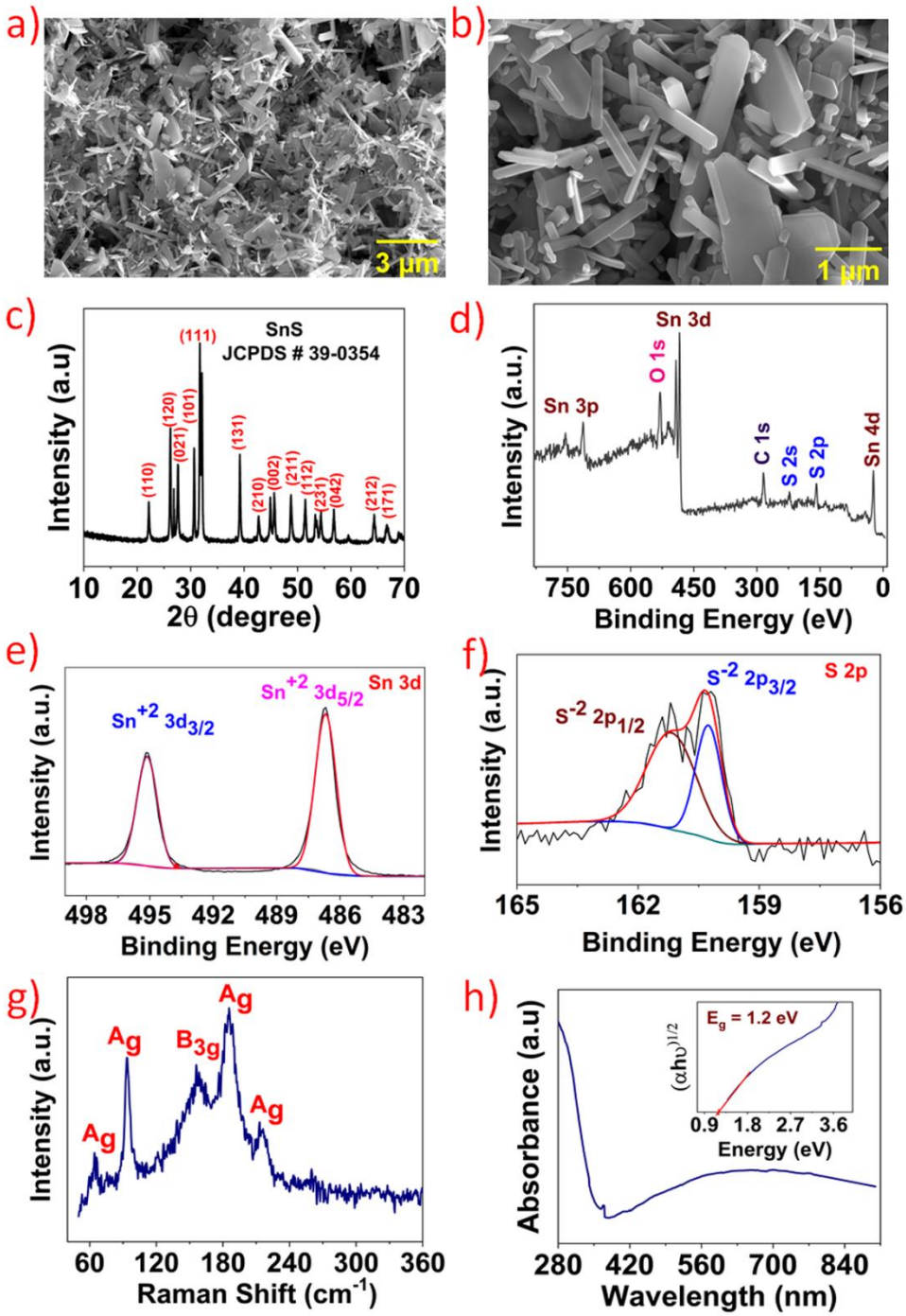

Figure 4.2: a,b) FESEM images of SnS deposited on PET sheet c) XRD pattern of SnS d-f) survey spectra of SnS deposited on PET sheet, and narrowband spectra of Sn3d and S2p g) Raman spectrum of synthesized SnS h) UV-vis absorption spectrum of prepared SnS; Tauc plot is displayed in the inset.

Surface morphology of the MoS_2 deposited on PET sheet was observed by FESEM imaging. As displayed in Figure 4.3a-b, microflower structure morphology was observed, wherein nanosheets are aggregated. Elemental analysis of synthesized MoS_2

shows the presence of molybdenum (Mo) and sulfur (S), Figure S18 (Appendix A). Structural characteristics of synthesized MoS_2 were studied by XRD analysis. As depicted in Figure 4.3c, XRD spectrum of MoS_2 contains peaks at 32.4°, 35.6°, 43.6°and 57.5° corresponding to (100), (103), (006), and (110). The broadening of MoS_2 XRD peaks is attributed to the low temperature hydrothermal synthesis, size of the crystallite and the large number of defects in MoS_2 [263,264]. Further a minor peak was noticed at ~ 14°, which confirms that the synthesized MoS_2 has few layers [180]. MoS_2 XRD spectrum matches well with mixed phase of hexagonal and rhombohedral, JCPDS # 37-1492 [179,265]. To further confirm the formation of MoS_2, elemental composition of synthesized MoS_2, XPS measurements were carried out. As displayed in Figure S19 (Appendix A), XPS survey spectrum contains peaks confirming the presence of Mo, S. In addition, oxygen peak is present in the XPS spectrum due to the partial oxidation of MoS_2 and also the presence of carbon peak is attributed to the stub used during the XPS measurements. As depicted in Figure 4.3d, narrowband XPS spectrum of Mo 3d was deconvoluted into two significant peaks centered at 228.6 eV and 232 eV, which can be ascribed to $Mo^{4+}3d_{5/2}$ and $Mo^{4+}3d_{3/2}$, respectively. Low-intensity peak was observed around 235.3 eV, which represents the oxidation state of (+6) of Mo. The presence of Mo^{6+} is attributed to the unreacted MoO_4^{2-} during synthesis of MoS_2. Furthermore, another low-intensity peak was observed at binding energy of 225.2 eV, which indicates S2s peak. Figure 4.3e depicts the narrow band XPS spectrum of S2p, which was deconvoluted into doublet peaks at 161.6 eV and 163.1 eV, assigned to $S2p_{3/2}$ and $S2p_{1/2}$, respectively and it reveals the S^{2-} oxidation state of S in MoS_2 [266]. To provide additional confirmation regarding the formation of MoS_2 and number of layers of prepared MoS_2, Raman analysis was carried out. As depicted in Figure 4.3f, Raman band at ~ 406 cm^{-1} and ~ 384 cm^{-1} are attributed to A_{1g} and E^1_{2g} modes. Two sulfur(S) atoms in-plane vibrations with respect to the molybdenum (Mo) atom belong to E^1_{2g} mode, while out-of-plane vibrations of sulfur(S) atoms correspond to A_{1g} mode. The Raman shift difference between A_{1g} and E^1_{2g} is ~ 22 cm^{-1}, which confirms three-layer formation of MoS_2 nanoflakes [182]. Furthermore, optical bandgap of synthesized MoS_2 was calculated from UV-visible absorption spectrum. As depicted in Figure 4.3g, synthesized MoS_2 exhibited higher absorption in visible region rather than NIR region. The UV-Vis spectrum shows four characteristic absorption peaks; two weak peaks between 600-700 nm are attributed to the A and B transitions to the split valence band, also broad absorbance peaks between

400- 500 nm ascribed to the C and D transitions [267–269]. Based on an established Tauc plot, the bandgap was determined to be ~ 1.47 eV, as shown in Figure 4.3h.

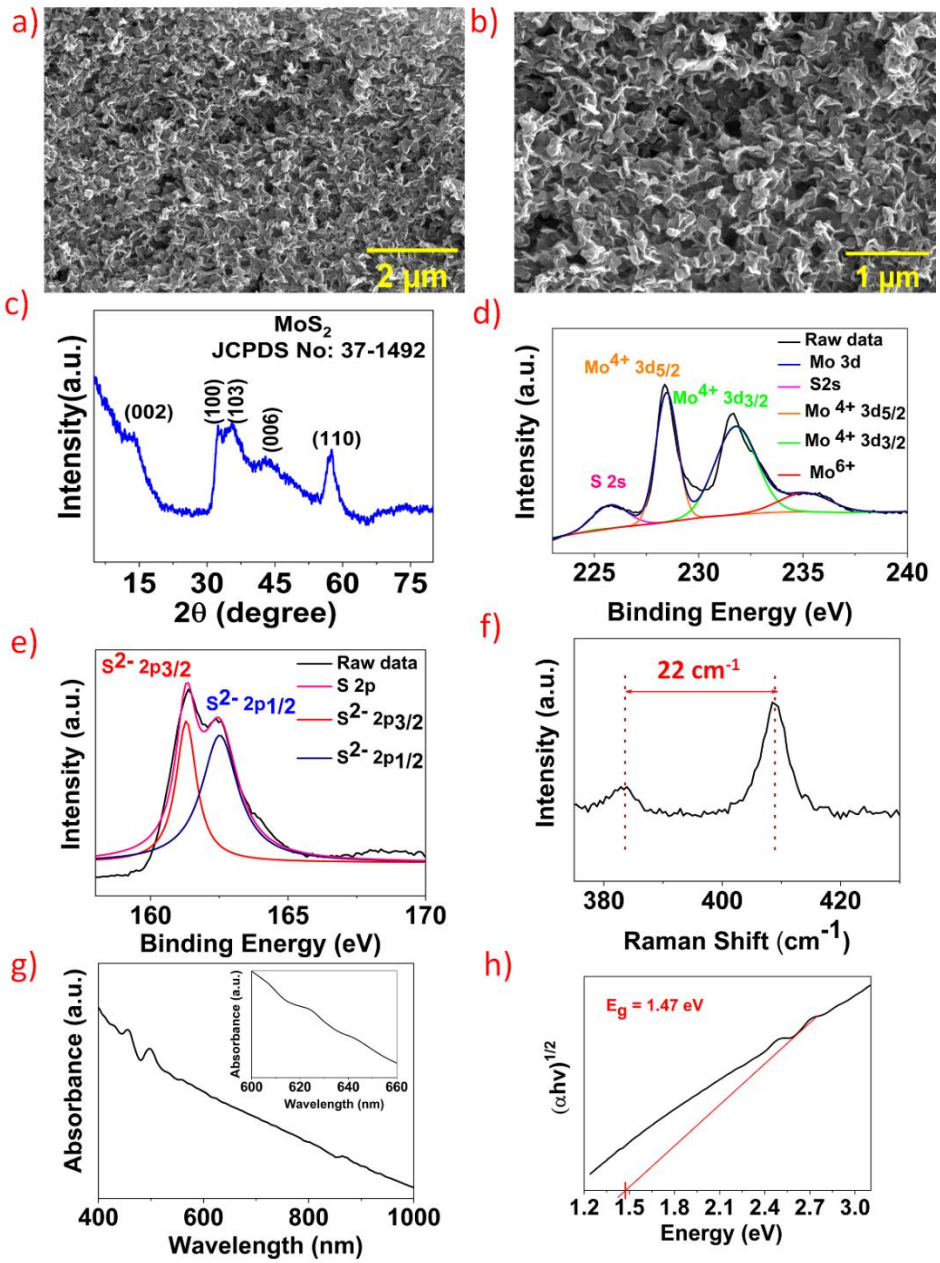

Figure 4.3: a-b) FESEM images of MoS_2 deposited on PET sheet, c) XRD spectra of MoS_2, d-e) Narrowband XPS spectrum of Mo 3d and S2p f) Raman spectrum of MoS_2 g) UV-vis spectrum of MoS_2 h) Graph shows the Tauc plot, wherein the bandgap was calculated to be ~ 1.47 eV.

Surface morphology of the fabricated p-SnS/n-MoS_2 device was observed using FESEM analysis. Figure 4.4a, shows the heterostructure interface between SnS and MoS_2, wherein the junction between SnS micro-belts and MoS_2 microflower structure can be

clearly seen. As fabricated SnS micro-belts were seen on top of the MoS_2 flowers structures, Figure 4.4b. Elemental mapping of the p-SnS/n-MoS_2 was also carried out and elemental mapping images are included in the Appendix A, Figure S20. Further, to confirm the SnS-MoS_2 heterojunction XRD analysis of the prepared SnS-MoS_2 heterojunction was performed. As shown in XRD spectrum, Figure 4.4c, peaks were observed at 22.16°, 26.21°, 27.6°, 30.65°,31.73°, 39.22°, 42.68°, 45.62°, 48.78°, 51.45°, 53.31°,56.8°,64.33°, and 66.45°.These peaks are ascribed to (110), (120),(021), (101), (111), (131), (210), (002), (211), (112), (231), (042), (212), and (171) respectively and matched orthorhombic SnS (JCPDS card number: 39-0354) [265]. Other characteristic peaks were observed at 14.2°, 32.35°, 42.62°, and 57.4° are corresponding to (002), (100), (006) and (110), indicating the mixed phase of rhombohedral and hexagonal MoS_2, JCPDS no: 37-1492 [57].

To provide further evidence, XPS analysis of the SnS/MoS_2 heterojunction was performed. All elements, Mo, Sn, and S can be seen in the XPS survey spectrum of SnS/MoS_2 heterostructure, Figure 4.4d. High resolution Sn 3d spectrum, as shown in Figure 4.4e, contains two peaks at binding energies of 486.1 eV and 494.2 eV, corresponding to Sn^{2+} $3d_{5/2}$ and Sn^{2+} $3d_{3/2}$. In addition, the peaks at 160.8 eV and 162 eV in S2p spectrum, Figure 4.4f, correspond to S^{2-} $2p_{3/2}$ and S^{2-} $2p_{1/2}$, respectively [179,270] As depicted in Mo 3d spectrum Figure 4.4g, two peaks are observed at 228 eV, and 231.2eV can be assigned to $Mo^{4+}3d_{5/2}$ and $Mo^{4+}3d_{3/2}$ and peak centered at 225.3 eV is attributed to S2s in MoS_2 [57,270].

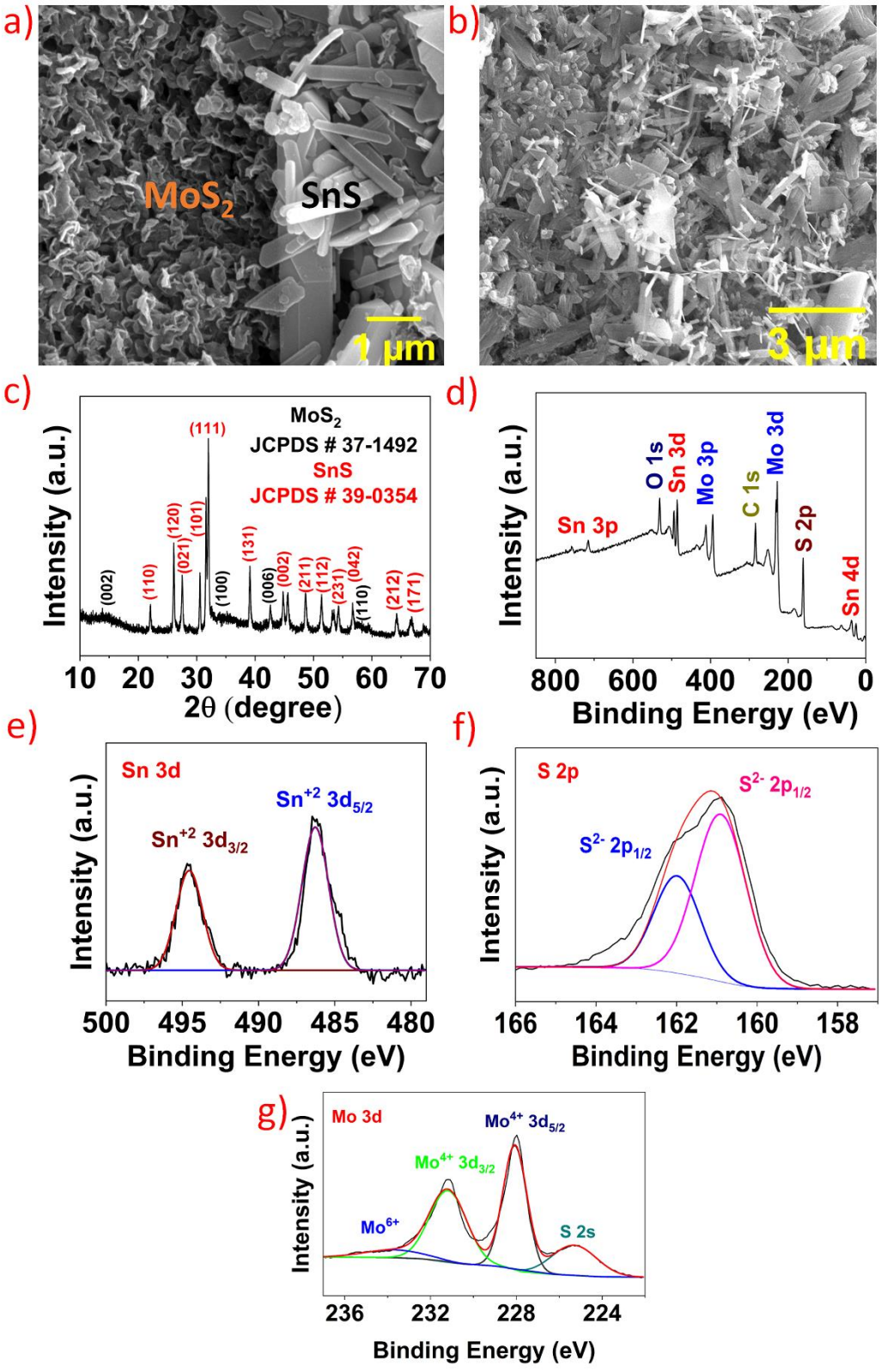
a)
MoS2
SnS
1 μm
b)
3 μm
c)
MoS2
JCPDS # 37-1492
SnS
JCPDS # 39-0354
(111)
(120)
(021)
(101)
(131)
(002)
(110)
(100)
(006)
(002)
(211)
(112)
(231)
(042)
(110)
(212)
(171)
Intensity (a.u.)
10 20 30 40 50 60 70
2θ (degree)
d)
Sn 3p
O 1s
Sn 3d
Mo 3p
C 1s
Mo 3d
S 2p
Sn 4d
Intensity (a.u.)
800 600 400 200 0
Binding Energy (eV)
e)
Sn 3d
Sn+2 3d5/2
Sn+2 3d3/2
Intensity (a.u.)
500 495 490 485 480
Binding Energy (eV)
f)
S 2p
S2- 2p1/2
S2- 2p1/2
Intensity (a.u.)
166 164 162 160 158
Binding Energy (eV)
g)
Mo 3d
Mo4+ 3d5/2
Mo4+ 3d3/2
Mo6+
S 2s
Intensity (a.u.)
236 232 228 224
Binding Energy (eV)

Figure 4.4: a,b) FESEM images of fabricated p-SnS/n-MoS_2 heterostructure, c) XRD pattern of the p-SnS/n-MoS_2 heterostructure d) XPS survey spectrum of p-SnS/n-MoS_2 heterojunction, e,f,g) Narrowband XPS spectrum of Sn3d, S 2p and Mo 3d.

Photodetection measurements:

As-fabricated p-SnS/n-MoS_2 heterojunction with Ag contacts was utilized as visible and NIR light detector. In order to make sure the photodetector was stable; it was left in the dark for over 10 hours before the photodetection measurements were performed. The I-V characteristics shown in Figure 4.5a demonstrate the rectifying behavior in the p-SnS/n-MoS_2 heterostructure. Through analysis, the ideality factor was determined to be 2.06 eV, while the Schottky barrier height was calculated to be 0.2778 eV. Deviation of the ideality factor value is attributed to the presence of surface states, defects formed during the hydrothermal synthesis and barrier inhomogeneity. In addition, to prove that there is no non-symmetric contact effect, I-V measurements of individual MoS_2 and SnS coated with metal(Ag) electrodes were performed and symmetrical I-V behavior was observed as shown in Appendix A, Figure S21. Further, under different light intensities, electrical measurements of the fabricated p-SnS/n-MoS_2 photodiode heterojunction was performed and as depicted in Figure 4.5b, current is increasing with an increase in light intensity. The rise in device current is related to the efficient separation of photogenerated electron-hole pairs. Similar photodetection measurements were repeated for NIR illumination and similar trend was noticed, Figure 4.5c. Further, time-dependent response of the fabricated photodetector with light on or off was studied. As presented in Figure 4.5d and 4.5e upon light illumination, the photocurrent increases sharply, then stabilizes in higher current, and the photocurrent decreases when the light illumination is turned off. This temporal response was repeated for multiple cycles exhibiting the excellent reliability and stability of the fabricated device. Furthermore, the fabricated device was tested with different light intensities and time-dependent response of the fabricated device with various Vis and NIR light intensities is depicted in Figure 4.5f and 5g, respectively. As shown in the graph, a rise in photocurrent was noticed as light intensity increased. In comparison to NIR light illumination, the device photocurrent changes more when exposed to visible light, indicating that comparatively, fabricated device responds better to visible light than to NIR light illumination. The device response well matches with UV-vis spectra (Figure 4.2h and Figure 4.3g) of MoS_2 and SnS, wherein higher absorbance was observed in visible region. The same experiments were

carried out on three fabricated devices and the same pattern was seen. The excellent performance of the fabricated p-SnS/n-MoS_2 heterostructure based broadband (visible and NIR) photodetector is ascribed to efficient separation of photoexcited charge carriers due to the built-in potential at the heterojunction and broadband absorption spectrum.

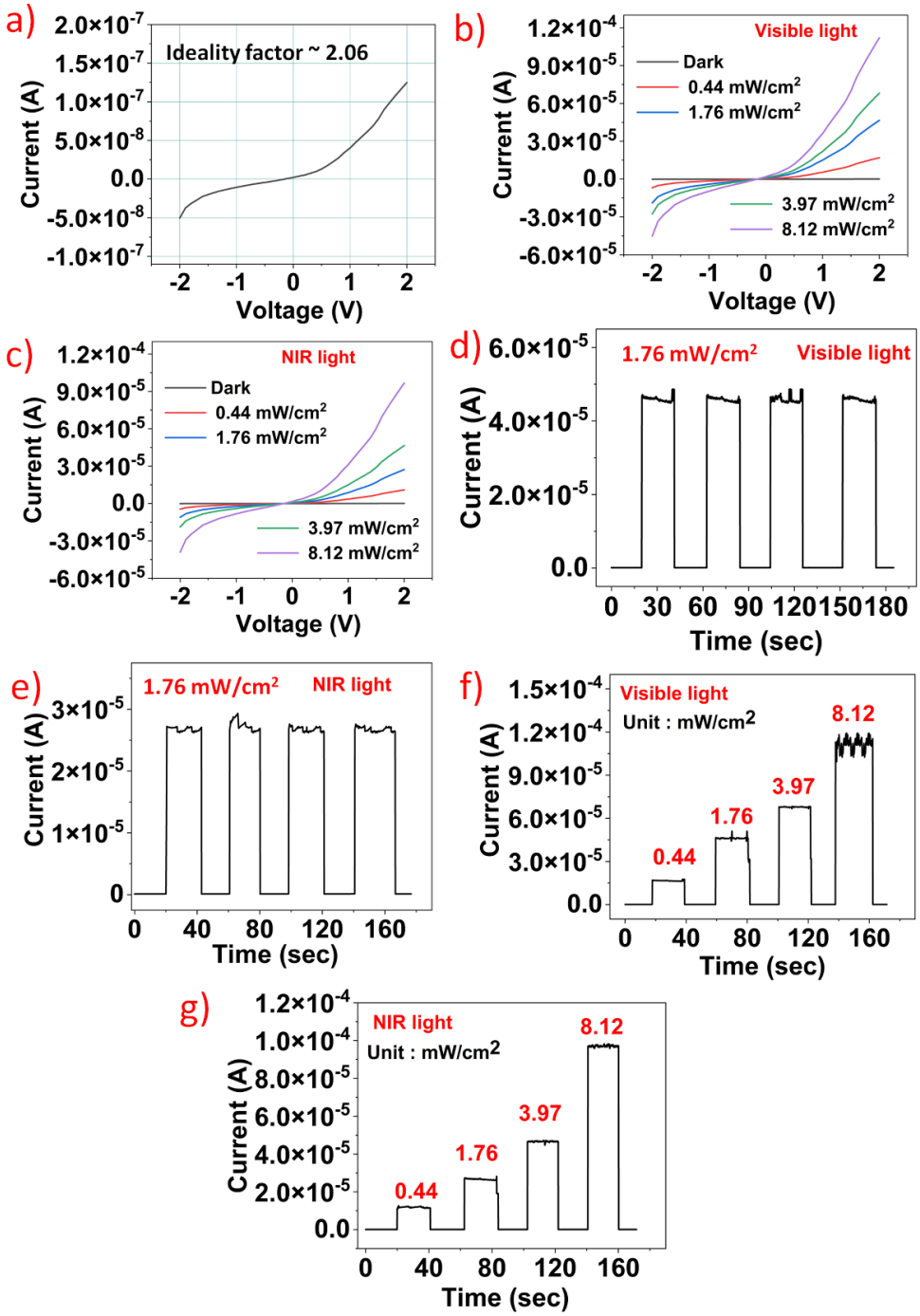

Figure 4.5: a) I-V plot of the p-SnS/n-MoS_2 heterostructure in dark under strain free state b-c) I-V plot of the heterojunction with various NIR and visible light intensities d-e) device photocurrent plotted over the time under constant visible and NIR light intensity,

1.76 mW/cm^2 f-g) the device photocurrent vs. time under various visible and NIR light intensities.

For photodetectors, external quantum efficiency (EQE), detectivity (D*), and responsivity(R) are critical parameters, and they are expressed as follows [161,271,272]:

$$R = I_{ph}/(P_{in} \times A)$$

$$EQE = hc \times (R/q\lambda)/100$$

$$D^* = (R \times \sqrt{A})/\sqrt{2 \times e \times I_{dark}}$$

where P_{in}, I_{ph}, I_{dark}, A, and q are intensity of light illuminated, photocurrent, dark current, active area of the device, and electron charge. Active area of the fabricated photodetector is approximately 48 mm^2. Photoresponsivity of device under visible and NIR light illumination was measured to be ~ 106.5 mA/W and ~ 68.4 mA/W, respectively, Figure 4.6a. The device photoresponsivity is higher under visible light illumination than under NIR illumination, further proving that the developed photodetector is more responsive to Vis light. Under visible and NIR light illuminations, the EQE of the fabricated device was determined to be ~ 23.85 % and ~ 10.88 %, respectively, Figure 4.6b.

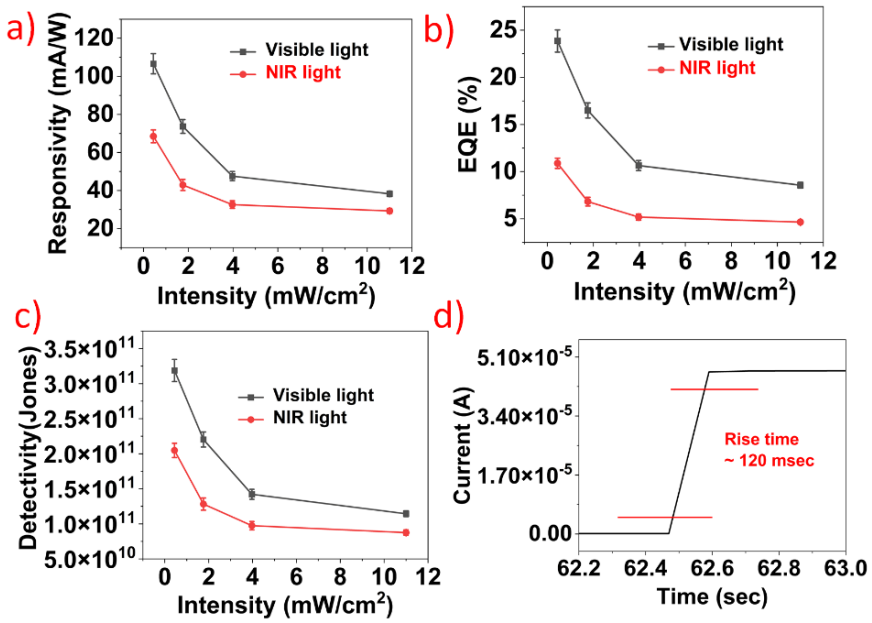

Figure 4.6: a-c) Responsivity, EQE, and detectivity of the fabricated p-SnS/n-MoS_2 heterostructure under Vis and NIR light illumination d) Under visible light illumination, the fabricated device rise time was found to be ~ 120 ms.

Furthermore, detectivity of the device under visible and NIR region was calculated to be ~ 3.18 × 10^{11} Jones and ~ 2.04 × 10^{11} Jones, respectively, as shown in Figure 4.6c. Rise time is also another critical parameter to be considered for evaluating the photodetector

performance. Rise time of the fabricated photodetector is taken as the time difference between $0.9I_{peak}$ and $0.1I_{peak}$, wherein I_{peak} is maximum photocurrent. The fabricated photodetector response time was measured to be ~ 120 msec, as shown in Figure 4.6d.

4.4 Piezo-phototronic effect on p-SnS/n-MoS_2 heterostructure

Various strains were applied on the device to examine the impact of strain on the sensitivity of the p-SnS/n-MoS_2 heterojunction, and change in the photodetection performance was analyzed as illustrated in Figure 4.7. Current-voltage (I-V) measurements of the fabricated p-SnS/n-MoS_2 photodiode under various applied strains were measured and as seen in Figure 4.7a, an increase in strain resulted in a decrease in current. The decrease in the device current is attributed to the increase in the depletion region at p-SnS/n-MoS_2 junction with the increase in applied strain. As shown in Figure 4.7b, with increase in applied strain Schottky barrier height is increased. The increase in Schottky barrier height with strain is attributed to the piezo-potential induced in MoS_2. Furthermore, the fabricated device was illuminated with different visible light intensities under various strains, the corresponding photocurrent vs. time is plotted Figure 4.7c. During the experiment, device was bent and increased the light intensity step by step. At 2 % of strain, the fabricated photodetector exhibited ~ 97 % increase in the photocurrent compared to without strain. Similar experiments were repeated under NIR illumination, as depicted in Figure 4.7d. Increased strain resulted in an increase in device photocurrent.The increase in photocurrent is attributed to the stronger electric field created at the interface of p-SnS/n-MoS_2 due to the bend-induced piezo-phototronic effect, which acts as an extra driving force for the separation of generated e-h pairs and increases the device photocurrent. Further, responsivity was calculated at various light illuminations and strains (0%, 0.5 %, 1%, 2 %) is plotted in Figure 4.7e and 7f. The responsivity of the device was increased with increase in strain because internal electric field at junction increases in strain applied. Maximum responsivity for visible and NIR light at strain of ~ 2 % and light intensity of 0.44 mW/cm^2 is ~ 211 mA/W and ~133 mA/W, respectively. In addition, Figure S22, Appendix A, shows the detectivity and EQE of the device under various strains and light intensities.

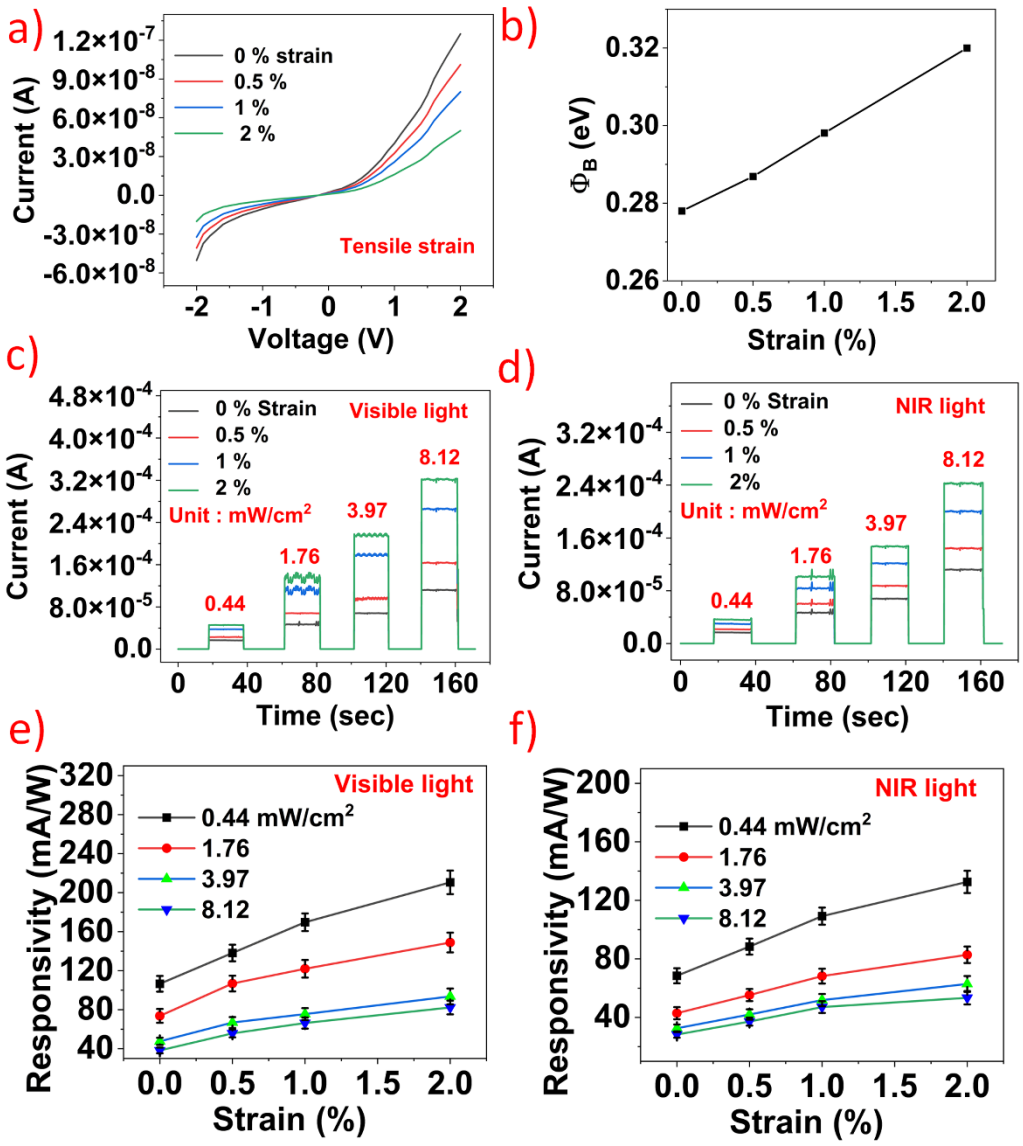

Figure 4.7: a) I-V characteristics of the fabricated heterojunction in dark under various applied strains, b) Plot representing the change in the Schottky barrier height with applied strain on the heterojunction, c-d) temporal response at different strains and light intensities, e-f) Responsivity of the fabricated piezo-phototronic photodetector under various strains.

Photodetection mechanism:

To elucidate the working mechanism for the enhancement in the photocurrent of fabricated p-SnS/n-MoS_2 photodetector, band diagram of p-SnS/n-MoS_2 heterostructure with and without strain are drawn, Figure 4.8. Work function is a critical parameter to be considered to analyze the band structure. Work function of the synthesized SnS and MoS_2 were calculated using UPS analysis. The difference between the photon energy of the exciting radiation and the cutoff energy can be used to determine the work function. The

cutoff energy is described as the maxima of the first derivative of the measured curve. Work function of the synthesized MoS_2 and SnS are found to be 4.31 eV and 5.01 eV, respectively. The optical bandgap of the MoS_2 and SnS were calculated from UV-vis absorption spectrum using well known Tauc plot technique and bandgap of the MoS_2 and SnS were ~ 1.47 eV and ~ 1.2 eV, respectively, (Figure 4.2h and Figure 4.3g). Due to the difference in energy levels, transfer of electrons and holes occurs across the junction, and it results in fermi level equilibrium state and formation of a strong built-in potential at p-SnS/n-MoS_2 interface. According to the UV-vis absorption spectra, Figure 4.3g, MoS_2 showed a significant absorbance in NIR and visible regions. When light is irradiated on n-MoS_2, e-h pairs are generated. The built-in electric field at the interface of p-SnS/n-MoS_2 effectively separates the photogenerated electron-hole pairs and collected by the two electrodes, thus suppress the carrier recombination dynamics and significantly improves the device current.

Further, under external strain the fabricated p-SnS/n-MoS_2 heterostructure photocurrent was increased significantly. The significant increase in the device photocurrent is ascribed to the bend-induced piezo-phototronic effect. The field of piezo-phototronics deals with piezoelectric, semiconductor, and photoexcitation properties. MoS_2 is n-type semiconductor with piezoelectric property and it is sensitive to visible and NIR light. When strain is applied on MoS_2, piezo-potential get induced in MoS_2 due to the dipole movements formed in non-centrosymmetric structure of MoS_2. Piezo-potential modifies the Schottky barrier height at the interface and widens the depletion region. The increase in depletion region width enhances the electrified at the interface of the p-SnS/n-MoS_2. The induced strong built-in potential facilitates the efficient separation and transportation of photogenerated charge carriers. Hence, due to piezo-phototronic effect, significant improvement in the photoresponsivity of p-SnS/n-MoS_2 heterostructure was observed, when the strain was applied.

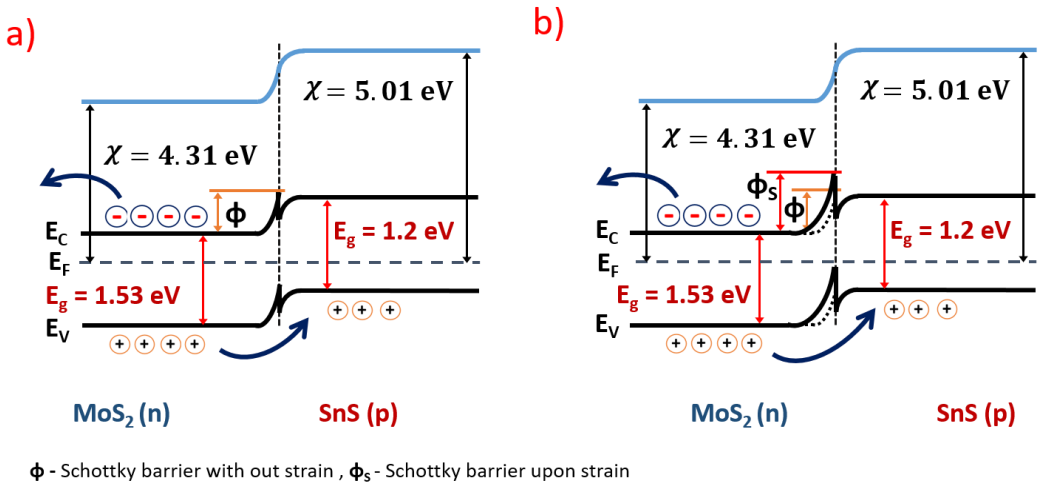

Figure 4.8: a) Energy band structure of p-SnS/n-MoS_2 heterostructure with light irradiation b) Energy band structure of p-SnS/n-MoS_2 heterojunction under light irradiation upon external strain, showing the modulation in Schottky barrier height.

Zhang et al. demonstrated a photodetector using n-MoS_2/p-CuO heterostructure and investigated the effect of strain on the fabricated device and observed the significant improvement in the photoresponse due to piezo-phototronic effect. However, deposition of MoS_2 and CuO are performed by expensive and high temperature CVD and sputtering techniques were used [240]. *Du et al*. fabricated mixed dimensional vdWs photodetector using WSe_2/ZnO heterostructure and noticed the improvement in responsivity of the device when external strain was applied [273]. *Liao et al.* demonstrated a Au-MgO-ZnO based UV photodetector and investigated strain modulation effect on the fabricated device due to piezo-phototronic effect [241] . *Lin et al.* demonstrated a n-MoS_2/p-WSe_2 vdWs heterostructure based flexible photodiode on PET substrate and studied the strain-tunable photodetection performance [235]. *Xue et al.* demonstrated the pressure-modulated heterostructure photodiode using MoS_2 (n-type) and GaN (p-type), and via piezo-phototronic effect the responsivity was enhanced by ~ 3.5 fold [238]. *Dai et al.* fabricated a flexible NIR photodetector using p-Si/n-CdS nanowires heterojunction. By applying compressive stain, photoresponsivity of the device was enhanced by ~ 366 times, due to piezo-phototronoic effect in CdS nanowires [274]. *Zhang et al.* designed a PVK/ZnO nanorods/Graphene hybrid heterojunction based UV light photodetector and observed the drastic enhancement of photoresponsivity due to piezo-potential induced at the ZnO/Graphene and PVK/ZnO junctions [275]. *Rai et al.* successfully fabricated a high performance broadband UV-visible piezo-phototronic photodetector using ZnO/ZnS

heterojunction [239]. In all the above reports, expensive, cleanroom fabrication techniques such as CVD, sputtering, pulse laser deposition, e-beam lithography, etc., were used for the device fabrication. In this work, piezo-phototronic effect photodetector was fabricated based on p-SnS/n-MoS_2 heterostructure using cost-effective, clean room free fabrication techniques. It is important note that the as shown in FESEM image (Figure 4.4a) surface of heterostructure is rough because MoS_2 and SnS were synthesized using solution process method and later spin coated on the PET substrate. Further research is in progress to improve the quality of heterostructure interface. The performance of the fabricated p-SnS/n-MoS_2 heterostructure is compared with piezotronic based photodetectors reported, as shown in Table 4.1.

Table 4.1: Performance of the fabricated piezo-phototronic photodetector is compared with the literature.

Device	**Fabrication technique**	**Substrate**	**Light of detection**	**Responsivity (mA/W)**	**Response time (msec)**	**Reference**
p-CuO/ n-MoS_2	Hydrothermal	Cellulose paper	Visible - NIR	42	-	[240]
WSe_2-ZnO	CVD, PMMA transfer	PET	White light	394	-	[273]
p-Si/n-CdS	RF magnetron sputtering, Hydrothermal, Etching	Flexible Si wafer	NIR light 1064 nm	19.4×10^3	36	[274]
PVK/ZnO/ Graphene	CVD, spin coating,	Cu foil	UV light 365 nm	80.6×10^3	150	[275]
ZnO/ZnS	PLD, PMMA transfer	ITO glass	UV – visible 385, 465, 520	2.5×10^3	-	[239]
n-MoS_2/p-GaN	MOCVD, exfoliation,	Sapphire substrate	365 nm	-	66	[238]
n-MoS_2/p-WSe_2	CVD, PMMA transfer	PET	532 nm	3.4	---	[235]
p-SnS/n-MoS_2	**Hydrothermal, Spin coating**	**PET sheet**	**Visible-NIR**	**211, 133**	**120**	**This work**

4.5 Conclusion

In conclusion, flexible, cost-effective broadband visible-NIR piezotronic photodetector was fabricated using p-SnS/n-MoS_2 heterostructure that presents excellent enhancement in photoresponsivity under strain. In the p-SnS/n-MoS_2 heterostructure, the ideality factor and height of the Schottky barrier were measured to be ~ 2.06 and ~ 0.2778 eV, respectively. The photoresponsivity of the fabricated photodetector was enhanced by ~ 97 % under a strain of ~ 2%. The enhancement originates from modulation of band structure at the junction due to piezo-phototronic effect. Due to piezo-phototronic effect height of the Schottky barrier at the junction increases, which accelerates the efficient separation and transport of photogenerated charge carriers across the junction. The maximum photoresponsivity of the device under ~ 2% strain in visible and NIR regions was ~ 211 mA/W and ~ 133 mA/W, respectively. The device response time was measured to be ~ 120 msec. The work may promote further research in the development of cost-effective, flexible, and high performance piezo-phototronic photodetectors for next-generation flexible and wearable optoelectronics.

CHAPTER 5

Fabrication of high performance and broadband photodetectors using mixed-dimensional vdW heterostrucutres

Use of 2D materials in photodetectors have some drawbacks such has limited spectral absorption due to the bandgap and limited absorption efficiency. The objective of this work is to overcome the limited spectral range problem of the pristine 2D materials based photodetectors. This can be achieved through the implementation of mixed-dimensional 0D/2D vdW heterostructure method. The incorporation of 0D QDs on 2D materials, with their tunable absorption through control over their size expands the spectral selectivity and also improves the devices absorption efficiency. In addition, the high mobility of TMDs facilitates the effective charge transport, thereby enabling the potential for large photoconductive gain.

5.1 All MoS_2 based 2D/0D Localized Unipolar Heterojunctions as a Flexible Broadband (UV-Vis-NIR) Photodetector

This work demonstrates the fabrication of all MoS_2 based 2D/0D unipolar heterojunctions using a simple one pot hydrothermal process and its utilization in flexible broadband photodetector covering the spectral range from ultraviolet to Near infrared. The discontinuous deposition of 0D MoS_2 which has absorbance in UV region on 2D MoS_2, having absorbance in visible and Near-infrared (NIR) region allow for broadband detection. Further, contact engineering was performed wherein both the metal contacts were fabricated on 2D MoS_2, thereby enabling effective capture of photogenerated carriers. Also, unipolar junction formed due to the Fermi level difference between 2D and 0D MoS_2 provides localized electric field which help in efficacious separation of photogenerated electron-hole pairs. Responsivity of the fabricated photodetector was calculated to be 7.56 mA W^{-1}, 12.8 mA W^{-1}, and 3.95 mA W^{-1} in UV, visible and NIR region, respectively, indicating that the fabricated device is more sensitive towards visible region. A detailed understanding of the photodetection mechanism of this unique heterostructure is presented by bandgap theory and trap states. The successful demonstration of such a cost-effective, scalable 2D/0D based broadband photodetector finds potential applications in optoelectronics, security, and wearable electronics.

5.1.1 Introduction

Flexible photodetectors have become a hotspot of research to develop low cost, highly sensitive, wearable optoelectronic devices, and gadgets. Commercial photodetectors fabricated using active materials such as Silicon [276] , Germanium [277], Ga-As [278], impose the factor of rigidity, which makes it difficult to integrate these devices into wearable optoelectronics technology. Furthermore, these photodetectors cannot absorb the multispectral radiations, which cover the entire electromagnetic spectrums. Various hybrid photodetectors have been reported, where the sensitizer materials were used to enhance the photocurrent by decreasing the electron-hole recombination rate, but there remains a challenge to achieve the wide range absorption of the electromagnetic spectrum [279,280]. The wideband photodetector provides a powerful tool that offers information extracted from the interaction of matter with the different wavelengths of light. However, the limitation lies in the high cost and limited performance of these photodetectors. Hence, there is an immediate need to explore the active semiconductor materials compatible with flexible substrates for realizing flexible photodetectors with wide range absorption of the electromagnetic spectrum.

Transition metal dichalcogenides (TMDs) are the emerging 2D materials, have tunable bandgap property that gives them a certain edge over the widely studied graphene for photodetection [1-3]**.** MoS_2 is one of the prominent TMDs that has outstanding potential to construct various optoelectronic devices due to high carrier mobility, reduced dimensionality, mechanical flexibility high sensitivity, and strong electron-hole confinement [281–284]. Owing to the narrow bandgap in the range of ~ 1.2 eV (bulk form) to ~ 1.8 eV (monolayer), MoS_2 shows strong absorption to the Visible and NIR region, rather than the UV region [285]. One of the ways to tackle this problem lies in constructing heterostructure with active semiconducting material, which has a higher bandgap and shows strong absorption to the UV and visible region, also inject photo carriers to improve the gain. On the other band, quantum dots (QDs) are interesting excitonic materials that have broad tunability of bandgaps, strong absorption to a broad range of electromagnetic spectrum from UV to IR, and high quantum efficiencies[286]. MoS_2 Quantum dots are n-type semiconducting material, which exhibits exceptional optical and electronic properties because of their quantum confinement and tunneling effects [287] . The number of edge states increases in the quantum regime due to the cationic and Sulphur vacancies, which leads to high in plane electron transport phenomena in the MoS_2 Quantum dots. Hence, MoS_2 QDs finds potential applications in the fields of

bioimaging [288], photocatalysis [289], photovoltaics [290], LED [291], and photodetectors [292]. However, the confinement of the charge carriers blocks the usage of quantum dots for photodetector applications [293].

2D-0D hybrid based photodetectors have gained focus in recent years because of their high performance and the formation of heterojunction between the quantum dots and the layered materials [294][295][296]. This architecture allows the injection of charge carriers from the large bandgap to narrow bandgap material leading to the accumulation of charges at the narrow bandgap region. Further, the confined charges can increase the carrier recombination, and thereby the device exhibits faster response time. This electronically coupled mixed dimensional heterostructure with features such as the high light absorption, band-tunability, and large-scale manufacturability of QDs makes it a potential architecture to develop high-performance photodetectors and overcomes the boundary issues faced in the quantum dot photodetectors. Recently, 0D-2D mixed dimensional Van der Waals heterostructure has been demonstrated to have several benefits such as less constrained interfacial states, easy preparation, reduced Columbic interactions [297]. *Chen et al*. have demonstrated a novel strategy to optimize the 0D-2D ($CsPbBr_3$-BP) heterostructure, which improves the carrier transfer efficiency [298]. *Pak et al*. fabricated a p-n junction by functionalizing 2D-MoS_2 (n-type) with MnO QDs (p-type) to suppress the dark current, which enhances the photocurrent [299] . However, most of the reported 0D-2D based photodetectors are not extensively studied for the use of wide range absorption in the electromagnetic spectrum and also use toxic materials such Pb, Hg, Cd, etc. [294][295][296]. Therefore, there still exists a need to explore the scope and applicability of such heterostructure with desired characteristics that follow the rule of ACT (accuracy, cost, and time) for developing low cost, environment-friendly, flexible, high-performance photodetectors.

In this work, we have fabricated a broadband photodetector based on a novel MoS_2 QDs/MoS_2 on a paper substrate by the classical drop-casting of the MoS_2 quantum dots solution on the MoS_2/paper and then contacts were made using Ag paste. MoS_2 has a hexagonal layered structure, in which layers of S-Mo-S interact with each other through Van der Waals forces and also MoS_2 QDs exhibits similar hexagonal lattice structure, there exists synergistic effect between MoS_2 flakes and MoS_2 QDs which improve the performance of the photodetector [300]. The formation of heterostructure between the MoS_2 flakes and MoS_2 quantum dots resulted in the enhanced photo absorbance, responsivity, faster response speed, and extended broadband photoresponse range (UV

region). Hence, the device exhibited a superior responsivity of 7.56 mA W^{-1}, 12.8 mA W^{-1}, and 3.95 mA W^{-1} in UV, visible, and NIR regions, respectively. The synergetic effect in this heterostructure leads to efficient photoinduced charge carrier separation in quantum dots and the associated charge transport in the 2D nanoflakes, which makes it a promising candidate for the future wearable electronic and optoelectronic devices. As per the authors' knowledge, this is the first demonstration of broadband (UV-Vis-NIR) photodetector based on MoS_2QDs/MoS_2 heterojunctions on a flexible cellulose paper substrate.

5.1.2 Experimental section

One-pot synthesis of MoS_2 flakes and MoS_2 Quantum dots (MoS_2 QDs)

Sodium Molybdate ($Na_2MO_4.2H_2O$), L- Cysteine, Silver(Ag) paste were procured from Sigma Aldrich. Deionized (DI) water was utilized throughout the experiments. In a typical procedure, 0.3 gm of $Na_2MO_4.2H_2O$ was dispersed in 10 ml of DI water and ultra-sonicated for 25 min. On the other hand, a solution of 0.3 gm of L-cysteine dissolved in 25 ml of DI water was prepared. Then both the solutions were properly mixed using a magnetic stirrer, which resulted in a yellow solution and was kept for violent stirring using a magnetic stirrer, and HCl was added to maintain a pH of 6.5. After thorough stirring for 30 min, the well-mixed solution was used for hydrothermal wherein the autoclave was kept at 200°C for 16 hr. The resultant solution after hydrothermal was centrifuged at 5000 rpm for 30 min. After this, the pale yellow supernatant and the black precipitate at the bottom of the centrifuge tube were collected and used for further experiments.

Characterization

The size distribution of the MoS_2 QDs was determined by Transmission electron microscopy (TEM). Also, the optical and electronic properties of the MoS_2 QDs and MoS_2 were observed by JASCO V-670 UV-visible spectrophotometer, and JASCO FP-6300 spectrophotometer used to measure the photoluminescence spectra, UV-Visible, and diffuse reflectance. In addition to that, Fourier transform IR spectroscopy (FTIR) was used to identify the surface functional groups on MoS_2 QDs. Moreover, the fluorescence exhibited by MoS_2 QDs was visualized under UV light illumination. Further, the electronic and chemical state of the MoS_2 QDs/MoS_2 were analyzed by XPS. Apart from this, the crystallinity of the MoS_2 was examined by using an X-ray diffractometer (XRD), Rigaku Ultima IV. The electrical measurements were done using

Kiteley source meter and wavelengths of the light sources used for photodetection of UV, Visible and NIR illumination are 365 nm, 554 nm, and 780 nm, respectively. All light sources were controlled with a spot diameter of ~ 0.28 cm.

Device fabrication

Simple, novel and cost-effective fabrication method of vacuum filtration was implemented for making large area device. The resultant MoS_2 flakes obtained from the synthesis was deposited on the cellulose paper using vacuum filtration followed by drying in a hot air oven at 60 ºC for 50 min. Subsequently MoS_2/paper was cut into 6 mm x 6 mm dimension and MoS_2 QDs solution was drop casted on it. Contacts were made using silver paste. Figure 5.1 depicts the schematic of the one pot synthesis of MoS_2 flakes and MoS_2 QDs via a facile hydrothermal process. The resultant contains black precipitate that contains the MoS_2 flakes, and the yellow supernatant contains the desired MoS_2 QDs. The image of the as-fabricated photodetector can be found in the Appendix A, Figure S23.

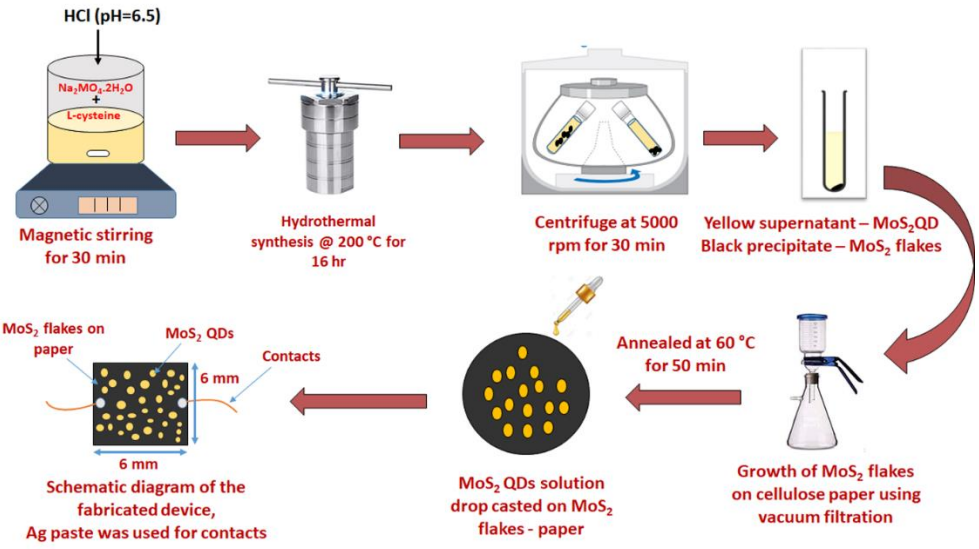

Figure 5.1: Schematic illustration of the MoS_2-QDs/MoS_2 flakes hybrid photodetector on paper.

5.1.3 Results and discussion

The surface morphology of the synthesized MoS_2 flakes was studied by FESEM analysis. Figure 5.2a displays the low-magnification FESEM image of suggesting the uniform deposition of MoS_2 flakes. The high magnification image reveals the flake like morphology of MoS_2 stacked together with coral like outer surface and has an average size of~ 200 nm, as seen in Figure 5.2b. The disordered stacking formed due to

agglomeration of the MoS_2 flakes with hollow coral structure favors the multiple scattering of light with enhanced photo absorption through structural absorption mechanism [301].Further, the TEM image as seen in Figure 5.2c shows the flake like morphology which confirms the formation of few layer MoS_2 and discretely distributed QD on flake thereby giving rise to this unique and exciting heterostructure. The morphology and morphology of the as-synthesized MoS_2QDs were studied by TEM analysis. Figure 5.2d, e shows TEM images of MoS_2 QDs which confirms the formation of uniformly dispersed MoS_2 QDs with nearly spherical morphology.

The average diameter of MoS_2 QDs was determined from the particle distribution graph, as shown in the Figure 5.2f and the average particle size calculated was 5.41 ± 1.32 nm. The polydispersity exhibited by the MoS_2 quantum dots is due to the surface functionalization occurred during the synthesis procedure. Figure 5.2g displays selective area electron diffraction (SAED) pattern of MoS_2QDs and it contains multiple rings and dominant (110) and (100) planes which confirms the polycrystalline nature of the MoS_2 QDs [288]. The inter planar distance of (100) plane was calculated to be 0.25 nm. The XRD pattern of the synthesized MoS_2 flakes on paper substrate is givne in Figure 5.2h. The existence of the (002), (100), (103), (006), (110) diffraction peaks clearly confirm the formation of MoS_2 and the pattern matches with the reported literature. (JCPDS No: 37-1492). We observe a weak diffraction pattern of 002 peak, which may be due to the perpendicular alignment of the nanoflakes to the surface and the higher intensity of the 100 plane indicates the formation of few layer MoS_2 with a large number of edge defects [302]. The interplanar distance of the (100) peak was calculated using Braggs equation and was found out to be 0.253 nm which matches the TEM result. The peak broadening in the XRD pattern is due to the amorphous functionalized quantum dots and the reaction temperature used in the hydrothermal synthesis. The crystallite size was calculated using the Debye Scherrer formula and was found out to be 1.04 nm.

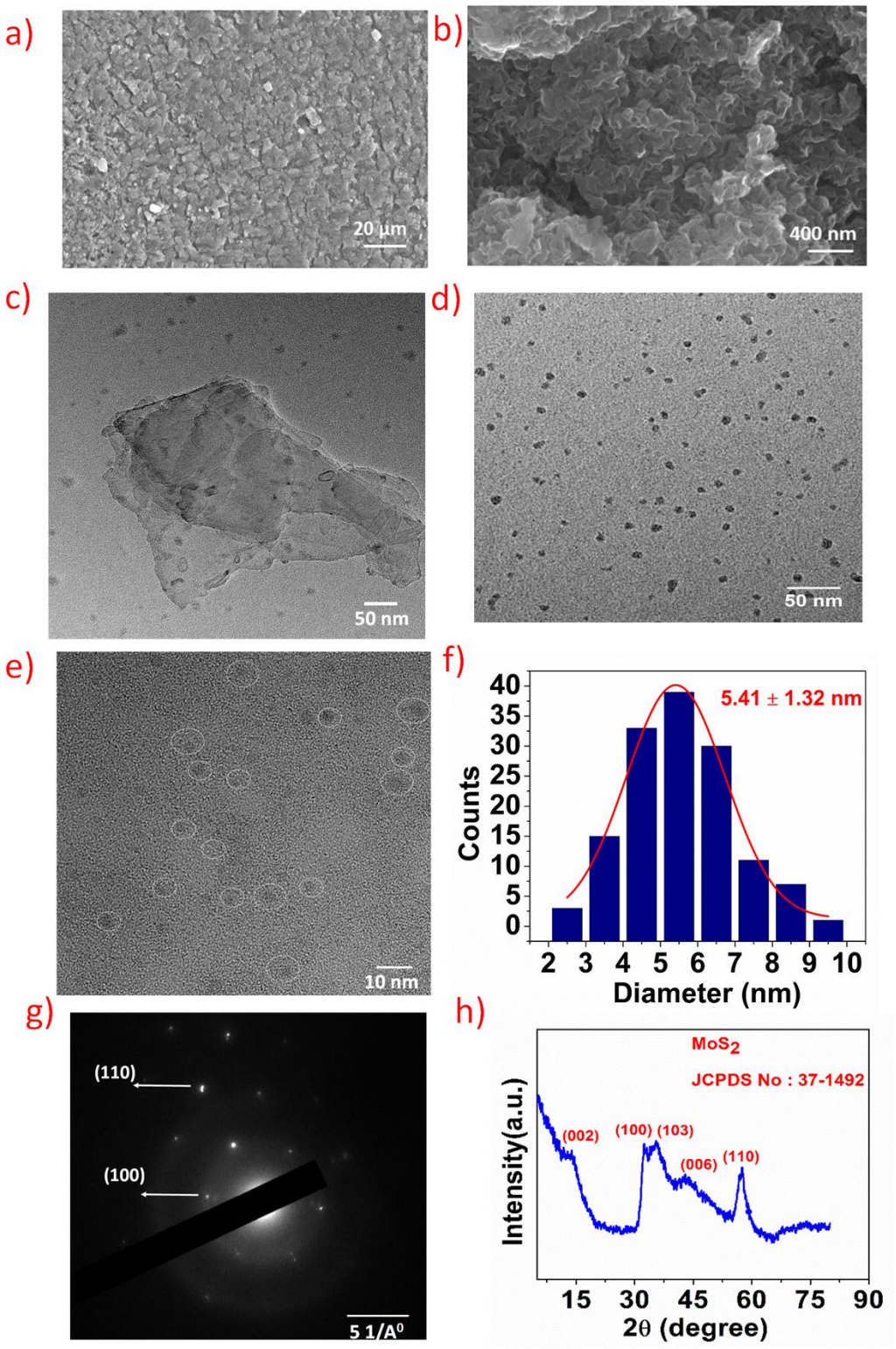

Figure 5.2: a) Low magnification of FESEM image of MoS_2 flakes b) High magnification FESEM image showing flakes structure of MoS_2 c) TEM image showing the MoS_2 flakes d) TEM image of MoS_2 QDs at 50 nm scale e) High resolution TEM image of MoS_2 QDs f) particle size distribution graph of as-synthesized MoS_2 QDs with an average diameter of 5.34 ± 1.36 nm g) SAED pattern h) XRD pattern of MoS_2 flakes.

The UV- visible spectra MoS_2 QDs displays the absorption peak at 254 nm resulting from the Π*→ Π* transition of the C=O peak of the functionalized group on MoS_2 QDs and characteristic shoulder peak at 312 nm [303] as seen in Figure 5.3a. This shows the excitonic features of MoS_2 QDs accounted to the blue shift in the Z, C, D exciton peaks which are generated by the bandgap transition at K point with energy slit from valence spin orbital coupling of the A and B exciton bands of MoS_2 QD [304]. The optical bandgap of MoS_2 QDs was calculated using Tauc plot and found out to be ~ 3.37 eV which shows strong absorption in the UV region as seen in the inset of Figure 5.3a. The increase in bandgap in case of MoS_2 quantum dots when compared to MoS_2 flakes can be ascertained to the quantum confinement effects seen in MoS_2 QDs. The prepared MoS_2 QDs exhibited bright blue fluorescence under 365 nm UV light illumination, as seen in inset of Figure 5.3b. The origin of excitation dependent PL in MoS_2 QDs can be accounted to the exciton recombination at the electron/hole trap made up by the vacancies of uncompensated sulfide and metal ions at the dangling bonds. The MoS_2 QDs showed strong blue fluorescence at an excitation wavelength of 360 nm with an intense emission peak at 440 nm due to direct band edge recombination. A redshift was observed in the emission peak of the MoS_2 QDs as the excitation wavelength was increased from 300 to 510 nm due to the transitions from different surface emissive states of the functionalized MoS_2 QDs. The functional groups of the MoS_2 QD was investigated by performing an FTIR analysis of the MoS_2 QDs solution, as seen below in Figure 5.3c. The Mo-S characteristic peak was observed at 640 cm^{-1} and the presence of OH peak at 3450 cm^{-1} and C=O peak at 1632 cm^{-1} shows the evidence of surface functionalization of MoS_2 QDs. In case of MoS_2 flakes, two strong absorptions due to the optical transitions in the higher density states and hence observed two peaks in the range of 400-500 nm [162].

The optical bandgap of MoS_2 flakes was measured to be ~ 1.36 eV from the absorption spectra showing absorption peaks in the visible and NIR region, and the graph can be found in the Appendix A, Figure S24. To further confirm the formation MoS_2, XPS analysis was performed for the fabricated device and the survey spectra of the MoS_2 QDs/MoS_2 device on paper substrate is as depicted in Figure 5.3d wherein all the signature peaks of Mo, S and C are observed. In Mo 3d spectra, as seen in Figure 5.3e the 2H Mo^{+4} $3d_{5/2}$,$3d_{3/2}$ doublet peaks and S 2s peak were observed at 228.3 eV, 231.6, and 225.3 eV respectively.

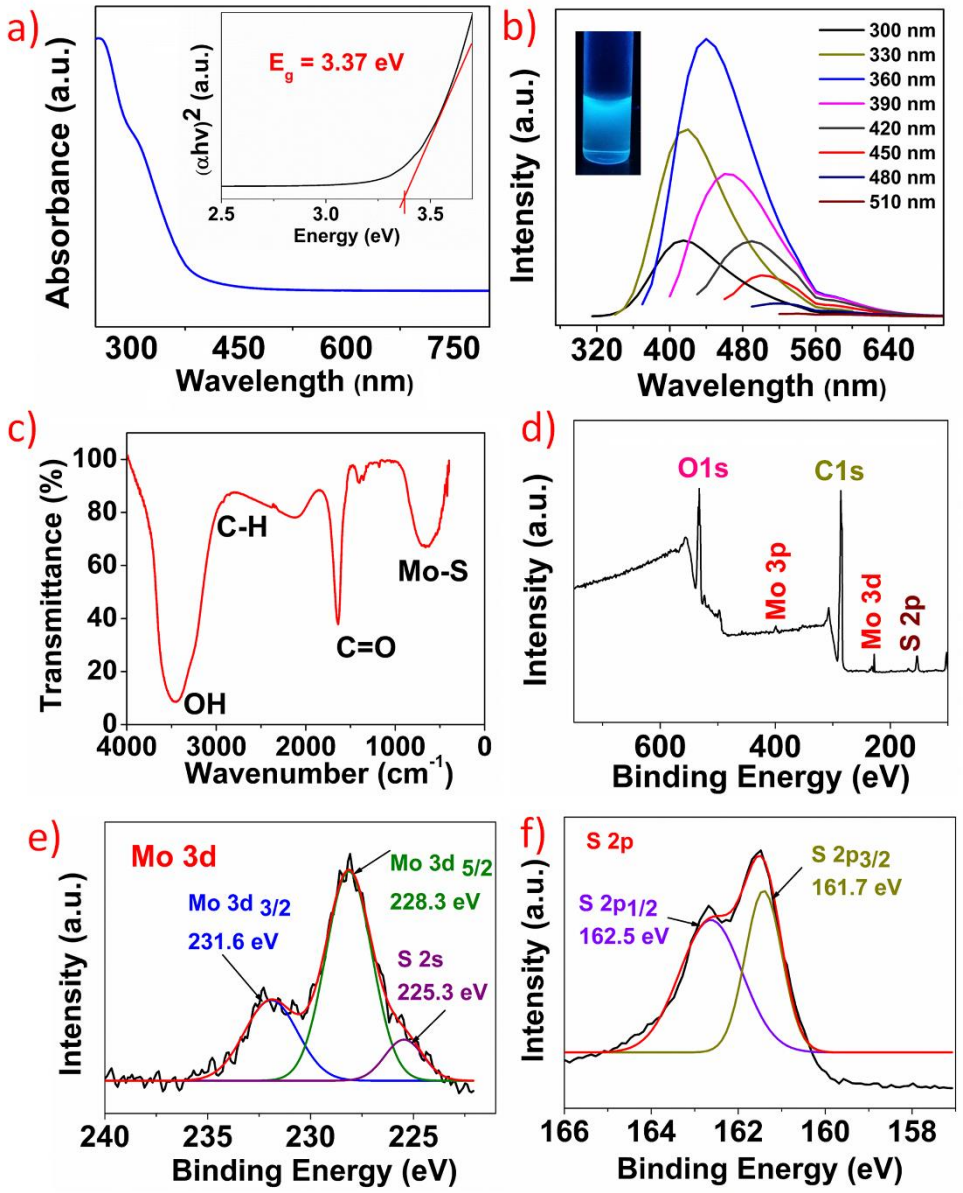

Figure 5.3: a) Absorption spectra of MoS_2 QDs and inset graph showing the Tauc plot, wherein E_g = 3.37 eV b) Photoluminescence spectra of MoS_2 QDs with various excitation wavelength from 300-510 nm and Strong fluorescence displayed by the MoS_2 QDs under 365 nm UV light illumination c) FTIR spectra of the surface functionalized MoS_2 QDS d) XPS survey spectra of MoS_2 QDs/MoS_2 on paper substrate e) High-resolution spectra Mo 3d f) High-resolution spectra of S 2p.

As shown in Figure 5.3f, high resolution S 2p spectra deconvoluted into doublet peaks $2P_{1/2}$ and $2P_{3/2}$ at 162.5 eV and 161.7 eV, which confirms the -2 oxidation state of sulfur in MoS_2 [305]. To study the chemical composition and number of layers Raman analysis was performed, in-plane (E^1_{2g}) and out-of-plane (A_{1g}) vibrational modes of MoS_2 were observed at 383 cm^{-1} and 405 cm^{-1} respectively in the Raman spectra, results are included

in the Appendix A, Figure S25. The wavenumber difference of ~ 23 cm^{-1} between the two peaks the formation of three layer MoS_2 nanoflakes [306,307].

Figure 5.4a shows the Current v/s Voltage (I-V) characteristics of the fabricated MoS_2QDs/ MoS_2 device for different UV light illumination with Ag paste as contacts and external voltage of 2 V. To stabilize the device, the fabricated photodetector was kept in the dark for 10 hr before the measurements were performed. As shown in Figure 5.4a, the fabricated sensor exhibited ohmic contacts. This is due to the fact that even though MoS_2 flake is functionalized with MoS_2 QDs, the metal contacts are taken from MoS_2 flake (lower bandgap material). This ensures the local electric field at the interface of MoS_2 flake and MoS_2 QDs and also maintaining the ohmic contact. It should be noted that when the device current was compared before and after functionalization with MoS_2 QDs, pristine MoS_2 flake exhibited higher current and lower resistance (Appendix A, Figure S26). This is due to the fact that post functionalization, MoS_2 flakes form local unipolar junctions with MoS_2 QD due to the difference in the Fermi level between the two thereby creating a small localized potential barrier which increases the resistance of the device thus decreasing the device current. It should further be noted that the local potential barriers assist in forming local electric field and hence help in the separation of the photogenerated electron-hole pair which improves the responsivity. Further, MoS_2 QDs also promote in increasing the absorbance in the UV region of the electromagnetic spectrum thereby improving the spectral sensitivity of the photodetector. Hence the utilization of MoS_2 QD has two advantages: 1) Assisting in the formation of local electric field and 2) increasing the absorbance spectra of the device in the UV region of the electromagnetic spectrum. Figure 5.4b, c displays the I-V characteristic of the fabricated photodetector towards visible and NIR spectra and as the intensity of the illuminated light increases, increment in the device current was observed, which can be attributed to the generation of the photogenerated carriers. Figure 5.4d shows the temporal response of the fabricated device under constant intensity UV light illumination and as can be observed, the device repeatedly was able to detect the illumination signifying the repeatable nature of the device. Similar experiments were carried out under Visible and NIR light illumination and as expected, the device was repeatedly able to detect both visible and NIR illumination, as shown in Figure 5.4 e, f.

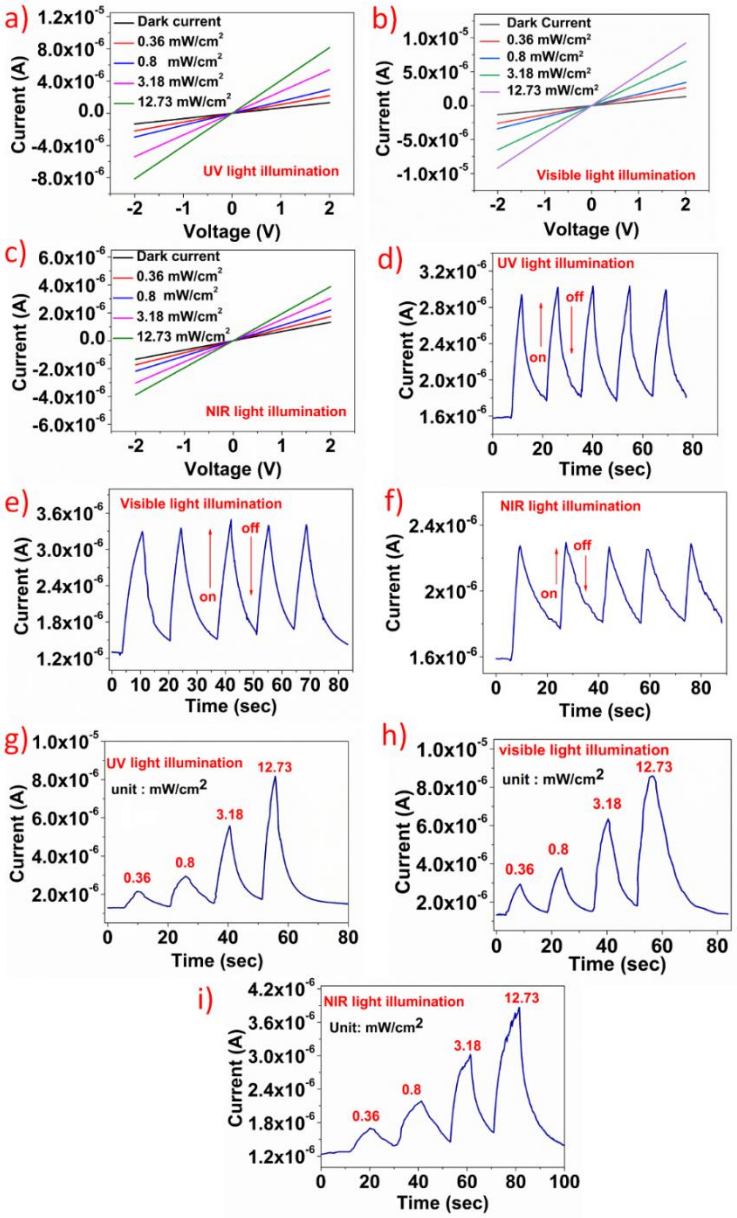

Figure 5.4: a,b,c) I-V characteristics of MoS_2 QDs/MoS_2 under different intensities of UV, visible, and NIR illumination, shows an increase in current with increase in light intensity d,e,f) Temporal response of MoS_2 QDs/MoS_2 under the constant intensity of UV, visible, and NIR illumination g,h,i) Temporal response of the MoS_2 QDs/MoS_2 under various UV, visible and NIR intensities.

The increment in the current for a fixed intensity of all three illuminations was performed and as compared to UV and NIR light illumination, the highest photocurrent was observed for visible light illumination, suggesting that the fabricated device was more responsive towards visible light. To further verify whether the device is more responsive in visible region, the fabricated photodetector was tested under varying light intensities values; Figure 5.4g shows the temporal response of the fabricated photodetector under

UV light illumination for different intensities, wherein the device current increases with increasing intensity that is consistent with I-V characteristics (Figure 4a). The same experiment was performed for visible and NIR light illuminations as shown in Figure 5.4h, i and results were consistent with the I-V characteristics (Figure 4b and c).

Responsivity(R_λ), External Quantum Efficiency (EQE) and detectivity (D*) are considered to be prominent figures of merit of a photodetector. Responsivity is defined as the photocurrent generated per unit power of incident light on sensing device and EQE is the ratio of number of charge carriers collected to the number of incident photons. Detectivity is defined as the ability of the photodetector to distinguish weak signals from noise and the equations of the responsivity(R_λ) and EQE and D* are given below:

$$R_\lambda = \frac{I_\lambda}{P_\lambda \text{ x } A}$$

$$\text{EQE } (\%) = hc \text{ x } \frac{R_\lambda}{e\,\lambda} \text{ x } 100$$

$$D^* = \frac{R_\lambda \times A^{1/2}}{(2 \times e \times I_{dark})^{1/2}}$$

Where, I_λ, P_λ, A, I_{dark} and e are photocurrent, incident power, active area of the device, dark current, and electron charge.

Active area of the fabricated device is 36 mm^2 and as seen in the Figure 5.5a, the responsivity of the fabricated device with varying intensities of UV, visible, and NIR illumination. Under UV light illumination, responsivity was calculated to be 7.56 mA W^{-1} at 0.36 mW cm^{-2} intensity and as the intensity increases, the responsivity value was found to be decreasing. This is due to the fact that as the illumination intensity increases, more photogenerated carriers are generated which reduces the built-in electric field and facilitates recombination. Hence the device shows higher responsivity at lower illumination intensity. Similar calculations were performed for visible and NIR light illumination and the value of the responsivity calculated for visible light illumination was found to be 12.8 mA W^{-1}. For NIR illumination, the responsivity value of the fabricated photodetector was found to be 3.95 mA W^{-1}. This further confirms that the fabricated device was more responsive towards visible light when compared to UV and NIR illumination. Although the fabricated photodetector shows much inferior performance to some of the reported MoS_2 based photodetectors which were fabricated using sophisticated and expensive cleanroom fabrication techniques such as Atomic layer

deposition (ALD), Chemical vapor deposition (CVD), photolithography [308–310], the performance is better than phototransistors based on graphene (R ~ 1 mA/W at Vg = 60 V) [311] or single layer MoS_2 (R ≤ 7.5 mA/W at Vg = 50 V) [309]. As shown in Figure 5.5b, EQE was calculated to be 2.56 %, 2.86 %, 0.62 % under UV, visible and NIR illumination, respectively. Similar trends were observed under all three illuminations i.e., as the illumination intensity increases, EQE was found to be decreasing. This is attributed to the fact that the EQE is directly proportional to responsivity.

Detectivity of the fabricated photodetector was calculated to be 1.23 x 10^9 Jones, 7.2x 10^9 Jones, 3.77 x 10^9 Jones for UV, visible, and NIR illumination, respectively as illustrated in Figure 5.5c, wherein decreasing trend observed with increase in intensity similar to the responsivity graph shown in Figure 5a. Also, the response spectrum is a key parameter of the photodetector. Response spectrum (responsivity v/s wavelength) of the fabricated photodetector is shown in Figure 5.5d. Response time of the photodetector is another important figure of merit to decide the performance. Rise time can be defined as time taken by the photodetector to rise from 10 % to 90 % of the maximum value of photocurrent and as can be seen from the Figure 5.5 c, d and e, the rise time was calculated to be ~ 2.9 sec, ~ 2.74 sec, and ~ 3.02 sec for UV, visible and NIR light illumination respectively. The reason for the slow response rate can be either the presence of trap states or charge impurity states or defects in the bandgap [310,312]. The defect states may be originated during the hydrothermal growth of MoS_2. Also, the rough surface of the cellulose paper substrate hinders the mobility of the photogenerated charge carriers. Furthermore, the discrete distribution of MoS_2 QDs on MoS_2 /paper results in improper band alignment, which increases the scattering and therefore decreases the mobility of the photogenerated carriers. It is important to note that discrete distribution is necessary for broadband photodetection, as uniform distribution of MoS_2 QDs on MoS_2 flakes would affect the absorbance of MoS_2 flakes in NIR and visible region. The response rate can be improved by polishing/smoothing the surface of the cellulose paper and optimizing the hydrothermal parameters to reduce the defects introduced during the synthesis. From the graph of responsivity v/s number of bending cycles, as seen in Figure 5.5f, a negligible change in the device performance was observed, which shows the robust nature of the device.

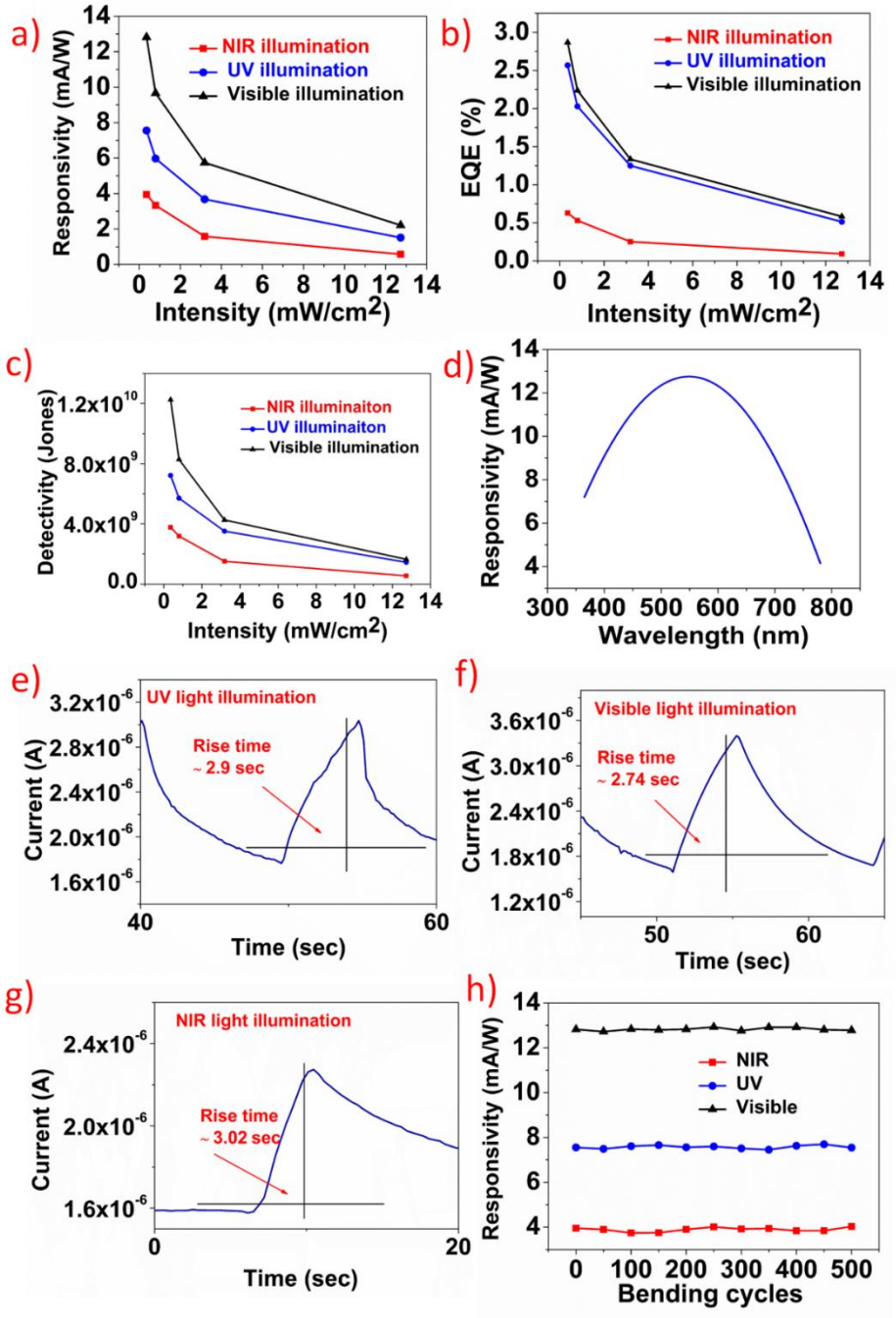

Figure 5.5: Wavelengths of UV, visible, and NIR monochromatic light sources utilized to perform the measurements are 365 nm, 554 nm, and 780 nm a) Responsivity of the MoS_2 QDs/MoS_2 photodetector under UV, visible and NIR illumination b) Graph showing the EQE (%) of UV, visible, and NIR illumination with various intensities c,d,e) Response time of fabricated photodetector f) Graph showing Responsivity v/s number of bending cycles.

5.1.4 Photodetection mechanism

The photodetection mechanism can be explained using the band structure of the hybrid. It has been reported that MoS_2 QDs are intrinsically more doped when compared to 2D MoS_2 due to the quantum confinement effects minimum energy level of conduction band (CB) in MoS_2 QDs increases compared the MoS_2 flakes [290,300]. The electron affinity of the MoS_2 and MoS_2 QDs is ~ 4.3 eV and ~ 3.9 eV [300,307]. The bandgap of MoS_2 flake is calculated to be ~ 1.36 eV and that of MoS_2 QD is ~ 3.37 eV. Based on the absorbance spectra, MoS_2 flake contributes to the visible and NIR absorbance and MoS_2 QDs absorb in UV range. Both MoS_2 flakes and MoS_2 QD being n-type forms a unipolar junction that forms a localized electric field at the interface of 2D/0D junction, as illustrated in Figure 5.6. It should be noted that the metal contacts are fabricated on MoS_2 flake which allows for the efficient collection of the photogenerated carriers. If the metal contacts were taken from 2D flake and 0D quantum dot it would result in the hole trapping and would further decrease the responsivity. When the UV light is illuminated, electron-hole pair are generated in MoS_2 QD and since conduction band of MoS_2 flake is at less energy level than the MoS_2 QD, the photogenerated electrons will transport to the flake and since the valence band energy of flake is higher than QD, the photogenerated holes will transport to the flake. Hence both the photogenerated electrons and hole are in 2D MoS_2 flake and since metal contacts are fabricated on MoS_2 flakes it allows for the effective collection of the carriers under the external electric field. Also, it should be noted that since 2D MoS_2 and 0D MoS_2 form a unipolar junction, they exhibit a localized electric field due to the difference in the Fermi level between the two. Since MoS_2 QDs are discretely distributed over MoS_2 flake, the electric fields are localized in the area where both flake and QDs form a junction. This localized electric field assists in the effective separation of the photogenerated carriers thus increasing the responsivity when compared to the pristine MoS_2 (Figure 5.6).

From the conventional electronic theory, the photocurrent gain is given by $G_{ph} = \frac{\tau}{t_{tr}}$, which indicates that the gain is the ratio of carrier lifetime (τ) and the transit time (t_{tr}) wherein the transit time is given by $t_{tr} = \frac{L^2}{\mu V_{ds}}$ [19]. Hence the photocurrent gain is also directly proportional to drift velocity, carrier lifetime and mobility (both electrons and holes) and inversely proportional to the square of the length. Since the process of synthesis involved is solution processed and also the material is deposited on cellulose paper whose surface is not smooth, it affects the mobility of the carriers. Due to the defect

states originated during the hydrothermal synthesis and also due to the cellulose paper substrate, the mobility of the carriers will be less and it increases the transit time; hence the responsivity is moderate as compared to various 2D materials based photodetectors. It should be noted that the study aims at improving the spectral range and also maintain a moderate responsivity which is achieved by the unique fabrication and choice of the materials.

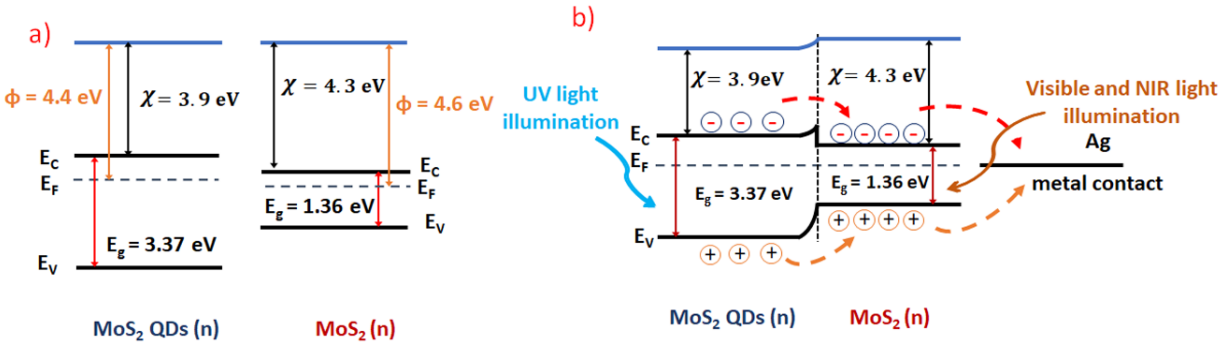

Figure 5.6: a) Schematic showing the individual energy band diagram of MoS_2 and MoS_2 QDs b) Energy band diagram of MoS_2 QDs/MoS_2 heterojunction.

There are multiple reports photodetectors fabricated using 2D materials and their hybirds with 1D and 0D. *Buscema et al. had* demonstrated the photodetector based on few layer black phosphorus for visible and NIR photodetection [313] . *Gomathi et al.* demonstrated the ZnS-MoS_2 based large area flexible broadband photodetector on a paper substrate [57]. There are reports on broadband band photodetectors based on 2D ZnO/ Graphene [314], Monolayer MoS_2 [315], SnS_2 nanosheets [316]. Furthermost the conventional photodetectors use Silicon as a substrate, which imparts rigidity and brings in the challenge to integrate the device for flexible electronic applications. Herein we demonstrate the one pot synthesis of 2D (flakes) and 0D (dots) MoS_2 via hydrothermal synthesis and the utilization of cost-effective, simple, and highly scalable vacuum filtration method for the device fabrication on flexible cellulose paper substrate. The novel fabricated MoS_2 /MoS_2 QDs unipolar hybrid photodetector exhibited a broad range of the detection of the electromagnetic spectrum covering UV-Visible and NIR. Table 5.1 provides a comparison of different broadband photodetectors based on 2D materials and their hybrids.

Active material	Substrate	Flexibility	Range of detection	Responsivity	Ref.
Few layered BP	Silicon	No	Vis-NIR	4.8 mA W^{-1}	[313]
ZnS- MoS_2	Paper	Yes	UV-Vis-NIR	17.85 μA W^{-1}	[57]
Graphene/ZnO	Eraser	Yes	UV-Vis-NIR	16.5 μA W^{-1}	[314]
Monolayer MoS_2	Sapphire	No	UV-Vis-NIR	8.4 mA W^{-1}	[315]
SnS_2 nanosheets	Polypropylene	Yes	UV-Vis-NIR	0.2 mA W^{-1}	[316]
MoS_2 QDs – MoS_2	**paper**	**Yes**	**UV-Vis-NIR**	**12.8 mA W^{-1}**	**This work**

Table 5.1: Performance comparison of various 2D materials based broadband photodetectors.

5.1.5 Conclusion

In summary, flexible broadband photodetector was demonstrated for the first time based on the MoS_2 2D/0D heterojunctions, wherein MoS_2 flakes and MoS_2 QDs were synthesized by one-pot hydrothermal method followed by a simple and highly scalable vacuum filtration method for the device fabrication on flexible cellulose paper substrate. The responsivity of device fabricated under UV, visible and NIR light illumination to be 7.56 mA W^{-1}, 12.8 mA W^{-1} and 3.95 mA $W^{-1,}$ respectively, indicating that the fabricated photodetector is more sensitive towards visible light illumination. MoS_2 QDs decorated on MoS_2 flakes are not only enhance the spectral sensitivity towards UV light but also form local electric fields, which assist in the effective electron-hole separation. Furthermore, the metal contacts were fabricated on MoS_2 flakes, which enhances the collection of the photogenerated carriers. This work provides a promising route to fabricate large area paper-based broadband photodetectors using 2D/0D heterojunctions, which finds diverse applications in the field of optoelectronics and flexible electronics.

5.2 Hybrid 0D-2D WS_2-QDs (n)/SnS (p) as Distributed Heterojunctions for Highly Responsive Flexible Broadband Photodetector

Even though there are reports on broadband photodetectors, the issue that remains unaddressed is the low responsivity value while increasing the spectral range. This work demonstrates the development of a distributed heterostructure based broadband (UV-Vis-NIR) photodetector with WS_2 Quantum Dots (QDs) randomly placed on tin sulfide nanosheets (WS_2-QDs/SnS) on a biodegradable cellulose paper substrate. The synergetic effect of visible-NIR light absorbance of SnS and UV light absorbance of WS_2-QDs is used to get broadband detection from UV to NIR region. Metal contacts were fabricated on SnS so that they can efficiently collect the photogenerated charge carriers. Thus, SnS layer in the device is used as a transport layer for the photogenerated electron-hole pairs in WS_2-QDs. Further, SnS being p-type and WS_2-QDs being n-type creates discontinuous distributed high electric field across the device, which accounts for the effective dissociation of generated electron and hole pairs, increases the responsivity significantly. Responsivity was found to be 0.655 A W^{-1}, 0.719 A W^{-1}, and 0.478 A W^{-1} under UV, visible (Vis), and near-infrared (NIR) regions of the electromagnetic spectrum, respectively. Here in this work, not only the spectral range is improved, but also responsivity is enhanced, which is a significant step ahead in flexible broadband photodetectors.

5.2.1 Introduction

In the last few years, significant research has been carried out on the fabrication of photodetectors due to their possible applications in a wide variety of areas like optical communication, image sensing, and surveillance. The research along the development of photodetectors was focused on enhancing the sensitivity in a particular area of the electromagnetic spectrum. Parallel research was towards increasing the spectral range of the photodetector [60]. Till date, many concepts have been reported for increasing the spectral range, which includes bandgap modulation [317], hybrid structures [318–320] discrete distribution [321,322] and contact engineering [323,324], etc. Even though there has been a success towards the development of broadband photodetector, the concern that remains fully unaddressed is the low responsivity values. Hence there is a need to develop a broadband photodetector that not only increases the spectral range but also focuses on improving the responsivity

The main concern regarding the improvement in the responsivity is the use of hybrid materials that are not compatible to each other, forms unipolar junction which creates low electric field [325,326]. Hence there is a need to systematically design and chose the materials that are not only compatible with each other but also create sufficient electric field for the separation of the photogenerated carriers. Widely used semiconductor materials for the fabrication of conventional photodetectors are GaN (UV, 250- 400 nm), silicon (visible, 450-700 nm), and InGaAs (NIR, 900 -1700 nm) [327,328]. The bandgap of these bulk materials cannot be tuned, hence in the past several years enormous research has been done on low-dimensional materials offering bandgap tunability by adjusting the nanoscale dimensions [329]. Following the discovery of graphene, 2D materials received a great deal of attention due to its exceptional optoelectronic and electronic properties[330].

Tin monosulfide (SnS) is a widely used p-type 2D transition metal monochalcogenide (MX, M= Ge, Sn; X=Se, S, etc.) with a layered orthorhombic crystal structure [331–333]. SnS has gathered significant interest and attention in photodetector manufacturing, solar cells, field-effect transistors, lithium-ion batteries due to its excellent electronic and optoelectronic properties, abundance in nature, tunable low bandgap, non-toxic nature, and low price [331,332,334–336]. In recent years, several reports have been published studying the photosensitivity of SnS. Liu's research group prepared SnS nanoribbons by solution phase synthesis, utilized it in photodetectors and filed-effect transistors [337]. *Zhang et al.* developed NIR photodetector using SnS nanosheets by conventional physical vapor deposition [332]. *Lu et al.* synthesized SnS nanoparticles by simple hydrothermal technique and investigated the photosensitive properties of SnS [338]. *Chang et al.* constructed a photodiode based on p-SnS nanoflakes and n-CdS nanorods heterojunction and further studied its visible light detection performance [331]. All of these research conclude that SnS is a superior choice for photodetector design. Usually, SnS exhibits higher absorption in Vis and NIR regions compared to UV region[339]. The poor UV absorption of SnS could be improved by making heterostructure with other nanomaterials and facilitate broadband photodetection with enhanced optical characteristics [3,161,296,340].

Quantum dots are one of such interesting 0D nanomaterial offering large tunable bandgaps and strong absorption in the UV region [98,341]. Recently, WS_2-QDs (n-type) have drawn greater attention in the research community due to their strong absorption in UV region, optoelectronic properties, efficient multiple carrier generation, size-dependent bandgap tunability, and many more [98,341–343] *Abid et al*. developed a UV

sensitive photodetector by decorating WS_2-QDs on reduced graphene oxide on a textile substrate [98]. To the best of the authors knowledge there is no available research on the development of broadband photodetector using WS_2-QDs/SnS hybrid structure on biodegradable paper substrate.

This work demonstrates the fabrication of UV-Vis-NIR (broadband) photodetector using on n-type 0D WS_2-QDs and p-type 2D SnS. Both WS_2-QDs and SnS were synthesized using a cost-effective and straightforward hydrothermal process. Using a highly scalable vacuum filtration method, synthesized SnS nanoflakes were deposited on cellulose paper substrate. Subsequently, synthesized WS_2-QDs were decorated SnS and making it a 0D-2D hybrid device for broadband photodetection. Metal contacts were fabricated on SnS for effective collection of generated charge carriers; thus SnS layer in the device is used as a transport layer for the generated electron-hole pairs in WS_2-QDs. The discontinuous distribution of WS_2-QDs on SnS forms a large number of localized p-n junctions creates high electric field which effectively separates the photogenerated carriers, thereby improving responsivity significantly. The responsivity of the photodetector was 0.478 A W^{-1}, 0.719 A W^{-1}, and 0.655 A W^{-1}, under NIR, Vis, and UV regions of electromagnetic spectrum, revealing that the device is more visible light sensitive. The highest responsivity in visible region is ascribed to strong absorbance of SnS in visible region in comparison to other regions. Successful demonstration of highly responsive flexible broadband photodetector projects potential applications in communication, security, etc.

5.2.2 Experimental Section

Characterization and materials

Ethylene Glycol, $SnCl_2.2H_2O$ (Tin (II) Chloride Dihydrate), and $Na_2S.9H_2O$ (Sodium Sulphide Nonahydrate) were purchased from Sigma-Aldrich. Morphology and size distribution of QDs were carried out using Transmission electron microscopy (TEM) Titan Themis 300kV, FEI. Structural characterization of SnS was studied by X-Ray Diffraction (XRD), Rigaku ULTIMA-IV (copper source). FESEM (Field emission scanning electron microscopy) study of synthesized SnS performed using FEI Apreo LoVac instrument. X-ray photoelectron spectroscopy (XPS) analysis was performed by Thermo Scientific K-Alpha instrument (X-ray source: 1486.6 eV, Al K-α source). To study the Raman spectra of the samples, Raman spectrometer LabRAM HR Evolution was used, laser excitation of 532 nm. JASCO V-670 UV-visible spectrophotometer was used to analyze the UV-vis spectroscopy of synthesized SnS and WS_2-QDs. Electrical

measurements (*I-V and I-t*) were carried out with a source meter (Keithley 2450). Light sources of a wavelength of 780 nm, 554 nm, and 365 nm were used for NIR, Visible (Vis), and UV light illuminations, respectively.

Synthesis and deposition of SnS on paper substrate:

SnS deposition on paper substrate was performed in two-steps: first solvothermal synthesis of SnS which was followed by the deposition of synthesized SnS nanostructure on the substrate using vacuum filtration. $SnCl_2.2H_2O$ (1 mmol) and of $Na_2S.9H_2O$ (2.5 mmol) were mixed in ethylene glycol (30 ml). Until it turned yellow, using the magnetic stirred the solution was vigorously stirred for 20 minutes. The solution was moved to autoclave (50 ml) reactor and maintained for 20 hours at 200°C in a hot air oven. Subsequently, the black color precipitates were washed multiple times using isopropyl alcohol (IPA) and deionized water (DI) and dried at 70ºC. As-synthesized black color SnS nanoparticles were deposited on cellulose paper substrate (thickness ~ 180 µm) of 2.5 cm x 2.5 cm dimensions by vacuum filtration, as illustrated in Figure 5.7. Thickness of the deposited SnS is approximately 100 µm.

Preparation of WS_2-QDs

WS_2-QDs were prepared by a one-step hydrothermal technique. To begin with, $Na_2W_2O_4.2H_2O$ (0.132 g) was dispersed in deionized (DI) water (12.5 ml). The solution was ultrasonicated for 10 minutes. To maintain pH of ~ 6.5, a sufficient volume of HCl (0.1 M diluted) was added. Later, L-cysteine (0.0242 g) was dispersed in DI water (25 ml) and the resulting solution was ultrasonicated for 25 min. Subsequently, solution was transferred to an autoclave and maintained for 20 hours at 200°C. The final solution was centrifuged for 30 min at 10,000 rpm and later, supernatant having WS_2-QDs was separated.

Device Fabrication:

Fabricated SnS/paper (2.5 cm × 2.5 cm) was cut into required dimensions of 0.6 cm × 0.6 cm. Later, 10 µl of synthesized WS_2-QDs were discretely decorated on SnS/paper device by a drop-casting method. Figure 5.7 shows complete procedure of the device fabrication.

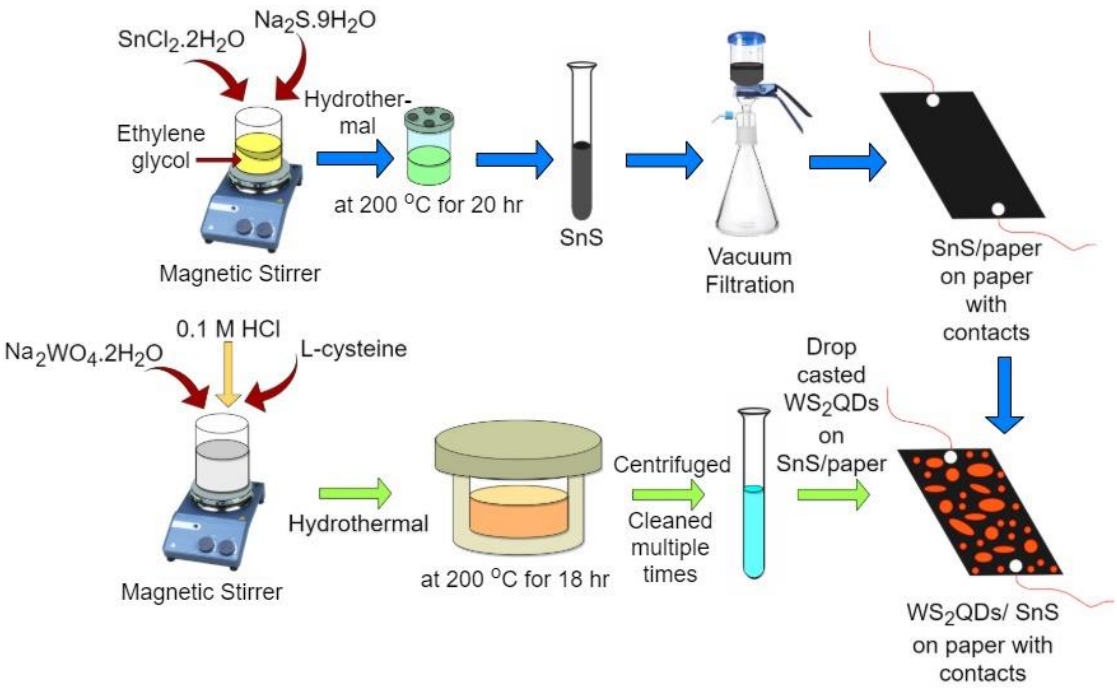

Figure 5.7: Illustration of complete fabrication of WS_2-QDs decorated SnS/paper.

5.2.3 Results and discussion

Characterization of SnS

Surface morphology of the SnS/paper was analyzed by FESEM study. As illustrated in the FESEM images (low-magnification) in Figure 5.8a and 5.8b, uniform deposition of SnS was observed and also microfiber structures of paper substrate were visible. From the high magnification FESEM images as illustrated in Figure 5.8c, nonuniform nanoflakes like morphology was noticed. The crystal structure and crystallinity of the prepared SnS was studied using XRD analysis. Figure 5.8d shows the XRD pattern of SnS/paper. In XRD pattern, peaks are observed at 26.03°, 31.6°, 39.41°, 42.11°, 45.73°, 48.8°, 51.22°, 53.27°, 56.81°, 64.24°, 66.43° and these peaks can be assigned to (1 2 0), (1 1 1), (1 3 1), (2 1 0), (0 0 2), (2 1 1), (1 1 2), (2 3 1), (0 4 2), (2 1 2), and (1 7 1) respectively. XRD pattern of synthesized SnS is in well match with JCPDS No: 39-0354, indicating orthorhombic structure [256,344]. Further, two more peaks located at 22° and 16° are attributed to the paper substrate [345]. XPS results were used to validate the chemical composition of the SnS. As shown in Figure 5.8e, the existence of S, Sn, O, and C elements was confirmed by the wideband spectra of SnS. As illustrated in Figure 5.8f, narrowband spectra of Sn 3d was curve fitted into two main peaks at 486.6 eV and 495.1 eV representing and Sn^{+2} $3d_{5/2}$ and Sn^{+2} $3d_{3/2}$. The S^{-2} valence state was confirmed by S 2p spectra, where it was curve fitted into two main peaks at 161.3 eV and 160.2 eV

and, they are ascribed to S^{-2} $2p_{1/2}$ and S^{-2} $2p_{3/2}$ respectively, as shown in Figure 5.8g. This is reaffirmed by the good agreement between these results and literature reports on SnS [346,347].

Raman Spectroscopy was performed to further verify the structural phases of SnS. Raman modes located at 214.1 cm^{-1}, 184.7 $cm^{-1,}$ 156.8 $cm^{-1,}$ 95.2 cm^{-1} and 64.1 cm^{-1} in Figure 5.8h, correspond to the different SnS optical phonon modes. Raman peaks detected at 95.2 cm^{-1} corresponds to the transverse optical mode of $A_{g,}$ and peaks at 214.1 cm^{-1} and 184.7 cm^{-1} were ascribed to the longitudinal optical mode of A_g. More peaks detected at 156.8 cm^{-1} and 64.1 cm^{-1} are due to the B_{3g} and combination of B_{2g} and A_g modes, respectively [256,348]. These results of Raman spectroscopy confirm that synthesized SnS is devoid of any impurity phases like Sn_2S_3 and SnS_2, which normally result in major peaks at 312 cm^{-1} and 308 cm^{-1}, respectively [260]. Optical Absorption spectra of SnS nanoflakes was analyzed using UV-vis absorption spectroscopy. As seen in Figure 5.8i, higher absorption was seen in visible region around ~ 630 nm compared to NIR and UV regions, which indicates that synthesized SnS nanoflakes are more sensitive to visible and it matches with literature [260,339]. The indirect bandgap of SnS nanoflakes was calculated using well established Tauc plot method, $(\alpha h\upsilon)^{1/2}$ vs. energy ($h\upsilon$) graph. Optical bandgap is ~ 1.2 eV, illustrated in the inset of Figure 5.8i.

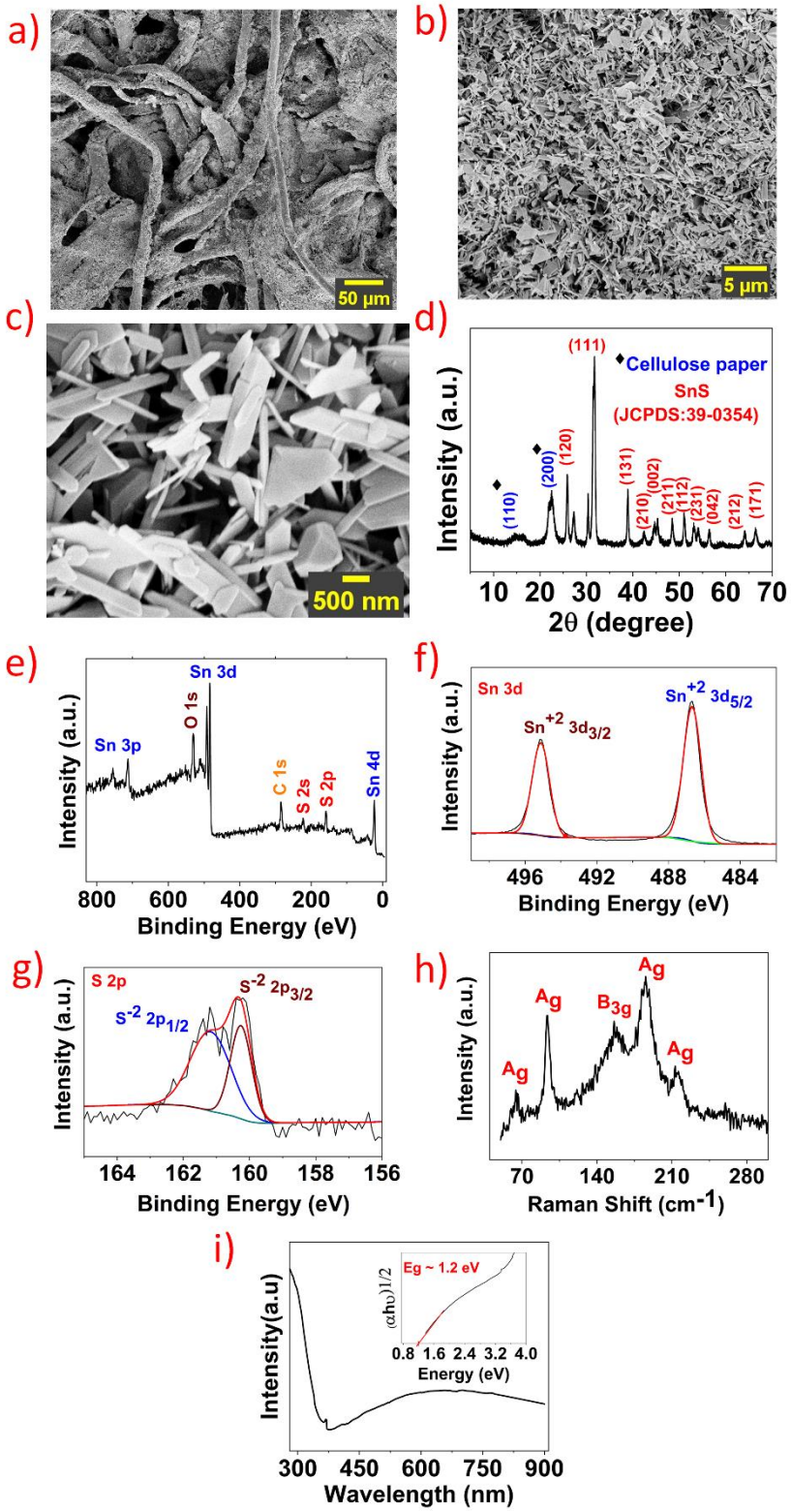

Figure 5.8: a,b,c) Low and high magnification FESEM images, and d) XRD spectrum of SnS coated on paper substrate. e) wideband spectrum of SnS/paper, f,g) High-resolution spectrum Sn 3d and S 2p. h) Graph showing Raman spectra of SnS, i) UV-vis absorption spectra of synthesized SnS, inset shows the Tauc plot.

Characterization of WS_2 QDs

Chemical composition of the synthesized WS_2-QDs were confirmed from the XPS analysis. As displayed in Figure 5.9a, survey spectra confirms the presence of W, S, O and C. The existence of O and C can be ascribed to CO_2 absorption in the air and tiny oxidation of W edges during the XPS measurements. High-resolution W4f spectra was fitted into two prominent peaks as displayed in Figure 5.9b. Peaks found at 34.7 eV and 32.3 eV are corresponding to W^{+4} $4f_{5/2}$ and W^{+4} $4f_{7/2}$ and, respectively and other weak peak located at 38.5 eV is attributed to the W^{+6} [349,350]. As illustrated in Figure 5.9c, narrow band S 2p spectra was deconvoluted into two significant peaks at 163.2 eV and 162.1 eV related to S $2p_{1/2}$ and S $2p_{3/2}$[349,351]. Photoluminescence (PL) spectra of synthesized WS_2-QDs at various wavelength excitations is displayed in Figure 5.9d. The PL peak shifted from 390 to 500 nm with excitation wavelengths ranging from 330 to 450 nm and redshift in emission peak was observed with an increase in excitation wavelength. Under UV light (365 nm) illumination WS_2-QDs exhibited a strong blue fluorescence, as illustrated in Figure 5.9d (inset). From the PL graph it was seen that emission is dependent on the excitation, maximum emission was observed at ~ 420 nm. This excitation dependence PL is due to the polydispersity of WS_2-QDs and it is well-matched with the literature [351,352]. Absorption spectra of synthesized WS_2-QDs is shown in Figure 5.9e and it shows two absorbance peaks around 280 and 360 nm, indicating that WS_2-QDs are suitable for UV light absorbance [98,353]. The direct bandgap of WS_2-QDs was measured using well established Tauc plot method, $(\alpha h\upsilon)^2$ vs. energy ($h\upsilon$) graph. The optical bandgap of synthesized WS_2-QDs is ~ 3.1 eV, as given in the inset of Figure 5.9e.

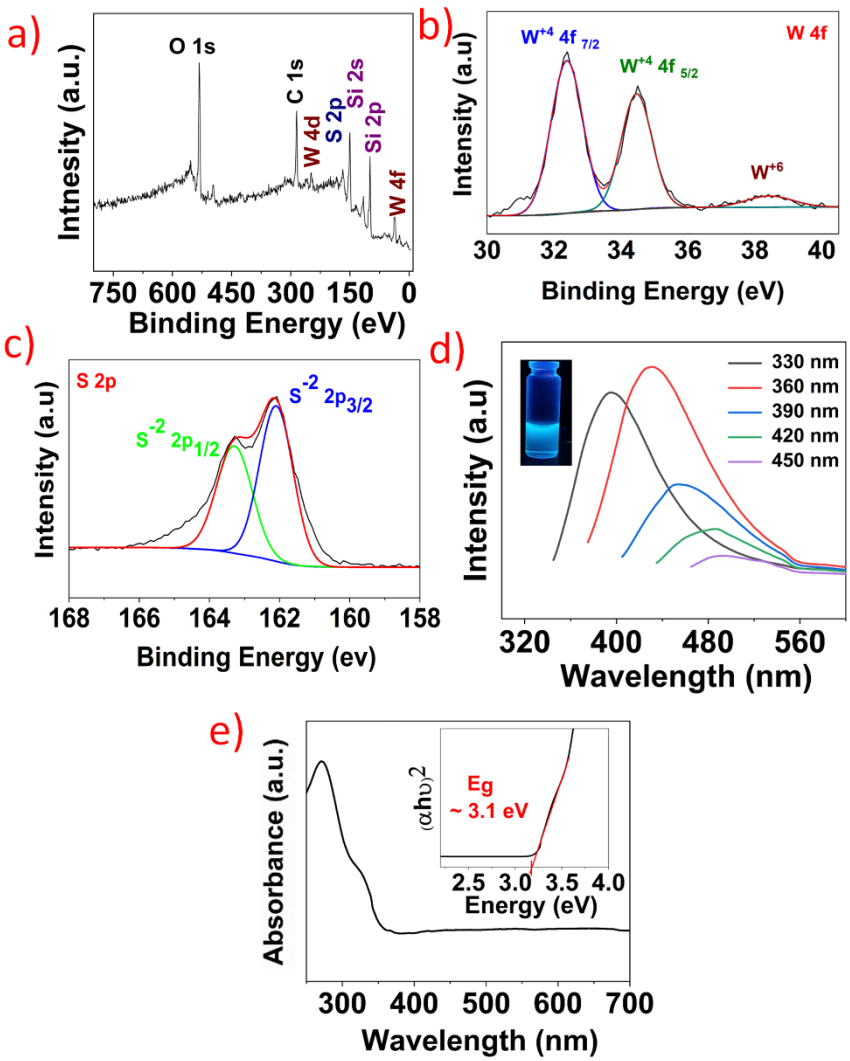

Figure 5.9: a) Survey spectrum of WS_2-QDs, drop casted on Si wafer b,c) Narrow band XPS spectrum of W 4f and S 2p d) Photoluminescence spectra of WS_2-QDs with various excitation wavelengths, inset displaying the image of WS_2-QDs under 365 nm light e) UV-vis spectra of synthesized WS_2-QDs and Tauc plot is included in the inset.

TEM analysis was carried out to find the particle size and morphology of the synthesized WS_2-QDs. Figure 5.10a and 5.10b show the TEM images, wherein a distribution of WS_2-QDs was noticed. Variation in the particle distribution is shown in Figure 5.10c, which is fitted with Log-Normal distribution and the average particle size was found to be ~ 5.38 ± 0.12 nm. Figure 5.10d displays the HRTEM image of the WS_2-QDs wherein crystal lattices are clearly visible, indicating high crystallinity and the calculated lattice spacing is approximately 2.7 Å which can be indexed to the (100) plane of WS_2. Further, SAED (Selected Area Electron Diffraction) pattern is illustrated in Figure 5.10e, and clear diffraction rings indicate the polycrystalline nature of synthesized WS_2-QDs. For

TEM analysis, WS_2-QDs/SnS solution was used instead of the device. WS_2-QDs/SnS solution was prepared by mixing WS_2-QDs in SnS nanoflakes (dispersed in ethanol) and then ultrasonicated for 40 minutes. Figure 5.10f shows the TEM image of the WS_2-QDs/SnS nanoflakes composite and wherein the discrete distribution of WS_2-QDs were observed on few-layer SnS flakes.

Further, the presence of WS_2-QDs decorated on SnS nanoflakes was confirmed by XPS analysis of the fabricated WS_2-QDs/SnS device. Figure S27(Appendix A), survey spectra of the device reveal the presence Sn, W, and S elements. XRD analysis of WS_2-QDs/SnS fabricated on paper substrate was performed and corresponding XRD pattern is included in Appendix A Figure S28. As seen in XRD pattern, Figure S28, peaks are observed at 26.03°, 31.6°, 39.41°, 42.11°, 45.73°, 48.8°, 51.22°, 53.27°, 56.81°, 64.24°, 66.43° and these peaks can be assigned to (1 2 0), (1 1 1), (1 3 1), (2 1 0), (0 0 2), (2 1 1), (1 1 2), (2 3 1), (0 4 2), (2 1 2), and (1 7 1) respectively. XRD pattern of synthesized SnS is in well match with JCPDS No: 39-0354, indicating the orthorhombic structure of SnS [256,344]. Further, two more peaks located at 16° and 22° are attributed the paper substrate [345]. Further WS_2-QDs XRD peaks are observed at 14.5°, 29.1°, 32.3°, and 33.5° corresponding to (0 0 2), (0 0 4), (1 0 0), and (1 0 1) crystal planes of WS_2, JCPDS No: 84-1398 [351,354]. Furthermore, to verify the discrete distribution of WS_2-QDs on SnS elemental mapping analysis was performed. Figure S29, (Appendix A) shows the results of fabricated WS_2-QDs/SnS elemental mapping.

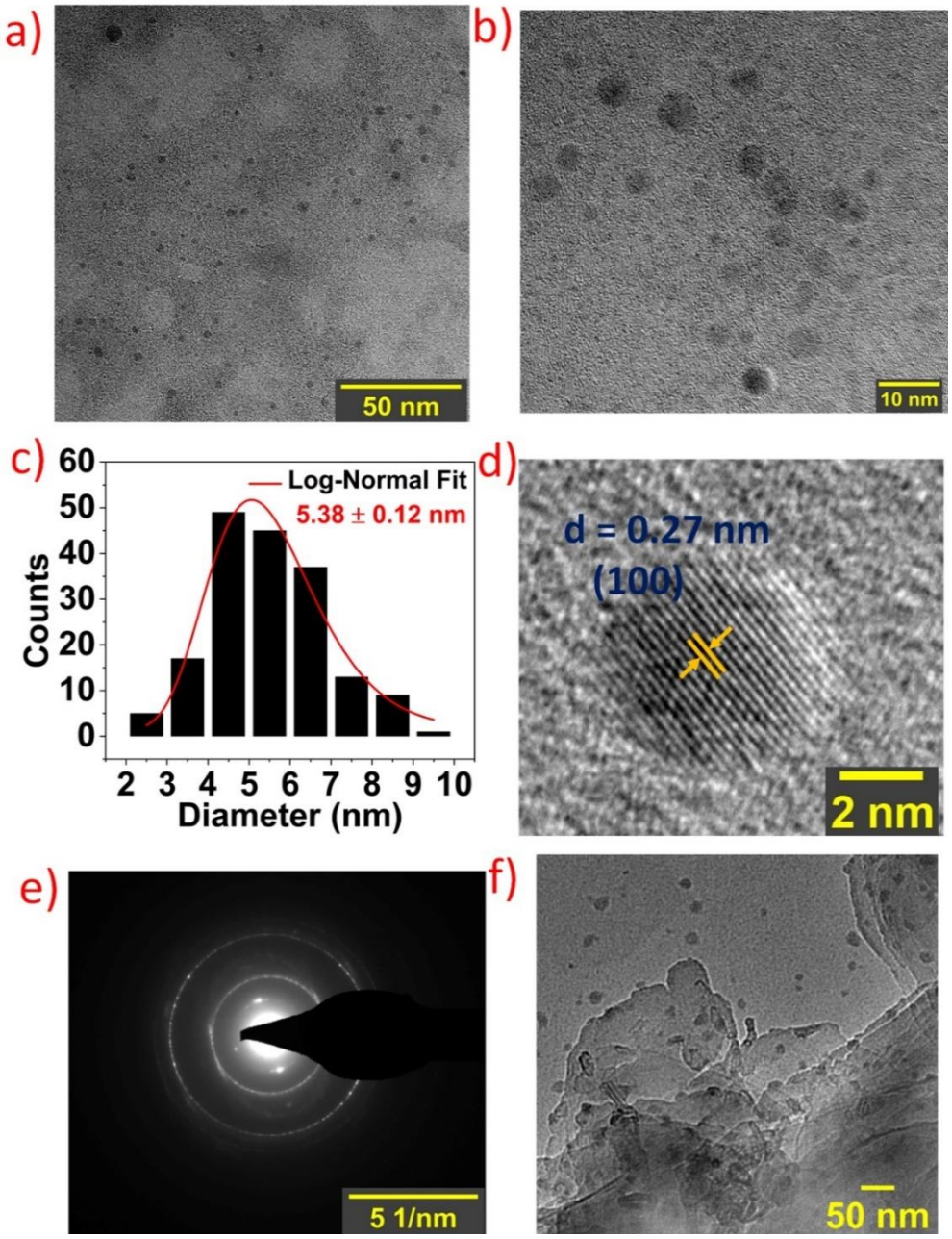

Figure 5.10: a,b) TEM images of prepared WS_2-QDs c) Particle size distribution graph of WS_2-QDs, average particle size was calculated to be ~ 5.38 ± 0.12 nm, Log-Normal fitting. d) HR-TEM image of WS_2-QD, lattice spacing was found to be ~ 0.27 nm e) SAED pattern of WS_2-QDs f) TEM image of SnS and WS_2-QDs composite, wherein WS_2-QDs are distributed on few-layer SnS nanoflakes.

Photodetection measurements

Photodetection characteristics of the prepared WS_2-QDs/SnS device were investigated by performing numerous comprehensive lab-based experiments. Figure 5.11(a-c) illustrates the I-V (current *vs.* voltage) characteristics of WS_2-QDs/SnS device under various regions of the electromagnetic spectrum, namely UV, Vis, and NIR. Prior to performing the measurements, the fabricated device was placed in the dark for around 10 hours in order to stabilize the device. As can be seen in Figure 5.11a, it was noticed that the device current increased with increasing intensity of UV light illuminated, exhibiting ohmic behavior. Figure 5.11b and 5.11c show similar current-voltage characteristics for Vis and NIR illuminations. As the light intensity increased, number of carriers generated increases that rises the device current. The temporal responses under constant light illuminations are displayed in Fig. 5(d-f). As seen in Figure 5.11d, the fabricated photodetector is capable of repeatedly detecting the UV light illumination, displaying the repeatable nature of the device. A similar experiment was conducted with Vis and NIR light illumination, and as illustrated by Figure 5.11e and 5.11f, the device was able to sense both Vis and NIR light illumination. The highest amount of increase in device current was noticed under Vis light, implying that the fabricated WS_2-QDs/SnS photodetector is more responsive to Vis light in comparison with UV and NIR light. For further examination of the responsivity of the device, the temporal response under various light intensities was analyzed. This temporal response under varying UV light illuminations of the fabricated WS_2-QDs/SnS photodetector was displayed in Figure 5.11g, where it was noticed that raising the intensity of the UV light caused an increase in photocurrent, which complies with the results obtained in I-V characteristics, Figure 5.11a. Similar experiments were performed for different intensities of Vis and NIR illuminations as displayed in Figure 5.11h and i, and the resulting graphs are compatible with the I-V characteristics obtained in Figure 5.11b and 5.11c, respectively.

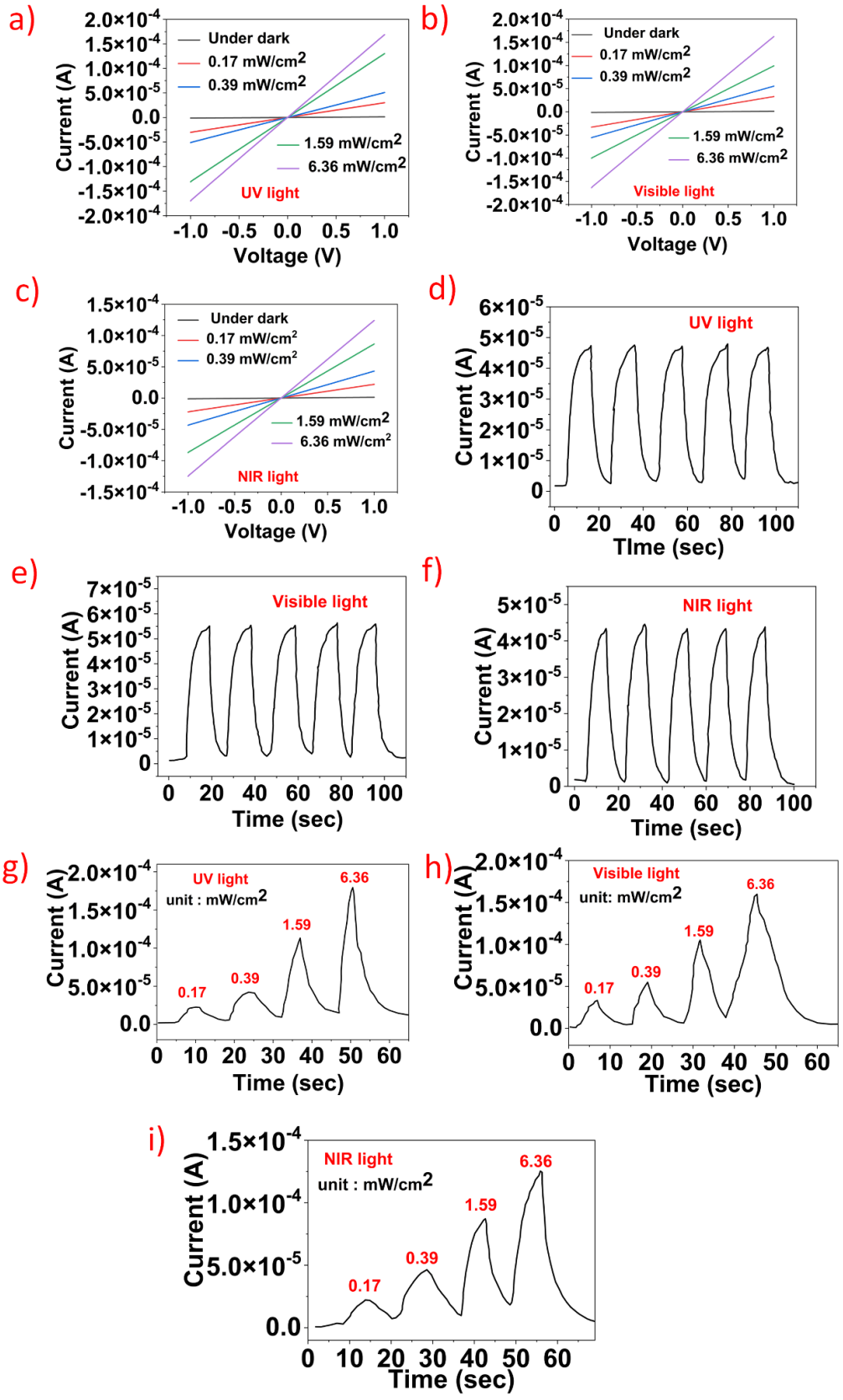
a)
Under dark
0.17 mW/cm2
0.39 mW/cm2
1.59 mW/cm2
6.36 mW/cm2
UV light
Current (A)
Voltage (V)
b)
Visible light
c)
NIR light
d)
Tlme (sec)
e)
Time (sec)
f)
g)
unit : mW/cm2
0.17
0.39
1.59
6.36
h)
unit: mW/cm2
i)

Figure 5.11: a, b, c) I-V characteristics of the device at various light illuminations d,e,f) device current vs. time graph of the device for constant illumination of 0.39 mW/cm^2, g,h,i) device current vs. time graph at different intensities of UV, Vis, and NIR illuminations.

Responsivity (Rλ) is described as the generated photocurrent by illuminated light per unit area on a sensing device. External Quantum Efficiency (EQE) is described as the number of photogenerated carriers collected to the incident photons on the surface of the device. Detectivity (D*) is measured by the capacity of the photodetector to differentiate weak signals from noise. Rλ, EQE, and D* are all important metrics to compute the efficiency of a photodetector. The equations representing Rλ, D* and EQE are given below :

$$R_\lambda = I_\lambda / (A \times P_\lambda)$$

$$D^* = (R_\lambda \times \sqrt{A}) / \sqrt{2 \times q \times I_{dark}}$$

$$EQE = hc \times (R_\lambda / e_\lambda) \times 100$$

where q, I_λ , *A*, P_λ, *and* I_{dark} *indicate* charge of the electron, device current under illumination, active area of the device, illuminated light power, and dark current. The value of the *A* is ~ 36 mm^2.

Under various UV, Vis, and NIR light illuminations, responsivity (Rλ) of WS_2-QDs/SnS device is shown in Figure 5.12a. Rλ of the device for UV illumination was measured to be 0.655 A W^{-1} and responsivity value was decreasing with increase in intensity which is consistent with previous reports [2,355]. This decreasing trend is attributed to the point that with the increase in intensity, a huge number of electron and hole pairs are generated, that increases recombination. Thus, at lower intensities, device exhibits higher responsivity. Similarly, the device responsivity under Vis and NIR light illumination was calculated be 0.719 AW^{-1} and 0.478 AW$^{-1,}$ respectively, shown in Figure 5.12a. These results further confirm that the sensitivity of device is more towards Vis light illumination rather than NIR and UV light. Furthermore, responsivity of pristine SnS device under Vis and NIR regions is displayed in Figure S30, Appendix A and it confirms that decorating with WS_2-QDs not only increased the detection range and but also enhanced the responsivity of the device. Detectivity (D*) of the photodetector under UV, Vis, and NIR was calculated be 4.29 × 10^{12}Jones, 4.71 × 10^{12} Jones and 3.13 × 10^{12} Jones, respectively, as displayed in Figure 5.12b. Furthermore, as seen in Figure 5.12c, EQE of device was found to be ~ 146 % under UV illumination. Similarly, it was calculated to

be ~ 161 % and ~ 76 % under visible light and NIR illumination, respectively. Another key figure of merit to evaluate the photodetector performance is rise time.

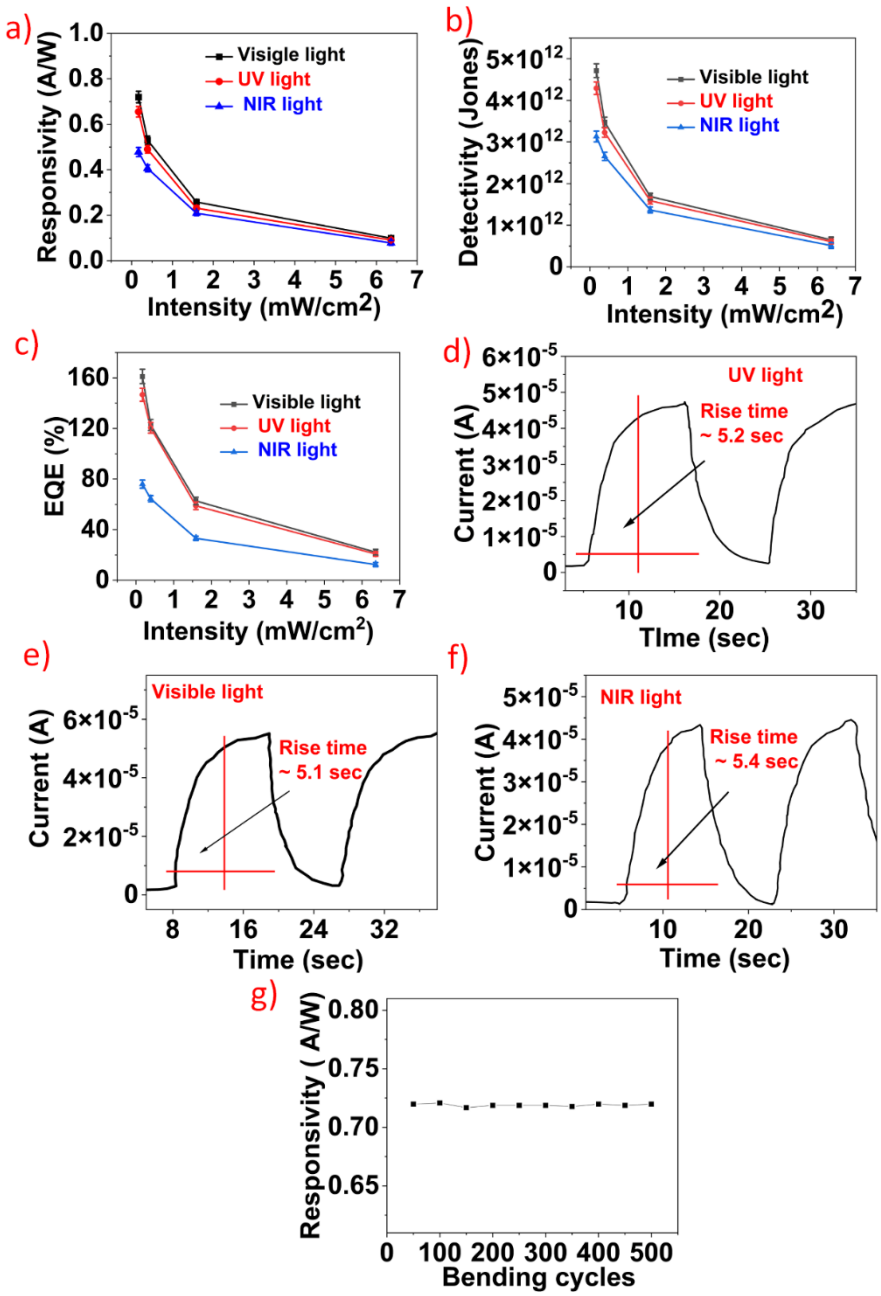

Figure 5.12: a) Responsivity b) Detectivity c) EQE (%) of the device for UV, Vis and NIR illuminations (N=3). d-f) Rise time under UV, Vis, and NIR illuminations, g) Graph shows the responsivity of fabricated photodetector over bending cycles, for visible light illumination.

Rise time of the device is described as the time taken to reach 90% of I_{max} from 10% of I_{max} by the device current, I_{max} represents peak value as illustrated in Figure 5.12(d-f), the rise time of the WS_2-QDs/SnS device was calculated to be ~ 5.4 sec, ~ 5.1 sec, and ~ 5.2

sec for NIR, Vis and UV light respectively. The presence of charge impurity, trap states, and defect states in SnS generated during hydrothermal process results in a slow response time for the device. Aside from that, the charge carrier mobility reduces as a result of the rough surface of the paper substrate. Also, the discontinuous distribution of WS_2 QDs on SnS leads to improper band alignment, that enhances scattering and, as a result, lowers the mobility of charge carriers. Also, flexibility and robust nature of the device were tested by applying 500 continuous bending cycles, wherein the sensor was bent by applying a strain of around ~ 2% and then brought back to the original position repeatedly. It was found that the device had a minor change in its performance, Figure 5.12g, indicating the durable and robust nature of the device.

5.2.3.1 Principle of operation

The photodetection mechanism of WS_2-QDs (n)/SnS(p) device can be analyzed using the band diagram, as illustrated in Figure 5.13. The electron affinity value of WS_2-QDs (n) is ~ 3.95 eV and that of 2D SnS (p) is ~ 3.9 eV, while the bandgap values for the same have been calculated to be ~ 3.1 eV and ~ 1.2 eV, respectively. From the absorbance spectra, it was observed that SnS contributes to the photoabsorbance in visible and NIR regions, while WS_2-QDs absorb in the UV region. As illustrated in Figure 5.13, WS_2-QDs, being n-type, and SnS, being p-type, results in the formation of a p-n junction that generates high localized electric fields at the 0D/2D junction interfaces. As WS_2-QDs are discretely distributed on SnS, there are many such SnS/WS_2-QD heterojunctions on the fabricated device which add up and contribute in creating a high electric field and assist in the effective separation of the generated electron-hole pairs. Further, metal contacts were formed on SnS, results in effective photogenerated charge carriers collection. When the fabricated device is exposed to UV illumination, electron-hole pairs are generated in WS_2-QDs. However, as energy level of SnS conduction band is lower than that of WS_2-QDs, the generated electrons are transported into SnS. Similarly, energy level of SnS valence band is greater than that of WS_2-QDs, and hence, the generated holes are transported into SnS. Since metal contacts are taken form SnS, it helps in the effective collection of these generated charge carriers under an external electric field and improves the device photocurrent. Furthermore, the resulting localized electric field aids in the effective separation of generated electron and hole pairs. Similarly, when the device is illuminated with Vis and NIR light, electron-hole pairs are generated in SnS and the charge carriers are collected at metal contacts, which improves the device current. Also,

by virtue of being sulfide compounds, SnS and WS_2 have a synergistic effect. This synergic effect results in an effective photoinduced charge-carrier separation in the WS_2-QDs and an associated charge transport in SnS, which significantly enhances the photo-absorbance of the device and its range.

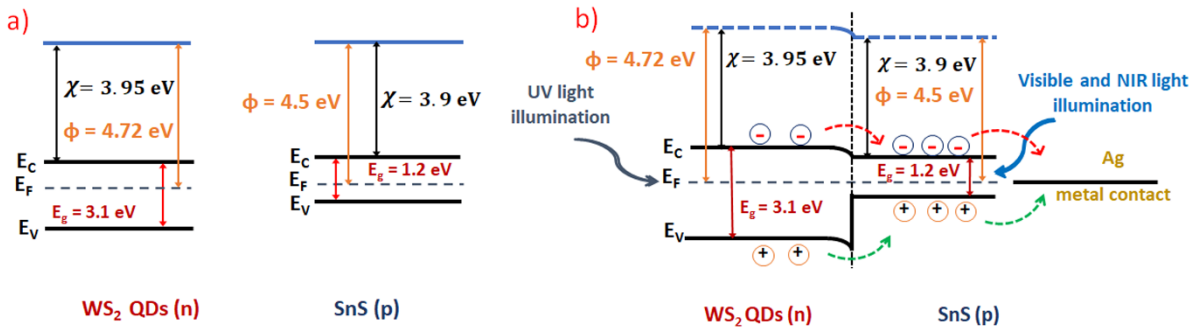

Figure 5.13: Illustrating the band structure of WS_2-QDs and SnS a) before contact b) after the formation p-n heterojunction with proposed charge separation mechanism.

There are multiple reports on the development of 0D-2D based photodetectors. *Huang et al.* a hybrid device by decorating CIS-QDs on SnS_2 nanosheets synthesized by a CVD method and observed significant enhancement in the photoresponsivity of the device [293]. *Hu et al.* fabricated a high-performance phototransistor using p-type single layer WSe_2 and PbS QDs used the hybrid approach [296]. *Ra et al.* demonstrated a high performance visible light photodetector by charge injection of 0D CdSe crystals to 2D MoS_2 nanosheets on SiO_2/Si substrate [356]. *Singh et al.* developed a high responsive 0D-2D nanocomposite based UV photodetector using 0D WS_2-QDs and 2D graphene on SiO_2/Si substrate [341]. All the above reports used rigid substrates such as Si wafer, which makes hinders their usage in wearable and flexible electronic applications and also used expensive, high temperature, and cleanroom fabrication techniques such as CVD. In this work, 0D/2D based UV-Vis-NIR photodetector was demonstrated using a low temperature, cost-effective hydrothermal synthesis technique. Synthesized WS_2-QDs were decorated discretely on SnS flakes to improve the broadband detection range and photoresponsivity of the photodetector. Performance of the fabricated photodetector compared with the literature of photodetectors is summarized in Table 5.2. Importantly, WS_2-QDs/SnS stands out in the comprehensive consideration of effective wavelength range, responsivity, scalability, and flexibility.

Material (0D/2D)	Substrate	Fabrication	Range of Detection	Responsivity (AW^{-1})	Flexibility	Ref.
InP QDs/BP	SiO_2/Si	Exfoliation,	Visible	10^9	No	[93]
PbS-QDs/WSe_2	SiO_2/Si	CVD	NIR	2 x 10^5	No	[296]
CdSe NCs/MoS_2	SiO_2/Si	PMMA transfer	Visible	2.5 x 10^5	No	[356]
WS_2 QDs/Graphene	SiO_2/Si	CVD, Hydrothermal	UV	1814	No	[341]
ZnCdSe/ MoS_2	SiO_2/Si	CVD	Visible	3.7 x 10^4	No	[357]
ZnO QDs/MoS_2	SiO_2/Si	CVD	UV	2.3 x 10^3	No	[358]
CIS-QDs/SnS_2	SiO_2/Si	CVD	Visible	630	No	[293]
n-WS_2 QDs/ p-SnS	**Cellulose paper substrate**	**Hydrothermal**	**UV-Vis-NIR**	**0.655, 0.719, 0.478**	**Yes**	**This work**

Table 5.2: Fabricated WS_2-QDs/SnS photodetector performance is compared with literature.

5.2.4 Conclusion

In conclusion, a flexible broadband photodetector was fabricated using 2D-SnS (p) and 0D-WS_2-QDs (n) on a paper substrate by scalable and facile hydrothermal and vacuum filtration processes. Under UV, Vis, and NIR illumination, responsivity of the device was measured to be 0.655 A W^{-1}, 0.719 A W^{-1}, and 0.478 A W^{-1}, respectively. WS_2-QDs decorated over SnS improve the device sensitivity for UV light and form localized p-n junctions that help in the effective dissociation of generated charge carriers (electron-hole pairs). Furthermore, metal contacts were made on SnS, enhanced the collection of photogenerated charge carriers.

5.3 Broadband, Ultra-high responsive monolayer MoS_2/SnS_2 Quantum Dot based mixed dimensional photodetector

Atomically thin two-dimensional (2D) materials have gained significant attention from the research community in the fabrication of high-performance optoelectronic devices. Even though there are various techniques to improve the responsivity of the photodetector, the key factor limiting the performance of the photodetectors is constrained photodetection spectral range in the electromagnetic spectrum. In this work, mixed-dimensional 0D/2D SnS_2-QDs/monolayer MoS_2 hybrid is fabricated for high-performance and broadband (UV-visible-NIR) photodetector. Monolayer MoS_2 is deposited on SiO_2/Si using chemical vapor deposition (CVD) and SnS_2-QDs are prepared using a low-cost solution process method. The high performance of the fabricated 0D/2D photodetector is ascribed to the band bending and built-in potential created at the junction of SnS_2-QDs and MoS_2, which enhances the injection and separation efficiency of the photoexcited charge carriers. Also mixed-dimensional structure suppresses the dark current of the photodetector. The decorated SnS_2-QDs on monolayer MoS_2 not only improves the performance of the device but also extends the spectral range to the UV region. Photoresponsivity of the device for UV, visible and NIR region is found to be ~ 278 A/W, ~ 435 A/W, and ~ 189 A/W, respectively. Fabricated devices showed maximum responsivity under the visible region attributed to the high absorbance of monolayer MoS_2. The response time of the fabricated device is measured to be ~ 100 msec. These results reveal that the development of mixed-dimensional (0D/2D) SnS_2-QDs/MoS_2 based high performance and the broadband photodetector is technologically promising for next-generation optoelectronic applications.

5.3.1 Introduction

With the rapid development in our daily life, there is a huge demand for high-performance and broadband photodetectors for applications such as optical communication, thermal imaging, medical imaging, and environmental monitoring [340,359,360]. Photoresponsivity indicates the light-sensing capability of the photodetector and represents one of the critical parameters of a photodetector. In recent years, significant research has been done by the scientific community to enhance the responsivity of a photodetector. Also, parallel research on increasing the spectral range of photodetector was also done. Various strategies include bandgap modulation, surface

interface engineering, discrete distribution, novel structure design, mixed-dimensional hybrid, etc.[361,362] have been reported to improve the photodetector performance. Despite the continuous development and responsivity improvement of photodetectors, the key factor limiting the performance of the photodetectors is the limited spectral range in the electromagnetic spectrum[2,65,363]. Hence, there is an urgent need to develop a powerful strategy or promising method which not only enhances the photoresponsivity but also extends the spectral range of the photodetector.

One of the effective techniques to enhance the photodetector performance is the construction of heterostructures. Most conventional broadband photodetectors use single-crystalline semiconductors such as Si, InGaAs, GaN, etc.[364–366]. These bulk materials suffer from a lack of bandgap tunability, complex manufacturing process, low operating temperature, and high driving voltage. Transition metal dichalcogenides (TMDs) have gained significant attention since the discovery of Graphene in 2004. TMDs are being investigated as possible options for next-generation optoelectronic and electrical devices due to their distinguished properties, which include atomically thin, tunable bandgap, high mobility, and excellent electronic and optical properties [330,355,360]. One of the most widely used and investigated 2D TMDs is molybdenum disulfide (MoS_2) because of its advantages, such as strong in-plane carrier mobility, layer-dependent bandgap, high absorption coefficient, and excellent stability [170,310,358]. Monolayer MoS_2 is extensively utilized for the fabrication of photodetectors due to particular optical properties which are not found in bulk materials, such as strong-light matter interaction, high mobility (200 cm^2/V.S), direct bandgap, etc. [111,367–369]. MoS_2 in monolayer exhibits a direct bandgap of ~ 1.8 eV because of quantum confinement, but MoS_2 in bulk has an indirect bandgap of ~ 1.3 eV [370,371]. *Wang et al.* demonstrated visible-NIR light detector based on monolayer MoS_2/Si heterostructure, showing a detectivity of 10^{13} Jones and ultrafast rise time (~ 3 μs) [138]. *Zhou et al.* constructed MoS_2/$SnSe_2$ van der Waals heterostructure based visible light photodetector with a high responsivity of 9×10^3 A/W [372]. Many photodetectors based on monolayer and few-layer MoS_2 were reported with high photoresponsivity and quick response time which confirms that MoS_2 has huge potential in the fabrication of photodetector. However, most of the MoS_2 based photodetectors reported showed spectral range limited to visible and NIR regions, because MoS_2 absorbs more light in the visible and near-infrared range than it does in the UV range. One solution to achieve broadband (UV to NIR) spectral response is creating a heterojunction with large bandgap, UV sensitive quantum dots (QDs), which

not only increase the spectral region to UV but also inject photogenerated carriers to enhance the photoresponse of the device[98,373]. Also, Interactions between 0D QDs and 2D large area crystals moieties can increase the dispersiveness and stability of QDs, and faster charge transfer from 2D nanoplates can limit charge recombination, resulting in significantly enhanced photodetection activity. Such combinations give rise to a considerably more extensive class of nano heterostructures, the characteristics of which may be tweaked to achieve desired results, opening new opportunities for the development of hybrid materials customized to specific applications.

Over the last few years, QDs have demonstrated potential for optoelectronic devices due to their high absorption properties, bandgap tunability by varying size, quantum confinement, and cost-effective synthesis procedures[374],[375]. In QDs, quantum confinement leads to the limited movement of charge carriers to a certain space which results in an increase of electron kinetic energy. This implies increased excitation energy and material energy gap; thus, QDs exhibit a high bandgap. Recently, n-type SnS_2-QDs attracted significant attention due to earth abundance and non-toxic nature, excellent optoelectronic properties, and along with a large bandgap of ~ 3.3 eV, strong UV light absorption[376]. Recently, *Li et al.* fabricated a UV light (λ=365 nm) photodetector based on SnS_2-QDs using cost-effective fabrication methods[376]. To the best of the authors' knowledge, no studies have been published on demonstrating SnS_2-QDs/monolayer-MoS_2 hybrid-based broadband (UV-Visible-NIR) photodetector.

This work demonstrates the SnS_2-QDs/MoS_2 heterojunction-based high-performance broadband photodetector. Here, MoS_2 crystals were grown on SiO_2/Si by CVD technique, and SnS_2-QDs were prepared using a cost-effective and low-temperature solution process method. Mixed-dimensional 0D/2D SnS_2-QDs/MoS_2 hybrid device was prepared by spin coating SnS_2-QDs on MoS_2 monolayers. Photoluminescence (PL) spectra recorded on different MoS_2 flakes revealed a redshifted and quenching effect of PL emission originated by charge transfer from SnS_2-QDs towards the MoS_2 crystals. It is important to highlight that the metal connections were obtained from a monolayer of MoS_2 for effective collection of photoexcited charge carriers. The photogenerated carriers in SnS_2-QDs are transported to MoS_2 due to energy level difference and thus, monolayer MoS_2 also works as a transport layer for injected photogenerated carriers from SnS_2-QDs. The discretely distributed SnS_2-QDs on monolayer MoS_2 creates many heterojunctions and results in an electric field, which promotes efficient separation and transportation of photoexcited charge carriers, as seen in the PL results. Also, NIR

photoresponse in the fabricated device arises from the electron doping of the MoS_2 originated by the charge transfer from the SnS_2-QD to the conduction band of the MoS_2 monolayer, as observed in PL measurements. Photoresponsivity of the fabricated SnS_2-QDs/MoS_2 device under UV, Vis, and NIR light illumination is ~ 278 A W^{-1}, ~ 435 A $W^{-1,}$ and ~ 189 A W^{-1}, respectively, demonstrating that the device responds better to visible light illumination. The highest photoresponsivity of the device in the visible region is attributed to the higher absorption of monolayer MoS_2 in the visible region. Detectivity of the device under UV, visible, and NIR light illumination was 4.589×10^{12} Jones, 7.19×10^{12} Jones, and 3.11×10^{12} Jones, respectively. The fabricated device showed a rise time of ~ 100 msec. This study may provide a technique for the realization of mixed dimensional 0D/2D based high-performance broadband photodetector for next-generation optoelectronic applications.

5.3.2 Experimental Section

CVD growth MoS_2 monolayers:

MoS_2 crystals were synthesized using an atmospheric pressure chemical vapor deposition (APCVD) system. Clean SiO_2/Si substrate was placed in the center of a hot-wall furnace on top of an alumina boat containing molybdenum dioxide (MoO_2 Sigma Aldrich 99%), a second boat containing sulfur (99.5% Alfa Aesar) was loaded 15 cm away from the furnace center. MoS_2 single layers were obtained by raising the temperature furnace to 750 ˚C at a 50 ˚C/min ramp and immediately cooling the system after reaching 750 ˚C. Ar gas was used as a carrier gas at a flow rate of 100 sccm.

Preparation of SnS_2 QDs:

SnS_2 QDs synthesis schematic view shown in Figure S31 and the synthesis route followed by a solvothermal process by adding 135mg tin chloride ($SnCl_2.2H_2O$) and 360 mg of $Na_2S.9H_20$ in 60 ml of ethylene glycol constantly swirling for 50 minutes. The solution was then transferred using a 77% filling ratio at 180 °C for 24 hours in a 50 ml Teflon-lined stainless-steel container. The resulting product was washed with deionized water and methanol three times following acclimatization to room temperature. Following drying, the yellow powder was created by heating it to 80 °C for 12 hours. Following the acquisition of SnS_2 powder (10 mg) was dissolved in NMP (20 ml) and sonicated for 6 hours in an ice bath to exfoliate the SnS_2. Later, centrifuged for 30 minutes at 7000 rpm to separate the supernatant. Again, the supernatant was centrifuged at 12000

rpm for 30 minutes, repeated centrifugation 2-3 times resulted in SnS_2 QDs being present in the final supernatant.

SnS_2-QDs/ ML MoS_2 device fabrication :

The design strategy for SnS_2-QDs/MoS_2 monolayer hybrid is depicted in Figure 5.14; the development process of 0D SnS_2 QDs on the surface of MoS_2 crystals on SiO_2/Si substrate followed by metal contact deposition. To fabricate the device, different weight percent of SnS_2-QDs were dissolved in 5 ml ethanol and drop-cast by spinning (2000 rpm) on as-grown CVD growth MoS_2 crystals, typical procedure schematic view shown in Figure 5.14. Based on AFM image, Figure S32, Appendix A, the calculated thickness of SnS_2-QDs is around 1.5 nm. Metallic alignment marks were used to record the position of the MoS_2 crystals, the contact pattern was then performed by standard electron beam lithography. Ti(10 nm)/Au(200 nm) metalization was deposited by thermal evaporation followed by a lift-off process to finish the fabrication.

Materials Characterization:

At room temperature (RT), microphotoluminescence and Raman spectroscopy were determined by a Jobin Yvon LABRAM HR EVOLUTION spectrometer fitted with a camera (CCD). A laser with a continuous wave frequency of 488 nm was used to produce the optical excitation. Bruker Innova AFM (Atomic Force Microscope) was utilized to evaluate the thickness and roughness of MoS_2 crystals in tapping mode. To evaluate the surface morphology and microstructure, high-resolution transmission electron microscopy (HRTEM) (JEOL-2000, Talos F200X), Hitachi HT 7700 transmission electron microscopy (TEM), and scanning electron microscopy (SEM) were utilized. Powder X-ray diffraction (XRD) (Japan Rigakul D/MAX2200V) with Cu K-alpha radiation was utilized to find the crystal phase of the product. A source meter (Keithley 2450) was utilized for photodetection measurements. For NIR, visible (Vis), and UV light illuminations, Light sources having wavelengths of 780 nm, 554 nm, and 365 nm were employed for NIR, Vis, and UV light illuminations, respectively.

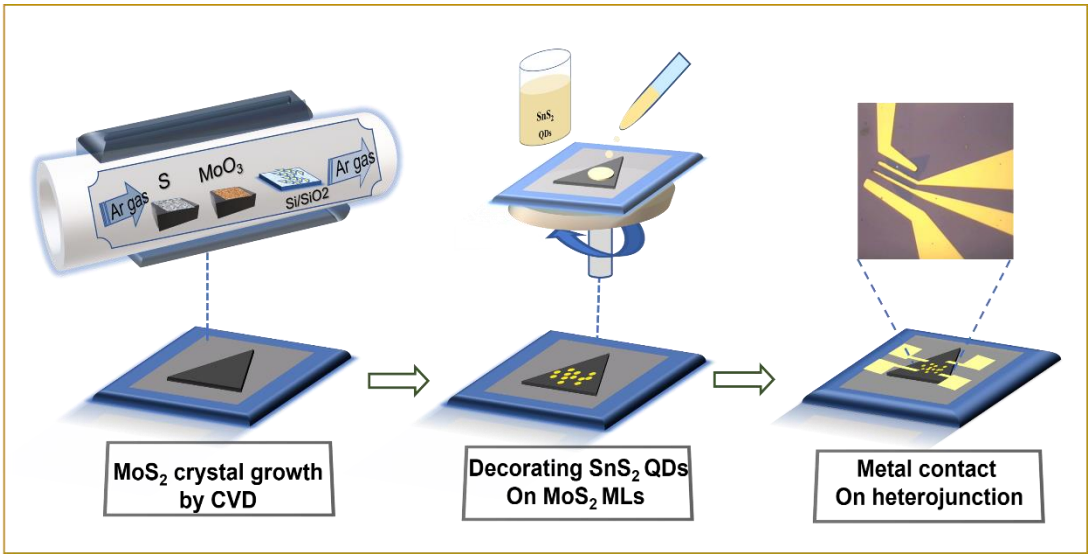

Figure 5.14: Schematic illustrates the CVD synthesis setup and several forms of heteroepitaxial development of SnS_2-QDs/MoS_2 heterojunction on SiO_2/Si substrate.

5.3.3 Results and discussion

Monolayer MoS_2 characterization:

FESEM analysis was used to investigate the morphology of the MoS_2 crystals grown on the SiO_2/Si. As shown in Figure 5.15a, triangular MoS_2 crystals with sizes up to 35 µm lateral dimension were observed along with some irregular shaped crystals. Additionally, atomic force microscopy (AFM) was used to determine the thickness and shape of the MoS_2 crystals. The thickness of the MoS_2 crystals was measured is around 0.7 nm (monolayer), as depicted in Figure 5.15b. Raman spectroscopy confirms the presence of MoS_2 single layer crystals, shown in Figure 5.15c, since the separation between the in-plane E_{2g} and out-place A_{1g} modes was found to be ~ 20 cm^{-1} [377,378]. XPS analysis was performed to understand the chemical composition of MoS_2 crystal. Narrow band XPS spectrum of Mo 3d and S 2p of MoS_2 deposited SiO_2/Si were presented in Figure 5.15d and 5.15e, respectively. The Mo 3d region contains two characteristic peaks located at 232.5 eV and 229.4 eV, corresponding to Mo $3d_{3/2}$ and Mo $3d_{5/2}$, respectively. The peaks located around 235, 231 and 228 eV are assigned to the Mo+6 and Mo+4 oxidation states of the MoO_3 used during the deposition[379]. The S 2p region shows two distinct peaks located at 163.56 eV and 162.41 eV corresponding to S $2p_{1/2}$ and S $2p_{3/2}$, respectively [378]. There is also an S 2s peak noticed centered at 226.7 eV corresponding to MoS_2.

There is no S 2p peak found at binding energies between 168 eV and 170 eV, which confirms that there is no oxidation of sulfur atoms in the sample.

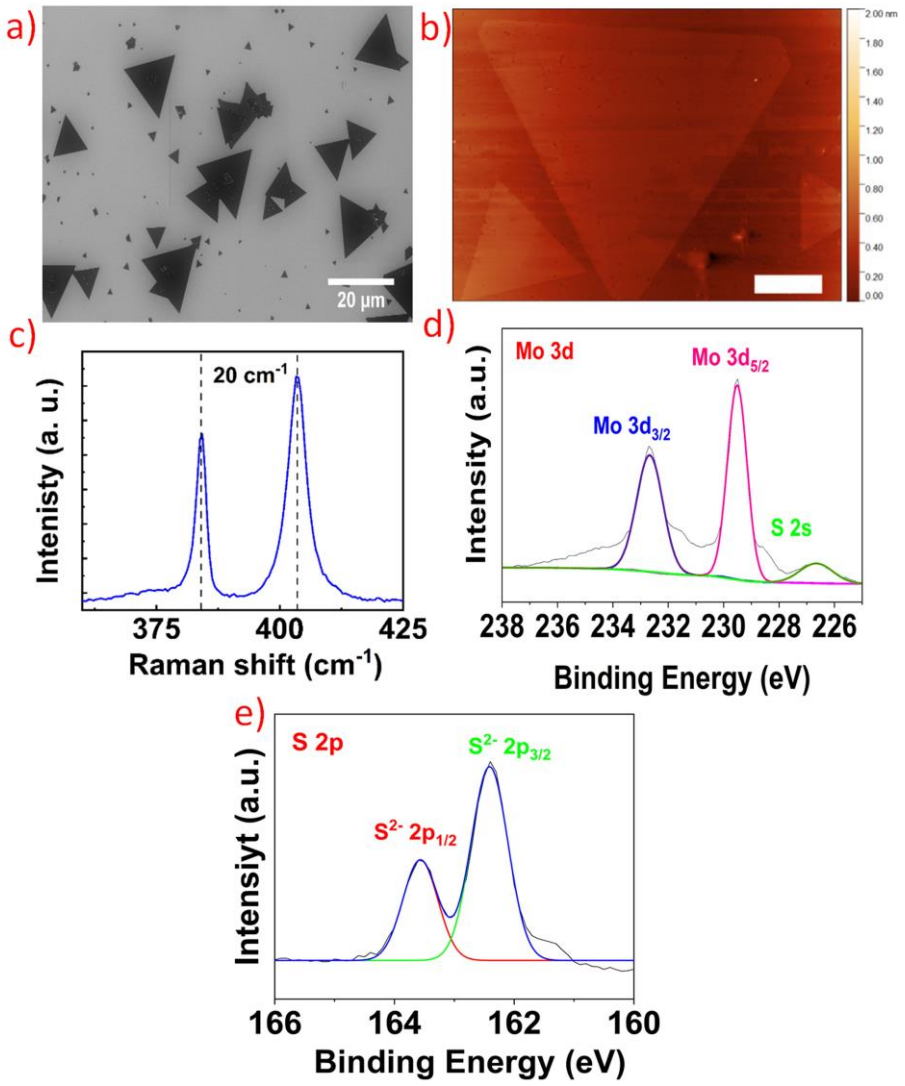

Figure 5.15: a) Surface morphology of MoS_2 crystals, FESEM image b) AFM topogram showing the MoS_2 crystal thickness of ~ 0.7 nm, Scale: 20 µm, c) graph shows the Raman spectrum of MoS_2 deposited on SiO_2/Si, d-e) Narrowband XPS spectrum of Mo 3d and S 2p.

SnS_2-QDs characterization:

Synthesized SnS_2 powder was used to prepare SnS_2-QDs. XRD and FESEM studies were used to investigate the crystallization and morphology of the synthesized SnS_2. Figure S33a depicts the XRD pattern of SnS_2, the crystal planes (202), (201), (111), (102), (101), (100), and (001), matched with the JCPDS # 23-0677, representing hexagonal SnS_2 [380] [381]. FESEM analysis was used to further characterize the surface morphology of synthesized SnS_2. As depicted in Figure S33b and Figure S33c individual SnS_2

nanoflakes formed micro flower-like shapes. TEM was used to observe the structure and morphology of the prepared SnS_2-QDs. As illustrated in Figure 5.16(a-b), SnS_2-QDs had a spherical shape with a wide range of sizes, indicating polydispersity. The mean size of the SnS_2-QDs was determined to be 4.47 ± 0.23 nm, as illustrated in Figure 5.16c and 5.16d shows a HRTEM images of SnS_2-QDs, where the lattice fringes were separated by a distance of 0.275 nm, corresponding to plane (101) of hexagonal SnS_2, JCPDS # 23-0677 [381].

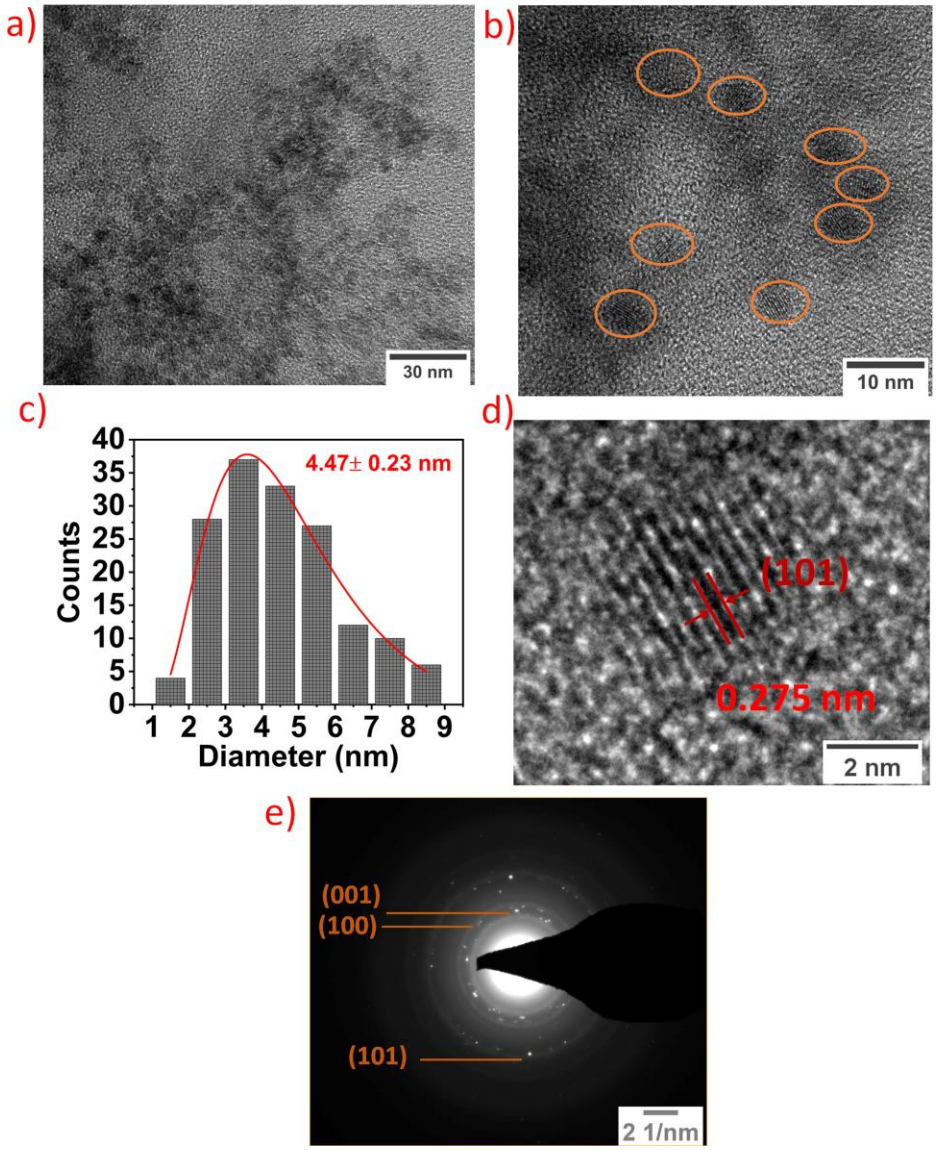

Figure 5.16: a-b) TEM analysis of the prepared SnS_2-QDs, c) plot illustrating the size distribution of prepared SnS_2-QDs, the mean size of the QDs was determined to be 4.47± 0.23 nm d) HRTEM image displaying lattice fringes e) SAED pattern of prepared SnS_2-QDs.

Additionally, the selected area electron diffraction (SAED) pattern reveals scattered dots, as illustrated in Figure 5.16e, while the presence of multiple rings verifies the polycrystalline nature and prominence of the hexagonal SnS_2 (101, 001, and 100) diffraction planes. Furthermore, XPS analysis was utilized to verify the surface chemical states and elemental composition. Two characteristics peaks were observed in narrowband spectra of Sn 3d at 495.2 eV and 486.6 eV, respectively, which are ascribed to Sn^{4+} $3d_{3/2}$ and Sn^{4+} $3d_{5/2}$ [382], Figure S34a, Appendix A.. Further, deconvoluted XPS spectra of S 2p can be found in Figure S34b, Appendix A. Two prominent peaks were identified in the spectrum at 162.8 eV and 161.3 eV, correspond to S^{-2} $2p_{1/2}$ and S^{-2} $2p_{3/2}$, respectively [383].

Figure 5.17b displays the morphology of the SnS_2-QDs/MoS_2 heterojunction recorded by AFM. The MoS_2 monolayer flake presents a typical triangular shape obtained after CVD growth, the inset of Figure 5.17b shows the dispersion of the SnS_2-QDs over the MoS_2 crystals. Even though we found a uniform distribution of the QDs, we observed a gradient (from the center to the edge) of the QDs density along the substrate. In addition, we also found QDs aggregation in some regions of the MoS_2, probably originated by surfactant properties.To further study the morphology of the heterojunction, HRTEM was further performed on the samples. The MoS_2-SnS_2 system was transferred on TEM grids using cellulose acetate[384] illustrated in the low magnification image (figure 5.17c).

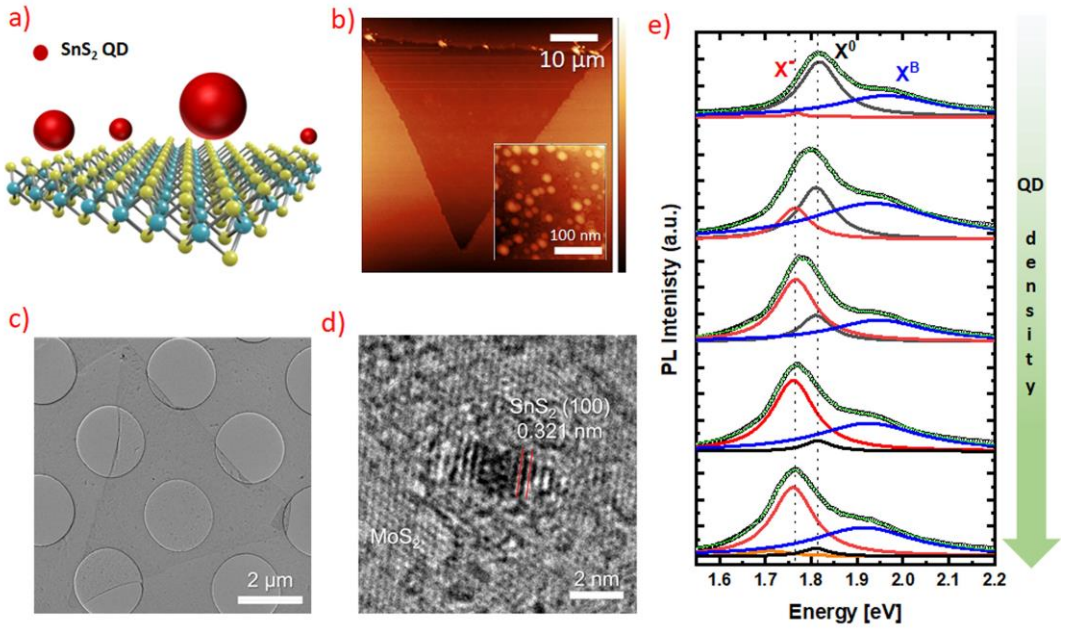

Figure 5.17: a) Schematic of the SnS_2 QDs/MoS_2 heterojunction. (b) AFM topography image of typical MoS_2 crystals after de SnS_2 QDs deposition. (c) low magnification

TEM, and (d) HRTEM images (e) Microphotoluminescence spectra of the different QD concentrations present on the heterojunction. The PL fitting reveals the presence of the exciton A (X^0), exciton B (X^B) and trion (X^-).

Figure 5.17d depicts an HRTEM image revealing an SnS_2 (3 - 4 nm) quantum dot lying on a MoS_2 monolayer. MoS_2 shows a hexagonal lattice, while the (100) plane of an SnS_2 QD can be viewed in this orientation. Additionally, as seen in Figure S35, Fast Fourier transform (FFT) diffraction analysis indicates that the SnS_2 QDs are randomly oriented above the MoS_2 crystals, and the area has been subjected to this image enables precise determination of the interlayer gap between two materials. Also, the region shown in the illustration by a red and yellow circle indicates the coexistence of the two materials. Figure 5.17e shows the results of the normalized PL spectra of five different MoS_2 MLs measured from the edge to the center of the sample where the SnS_2 QD density is higher using a 488 nm CW laser. The PL peak redshifts from 1.82 to 1.76 eV towards higher QDs concentration, and the PL emission intensity quenches in the same trend (Figure S36). To understand the origin of this behavior, we decomposed each spectrum through a Lorentzian fitting where three principal features attributed to the exciton A (or neutral exciton X^0) centered around 1.82 eV, the exciton B (X^B) peaked at 1.94 eV, and the charged exciton or trion (X^-) located at 1.77 eV can be identified. One can see that the spectral weight of the exciton A decreases quickly, whereas the contribution of the trion significantly increases with the QD concentration. These results suggest a high presence of electrons on the MoS_2 crystals induced by the SnS_2 QDs. Similar effects have been reported in 0D-2D systems such as MoS_2 MLs decorated with WS_2 and carbon QDs [385,386] and in vertical TMDs heterostructures [387], where the mechanism responsible for modifying the PL properties of the MoS_2 is the charge transfer from the QDs to MoS_2 layer. As we will further discuss in the optoelectronic properties of the SnS_2-MoS_2 heterojunction, upon illumination, the photoexcited electrons generated on the SnS_2 tend to diffuse towards the MoS_2 single layer due to the band alignment of both materials. Therefore, these electrons induce n-type doping of the MoS_2, generating non-radiative channels such as trions explaining the red-shifting and the quenching of the PL. Moreover, the A_1' (in-plane) mode of the Raman spectra recorded on (Figure S36) MoS_2 flakes containing a higher QD density exhibit a red-shift of approximately 1.5 cm^{-1} compared to lower QD density while the E' mode remains unaffected, confirming the n-doping assumption found in the PL as a result of the charge transfer.

Photodetection measurements:

Figure 5.18a-c depicts the current-voltage(I-V) characteristics of the SnS_2-QDs/MoS_2 photodetector for various UV, visible, and NIR light intensities. I-V characteristics showed a linear relationship between current and voltage, indicating that metal contacts (Ti/Au) made on the monolayer MoS_2 exhibit no significant Schottky barrier formed at metal-semiconductor interface. The increase in device current under light illumination is ascribed to the generation electron-hole (e-h) pairs, followed by the quick and efficient transportation and separation of photogenerated electron-hole pairs. Based on the electron affinities of SnS_2 and MoS_2, the conduction band offset between these materials is expected to be small, increasing the photogenerated carrier collection at the contacts. In addition, the incorporation of SnS_2-QDs extends the absorption in the UV region, thereby increasing the sensing spectrum of the fabricated device. Creating a heterojunction with SnS_2-QDs on monolayer MoS_2 has two primary advantages: i) extending the absorption spectrum of the fabricated device to the UV region and ii) promoting the efficient separation and transportation of photoexcited charge carriers across the depletion region.

The temporal response of the device was studied under different light illuminations. All time-dependent measurements were carried out at a bias voltage of 1 volt. Figure 5.18d-f display the temporal response of the photodetector at constant light irradiation (~ 1.41 mW/cm^2) of UV, visible, and NIR light. As depicted in Figure 5.18d-f, the photocurrent increases sharply upon light illumination, then stabilizes at a higher current, and the photocurrent decreases when the light illumination is turned off. This temporal response was repeated for multiple cycles exhibiting the excellent reliability and stability of the fabricated device. From the above photodetection measurements, it was observed that the variation in device current is greater under visible light followed by UV and NIR light because monolayer MoS_2 is more sensitive to visible light, proving that the photodetector is more responsive to visible region.

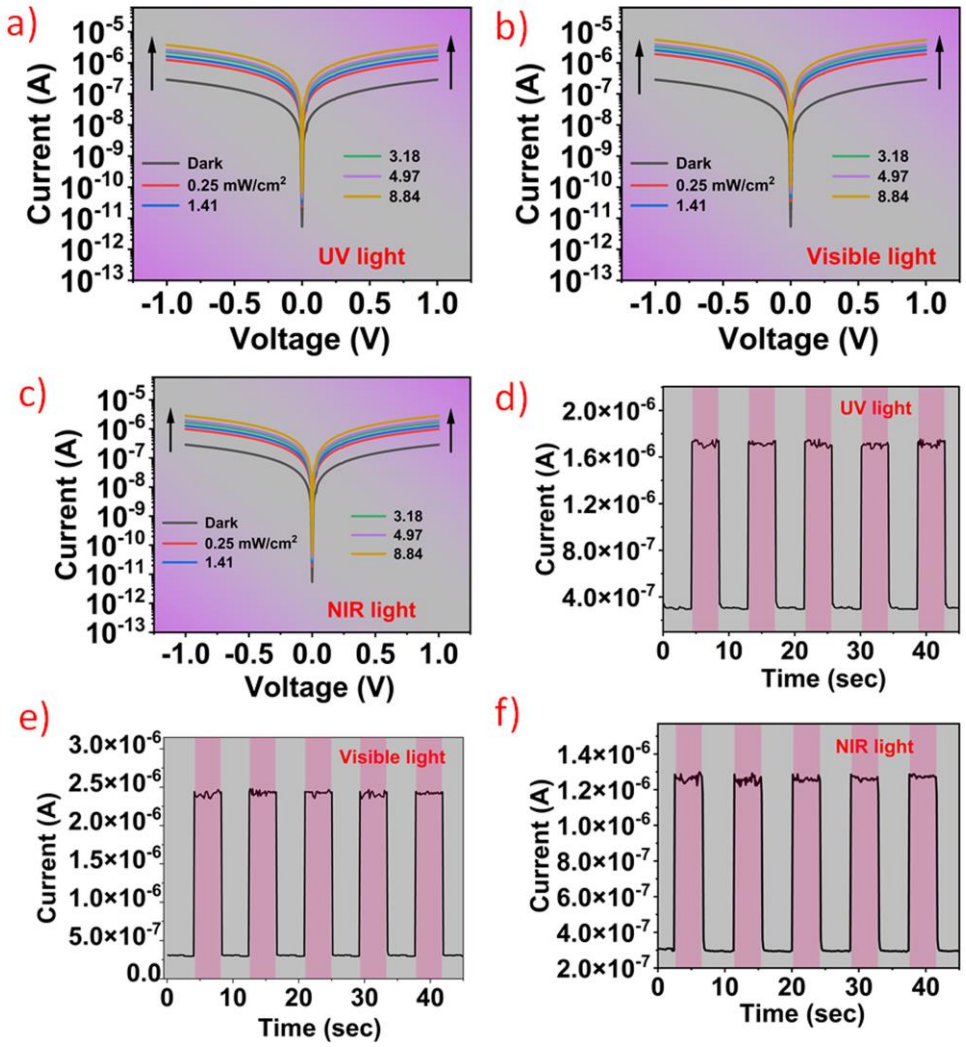

Figure 5.18: a-c) I-V plots under various intensities of UV, visible, and NIR light d-f) time-dependent photoresponse of the fabricated photodetector at constant UV, visible, and NIR light illumination, 1.41 mW/cm^2.

The power-dependent photo sensing performance of the device under UV, visible, and NIR light illumination was verified, and the temporal response plots are shown in Figure 5.19a-c. The rise in device photocurrent with an increase in intensity of illuminated light can be seen in the temporal response, compatible with I-V characteristics (Figure 5.18a-c). For photodetectors, photoresponsivity (R), external quantum efficiency (EQE), specific detectivity (D*) are the most critical characteristic parameters and they are calculated by the following equations [161,271,272]:

$$R = I_{ph}/(P_{in} \times A)$$

$$D^* = (R \times A^{1/2})/\sqrt{2 \times e \times I_{dark}}$$

$$EQE = hc \times (R/q\lambda) \times 100$$

where P_{in}, I_{ph}, I_{dark}, $\boldsymbol{\lambda}$, A, h, c, and q are the intensity of light illuminated, photocurrent, dark current, the wavelength of light illuminated, active area of the device, Planck's constant, speed of light, and electron charge. Photoresponsivity of the photodetector is described as device photocurrent (I_{ph}) generated per unit power of irradiation light on unit area of a photodetector. The ability of the photodetector to identify a weak optical signal is defined as the detectivity. Detectivity is measured in Jones, 1 Jones is equal to 1 $cmHz^{1/2}/W$. The number of charge carriers produced per incident photons is referred to as the EQE.

The calculated responsivity of the fabricated SnS_2-QDs/MoS_2 photodetector as a function of UV, Vis, and NIR light was found to be ~ 278 A/W, ~ 435 A/W, and ~ 189 A/W, respectively, Figure 5.19d. From the responsivity plot, it was noticed that responsivity of the device decreased with an increase in light intensity illuminated, which matches with the literature [93,170], the reason for this trend can be attributed to the larger scattering and recombination probability under strong light illumination compared weak light illumination. In addition, the photodetection performance of pristine monolayer MoS_2 was investigated and the photoresponsivity was found to be ~ 317 A/W and ~ 85 A/W, under Vis and NIR light, respectively, and the corresponding results can be found in the Appendix A, Figure S37.

Further, EQE (%) of the fabricated device was calculated to be 9.58×10^4, 10.7×10^4, and 2.99×10^4 for UV, Vis, and NIR light illumination, respectively, Figure 5.19e. The high EQE value of fabricated SnS_2-QDs/MoS_2 photodetector can be assigned to the large number of photoexcited charge carriers and the accumulation of charge carriers by SnS_2-QDs. On the other hand, the detectivity under UV, Vis, and NIR light was 4.589×10^{12} Jones, 7.19×10^{12} Jones, and 3.11×10^{12} Jones, respectively, Figure 5.19f. Rise time is also another critical parameter to be considered for evaluating the photodetector performance. The response time of the fabricated device is taken as the time difference between $0.9I_m$ and $0.1I_m$, wherein I_m is the maximum photocurrent. As seen in Figure 5.19g, the fabricated device response time was measured to be ~ 100 msec. Furthermore, photodetection performance of the few-layer MoS_2 decorated with SnS_2-QDs was

investigated and the photoresponsivity was found to be ~ 146 A/W and ~ 83 A/W, respectively, Figure S38, Appendix A.

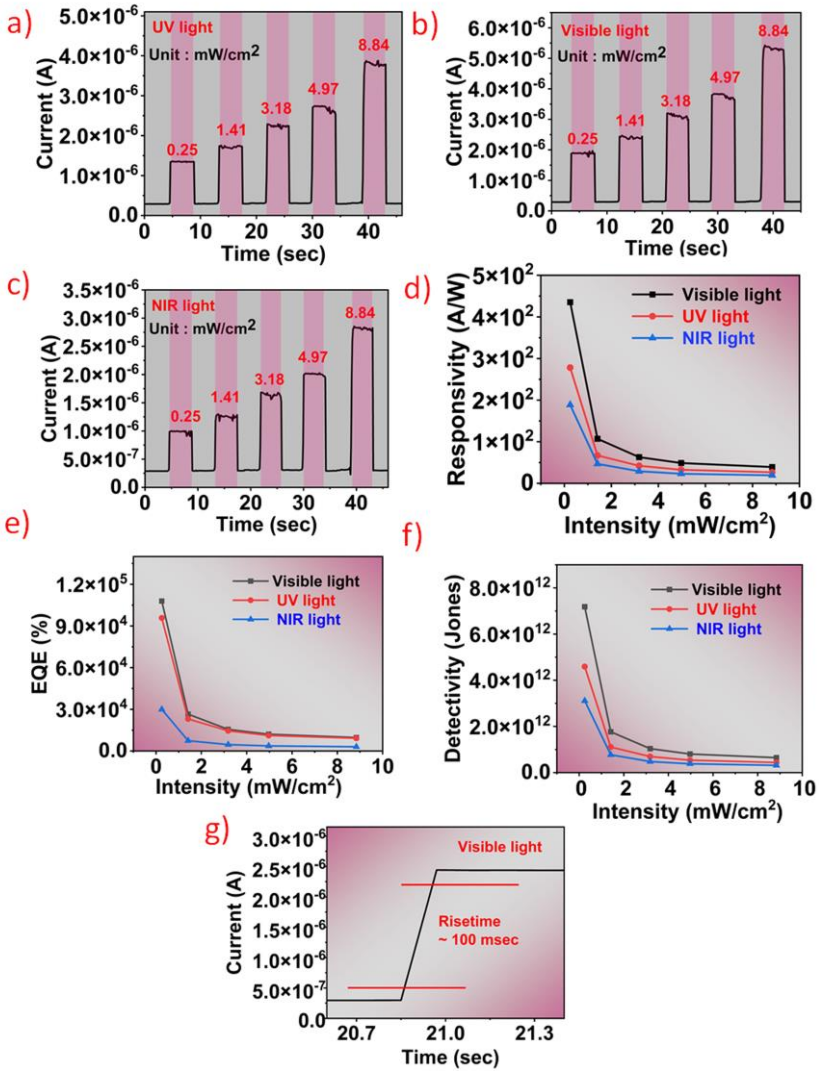

Figure 5.19: a-c) Time-dependent photoresponse of the photodetector with the function of UV, visible, and NIR light intensities d-f) photoresponsivity, EQE, and detectivity of the fabricated SnS_2-QDs/MoS_2 device, g) Graph illustrating the response time of the device and it was measured to be ~ 100 msec.

5.3.3.1 Photodetection mechanism

Figure 5.20a depicts a 3D schematic design of the constructed device and Figure 5.20b the sketch of the band profile of the SnS_2-QDs/MoS_2 heterojunction. The electron affinity and bandgap of 0D SnS_2-QDs and monolayer 2D MoS_2 are 4.16 eV, 3.3 eV, and 3.9 eV, 1.8 eV, respectively. Due to the difference in energy levels, band bending occurs at the junction of SnS_2-QDs and MoS_2, which results in built-in potential at 0D/2D interface. Since SnS_2-QDs are discretely decorated on monolayer MoS_2, the fabricated device contains many 0D/2D junctions, which add up and provide a built-in electric field. The

built-in potential formed across SnS_2-QDs/MoS_2 junction promotes the separation and transportation of charge carriers on the surface of monolayer MoS_2. Furthermore, metal contacts are taken from monolayer MoS_2, promoting the effective collection of photogenerated charge carriers at electrodes. High bandgap SnS_2-QDs are sensitive to UV light, and monolayer MoS_2 exhibits to the photoabsorbance in the Vis and NIR region. When SnS_2-QDs/MoS_2 junctions are illuminated with UV light, e-h pairs get generated in SnS_2-QDs.The photogenerated electrons move to monolayer MoS_2 because the conduction band of SnS_2-QDs is at a higher energy level compared to monolayer MoS_2. Further, photogenerated holes are transported into monolayer MoS_2, which can be attributed to the difference in valence band energy level of SnS_2-QDs and monolayer MoS_2. Since two electrodes are made on monolayer MoS_2, these photoexcited charge carriers get collected efficiently under externally applied bias due to the high conductivity and ballistic/collision free transport nature monolayer MoS_2, thus MoS_2 supports a transport expressway for injected carriers and improves the device photocurrent. Furthermore, the built-in potential formed at SnS_2-QDs/MoS_2 interface promotes the effective separation and transportation of photoexcited charge carriers. Similarly, when visible and NIR light is illuminated on the fabricated photodetector, e-h pairs are generated in MoS_2 and these photogenerated carriers are collected by electrodes effectively, thus improving the device photocurrent.

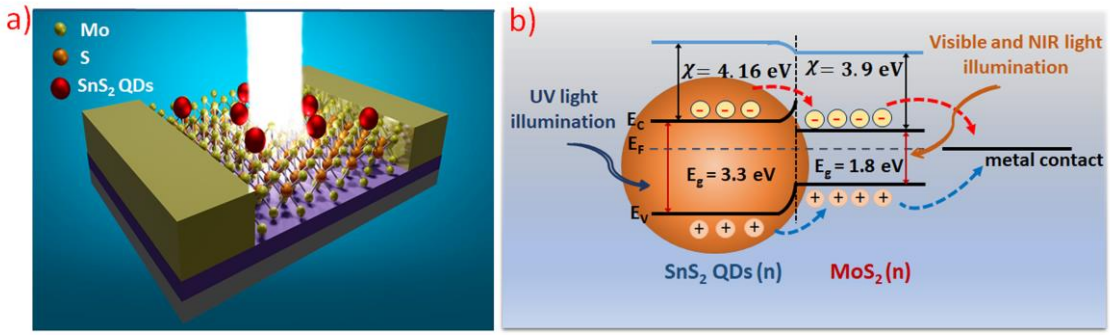

Figure 5.20: a) 3D schematic representation of MoS_2/SnS_2 QDs heterojunction, b) Schematic illustration of SnS_2-QDs and monolayer MoS_2 band structure after the formation of heterojunction with proposed e-h pair separation.

The performance comparison of the fabricated SnS_2-QDs/MoS_2 with another van der Waals (vdW) heterostructure-based photodetectors reported in the literature is presented in Table 5.3. *Zheng et al.* fabricated UV-visible photodetector using CdS/MoS_2

heterostructure and reported that photoresponsivity of the CdS/MoS_2 heterostructure significantly improved compared to the pristine MoS_2[388]. *Tao et al.* proposed a mixed-dimensional vdW heterojunction photodetector based on Te-NWs/ReS_2 and the device showed excellent responsivity under visible region and short response time [71]. Xue et al. reported a few-layer MoS_2/WS_2 vertical heterostructure based visible light photodetector with high responsivity [389]. *Ying et al.* demonstrated a UV light detector using $BaTiO_3$ nanoparticles/MoS_2 heterojunction, and the device showed remarkable photodetection performance [390]. *Um et al.* demonstrated a nanosheet-on-1D heterojunction photodetector using MoS_2 nanosheets and CuO nanowire with ultrahigh photoresponsivity [85]. *Mukherjee et al.* studied the optical properties of discretely distributed Au nanoclusters (NCs) on layered MoS_2. Due to the plasmonic effect of decorated Au NCs, Au NCs/MoS_2 based photodetector showed high responsivity [230]. Most of the above reports suffers from the limited photodetection spectral range, which is crucial for some of practical applications. Our results show that the proposed photodetector design, using 0D SnS_2-QDs and 2D monolayer MoS_2, can be broadband (UV-visible-NIR) without compromising the responsivity. It is important to note that as the size of QDs increases, the quantum confinement effect will be less and hence the absorbance QDs will shift to visible due to the change in the bandgap. Hence the responsivity of the device might be less for UV region, affecting the spectral range of the prepared device. In addition, decoration of the large diameter QDs decreases the light exposure area MoS_2 which further decrease the photoresponsivity of the fabricated device. It is obvious that with the decrease of QDs size quantum confinement effect becomes more apparent[391]. When the MoS_2 is decorated with lower diameter QDs then the light exposure area of MoS_2 increases and hence responsivity increases. Also, due to the large bandgap of low dimensional QDs, the prepared device is sensitive UV region. Further research is in progress to determine whether the size of SnS_2-QDs decorated on MoS_2 flakes can change the performance of the device.

Table 5.3: Comparison of the fabricated SnS_2-QDs/MoS_2 photodetector performance with another van der Waals heterostructure-based photodetectors reported in the literature.

Materials	**Substrate**	**Fabrication Method**	**Wavelength/ spectral range**	**Responsivity (AW^{-1})**	**Response time (sec)**	**Ref.**
CdS/MoS_2	SiO_2/Si	CVD, Epitaxial growth	UV-Visible	3.91	0.01	[388]
Te NWs/ReS_2	SiO_2/Si	Spin-coating, dry transfer,	Visible light (632 nm)	180	0.005	[71]
MoS_2/WS_2	PDMS substrate	Therm.Red., Sulf. process.	Visible light (450 nm)	2.3	-	[389]
MoS_2/$MoTe_2$	SiO_2/Si	CVT, exfoliation, PMMA transfer	Visible light (532 nm)	0.15	0.068	[392]
MoS_2/GaAs	GaAS	Solution processed	Visible	0.446	17×10^{-6}	[393]
MoS_2/Graphene	SiO_2/Si	CVD	Visible	10^7	-	[92]
$BaTiO_3$nanoparticles /MoS_2	SiO_2/Si	CVD, spin coating	UV (365 nm)	120	0.7	[390]
CuO NWs/MoS_2	SiO_2/Si	Ther.oxi., mech. exfoi,,wet trans.	Visible light	157.6	0.034	[85]
MoS_2/TiO_2 nanoflowers	Ti foil	CVD, solvothermal	UV, visible	35.9, 18.5	0.033	[394]
Au NCs/MoS_2	SiO_2/Si	PVD, dewetting	Visible (640 nm)	1.5	0.0065	[230]
SnS_2-QDs/MoS_2	**SiO_2/Si**	**CVD, spin coating**	**UV, visible, NIR**	**278 ,435, 189**	**0.1**	**This work**

5.3.4 Conclusion

In summary, this work demonstrates the fabrication of high performance and broadband photodetector using mixed-dimensional vdW heterostructure based on 0D SnS_2-QDs and monolayer MoS_2. Single MoS_2 was grown on Si wafer using CVD, and SnS_2-QDs were prepared using low-cost solution process method. SnS_2-QDs/MoS_2 heterostructure was fabricated by spin-coating synthesized SnS_2-QDs on monolayer MoS_2. Monolayer MoS_2 is visible, and NIR light sensitive and discretely distributed SnS_2-QDs extends the photodetection range to UV region. Thus, broadened the photodetection range of SnS_2-QDs/MoS_2 from UV to NIR. Further, the built-in electric field formed at the junction of

SnS_2-QDs and monolayer MoS_2 facilitates the effective separation of photoexcited charge carriers and thus improves the performance of the fabricated device. Photoresponsivity of the device for UV, Vis, and NIR was found to be ~ 278 A/W, ~ 435 A/W, and 189 A/W, respectively. Detectivity of the device for UV, visible, and NIR light illumination was measured to be 4.589×10^{12} Jones, 7.19×10^{12} Jones, and 3.11×10^{12} Jones. The response time of the device was determined to be ~ 100 msec. This work may promote the potential pathway to develop mixed-dimensional vdW heterostructure based broadband and high-performance photodetectors for next-generation optoelectronic applications.

CHAPTER 6
Conclusions and future prospectives

6.1 Conclusions

In conclusion, chapter 2 demonstrates the fabrication of 2D materials based high performance photodetectors on flexible substrates using transport layer method. The integration of transport layer assist in the transportation and collection of photogenerated carries of active semiconductor materials thus improves the performance of the device. Recently, a new family of 2D transitional metal carbides, nitirdes called as MXene has attracted significant attention in the research community as a transport layer due to its high electrical conductivity, easy tunable structure, and MXene is an efficient 2D alternative to graphene. By using MXene as transport layer and ReS_2 as a photosensitive layer, high performance photodetector was fabricated and observed a significant change in the sensitivity compared to pristine ReS_2 device.

Chapter 3 demonstrates the fabrication of high performance photodetectors using plasmonic effect. In 2D materials, most light will still transmit through the thin layers of the material. To make the 2D materials viable for practical photodetector applications, it is much need to improve the light-matter interaction of the material. One effective method to improve the light-matter interaction of the 2D materials is integration of plasmonic metal NPs on 2D materials. This can be achieved by either decorating/patterning plasmonic NPs on top of 2D materials and it can increase the light absorption at certain wavelengths. Photodetectors were prepared by integrating metal NPs (Au, Pt, and Pd) on MoS_2 and ReS_2 and also detailed photodetection mechanism was included. Significant change in the photodetection performance was observed after integrating metal NPs compared to the pristine materials due to the plasmonic effect of metal NPs.

Chapter 4 demonstrates the fabrication of p-n heterostructure based photodetector with piezo-phototronic effect for the enhancement of photoresponsivity. Flexible PET sheet was used as substrate. Solution-processed p-type SnS and n-type MoS_2 were used to fabricate p-n heterostructure. It is well known that odd layer n-MoS_2 shows the piezotronic effect and by applying external strain on the fabricated device, the change in the photodetection performance of the was observed. Detailed piezo-phototronic effect based photodetection mechanism was discussed.

Chapter 5 demonstrates the development of a fabrication technique which not only enhances the photoresponsivity but also extends the spectral range of the 2D materials based photodetectors. The utilization of 2D materials in photodetectors have some drawbacks such has limited spectral absorption due to the bandgap and limited absorption efficiency. This is achieved through the implementation of mixed-dimensional 0D/2D vdW heterostructure method. 0D quantum dots (QDs) (MoS_2 QDs, SnS_2-QDs, WS_2-QDs) are decorated on the layered 2D material (MoS_2, SnS) were used to fabricate 0D/2D vdW heterostructures. This compelling synergy combines strong and size-tunable light absorption of QDs, efficient charge separation at the QD/TMDs interface and fast carrier transport through the 2D channel. Thus, mixed-dimensional vdW 0D/2D heterostructure based photodetectors results in large photoconductive gain compared to pristine 2D materials. Also, the detailed photodetection mechanism of mixed-dimensional vdW heterostructure was discussed.

6.2 Future prospectives

Layered 2D materials have potential to trigger a revolution in a wide range of applications such as photoelectric and photovoltaic application due to their extraordinary electronic and optoelectronic applications especially in photodetection application. Although considerable work has been done on the enhancement of photodetection performance of 2D materials using various techniques such as plasmonic effect, piezo-phototronic effect, employing transport layer, mixed-dimensional vdW heterostructures and so forth. But still there are several challenges to be addressed. Based on the results and knowledge achieved through PhD, some aspects and potential research prospectives in the field of 2D materials based photodetectors are given below:

1. The detailed investigation is needed to further analyze the effect of integrated QDs variation and metal NPs size variation on the photoresponse of the 2D materials based devices.
2. The concept of mixed-dimensional vdW heterostructures can be utilized beyond photodetection applications including solar cells and LEDs.
3. Various other combinations 2D channel materials and QDs based devices for optoelectronic applications can be investigated.

4. 2D TMDs semiconductor materials improve electron mobility in very thin channels, but volume manufacturing remains challenging. For practical commercial applications, high quality 2D crystals and large-scale fabrication techniques are needed. Developing techniques to grow high-quality crystalline 2D materials at wafer-scale still remains full of challenges. In the recent years, wafer scale growth of pristine 2D materials have been demonstrated using CVD method. However, further improvement is foreseen in developing high mobility, reduction in lattice disorder, and defect-free large area films. Yet, there is a gap in achieving cost-effective, easy-processing, and CMOS-compatible wafer-scale 2D materials for electronic industry standards.

5. Until now Si technology is dominated due to their extradentary properties and mature technology. But Si wafers are rigid and unbendable that hinders them for the use of next generation flexible optoelectronics applications. One of the solutions can be making commercially available Si wafer flexible by reducing the thickness to few μm using etching process. This flexible Si wafer can be used to grow high quality 2D materials using CVD method for various optoelectronic applications such as photodetectors, solar cells, LEDs.
6. There is a lack of fully understanding of nanomaterials based device physics that governs the carriers transportation across the low dimensional vdW heterostructures. Usually, Richardson's law designed for bulk materials is used for the initial understanding of the thermionic emission mechanism of carrier transport across the 2D semiconductor heterojunctions. It is important to note that 2D materials are atomically thin, which is comparable or even less than the de Broglie wavelength. Thus, it is not appropriate to utilize the bulk transport mechanism to low dimensional materials based vdW heterostructures. Due to a lack of understanding of charge carriers transportation over vdW heterostructures, it is difficult to carry out simulations for devices based on vdW heterostructure utilizing device simulators such as T-CAD to get the optimized parameters which are very useful for the development of high-performance electron devices.
7. The basic principle of the semiconductor based electronic devices depends on the control of the charge carriers movement in the semiconductor. The contact between semiconductor and metal electrode affects the flow of charge carriers.

Hence, low contact resistance in 2D materials based optoelectronic devices is necessary for obtaining effective carrier transportation, high photoresponsivity, and high-frequency operation. Great efforts have been made to optimize the metal contacts suitable for 2D materials using various techniques such as using edge contact, metalized and degenerate doping of 2D materials, and so on. Even though there are number techniques to achieve low contact resistance, yet new strategies to reduce the contact resistance are required for further enhancement of the device performance.

BIBLIOGRAPHY

[1] Z. Zheng, J. Yao, L. Zhu, W. Jiang, B. Wang, G. Yang, J. Li, *Mater. Horizons* **2018**, *5*, 727.

[2] J. Yao, G. Yang, *Nanoscale* **2020**, *12*, 454.

[3] J. Yao, G. Yang, *Small* **2018**, *14*, 2.

[4] J. Mao, Y. Yu, L. Wang, X. Zhang, Y. Wang, Z. Shao, J. Jie, *Adv. Sci.* **2016**, *3*, 1600018.

[5] L. H. Zeng, D. Wu, S. H. Lin, C. Xie, H. Y. Yuan, W. Lu, S. P. Lau, Y. Chai, L. B. Luo, Z. J. Li, Y. H. Tsang, *Adv. Funct. Mater.* **2019**, *29*, 1.

[6] Flexible Electronics Market Size to Hit USD 61 Bn by 2030.

[7] C. Yan, C. Gong, P. Wangyang, J. Chu, K. Hu, C. Li, X. Wang, X. Du, T. Zhai, Y. Li, *Adv. Funct. Mater.* **2018**, *28*, 1803305.

[8] J. Cheng, C. Wang, X. Zou, L. Liao, *Adv. Opt. Mater.* **2019**, *7*, 1.

[9] D. Jariwala, T. J. Marks, M. C. Hersam, *Nat. Mater.* **2017**, *16*, 170.

[10] K. S. Novoselov, A. K. Geim, S. V Morozov, D. Jiang, Y. Zhang, S. V Dubonos, I. V Grigorieva, A. A. Firsov, *Science (80-.).* **2004**, *306*, 666.

[11] X. Cai, Y. Luo, B. Liu, H. M. Cheng, *Chem. Soc. Rev.* **2018**, *47*, 6224.

[12] R. P. Feynman, *J. microelectromechanical Syst.* **1992**, *1*, 60.

[13] K. J. Koski, Y. Cui, *ACS Nano* **2013**, *7*, 3739.

[14] F. Yan, Z. Wei, X. Wei, Q. Lv, W. Zhu, K. Wang, *Small Methods* **2018**, *2*, 1700349.

[15] Y. Liu, Y. Huang, X. Duan, *Nature* **2019**, *567*, 323.

[16] Z. Cheng, R. Cao, K. Wei, Y. Yao, X. Liu, J. Kang, J. Dong, Z. Shi, H. Zhang, X. Zhang, *Adv. Sci.* **2021**, *8*, 2003834.

[17] Q. Ma, G. Ren, K. Xu, J. Z. Ou, *Adv. Opt. Mater.* **2021**, *9*, 2001313.

[18] K. Chandra Sekhar Reddy, F. J. Willars-Rodríguez, R. Ramirez Bon, *Nanotechnology* **2020**, *32*, 095202.

[19] G. Wang, Y. Zhang, C. You, B. Liu, Y. Yang, H. Li, A. Cui, D. Liu, H. Yan, *Infrared Phys. Technol.* **2018**, *88*, 149.

[20] B. P. Yalagala, A. S. Dahiya, R. Dahiya, *Opto-Electronic Adv.* **2022**, 220020.

[21] F. Gao, H. Yang, P. Hu, *Small Methods* **2018**, *2*, 1700384.

[22] S. N. Kajale, S. Yadav, Y. Cai, B. Joy, D. Sarkar, *iScience* **2021**, *24*, 103513.

[23] F. Giannazzo, G. Greco, F. Roccaforte, S. S. Sonde, *Cryst. 2018, Vol. 8, Page 70*

2018, *8*, 70.

[24] P. Zhang, F. Wang, M. Yu, X. Zhuang, X. Feng, *Chem. Soc. Rev.* **2018**, *47*, 7426.

[25] X. Zhang, L. Hou, A. Ciesielski, P. Samorì, *Adv. Energy Mater.* **2016**, *6*, 1600671.

[26] N. Ashraf, M. Isa khan, A. Majid, M. Rafique, M. B. Tahir, *Chinese J. Phys.* **2020**, *66*, 246.

[27] H. Hu, A. Zavabeti, H. Quan, W. Zhu, H. Wei, D. Chen, J. Z. Ou, *Biosens. Bioelectron.* **2019**, *142*, 111573.

[28] C. Anichini, W. Czepa, D. Pakulski, A. Aliprandi, A. Ciesielski, P. Samorì, *Chem. Soc. Rev.* **2018**, *47*, 4860.

[29] Y. Pang, Z. Yang, Y. Yang, T.-L. Ren, *Small* **2020**, *16*, 1901124.

[30] H. Yang, T. Xue, F. Li, W. Liu, Y. Song, *Adv. Mater. Technol.* **2019**, *4*, 1800574.

[31] S. Chen, R. Li, X. Li, J. Xie, *Adv. Drug Deliv. Rev.* **2018**, *132*, 188.

[32] N. Panwar, A. M. Soehartono, K. K. Chan, S. Zeng, G. Xu, J. Qu, P. Coquet, K.-T. Yong, X. Chen, *Chem. Rev.* **2019**, *119*, 9559.

[33] K. Liao, P. Lei, M. Tu, S. Luo, T. Jiang, W. Jie, J. Hao, *ACS Appl. Mater. Interfaces* **2021**, *13*, 32606.

[34] B. Yalagala, S. Khandelwal, D. J, S. Badhulika, *Mater. Sci. Semicond. Process.* **2019**, *104*, 104673.

[35] B. Yalagala, P. Sahatiya, V. Mattela, S. Badhulika, *ACS Appl. Electron. Mater.* **2019**, *1*, 883.

[36] B. P. Yalagala, S. A. Sankaranarayanan, A. K. Rengan, S. R. K. Vanjari, *ACS Sustain. Chem. Eng.* **2022**, *10*, 4473.

[37] U. Pierre Claver, G. Zhao, *Adv. Eng. Mater.* **2021**, *23*, 2001187.

[38] M. Zhu, X. Du, S. Liu, J. Li, Z. Wang, T. Ono, *J. Mater. Chem. C* **2021**, *9*, 9083.

[39] S. A. Han, J. Lee, J. Lin, S.-W. Kim, J. H. Kim, *Nano Energy* **2019**, *57*, 680.

[40] R. Zhang, H. Olin, *EcoMat* **2020**, *2*, e12062.

[41] L. Sarkar, M. V Sushma, B. P. Yalagala, A. K. Rengan, S. G. Singh, S. R. K. Vanjari, *Nanotechnology* **2022**, *33*, 265403.

[42] Y. Huang, Y.-H. Pan, R. Yang, L.-H. Bao, L. Meng, H.-L. Luo, Y.-Q. Cai, G.-D. Liu, W.-J. Zhao, Z. Zhou, *Nat. Commun.* **2020**, *11*, 1.

[43] E. Gao, S.-Z. Lin, Z. Qin, M. J. Buehler, X.-Q. Feng, Z. Xu, *J. Mech. Phys. Solids* **2018**, *115*, 248.

[44] A. Ambrosi, M. Pumera, *Chem. Soc. Rev.* **2018**, *47*, 7213.

[45] Y. Yang, H. Hou, G. Zou, W. Shi, H. Shuai, J. Li, X. Ji, *Nanoscale* **2019**, *11*, 16.

[46] C. Huo, Z. Yan, X. Song, H. Zeng, *Sci. Bull.* **2015**, *60*, 1994.

[47] S. Witomska, T. Leydecker, A. Ciesielski, P. Samorì, *Adv. Funct. Mater.* **2019**, *29*, 1901126.

[48] W. Hao, C. Marichy, C. Journet, *2D Mater.* **2018**, *6*, 12001.

[49] J. Cai, X. Han, X. Wang, X. Meng, *Matter* **2020**, *2*, 587.

[50] Z. Cai, B. Liu, X. Zou, H.-M. Cheng, *Chem. Rev.* **2018**, *118*, 6091.

[51] V. M. Arellano Arreola, M. F. Salazar, T. Zhang, K. Wang, A. H. Barajas Aguilar, K. Chandra Sekhar Reddy, E. Strupiechonski, M. Terrones, A. de Luna Bugallo, *2D Mater.* **2021**, *8*, 025033.

[52] T. Zhang, L. Fu, *Chem* **2018**, *4*, 671.

[53] S. Bhowmik, A. Govind Rajan, *iScience* **2022**, *25*, 103832.

[54] H. Samassekou, A. Alkabsh, M. Wasala, M. Eaton, A. Walber, A. Walker, O. Pitkänen, K. Kordas, S. Talapatra, T. Jayasekera, *2D Mater.* **2017**, *4*, 21002.

[55] J. Tao, J. Chai, X. Lu, L. M. Wong, T. I. Wong, J. Pan, Q. Xiong, D. Chi, S. Wang, *Nanoscale* **2015**, *7*, 2497.

[56] Y. Koçak, Y. Akaltun, E. Gür, *J. Phys. Conf. Ser.* **2016**, *707*, 12028.

[57] P. T. P. T. Gomathi, P. Sahatiya, S. Badhulika, *Adv. Funct. Mater.* **2017**, *27*, DOI: 10.1002/adfm.201701611.

[58] R. Bhardwaj, V. Selamneni, U. N. Thakur, P. Sahatiya, A. Hazra, *New J. Chem.* **2020**, *44*, 16613.

[59] D. Tyagi, H. Wang, W. Huang, L. Hu, Y. Tang, Z. Guo, Z. Ouyang, H. Zhang, *Nanoscale* **2020**, *12*, 3535.

[60] M. Long, P. Wang, H. Fang, W. Hu, *Adv. Funct. Mater.* **2019**, *29*, 1.

[61] J. Jiang, Y. Wen, H. Wang, L. Yin, R. Cheng, C. Liu, L. Feng, J. He, *Adv. Electron. Mater.* **2021**, *7*, 2001125.

[62] K. Chee, *Advances in Photodetectors: Research and Applications*, IntechOpen, **2019**.

[63] X. Wang, Y. Cui, T. Li, M. Lei, J. Li, Z. Wei, *Adv. Opt. Mater.* **2019**, *7*, 1801274.

[64] J. Shim, D.-H. Kang, Y. Kim, H. Kum, W. Kong, S.-H. Bae, I. Almansouri, K. Lee, J.-H. Park, J. Kim, *Carbon N. Y.* **2018**, *133*, 78.

[65] R. Liu, F. Wang, L. Liu, X. He, J. Chen, Y. Li, T. Zhai, *Small Struct.* **2021**, *2*, 2000136.

[66] W. Li, T. Wang, X. Dai, X. Wang, C. Zhai, Y. Ma, S. Chang, *Solid State Commun.* **2016**, *225*, 32.

[67] Q. Zhang, H. Ying, X. Li, R. Xiang, Y. Zheng, H. Wang, J. Su, M. Xu, X. Zheng,

S. Maruyama, *ACS Appl. Mater. Interfaces* **2021**, *13*, 31861.

[68] Y. Wang, H. Wang, S. M. Gali, N. Turetta, Y. Yao, C. Wang, Y. Chen, D. Beljonne, P. Samorì, *Adv. Funct. Mater.* **2021**, *31*, 2103353.

[69] P. Chauhan, A. B. Patel, G. K. Solanki, K. D. Patel, V. M. Pathak, C. K. Sumesh, S. Narayan, P. K. Jha, *Appl. Surf. Sci.* **2021**, *536*, 147739.

[70] C. S. R. Kolli, V. Selamneni, B. A. Muñiz Martínez, A. Fest Carreno, D. Emanuel Sanchez, M. Terrones, E. Strupiechonski, A. De Luna Bugallo, P. Sahatiya, *ACS Appl. Mater. Interfaces* **2022**, *14*, 15415.

[71] J.-J. Tao, J. Jiang, S.-N. Zhao, Y. Zhang, X.-X. Li, X. Fang, P. Wang, W. Hu, Y. H. Lee, H.-L. Lu, D.-W. Zhang, *ACS Nano* **2021**, *15*, 3241.

[72] Y. Pak, W. Park, N. Alaal, Y. Kumaresan, S. A. Aravindh, S. Mitra, B. Xin, J.-W. Min, H. Kim, N. Lim, *ACS Appl. Electron. Mater.* **2020**, *2*, 838.

[73] D. Wu, J. Guo, C. Wang, X. Ren, Y. Chen, P. Lin, L. Zeng, Z. Shi, X. J. Li, C.-X. Shan, *ACS Nano* **2021**, *15*, 10119.

[74] Y. Zhang, Y. Ma, Y. Wang, X. Zhang, C. Zuo, L. Shen, L. Ding, *Adv. Mater.* **2021**, *33*, 2006691.

[75] B. Ezhilmaran, A. Patra, S. Benny, S. M. R., A. V. V., S. V. Bhat, C. S. Rout, *J. Mater. Chem. C* **2021**, *9*, 6122.

[76] J. C. Campbell, *J. Light. Technol.* **2016**, *34*, 278.

[77] S. Lei, F. Wen, L. Ge, S. Najmaei, A. George, Y. Gong, W. Gao, Z. Jin, B. Li, J. Lou, *Nano Lett.* **2015**, *15*, 3048.

[78] O. Lopez-Sanchez, D. Dumcenco, E. Charbon, A. Kis, *arXiv Prepr. arXiv1411.3232* **2014**, DOI: 10.48550/arXiv.1411.3232.

[79] D. Kufer, G. Konstantatos, *Nano Lett.* **2015**, *15*, 7307.

[80] A. Pospischil, T. Mueller, *Appl. Sci.* **2016**, *6*, 78.

[81] R. N. Zitter, *Phys. Rev.* **1958**, *112*, 852.

[82] J. Mannhart, D. G. Schlom, *Science (80-.).* **2010**, *327*, 1607.

[83] H. Kroemer, *Rev. Mod. Phys.* **2001**, *73*, 783.

[84] T.-H. Tsai, A. K. Sahoo, H.-K. Syu, Y.-C. Wu, M.-Y. Tsai, M.-D. Siao, Y.-C. Yang, Y.-F. Lin, R.-S. Liu, P.-W. Chiu, *ACS Appl. Electron. Mater.* **2021**, *3*, 4291.

[85] D.-S. Um, Y. Lee, S. Lim, S. Park, H. Lee, H. Ko, *ACS Appl. Mater. Interfaces* **2016**, *8*, 33955.

[86] S. Mukherjee, S. Jana, T. K. Sinha, S. Das, S. K. Ray, *Nanoscale Adv.* **2019**, *1*, 3279.

[87] T. Roy, M. Tosun, X. Cao, H. Fang, D.-H. Lien, P. Zhao, Y.-Z. Chen, Y.-L. Chueh, J. Guo, A. Javey, *ACS Nano* **2015**, *9*, 2071.

[88] X. Yan, C. Liu, C. Li, W. Bao, S. Ding, D. W. Zhang, P. Zhou, *Small* **2017**, *13*, 1701478.

[89] A. Nourbakhsh, A. Zubair, M. S. Dresselhaus, T. Palacios, *Nano Lett.* **2016**, *16*, 1359.

[90] J. Lee, N. T. Duong, S. Bang, C. Park, D. A. Nguyen, H. Jeon, J. Jang, H. M. Oh, M. S. Jeong, *Nano Lett.* **2020**, *20*, 2370.

[91] C. Lei, Y. Ma, X. Xu, T. Zhang, B. Huang, Y. Dai, *J. Phys. Chem. C* **2019**, *123*, 23089.

[92] W. Zhang, C.-P. Chuu, J.-K. Huang, C.-H. Chen, M.-L. Tsai, Y.-H. Chang, C.-T. Liang, Y.-Z. Chen, Y.-L. Chueh, J.-H. He, M.-Y. Chou, L.-J. Li, *Sci. Rep.* **2014**, *4*, 3826.

[93] D.-H. Kwak, P. Ramasamy, Y.-S. Lee, M.-H. Jeong, J.-S. Lee, *ACS Appl. Mater. Interfaces* **2019**, *11*, 29041.

[94] D. Kufer, G. Konstantatos, *Acs Photonics* **2016**, *3*, 2197.

[95] S. Kim, J. Maassen, J. Lee, S. M. Kim, G. Han, J. Kwon, S. Hong, J. Park, N. Liu, Y. C. Park, I. Omkaram, J.-S. Rhyee, Y. K. Hong, Y. Yoon, *Adv. Mater.* **2018**, *30*, 1705542.

[96] M. M. Furchi, D. K. Polyushkin, A. Pospischil, T. Mueller, *Nano Lett.* **2014**, *14*, 6165.

[97] V. Selamneni, P. Anand P, A. Singh, P. Sahatiya, *ACS Appl. Electron. Mater.* **2021**, *3*, 4105.

[98] Abid, P. Sehrawat, C. M. Julien, S. S. Islam, *ACS Appl. Mater. Interfaces* **2020**, *12*, 39730.

[99] V. Selamneni, S. Kanungo, P. Sahatiya, *Mater. Adv.* **2021**, *2*, 2373.

[100] K. Charipar, H. Kim, A. Piqué, N. Charipar, *Nanomater. 2020, Vol. 10, Page 1648* **2020**, *10*, 1648.

[101] Z. Kang, Y. Ma, X. Tan, M. Zhu, Z. Zheng, N. Liu, L. Li, Z. Zou, X. Jiang, T. Zhai, Y. Gao, *Adv. Electron. Mater.* **2017**, *3*, 1700165.

[102] H. Xu, A. Ren, J. Wu, Z. Wang, *Adv. Funct. Mater.* **2020**, *30*, 2000907.

[103] K. Montazeri, M. Currie, L. Verger, P. Dianat, M. W. Barsoum, B. Nabet, *Adv. Mater.* **2019**, *31*, 1903271.

[104] W. Ouyang, J. Chen, J.-H. He, X. Fang, *Adv. Electron. Mater.* **2020**, *6*, 2000168.

[105] H. Kim, H. N. Alshareef, *ACS Mater. Lett.* **2020**, *2*, 55.

[106] T. Dong, J. Simões, Z. Yang, *Adv. Mater. Interfaces* **2020**, *7*, 1901657.

[107] H. Qiao, Z. Huang, X. Ren, S. Liu, Y. Zhang, X. Qi, H. Zhang, *Adv. Opt. Mater.* **2020**, *8*, 1900765.

[108] T. Fan, Z. Xie, W. Huang, Z. Li, H. Zhang, *Nanotechnology* **2019**, *30*, 114002.

[109] Y. Zhang, P. Huang, J. Guo, R. Shi, W. Huang, Z. Shi, L. Wu, F. Zhang, L. Gao, C. Li, *Adv. Mater.* **2020**, *32*, 2001082.

[110] M. Chhowalla, H. S. Shin, G. Eda, L.-J. Li, K. P. Loh, H. Zhang, *Nat. Chem.* **2013**, *5*, 263.

[111] G. Eda, H. Yamaguchi, D. Voiry, T. Fujita, M. Chen, M. Chhowalla, *Nano Lett.* **2011**, *11*, 5111.

[112] M. Rahman, K. Davey, S.-Z. Qiao, *Adv. Funct. Mater.* **2017**, *27*, 1606129.

[113] Y. Xiong, H. Chen, D. W. Zhang, P. Zhou, *Phys. status solidi – Rapid Res. Lett.* **2019**, *13*, 1800658.

[114] X. Li, F. Cui, Q. Feng, G. Wang, X. Xu, J. Wu, N. Mao, X. Liang, Z. Zhang, J. Zhang, H. Xu, *Nanoscale* **2016**, *8*, 18956.

[115] S. Tongay, H. Sahin, C. Ko, A. Luce, W. Fan, K. Liu, J. Zhou, Y.-S. Huang, C.-H. Ho, J. Yan, D. F. Ogletree, S. Aloni, J. Ji, S. Li, J. Li, F. M. Peeters, J. Wu, *Nat. Commun.* **2014**, *5*, 3252.

[116] N. Gao, S. Zhou, N. Liu, Y. Bai, J. Zhao, *J. Mater. Chem. C* **2018**, *6*, 6764.

[117] F. Liu, S. Zheng, X. He, A. Chaturvedi, J. He, W. L. Chow, T. R. Mion, X. Wang, J. Zhou, Q. Fu, H. J. Fan, B. K. Tay, L. Song, R.-H. He, C. Kloc, P. M. Ajayan, Z. Liu, *Adv. Funct. Mater.* **2016**, *26*, 1169.

[118] J. Shim, A. Oh, D.-H. Kang, S. Oh, S. K. Jang, J. Jeon, M. H. Jeon, M. Kim, C. Choi, J. Lee, S. Lee, G. Y. Yeom, Y. J. Song, J.-H. Park, *Adv. Mater.* **2016**, *28*, 6985.

[119] K. Chaudhuri, M. Alhabeb, Z. Wang, V. M. Shalaev, Y. Gogotsi, A. Boltasseva, *ACS Photonics* **2018**, *5*, 1115.

[120] Z. Wang, H. Kim, H. N. Alshareef, *Adv. Mater.* **2018**, *30*, 1706656.

[121] J. Xu, J. Shim, J.-H. Park, S. Lee, *Adv. Funct. Mater.* **2016**, *26*, 5328.

[122] S. Lai, S. K. Jang, J. H. Cho, S. Lee, *Nanoscale* **2018**, *10*, 5191.

[123] M. Naguib, V. N. Mochalin, M. W. Barsoum, Y. Gogotsi, *Adv. Mater.* **2014**, *26*, 992.

[124] L. Gao, C. Ma, S. Wei, A. V Kuklin, H. Zhang, H. Ågren, *ACS Nano* **2021**, *15*, 954.

[125] M. Khazaei, A. Ranjbar, M. Arai, T. Sasaki, S. Yunoki, *J. Mater. Chem. C* **2017**, *5*, 2488.

[126] R. Ibragimova, P. Erhart, P. Rinke, H.-P. Komsa, *J. Phys. Chem. Lett.* **2021**, *12*, 2377.

[127] S. Chertopalov, V. N. Mochalin, *ACS Nano* **2018**, *12*, 6109.

[128] V. Adepu, N. Bokka, V. Mattela, P. Sahatiya, *New J. Chem.* **2021**, *45*, 5855.

[129] V. Adepu, V. Mattela, P. Sahatiya, *J. Mater. Chem. B* **2021**, *9*, 4523.

[130] Y. Von Lim, S. Huang, Q. Wu, Y. Zhang, D. Kong, Y. Wang, T. Xu, Y. Shi, Q. Ge, L. K. Ang, H. Y. Yang, *Nano Energy* **2019**, *61*, 626.

[131] Z. Yu, W. Feng, W. Lu, B. Li, H. Yao, K. Zeng, J. Ouyang, *J. Mater. Chem. A* **2019**, *7*, 11160.

[132] M. Benchakar, L. Loupias, C. Garnero, T. Bilyk, C. Morais, C. Canaff, N. Guignard, S. Morisset, H. Pazniak, S. Hurand, P. Chartier, J. Pacaud, V. Mauchamp, M. W. Barsoum, A. Habrioux, S. Célérier, *Appl. Surf. Sci.* **2020**, *530*, 147209.

[133] P. A. Rasheed, R. P. Pandey, K. Rasool, K. A. Mahmoud, *Sensors Actuators, B Chem.* **2018**, *265*, 652.

[134] V. Presser, M. Naguib, L. Chaput, A. Togo, G. Hug, M. W. Barsoum, *J. Raman Spectrosc.* **2012**, *43*, 168.

[135] M. Hu, Z. Li, T. Hu, S. Zhu, C. Zhang, X. Wang, *ACS Nano* **2016**, *10*, 11344.

[136] L. Wang, H. Zhang, B. Wang, C. Shen, C. Zhang, Q. Hu, A. Zhou, B. Liu, *Electron. Mater. Lett.* **2016**, *12*, 702.

[137] M. Alhabeb, K. Maleski, B. Anasori, P. Lelyukh, L. Clark, S. Sin, Y. Gogotsi, *Chem. Mater.* **2017**, *29*, 7633.

[138] L. Wang, J. Jie, Z. Shao, Q. Zhang, X. Zhang, Y. Wang, Z. Sun, S.-T. Lee, *Adv. Funct. Mater.* **2015**, *25*, 2910.

[139] H. Shang, H. Chen, M. Dai, Y. Hu, F. Gao, H. Yang, B. Xu, S. Zhang, B. Tan, X. Zhang, P. Hu, *Nanoscale Horiz.* **2020**, *5*, 564.

[140] M. K. Hudait, S. B. Krupanidhi, *Mater. Sci. Eng. B* **2001**, *87*, 141.

[141] S. A. Mirkhani, A. Shayesteh Zeraati, E. Aliabadian, M. Naguib, U. Sundararaj, *ACS Appl. Mater. Interfaces* **2019**, *11*, 18599.

[142] R. Bessler, U. Duerig, E. Koren, *Nanoscale Adv.* **2019**, *1*, 1702.

[143] J. Jiang, C. Ling, T. Xu, W. Wang, X. Niu, A. Zafar, Z. Yan, X. Wang, Y. You, L. Sun, *arXiv Prepr. arXiv1808.06093* **2018**.

[144] F. H. L. Koppens, T. Mueller, P. Avouris, A. C. Ferrari, M. S. Vitiello, M. Polini, *Nat. Nanotechnol.* **2014**, *9*, 780.

[145] Z. Chen, X. Li, J. Wang, L. Tao, M. Long, S.-J. Liang, L. K. Ang, C. Shu, H. K. Tsang, J.-B. Xu, *ACS Nano* **2017**, *11*, 430.

[146] H. Wang, P. Zhang, Z. Zang, *Appl. Phys. Lett.* **2020**, *116*, 162103.

[147] G. Luo, Z. Zhang, J. Jiang, Y. Liu, W. Li, J. Zhang, X. Hao, W. Wang, *RSC Adv.* **2021**, *11*, 7682.

[148] Y. Tang, H. Hao, Y. Kang, Q. Liu, Y. Sui, K. Wei, X. Cheng, T. Jiang, *ACS Appl. Mater. Interfaces* **2020**, *12*, 53475.

[149] A. Varghese, D. Saha, K. Thakar, V. Jindal, S. Ghosh, N. V Medhekar, S. Ghosh, S. Lodha, *Nano Lett.* **2020**, *20*, 1707.

[150] R. Wadhwa, A. V Agrawal, D. Kushavah, A. Mushtaq, S. K. Pal, M. Kumar, *Appl. Surf. Sci.* **2021**, *569*, 150949.

[151] J. Ahn, J.-H. Kyhm, H. K. Kang, N. Kwon, H.-K. Kim, S. Park, D. K. Hwang, *ACS Photonics* **2021**, *8*, 2650.

[152] Z. Wang, P. Zeng, S. Hu, X. Wu, J. He, Z. Wu, W. Wang, P. Zheng, H. Zheng, L. Zheng, D. Huo, Y. Zhang, *Nanotechnology* **2021**, *32*, 465201.

[153] J.-K. Qin, G. Qiu, W. He, J. Jian, M.-W. Si, Y.-Q. Duan, A. Charnas, D. Y. Zemlyanov, H.-Y. Wang, W.-Z. Shao, L. Zhen, C.-Y. Xu, P. D. Ye, *Adv. Funct. Mater.* **2018**, *28*, 1806254.

[154] B. Mukherjee, A. Zulkefli, R. Hayakawa, Y. Wakayama, S. Nakaharai, *ACS Photonics* **2019**, *6*, 2277.

[155] Y. Yang, W. Gao, *Chem. Soc. Rev.* **2019**, *48*, 1465.

[156] J. Lin, Z. Zhu, C. F. Cheung, F. Yan, G. Li, *J. Mater. Chem. C* **2020**, *8*, 10587.

[157] C. Xie, F. Yan, *Small* **2017**, *13*, 1.

[158] S. Huang, Y. Liu, Y. Zhao, Z. Ren, C. F. Guo, *Adv. Funct. Mater.* **2019**, *29*, 1805924.

[159] A. Nathan, A. Ahnood, M. T. Cole, S. Lee, Y. Suzuki, P. Hiralal, F. Bonaccorso, T. Hasan, L. Garcia-Gancedo, A. Dyadyusha, S. Haque, P. Andrew, S. Hofmann, J. Moultrie, D. Chu, A. J. Flewitt, A. C. Ferrari, M. J. Kelly, J. Robertson, G. A. J. Amaratunga, W. I. Milne, *Proc. IEEE* **2012**, *100*, 1486.

[160] S. Yip, L. Shen, J. C. Ho, *J. Semicond.* **2019**, *40*, 111602.

[161] V. Selamneni, S. K. Ganeshan, P. Sahatiya, *J. Mater. Chem. C* **2020**, *8*, 11593.

[162] P. Sahatiya, S. S. Jones, S. Badhulika, *Appl. Mater. Today* **2018**, *10*, 106.

[163] S. Kunwar, S. Pandit, J.-H. Jeong, J. Lee, *Nano-Micro Lett.* **2020**, *12*, 91.

[164] Y. Salamin, P. Ma, B. Baeuerle, A. Emboras, Y. Fedoryshyn, W. Heni, B. Cheng, A. Josten, J. Leuthold, *ACS Photonics* **2018**, *5*, 3291.

[165] S. Manzeli, D. Ovchinnikov, D. Pasquier, O. V Yazyev, A. Kis, **n.d.**, DOI: 10.1038/natrevmats.2017.33.

[166] S. Bertolazzi, J. Brivio, A. Kis, *ACS Nano* **2011**, *5*, 9703.

[167] S.-L. Li, K. Tsukagoshi, E. Orgiu, P. Samorì, *Chem. Soc. Rev.* **2016**, *45*, 118.

[168] F. Yu, M. Hu, F. Kang, R. Lv, *Prog. Nat. Sci. Mater. Int.* **2018**, *28*, 563.

[169] S. Catalán-Gómez, S. Garg, A. Redondo-Cubero, N. Gordillo, A. de Andrés, F. Nucciarelli, S. Kim, P. Kung, J. L. Pau, *Nanoscale Adv.* **2019**, *1*, 884.

[170] H. S. Nalwa, *RSC Adv.* **2020**, *10*, 30529.

[171] A. Sobhani, A. Lauchner, S. Najmaei, C. Ayala-Orozco, F. Wen, J. Lou, N. J. Halas, *Appl. Phys. Lett.* **2014**, *104*, 31112.

[172] H. Qiu, M. Wang, L. Li, J. Li, Z. Yang, M. Cao, *Sensors Actuators B Chem.* **2018**, *255*, 1407.

[173] B. Sun, Z. Wang, Z. Liu, X. Tan, X. Liu, T. Shi, J. Zhou, G. Liao, *Adv. Funct. Mater.* **2019**, *29*, 1900541.

[174] J. Wu, Y. Lu, Z. Wu, S. Li, Q. Zhang, Z. Chen, J. Jiang, S. Lin, L. Zhu, C. Li, Q. Liu, *Sensors Actuators B Chem.* **2018**, *261*, 279.

[175] R. Kumar, A. Sharma, M. Kaur, S. Husale, *Adv. Opt. Mater.* **2017**, *5*, 1700009.

[176] C. Langhammer, B. Kasemo, I. Zorić, *J. Chem. Phys.* **2007**, *126*, 194702.

[177] M. V. Dozzi, A. Candeo, G. Marra, C. D'Andrea, G. Valentini, E. Selli, *J. Phys. Chem. C* **2018**, *122*, 14326.

[178] C. Langhammer, Z. Yuan, I. Zorić, B. Kasemo, *Nano Lett.* **2006**, *6*, 833.

[179] V. Selamneni, P. Barya, N. Deshpande, P. Sahatiya, *IEEE Sens. J.* **2019**, *19*, 11255.

[180] X. Wang, Z. Zhang, Y. Chen, Y. Qu, Y. Lai, J. Li, *J. Alloys Compd.* **2014**, *600*, 84.

[181] X. Zhang, W. P. Han, J. B. Wu, S. Milana, Y. Lu, Q. Q. Li, A. C. Ferrari, P. H. Tan, *Phys. Rev. B* **2013**, *87*, 115413.

[182] K.-K. Liu, W. Zhang, Y.-H. Lee, Y.-C. Lin, M.-T. Chang, C.-Y. Su, C.-S. Chang, H. Li, Y. Shi, H. Zhang, C.-S. Lai, L.-J. Li, *Nano Lett.* **2012**, *12*, 1538.

[183] X. Liang, Z. Wang, C. Liu, *Nanoscale Res. Lett.* **2009**, *5*, 124.

[184] L. K. Preethi, R. P. Antony, T. Mathews, S. Dash, A. K. Tyagi, *J. Nanosci. Nanotechnol.* **2016**, *16*, 10087.

[185] R. Wojcieszak, M. J. Genet, P. Eloy, P. Ruiz, E. M. Gaigneaux, *J. Phys. Chem. C* **2010**, *114*, 16677.

[186] S. Eustis, M. A. El-Sayed, *Chem. Soc. Rev.* **2006**, *35*, 209.

[187] J. R. Nasr, N. Simonson, A. Oberoi, M. W. Horn, J. A. Robinson, S. Das, *ACS Nano* **2020**, *14*, 15440.

[188] H. Tang, C.-J. Chen, Z. Huang, J. Bright, G. Meng, R.-S. Liu, N. Wu, *J. Chem. Phys.* **2020**, *152*, 220901.

[189] A. R. Shafiqa, A. Abdul Aziz, B. Mehrdel, *J. Phys. Conf. Ser.* **2018**, *1083*, 12040.

[190] M. J. Park, K. Park, H. Ko, *Appl. Surf. Sci.* **2018**, *448*, 64.

[191] B. Rahmati, I. Hajzadeh, M. Taheri, R. Karimzadeh, S. Mohajerzadeh, S. M. Mohseni, *Appl. Surf. Sci.* **2019**, *490*, 165.

[192] M. I. Stockman, *Phys. Today* **2011**, *64*, 39.

[193] A. Rajan, G. Kaur, A. Paliwal, H. K. Yadav, V. Gupta, M. Tomar, *J. Phys. D. Appl. Phys.* **2014**, *47*, 425102.

[194] Z. Guo, D. Jiang, M. Zhao, F. Guo, J. Pei, R. Liu, L. Sun, N. Hu, G. Zhang, *Solid. State. Electron.* **2016**, *124*, 24.

[195] C. L. Hsu, Y. C. Wang, S. P. Chang, S. J. Chang, *ACS Appl. Nano Mater.* **2019**, *2*, 6343.

[196] Y. Li, J. G. Distefano, A. A. Murthy, J. D. Cain, E. D. Hanson, Q. Li, F. C. Castro, X. Chen, V. P. Dravid, *ACS Nano* **2017**, *11*, 10321.

[197] J. Guo, S. Li, Z. He, Y. Li, Z. Lei, Y. Liu, W. Huang, T. Gong, Q. Ai, L. Mao, Y. He, Y. Ke, S. Zhou, B. Yu, *Appl. Surf. Sci.* **2019**, *483*, 1037.

[198] X. Liu, F. Li, M. Xu, J. Qi, *RSC Adv.* **2018**, *8*, 28041.

[199] L. Z. Hao, W. Gao, Y. J. Liu, Y. M. Liu, Z. D. Han, Q. Z. Xue, J. Zhu, *Phys. Chem. Chem. Phys.* **2016**, *18*, 1131.

[200] W. Heng, S. Solomon, W. Gao, *Adv. Mater.* **2021**, *n/a*, 2107902.

[201] Y. Li, J. G. DiStefano, A. A. Murthy, J. D. Cain, E. D. Hanson, Q. Li, F. C. Castro, X. Chen, V. P. Dravid, *ACS Nano* **2017**, *11*, 10321.

[202] M. Shrivastava, V. Ramgopal Rao, *Nano Lett.* **2021**, *21*, 6359.

[203] T. Vincent, J. Liang, S. Singh, E. G. Castanon, X. Zhang, A. McCreary, D. Jariwala, O. Kazakova, Z. Y. Al Balushi, *Appl. Phys. Rev.* **2021**, *8*, 41320.

[204] V. Selamneni, S. Sukruth, P. Sahatiya, *FlatChem* **2022**, 100379.

[205] B. Kang, Y. Kim, W. J. Yoo, C. Lee, *Small* **2018**, *14*, 1.

[206] X. Jing, C. Lin, D. Ya-Wei, C. Qian, S. Qing-Qing, D. Shi-Jin, Z. Hao, Z. D. Wei, *Sci. Adv.* **2022**, *3*, e1602246.

[207] J. Li, C. Nie, F. Sun, L. Tang, Z. Zhang, J. Zhang, Y. Zhao, J. Shen, S. Feng, H. Shi, *ACS Appl. Mater. Interfaces* **2020**, *12*, 8429.

[208] S. Li, X. Chen, F. Liu, Y. Chen, B. Liu, W. Deng, B. An, F. Chu, G. Zhang, S. Li, X. Li, Y. Zhang, *ACS Appl. Mater. Interfaces* **2019**, *11*, 11636.

[209] F. Sun, C. Nie, J. Fu, W. Xiong, Y. Zhi, X. Wei, *ACS Appl. Mater. Interfaces* **2022**, *14*, 26245.

[210] E. Liu, M. Long, J. Zeng, W. Luo, Y. Wang, Y. Pan, W. Zhou, B. Wang, W. Hu, Z. Ni, Y. You, X. Zhang, S. Qin, Y. Shi, K. Watanabe, T. Taniguchi, H. Yuan, H. Y. Hwang, Y. Cui, F. Miao, D. Xing, *Adv. Funct. Mater.* **2016**, *26*, 1938.

[211] E. Zhang, Y. Jin, X. Yuan, W. Wang, C. Zhang, L. Tang, S. Liu, P. Zhou, W. Hu, F. Xiu, *Adv. Funct. Mater.* **2015**, *25*, 4076.

[212] P. Sahatiya, C. S. K. Reddy, S. Badhulika, *J. Mater. Chem. C* **2017**, *5*, 12728.

[213] J. Zhou, M. Xie, H. Ji, A. Cui, Y. Ye, K. Jiang, L. Shang, J. Zhang, Z. Hu, J. Chu, *ACS Appl. Mater. Interfaces* **2020**, *12*, 18674.

[214] A. Thakran, A. Nain, M. Kataria, C. R. Paul Inbaraj, H.-Y. Lin, H.-I. Lin, Y.-M. Liao, C.-F. Hou, C.-C. Wang, H.-T. Chang, *ACS Photonics* **2021**, *8*, 2955.

[215] J.-A. A. J.-A. Huang, L.-B. B. L.-B. Luo, *Adv. Opt. Mater.* **2018**, *6*, 1701282.

[216] H. Chen, L. Su, M. Jiang, X. Fang, *Adv. Funct. Mater.* **2017**, *27*, 1704181.

[217] K. Thakar, B. Mukherjee, S. Grover, N. Kaushik, M. Deshmukh, S. Lodha, *ACS Appl. Mater. Interfaces* **2018**, *10*, 36512.

[218] V. Selamneni, V. Adepu, H. Raghavan, P. Sahatiya, *FlatChem* **2022**, *33*, 100363.

[219] M. Hafeez, L. Gan, H. Li, Y. Ma, T. Zhai, *Adv. Funct. Mater.* **2016**, *26*, 4551.

[220] Q. Zhang, S. Tan, R. G. Mendes, Z. Sun, Y. Chen, X. Kong, Y. Xue, M. H. Rümmeli, X. Wu, S. Chen, L. Fu, *Adv. Mater.* **2016**, *28*, 2616.

[221] J.-P. Sylvestre, S. Poulin, A. V Kabashin, E. Sacher, M. Meunier, J. H. T. Luong, *J. Phys. Chem. B* **2004**, *108*, 16864.

[222] Z. Miao, L. Chen, R. Wang, R. Yuan, F. Zhou, P. Lv, X. Zhang, Q. Wang, *Mater. Res. Express* **2018**, *5*, 25505.

[223] F. Qi, Y. Chen, B. Zheng, J. He, Q. Li, X. Wang, B. Yu, J. Lin, J. Zhou, P. Li, *J. Mater. Sci.* **2017**, *52*, 3622.

[224] N. T. Khoa, S. W. Kim, D.-H. Yoo, E. J. Kim, S. H. Hahn, *Appl. Catal. A Gen.* **2014**, *469*, 159.

[225] L.-L. Nguyen, Q.-H. Le, V.-N. Pham, M. Bastide, S. Gam-Derouich, V.-Q. Nguyen, J.-C. Lacroix, *Nanomater.* **2021**, *11*, DOI: 10.3390/nano11081957.

[226] S. Manzhos, G. Giorgi, J. Lüder, M. Ihara, *Adv. Phys. X* **2021**, *6*, 1908848.

[227] S. Pillai, K. R. Catchpole, T. Trupke, M. A. Green, *J. Appl. Phys.* **2007**, *101*, 93105.

[228] R. Maiti, T. K. Sinha, S. Mukherjee, B. Adhikari, S. K. Ray, *Plasmonics* **2016**, *11*, 1297.

[229] C.-L. Hsu, Y.-C. Wang, S.-P. Chang, S.-J. Chang, *ACS Appl. Nano Mater.* **2019**, *2*, 6343.

[230] S. Mukherjee, R. K. Chowdhury, D. Karmakar, M. Wan, C. Jacob, S. Das, S. K. Ray, *J. Phys. Chem. C* **2021**, *125*, 11023.

[231] C. Pan, J. Zhai, Z. L. Wang, *Chem. Rev.* **2019**, *119*, 9303.

[232] P. Lin, C. Pan, Z. L. Wang, *Mater. Today Nano* **2018**, *4*, 17.

[233] X. Han, M. Chen, C. Pan, Z. L. Wang, *J. Mater. Chem. C* **2016**, *4*, 11341.

[234] D. Xiong, W. Deng, G. Tian, Y. Gao, X. Chu, C. Yan, L. Jin, Y. Su, W. Yan, W. Yang, *Nanoscale* **2019**, *11*, 3021.

[235] P. Lin, L. Zhu, D. Li, L. Xu, C. Pan, Z. Wang, *Adv. Funct. Mater.* **2018**, *28*, 1802849.

[236] F. Wang, P. Luo, Y. Zhang, Y. Huang, Q. Zhang, Y. Li, T. Zhai, *Sci. China Mater.* **2020**, *63*, 1537.

[237] L. Liu, T. Zhai, *InfoMat* **2021**, *3*, 3.

[238] F. Xue, L. Yang, M. Chen, J. Chen, X. Yang, L. Wang, L. Chen, C. Pan, Z. L. Wang, *NPG Asia Mater.* **2017**, *9*, e418.

[239] S. C. Rai, K. Wang, Y. Ding, J. K. Marmon, M. Bhatt, Y. Zhang, W. Zhou, Z. L. Wang, *ACS Nano* **2015**, *9*, 6419.

[240] K. Zhang, M. Peng, W. Wu, J. Guo, G. Gao, Y. Liu, J. Kou, R. Wen, Y. Lei, A. Yu, Y. Zhang, J. Zhai, Z. L. Wang, *Mater. Horizons* **2017**, *4*, 274.

[241] Q. Liao, M. Liang, Z. Zhang, G. Zhang, Y. Zhang, *Nano Res.* **2015**, *8*, 3772.

[242] B. Yalagala, P. Sahatiya, V. Mattela, S. Badhulika, *ACS Appl. Electron. Mater.* **2019**, *1*, 883.

[243] P. Sahatiya, S. Badhulika, *J. Mater. Chem. C* **2017**, *5*, 11436.

[244] W. Wu, L. Wang, Y. Li, F. Zhang, L. Lin, S. Niu, D. Chenet, X. Zhang, Y. Hao, T. F. Heinz, J. Hone, Z. L. Wang, *Nature* **2014**, *514*, 470.

[245] H. Zhu, Y. Wang, J. Xiao, M. Liu, S. Xiong, Z. J. Wong, Z. Ye, Y. Ye, X. Yin, X. Zhang, *Nat. Nanotechnol.* **2015**, *10*, 151.

[246] L. Tang, B. Zhang, T. Peng, Z. He, C. Yan, J. Mao, K. Dai, X. Wu, J. Zheng, *Nano Energy* **2021**, *90*, 106568.

[247] K. Si, J. Ma, C. Lu, Y. Zhou, C. He, D. Yang, X. Wang, X. Xu, *Appl. Surf. Sci.* **2020**, *507*, 145082.

[248] H. Wu, X. Lu, G. Wang, K. Peng, H. Chi, B. Zhang, Y. Chen, C. Li, Y. Yan, L. Guo, C. Uher, X. Zhou, X. Han, *Adv. Energy Mater.* **2018**, *8*, 1800087.

[249] W. Yu, F. Shu, Y. Huang, F. Yang, Q. Meng, Z. Zou, J. Wang, Z. Zeng, G. Zou, S. Deng, *J. Mater. Chem. A* **2020**, *8*, 20677.

[250] G. Liu, Y. Li, B. Li, H. Tian, C. Fan, Y. Zhang, Z. Hua, M. Wang, H. Zheng, E. Li, *J. Mater. Chem. C* **2018**, *6*, 10036.

[251] I. M. D. L. Santos, H. J. Cortina-Marrero, L. Hechavarri\'\ia-Difur, F. J. Sánchez-Rodr\'\iguez, C. A. Meza-Avendaño, J. A. Borrego-Pérez, V. I. Moreno-Oliva, E. Román-Hernández, M. Courel, **2020**, *35*, 115010.

[252] H.-S. Yun, B. Park, Y. C. Choi, J. Im, T. J. Shin, S. Il Seok, *Adv. Energy Mater.* **2019**, *9*, 1901343.

[253] H. Khan, N. Mahmood, A. Zavabeti, A. Elbourne, M. A. Rahman, B. Y. Zhang, V. Krishnamurthi, P. Atkin, M. B. Ghasemian, J. Yang, G. Zheng, A. R. Ravindran, S. Walia, L. Wang, S. P. Russo, T. Daeneke, Y. Li, K. Kalantar-Zadeh, *Nat. Commun.* **2020**, *11*, 3449.

[254] V. A. Cao, M. Kim, W. Hu, S. Lee, S. Youn, J. Chang, H. S. Chang, J. Nah, *ACS Nano* **2021**, *15*, 10428.

[255] M. N. Blonsky, H. L. Zhuang, A. K. Singh, R. G. Hennig, *ACS Nano* **2015**, *9*, 9885.

[256] J. Xia, X.-Z. Li, X. Huang, N. Mao, D.-D. Zhu, L. Wang, H. Xu, X.-M. Meng, *Nanoscale* **2016**, *8*, 2063.

[257] M. Devika, N. Koteeswara Reddy, K. Ramesh, H. R. Sumana, K. R. Gunasekhar, E. S. R. Gopal, K. T. Ramakrishna Reddy, *Semicond. Sci. Technol.* **2006**, *21*, 1495.

[258] A. Artemenko, A. Choukourov, D. Slavinska, H. Biederman, *WDS Proc. Contr. Pap* **2009**, *3*, 175.

[259] J. Wang, Y. Lu, N. Zhang, X. Xiang, J. Liang, J. Chen, *RSC Adv.* **2016**, *6*, 95805.

[260] T. S. Reddy, M. C. S. Kumar, *RSC Adv.* **2016**, *6*, 95680.

[261] J. Xia, X. Z. Li, X. Huang, N. Mao, D. D. Zhu, L. Wang, H. Xu, X. M. Meng, *Nanoscale* **2016**, *8*, 2063.

[262] J. R. Brent, D. J. Lewis, T. Lorenz, E. A. Lewis, N. Savjani, S. J. Haigh, G. Seifert, B. Derby, P. O. Brien, **n.d.**, 3.

[263] J. Xie, H. Zhang, S. Li, R. Wang, X. Sun, M. Zhou, J. Zhou, X. W. (David) Lou, Y. Xie, *Adv. Mater.* **2013**, *25*, 5807.

[264] J. Xie, J. Zhang, S. Li, F. Grote, X. Zhang, H. Zhang, R. Wang, Y. Lei, B. Pan, Y. Xie, *J. Am. Chem. Soc.* **2013**, *135*, 17881.

[265] S. Palanisamy, P. Periasamy, K. Subramani, A. P. Shyma, R. Venkatachalam, *J. Alloys Compd.* **2018**, *731*, 936.

[266] T. Leelasree, V. Selamneni, T. Akshaya, P. Sahatiya, H. Aggarwal, *J. Mater. Chem. B* **2020**, *8*, DOI: 10.1039/D0TB01748E.

[267] L. Zhang, L. Sun, S. Liu, Y. Huang, K. Xu, F. Ma, *RSC Adv.* **2016**, *6*, 60318.

[268] R. M. Clark, B. J. Carey, T. Daeneke, P. Atkin, M. Bhaskaran, K. Latham, I. S. Cole, K. Kalantar-zadeh, *Nanoscale* **2015**, *7*, 16763.

[269] A. Midya, A. Ghorai, S. Mukherjee, R. Maiti, S. K. Ray, *J. Mater. Chem. A* **2016**, *4*, 4534.

[270] M. Diao, H. Li, R. Hou, Y. Liang, J. Wang, Z. Luo, Z. Huang, C. Zhang, *ACS Appl. Mater. Interfaces* **2020**, *12*, 7423.

[271] V. Selamneni, N. Nerurkar, P. Sahatiya, *IEEE Sensors Lett.* **2020**, *4*, 1.

[272] B. P. Yalagala, P. Sahatiya, C. sekhar R. Kolli, S. Khandelwal, V. Mattela, S. Badhulika, *ACS Appl. Nano Mater.* **2019**, *2*, 937.

[273] J. Du, Q. Liao, M. Hong, B. Liu, X. Zhang, H. Yu, J. Xiao, L. Gao, F. Gao, Z. Kang, Z. Zhang, Y. Zhang, *Nano Energy* **2019**, *58*, 85.

[274] Y. Dai, X. Wang, W. Peng, H. Zou, R. Yu, Y. Ding, C. Wu, Z. L. Wang, *ACS Nano* **2017**, *11*, 7118.

[275] X. Zhang, J. Zhang, B. Leng, J. Li, Z. Ma, W. Yang, F. Liu, B. Liu, *Adv. Mater. Interfaces* **2019**, *6*, 1970145.

[276] Z. Wang, R. Yu, X. Wen, Y. Liu, C. Pan, W. Wu, Z. L. Wang, *ACS Nano* **2014**, *8*, 12866.

[277] L. Tang, S. E. Kocabas, S. Latif, A. K. Okyay, D.-S. Ly-Gagnon, K. C. Saraswat, D. A. B. Miller, *Nat. Photonics* **2008**, *2*, 226.

[278] J. Wu, Z. Li, D. Shao, M. O. Manasreh, V. P. Kunets, Z. M. Wang, G. J. Salamo, B. D. Weaver, *Appl. Phys. Lett.* **2009**, *94*, 171102.

[279] E. O. Polat, G. Mercier, I. Nikitskiy, E. Puma, T. Galan, S. Gupta, M. Montagut, J. J. Piqueras, M. Bouwens, T. Durduran, G. Konstantatos, S. Goossens, F. Koppens, *Sci. Adv.* **2023**, *5*, eaaw7846.

[280] L. H. Zeng, Q. M. Chen, Z. X. Zhang, D. Wu, H. Yuan, Y. Y. Li, W. Qarony, S. P. Lau, L. B. Luo, Y. H. Tsang, *Adv. Sci.* **2019**, *6*, DOI: 10.1002/advs.201901134.

[281] D. Wu, Z. Lou, Y. Wang, Z. Yao, T. Xu, Z. Shi, J. Xu, Y. Tian, X. Li, Y. H. Tsang, *Sol. Energy Mater. Sol. Cells* **2018**, *182*, 272.

[282] D. Wu, C. Jia, F. Shi, L. Zeng, P. Lin, L. Dong, Z. Shi, Y. Tian, X. Li, J. Jie, *J. Mater. Chem. A* **2020**, *8*, 3632.

[283] C. Jia, D. Wu, E. Wu, J. Guo, Z. Zhao, Z. Shi, T. Xu, X. Huang, Y. Tian, X. Li, *J. Mater. Chem. C* **2019**, *7*, 3817.

[284] Z. Lou, L. Zeng, Y. Wang, D. Wu, T. Xu, Z. Shi, Y. Tian, X. Li, Y. H. Tsang, *Opt. Lett.* **2017**, *42*, 3335.

[285] H. Huang, C. Du, H. Shi, X. Feng, J. Li, Y. Tan, W. Song, *Part. Part. Syst. Charact.* **2015**, *32*, 72.

[286] A. Mushtaq, S. Ghosh, A. S. Sarkar, S. K. Pal, *ACS Energy Lett.* **2017**, *2*, 1879.

[287] N. S. Arul, V. D. Nithya, *RSC Adv.* **2016**, *6*, 65670.

[288] Y. Zhong, F. Xue, P. Wei, R. Li, C. Cao, T. Yi, *Nanoscale* **2018**, *10*, 21298.

[289] Q. Wang, J. Huang, H. Sun, Y. H. Ng, K. Q. Zhang, Y. Lai, *ChemSusChem* **2018**, *11*, 1708.

[290] L. Najafi, B. Taheri, B. Martín-García, S. Bellani, D. Di Girolamo, A. Agresti, R.

Oropesa-Nuñez, S. Pescetelli, L. Vesce, E. Calabrò, M. Prato, A. E. Del Rio Castillo, A. Di Carlo, F. Bonaccorso, *ACS Nano* **2018**, *12*, 10736.

[291] W. Yin, X. Bai, X. Zhang, J. Zhang, X. Gao, W. W. Yu, *Part. Part. Syst. Charact.* **2019**, *36*, 1800362.

[292] S. S. Sarkar, S. Mukherjee, R. K. Khatri, S. K. Ray, *Nanotechnology* **2020**, *31*, 135203.

[293] Y. Huang, X. Zhan, K. Xu, L. Yin, Z. Cheng, C. Jiang, Z. Wang, J. He, *Appl. Phys. Lett.* **2016**, *108*, 13101.

[294] D. Kufer, I. Nikitskiy, T. Lasanta, G. Navickaite, F. H. L. Koppens, G. Konstantatos, *Adv. Mater.* **2015**, *27*, 176.

[295] Z. Zheng, L. Gan, J. Zhang, F. Zhuge, T. Zhai, *Adv. Sci.* **2017**, *4*, 1600316.

[296] C. Hu, D. Dong, X. Yang, K. Qiao, D. Yang, H. Deng, S. Yuan, J. Khan, Y. Lan, H. Song, J. Tang, *Adv. Funct. Mater.* **2017**, *27*, 1603605.

[297] F. Prins, A. J. Goodman, W. A. Tisdale, *Nano Lett.* **2014**, *14*, 6087.

[298] K. Chen, Y. Wang, J. Liu, J. Kang, Y. Ge, W. Huang, Z. Lin, Z. Guo, Y. Zhang, H. Zhang, *Nanoscale* **2019**, *11*, 16852.

[299] Y. Pak, S. Mitra, N. Alaal, B. Xin, S. Lopatin, D. Almalawi, J.-W. Min, H. Kim, W. Kim, G.-Y. Jung, *Appl. Phys. Lett.* **2020**, *116*, 112102.

[300] H. Wu, Z. Kang, Z. Zhang, Z. Zhang, H. Si, Q. Liao, S. Zhang, J. Wu, X. Zhang, Y. Zhang, *Adv. Funct. Mater.* **2018**, *28*, 1802015.

[301] J. Han, J. Li, W. Liu, H. Li, X. Fan, K. Huang, *Opt. Commun.* **2020**, *473*, 125931.

[302] C. Jia, D. Wu, E. Wu, J. Guo, Z. Zhao, Z. Shi, T. Xu, X. Huang, Y. Tian, X. Li, *J. Mater. Chem. C* **2019**, *7*, 3817.

[303] W. Gu, Y. Yan, C. Zhang, C. Ding, Y. Xian, *ACS Appl. Mater. Interfaces* **2016**, *8*, 11272.

[304] X. Wang, Q. Wu, K. Jiang, C. Wang, C. Zhang, *Sensors Actuators, B Chem.* **2017**, *252*, 183.

[305] L. Wang, J. Jie, Z. Shao, Q. Zhang, X. Zhang, Y. Wang, Z. Sun, S. T. Lee, *Adv. Funct. Mater.* **2015**, *25*, 2910.

[306] Y. Wang, X. Huang, D. Wu, R. Zhuo, E. Wu, C. Jia, Z. Shi, T. Xu, Y. Tian, X. Li, *J. Mater. Chem. C* **2018**, *6*, 4861.

[307] P. Xiao, J. Mao, K. Ding, W. Luo, W. Hu, X. Zhang, X. Zhang, J. Jie, *Adv. Mater.* **2018**, *30*, 1801729.

[308] W. Choi, M. Y. Cho, A. Konar, J. H. Lee, G. B. Cha, S. C. Hong, S. Kim, J. Kim, D. Jena, J. Joo, S. Kim, *Adv. Mater.* **2012**, *24*, 5832.

[309] Z. Yin, H. Li, H. Li, L. Jiang, Y. Shi, Y. Sun, G. Lu, Q. Zhang, X. Chen, H. Zhang,

ACS Nano **2012**, *6*, 74.

[310] O. Lopez-Sanchez, D. Lembke, M. Kayci, A. Radenovic, A. Kis, *Nat. Nanotechnol.* **2013**, *8*, 497.

[311] F. Xia, T. Mueller, Y. Lin, A. Valdes-Garcia, P. Avouris, *Nat. Nanotechnol.* **2009**, *4*, 839.

[312] W. Zhang, J.-K. Huang, C.-H. Chen, Y.-H. Chang, Y.-J. Cheng, L.-J. Li, *Adv. Mater.* **2013**, *25*, 3456.

[313] M. Buscema, D. J. Groenendijk, S. I. Blanter, G. A. Steele, H. S. J. Van Der Zant, A. Castellanos-Gomez, *Nano Lett.* **2014**, *14*, 3347.

[314] P. Sahatiya, S. S. Jones, P. T. Gomathi, S. Badhulika, *2D Mater.* **2017**, *4*, aa6534.

[315] Y. H. Zhou, H. N. An, C. Gao, Z. Q. Zheng, B. Wang, *Mater. Lett.* **2019**, *237*, 298.

[316] Y. Tao, X. Wu, W. Wang, J. Wang, *J. Mater. Chem. C* **2015**, *3*, 1347.

[317] L. Su, Y. Zhu, D. Yong, M. Chen, X. Ji, Y. Su, X. Gui, B. Pan, R. Xiang, Z. Tang, *ACS Appl. Mater. Interfaces* **2014**, *6*, 14152.

[318] B. Wang, Y. Zhou, Z. Huang, H. Qiao, C. Duan, X. Ren, Z. Wang, J. Zhong, X. Qi, *Mater. Today Nano* **2021**, *14*, 100109.

[319] H. Qiao, Z. Li, Z. Huang, X. Ren, J. Kang, M. Qiu, Y. Liu, X. Qi, J. Zhong, H. Zhang, *Appl. Mater. Today* **2020**, *20*, 100765.

[320] X. Ren, B. Wang, Z. Huang, H. Qiao, C. Duan, Y. Zhou, J. Zhong, Z. Wang, X. Qi, *FlatChem* **2021**, *25*, 100215.

[321] P. Sahatiya, C. S. Reddy K, S. Badhulika, *J. Mater. Chem. C* **2017**, *5*, 12728.

[322] W. Zheng, T. Xie, Y. Zhou, Y. L. Chen, W. Jiang, S. Zhao, J. Wu, Y. Jing, Y. Wu, G. Chen, Y. Guo, J. Yin, S. Huang, H. Q. Xu, Z. Liu, H. Peng, *Nat. Commun.* **2015**, *6*, 6972.

[323] Y. Dang, G. Tong, W. Song, Z. Liu, L. Qiu, L. K. Ono, Y. Qi, *J. Mater. Chem. C* **2020**, *8*, 276.

[324] Q. Wang, C. Zhou, Y. Chai, *Nanoscale* **2020**, *12*, 8109.

[325] V. Q. Dang, T. Q. Trung, D.-I. Kim, L. T. Duy, B.-U. Hwang, D.-W. Lee, B.-Y. Kim, L. D. Toan, N.-E. Lee, *Small* **2015**, *11*, 3054.

[326] N. D. Akhavan, G. A. Umana-Membreno, R. Gu, J. Antoszewski, L. Faraone, *IEEE Trans. Electron Devices* **2018**, *65*, 4340.

[327] H. Wang, D. H. Kim, *Chem. Soc. Rev.* **2017**, *46*, 5204.

[328] Q. Yang, Q. Wu, W. Luo, W. Yao, S. Yan, J. Shen, *Mater. Res. Express* **2019**, *6*, 116208.

[329] C.-Z. Ning, L. Dou, P. Yang, *Nat. Rev. Mater.* **2017**, *2*, 17070.

[330] R. Mas-Ballesté, C. Gómez-Navarro, J. Gómez-Herrero, F. Zamora, *Nanoscale* **2011**, *3*, 20.

[331] Y. Chang, J. Wang, F. Wu, W. Tian, W. Zhai, *Adv. Funct. Mater.* **2020**, *30*, 2001450.

[332] Z. Zhang, J. Yang, K. Zhang, S. Chen, F. Mei, G. Shen, *J. Mater. Chem. C* **2017**, *5*, 11288.

[333] M. S. Mahdi, K. Ibrahim, A. Hmood, N. M. Ahmed, S. A. Azzez, F. I. Mustafa, *RSC Adv.* **2016**, *6*, 114980.

[334] V. Krishnamurthi, H. Khan, T. Ahmed, A. Zavabeti, S. A. Tawfik, S. K. Jain, M. J. S. Spencer, S. Balendhran, K. B. Crozier, Z. Li, L. Fu, M. Mohiuddin, M. X. Low, B. Shabbir, A. Boes, A. Mitchell, C. F. McConville, Y. Li, K. Kalantar-Zadeh, N. Mahmood, S. Walia, *Adv. Mater.* **2020**, *32*, 2004247.

[335] H. S. Lee, J. Y. Cho, R. Nandi, P. S. Pawar, K. E. Neerugatti, C. T. K. Mai, D.-K. Lee, J. Heo, *ACS Appl. Energy Mater.* **2020**, *3*, 10393.

[336] V. Selamneni, A. Kunchur, P. Sahatiya, *IEEE Sens. J.* **2021**, *21*, 5143.

[337] Z. Deng, D. Cao, J. He, S. Lin, S. M. Lindsay, Y. Liu, *ACS Nano* **2012**, *6*, 6197.

[338] F. Lu, J. Yang, R. Li, N. Huo, Y. Li, Z. Wei, J. Li, *J. Mater. Chem. C* **2015**, *3*, 1397.

[339] T. Rath, L. Gury, I. Sánchez-Molina, L. Martínez, S. A. Haque, *Chem. Commun.* **2015**, *51*, 10198.

[340] Y. H. Zhou, Z. Bin Zhang, P. Xu, H. Zhang, B. Wang, *Nanoscale Res. Lett.* **2019**, *14*, 364.

[341] V. K. Singh, S. M. Yadav, H. Mishra, R. Kumar, R. S. Tiwari, A. Pandey, A. Srivastava, *ACS Appl. Nano Mater.* **2019**, *2*, 3934.

[342] D.-R. Hang, D.-Y. Sun, C.-H. Chen, H.-F. Wu, M. M. C. Chou, S. E. Islam, K. H. Sharma, *Nanoscale Res. Lett.* **2019**, *14*, 271.

[343] T.-H. Tsai, Z.-Y. Liang, Y.-C. Lin, C.-C. Wang, K.-I. Lin, K. Suenaga, P.-W. Chiu, *ACS Nano* **2020**, *14*, 4559.

[344] M. Devika, N. K. Reddy, K. Ramesh, H. R. Sumana, K. R. Gunasekhar, E. S. R. Gopal, K. T. R. Reddy, *Semicond. Sci. Technol.* **2006**, *21*, 1495.

[345] V. Selamneni, H. Raghavan, A. Hazra, P. Sahatiya, *Adv. Mater. Interfaces* **2021**, 2001988.

[346] K.-S. Park, Y.-J. Choi, J.-G. Kang, Y.-M. Sung, J.-G. Park, *Nanotechnology* **2011**, *22*, 285712.

[347] J. Wang, Y. Lu, N. Zhang, X. Xiang, J. Liang, J. Chen, *RSC Adv.* **2016**, *6*, 95805.

[348] J. R. Brent, D. J. Lewis, T. Lorenz, E. A. Lewis, N. Savjani, S. J. Haigh, G. Seifert, B. Derby, P. O'Brien, *J. Am. Chem. Soc.* **2015**, *137*, 12689.

[349] Y. Yan, C. Zhang, W. Gu, C. Ding, X. Li, Y. Xian, *J. Phys. Chem. C* **2016**, *120*, 12170.

[350] R. Das, A. Bora, P. K. Giri, *J. Mater. Chem. C* **2020**, *8*, 7935.

[351] W. Yin, X. Zhang, X. Bai, D. Xue, X. Zhuang, H. Song, W. W. Yu, *Chempluschem* **2018**, *83*, 1052.

[352] M. O. Valappil, A. Anil, M. Shaijumon, V. K. Pillai, S. Alwarappan, *Chem. – A Eur. J.* **2017**, *23*, 9144.

[353] N. Pallikkarathodi Mani, J. Cyriac, *New J. Chem.* **2020**, *44*, 10840.

[354] W. Yin, X. Bai, P. Chen, X. Zhang, L. Su, C. Ji, H. Gao, H. Song, W. W. Yu, *ACS Appl. Mater. Interfaces* **2018**, *10*, 43824.

[355] M. Long, P. Wang, H. Fang, W. Hu, **2019**, *1803807*, 1.

[356] H.-S. Ra, D.-H. Kwak, J.-S. Lee, *Nanoscale* **2016**, *8*, 17223.

[357] S. Zhang, X. Wang, Y. Chen, G. Wu, Y. Tang, L. Zhu, H. Wang, W. Jiang, L. Sun, T. Lin, H. Shen, W. Hu, J. Ge, J. Wang, X. Meng, J. Chu, *ACS Appl. Mater. Interfaces* **2019**, *11*, 23667.

[358] G. Nazir, M. F. M. F. Khan, I. Akhtar, K. Akbar, P. Gautam, H. Noh, Y. Seo, S.-H. S. H. Chun, J. Eom, *RSC Adv.* **2017**, *7*, 16890.

[359] L. Yang, N. Yi, J. Zhu, Z. Cheng, X. Yin, X. Zhang, H. Zhu, H. Cheng, *J. Mater. Chem. A* **2020**, *8*, 6487.

[360] T. Mueller, F. Xia, P. Avouris, *Nat. Photonics* **2010**, *4*, 297.

[361] Z. Jia, J. Xiang, F. Wen, R. Yang, C. Hao, Z. Liu, *ACS Appl. Mater. Interfaces* **2016**, *8*, 4781.

[362] Z. Jia, S. Li, J. Xiang, F. Wen, X. Bao, S. Feng, R. Yang, Z. Liu, *Nanoscale* **2017**, *9*, 1916.

[363] J. Fang, Z. Zhou, M. Xiao, Z. Lou, Z. Wei, G. Shen, *InfoMat* **2020**, *2*, 291.

[364] L. Shi, S. Nihtianov, *IEEE Sens. J.* **2012**, *12*, 2453.

[365] L. Mingsheng, G. Anyuan, W. Peng, X. Hui, O. Claudia, P. Chen, F. Yajun, L. Erfu, C. Xiaoshuang, L. Wei, N. Tom, X. Jianbin, W. Xiaomu, H. Weida, M. Feng, *Sci. Adv.* **2021**, *3*, e1700589.

[366] M. Mikulics, M. Marso, P. Javorka, P. Kordoš, H. Lüth, M. Kočan, A. Rizzi, S. Wu, R. Sobolewski, *Appl. Phys. Lett.* **2005**, *86*, 211110.

[367] B. Radisavljevic, A. Radenovic, J. Brivio, V. Giacometti, A. Kis, *Nat. Nanotechnol.* **2011**, *6*, 147.

[368] P. Ni, A. De Luna Bugallo, V. M. Arellano Arreola, M. F. Salazar, E. Strupiechonski, V. Brändli, R. Sawant, B. Alloing, P. Genevet, *ACS Photonics* **2019**, *6*, 1594.

[369] P. Ni, A. De Luna Bugallo, X. Yang, V. M. Arellano Arreola, M. Flores Salazar, E. Strupiechonski, B. Alloing, C. Shan, P. Genevet, *J. Phys. D. Appl. Phys.* **2019**, *52*, 374001.

[370] A. Splendiani, L. Sun, Y. Zhang, T. Li, J. Kim, C.-Y. Chim, G. Galli, F. Wang, *Nano Lett.* **2010**, *10*, 1271.

[371] R. S. Sundaram, M. Engel, A. Lombardo, R. Krupke, A. C. Ferrari, P. Avouris, M. Steiner, *Nano Lett.* **2013**, *13*, 1416.

[372] X. Zhou, N. Zhou, C. Li, H. Song, Q. Zhang, X. Hu, L. Gan, H. Li, J. Lü, J. Luo, J. Xiong, T. Zhai, *2D Mater.* **2017**, *4*, 25048.

[373] M. Gong, Q. Liu, B. Cook, B. Kattel, T. Wang, W.-L. Chan, D. Ewing, M. Casper, A. Stramel, J. Z. Wu, *ACS Nano* **2017**, *11*, 4114.

[374] D. V Talapin, J.-S. Lee, M. V Kovalenko, E. V Shevchenko, *Chem. Rev.* **2010**, *110*, 389.

[375] K. C. R., L. Efrat, S. E. H., T. D. V., *Science (80-.).* **2016**, *353*, aac5523.

[376] Y. Li, L. Tang, R. Li, J. Xiang, K. S. Teng, S. P. Lau, *Chinese Phys. B* **2019**, *28*, 37801.

[377] K. Gołasa, M. Grzeszczyk, R. Bożek, P. Leszczyński, A. Wysmołek, M. Potemski, A. Babiński, *Solid State Commun.* **2014**, *197*, 53.

[378] M. Velický, M. A. Bissett, C. R. Woods, P. S. Toth, T. Georgiou, I. A. Kinloch, K. S. Novoselov, R. A. W. Dryfe, *Nano Lett.* **2016**, *16*, 2023.

[379] D. O. Scanlon, G. W. Watson, D. J. Payne, G. R. Atkinson, R. G. Egdell, D. S. L. Law, *J. Phys. Chem. C* **2010**, *114*, 4636.

[380] J. Matmin, M. A. Jalani, H. Osman, Q. Omar, N. Ab'lah, K. Elong, M. F. Kasim, *Nanomaterials* **2019**, *9*, DOI: 10.3390/nano9020264.

[381] S. H. Chaki, M. P. Deshpande, D. P. Trivedi, J. P. Tailor, M. D. Chaudhary, K. Mahato, *Appl. Nanosci.* **2013**, *3*, 189.

[382] K. Li, S. Yan, Z. Lin, X. Dai, P. Qu, *Synth. Met.* **2016**, *217*, 138.

[383] Y.-J. Yuan, D.-Q. Chen, X.-F. Shi, J.-R. Tu, B. Hu, L.-X. Yang, Z.-T. Yu, Z.-G. Zou, *Chem. Eng. J.* **2017**, *313*, 1438.

[384] T. Zhang, K. Fujisawa, T. Granzier-Nakajima, F. Zhang, Z. Lin, E. Kahn, N. Perea-López, A. L. Elías, Y.-T. Yeh, M. Terrones, *ACS Appl. Nano Mater.* **2019**, *2*, 5320.

[385] L. P. L. Mawlong, A. Bora, P. K. Giri, *Sci. Rep.* **2019**, *9*, 19414.

[386] L. Vallan, R. Canton-Vitoria, H. B. Gobeze, Y. Jang, R. Arenal, A. M. Benito, W. K. Maser, F. D'Souza, N. Tagmatarchis, *J. Am. Chem. Soc.* **2018**, *140*, 13488.

[387] V. Carozo, K. Fujisawa, R. Rao, E. Kahn, J. R. Cunha, T. Zhang, D. Rubin, M. F. Salazar, A. de Luna Bugallo, S. Kar, M. Terrones, *2D Mater.* **2018**, *5*, 31016.

[388] W. Zheng, W. Feng, X. Zhang, X. Chen, G. Liu, Y. Qiu, T. Hasan, P. Tan, P. A. Hu, *Adv. Funct. Mater.* **2016**, *26*, 2648.

[389] Y. Xue, Y. Zhang, Y. Liu, H. Liu, J. Song, J. Sophia, J. Liu, Z. Xu, Q. Xu, Z. Wang, J. Zheng, Y. Liu, S. Li, Q. Bao, *ACS Nano* **2016**, *10*, 573.

[390] H. Ying, X. Li, H. Wang, Y. Wang, X. Hu, J. Zhang, X. Zhang, Y. Shi, M. Xu, Q. Zhang, *Adv. Opt. Mater.* **2020**, *8*, 2000430.

[391] W. Tian, D. Liu, F. Cao, L. Li, *Adv. Opt. Mater.* **2017**, *5*, 1600468.

[392] B. Wang, S. Yang, C. Wang, M. Wu, L. Huang, Q. Liu, C. Jiang, *Nanoscale* **2017**, *9*, 10733.

[393] Z. Xu, S. Lin, X. Li, S. Zhang, Z. Wu, W. Xu, Y. Lu, S. Xu, *Nano Energy* **2016**, *23*, 89.

[394] K. K. Paul, L. P. L. Mawlong, P. K. Giri, *ACS Appl. Mater. Interfaces* **2018**, *10*, 42812.

APPENDIX A

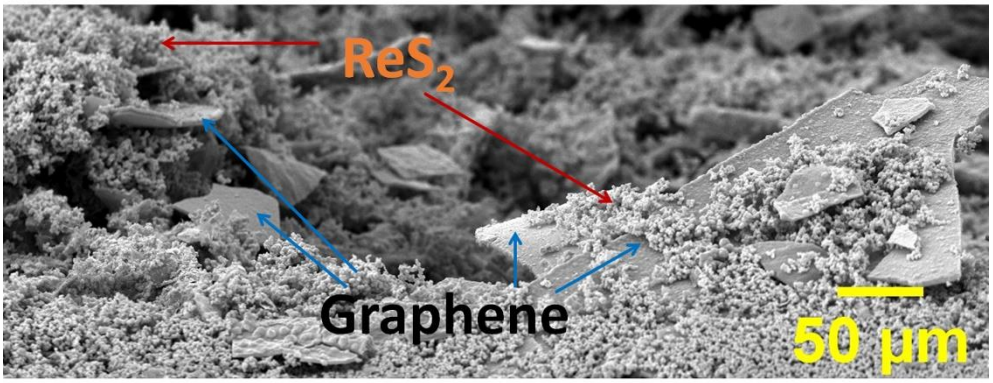

Figure S1: Cross-sectional view FESEM images of the fabricated ReS_2/Graphene device.

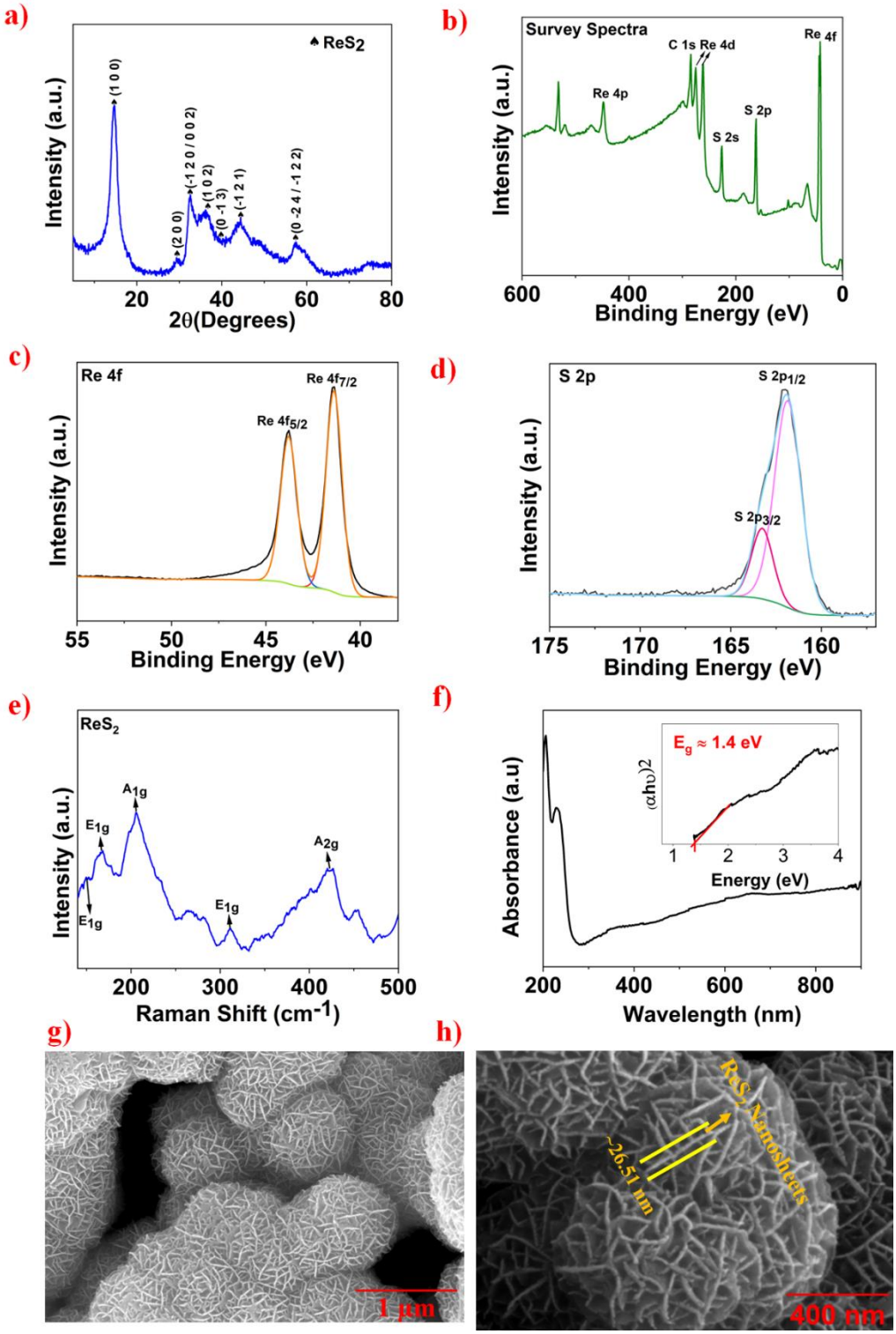

Figure S2: a) Pristine ReS_2 XRD spectra, b) Pristine ReS_2 XPS survey spectra, c-d) Deconvoluted XPS spectra of elements Re 4f and S 2p, e) Pristine ReS_2 Raman spectra, f) UV-Visible spectra of pristine ReS_2, inset showing the Tacu plot wherein the direct bandgap was calculated to be ~ 1.4 eV g-h) Surface morphology images obtained using FESEM for pristine ReS_2 thin film deposited on the cellulose paper at low, high magnifications, respectively.

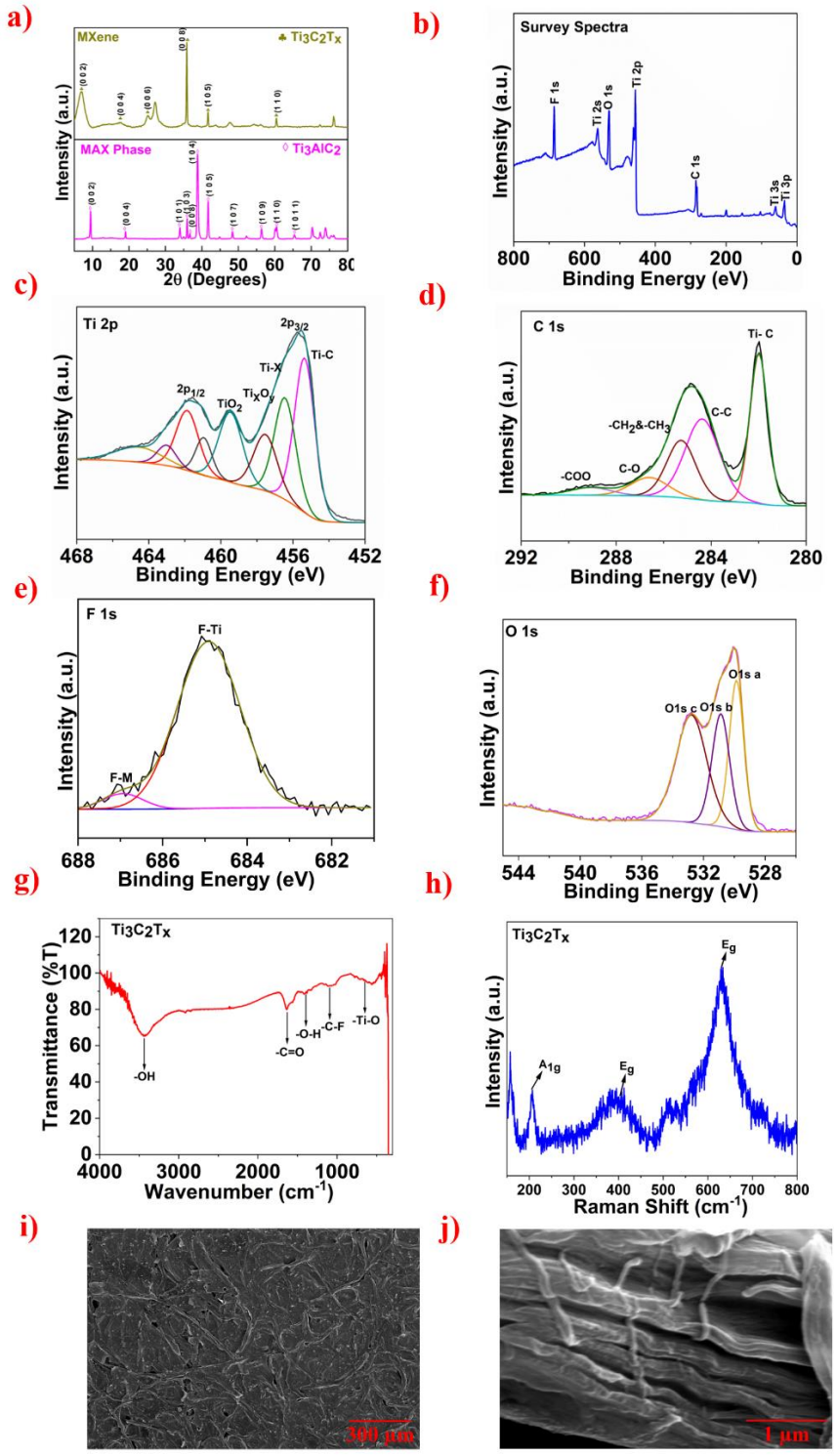

Figure S3: a) XRD pattern of Ti_3AlC_2, $Ti_3C_2T_x$, b) XPS survey spectra of $Ti_3C_2T_x$ for the B.E. ranging in between 0 to 800 eV, c-f) are deconvoluted XPS spectra of Ti 2p, C 1s, F 1s, O1s respectively, g) FTIR spectra of $Ti_3C_2T_x$, h) Raman spectra of $Ti_3C_2T_x$, i-j) are FESEM images of pristine $Ti_3C_2T_x$ thin film deposited on cellulose paper in top, cross-sectional view.

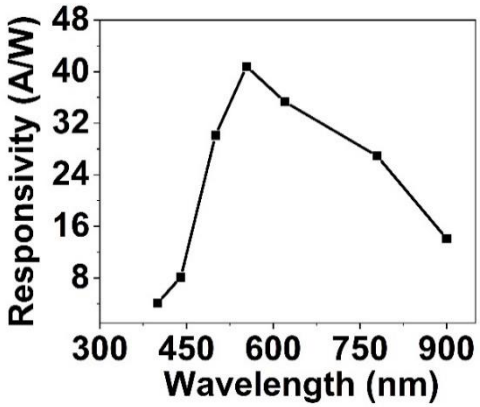

Figure S4: Response spectrum of the fabricated $ReS_2/Ti_3C_2T_X$ photodetector.

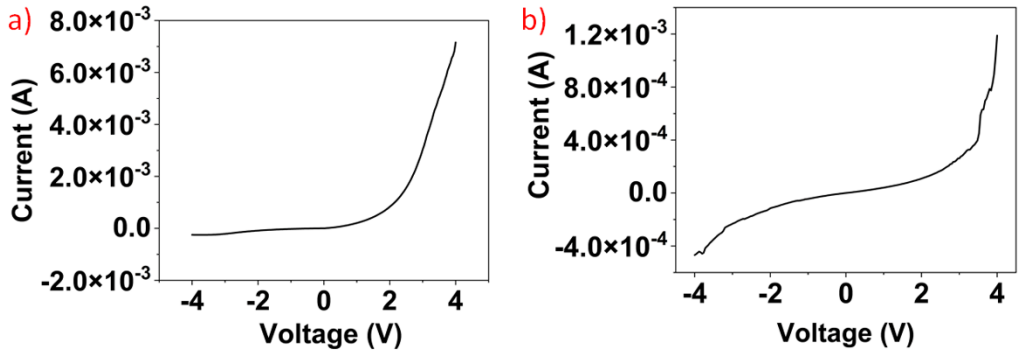

Figure S5: current-voltage (I-V) characteristics of a) $Ti_3C_2T_X$/Ag b) Graphene/Ag.

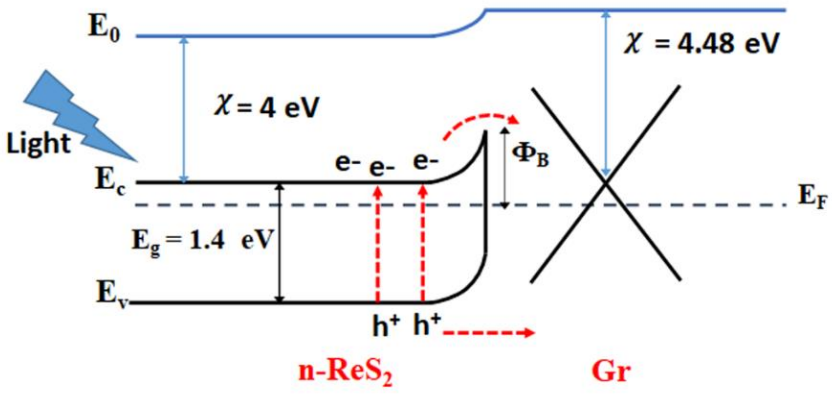

Figure S6: Schematic illustration of energy band diagram of ReS_2/Gr.

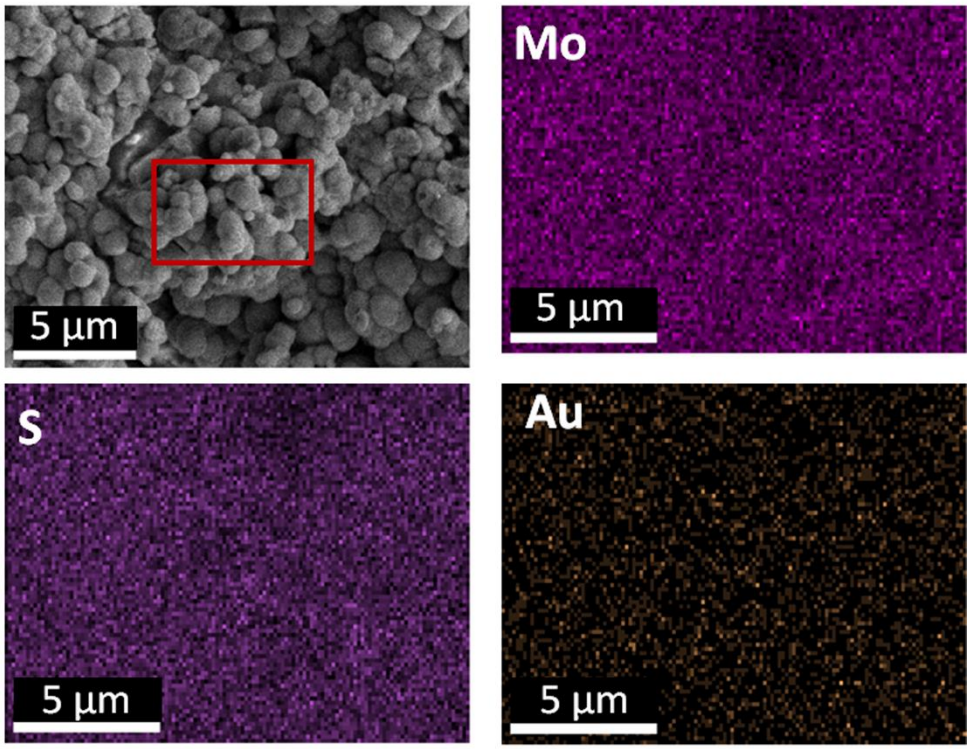

Figure S7: Compositional elemental mapping of MoS_2 decorated with Au- NPs.

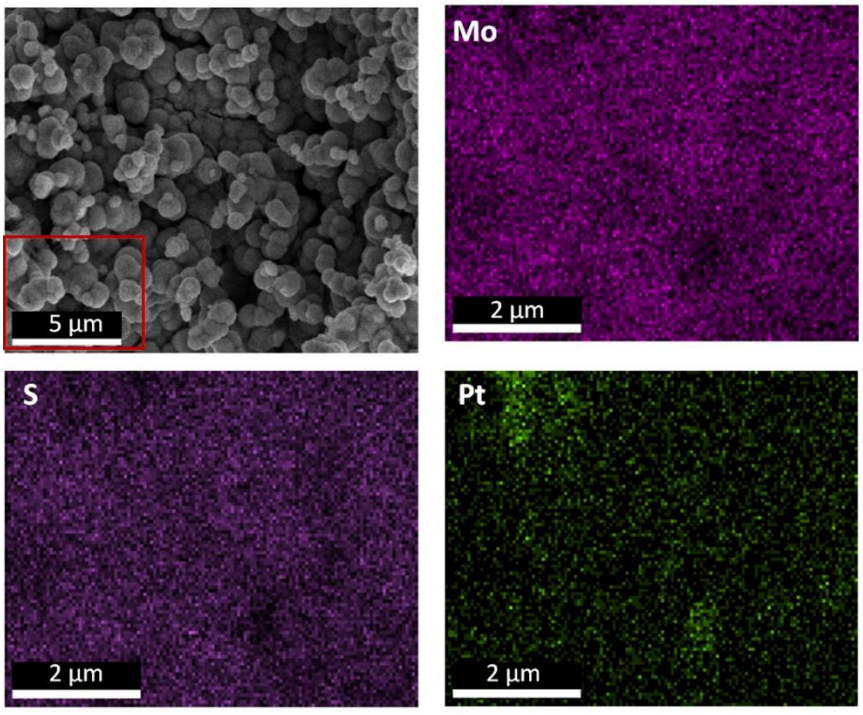

Figure S8: Compositional elemental mapping of MoS_2 decorated with Pt- NPs.

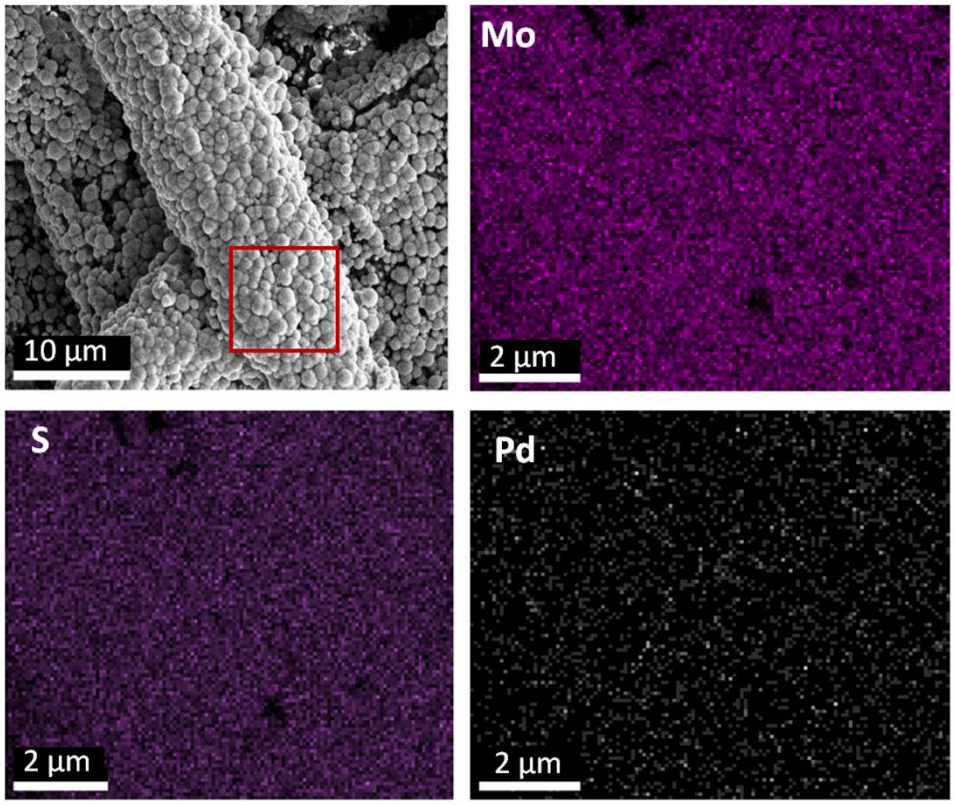

Figure S9: Compositional elemental mapping of MoS_2 decorated with Pd- NPs.

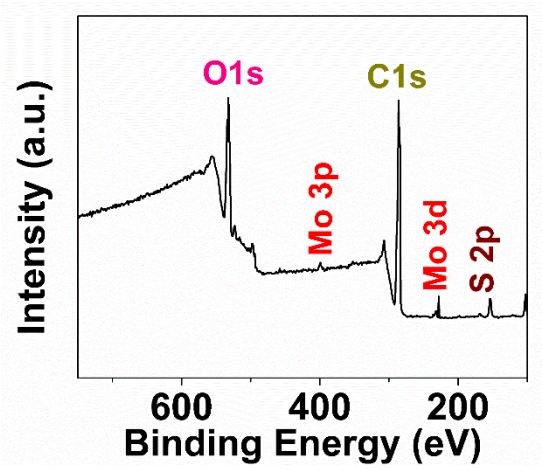

Figure S10: Broadband XPS spectra of MoS_2 grown on paper.

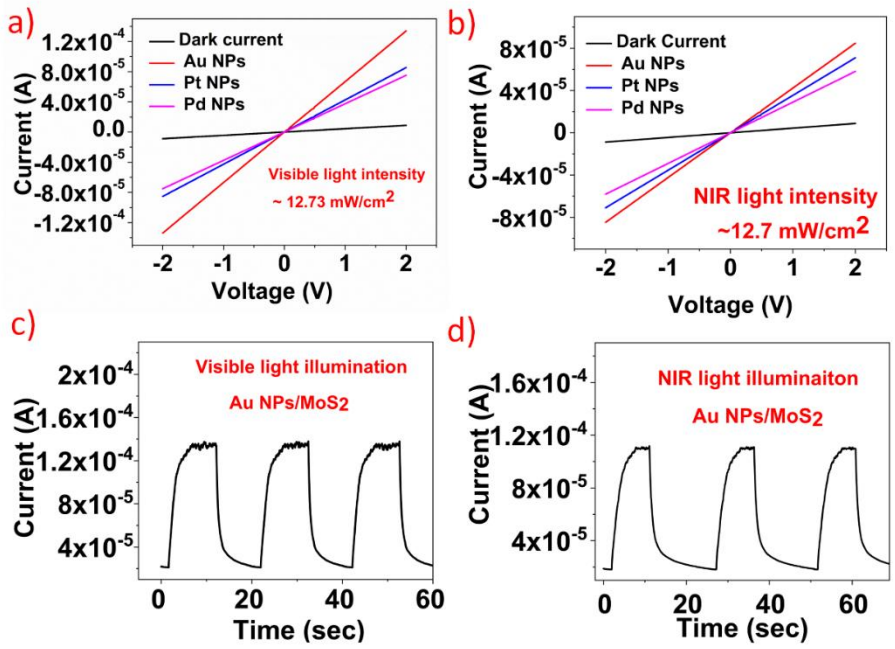

Figure S11: Current- voltage curves of the fabricated devices (Au-NPs, Pt-NPs, and Pd-NPs decorated on MoS_2) under: a) visible light intensity of ~ 12.73 mW/cm^2 b) NIR light intensity of ~ 12.73 mW/cm^2. Temporal response of the fabricated device (Au-NPs/MoS_2) under: c) visible light illumination with intensity of ~ 12.73mW/cm^2 d) NIR light illumination with intensity of ~ 12.73 mW/cm^2.

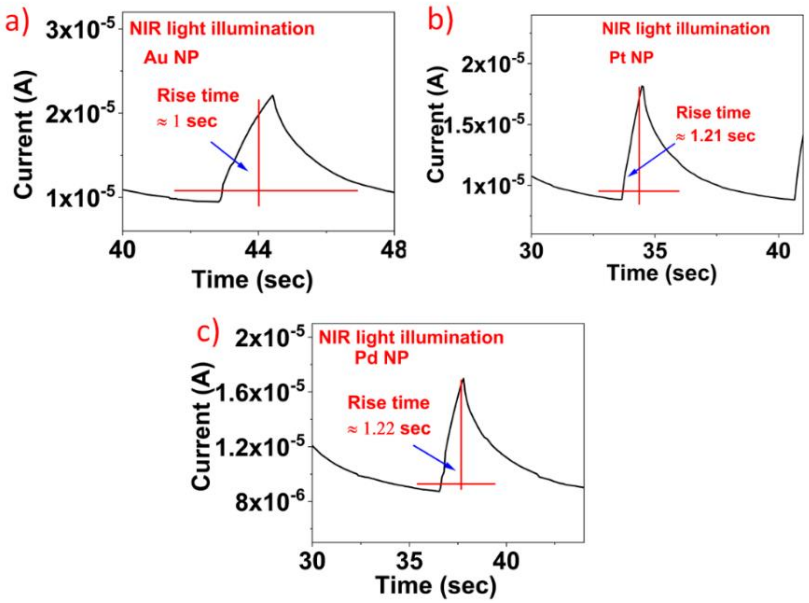

Figure S12: a,b,c) Graphs showing the response time of the fabricated photodetectors (Au, Pt, Pd-NPs/MoS_2) under NIR illumination.

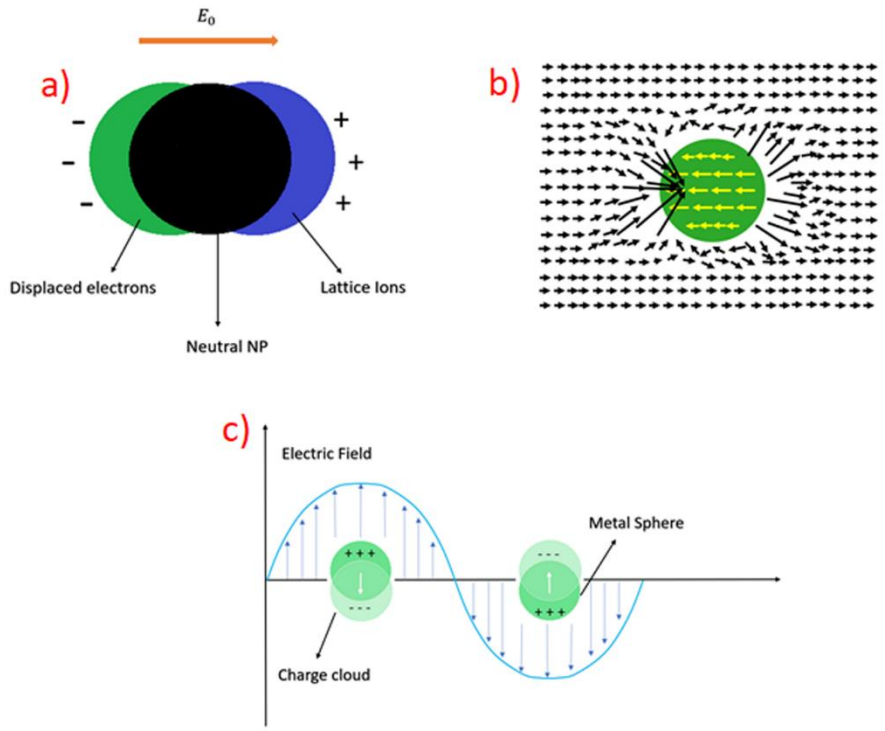

Figure S13: a) Representation of the displacement of the charge clouds b) Enhanced electric field in the vicinity of the nanoparticle c) Oscillation of the dipoles when light is incident on the nanoparticle.

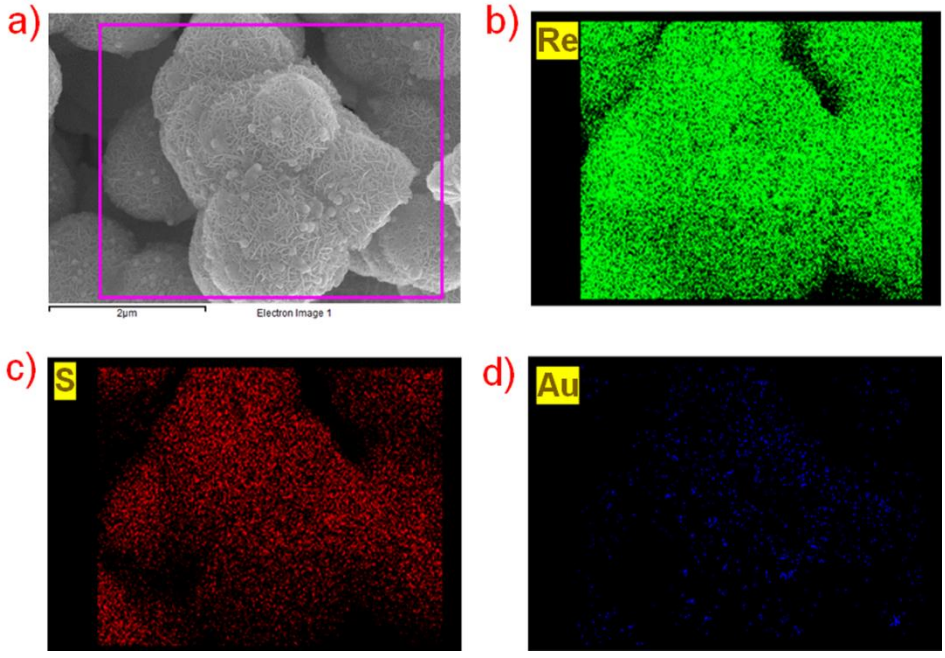

Figure S14: Elemental mapping of ReS_2 film decorated with Au-NPs.

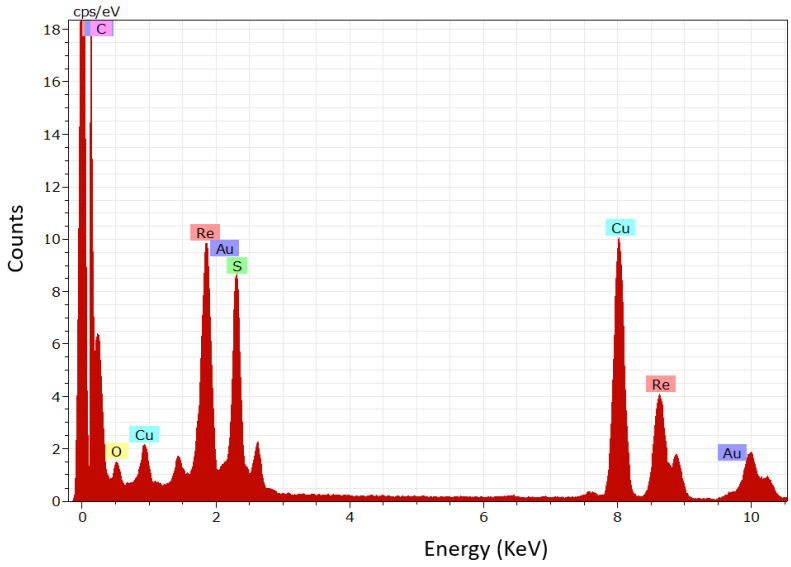

Figure S15: EDS spectrum of Au-NP/ReS_2 heterojunction.

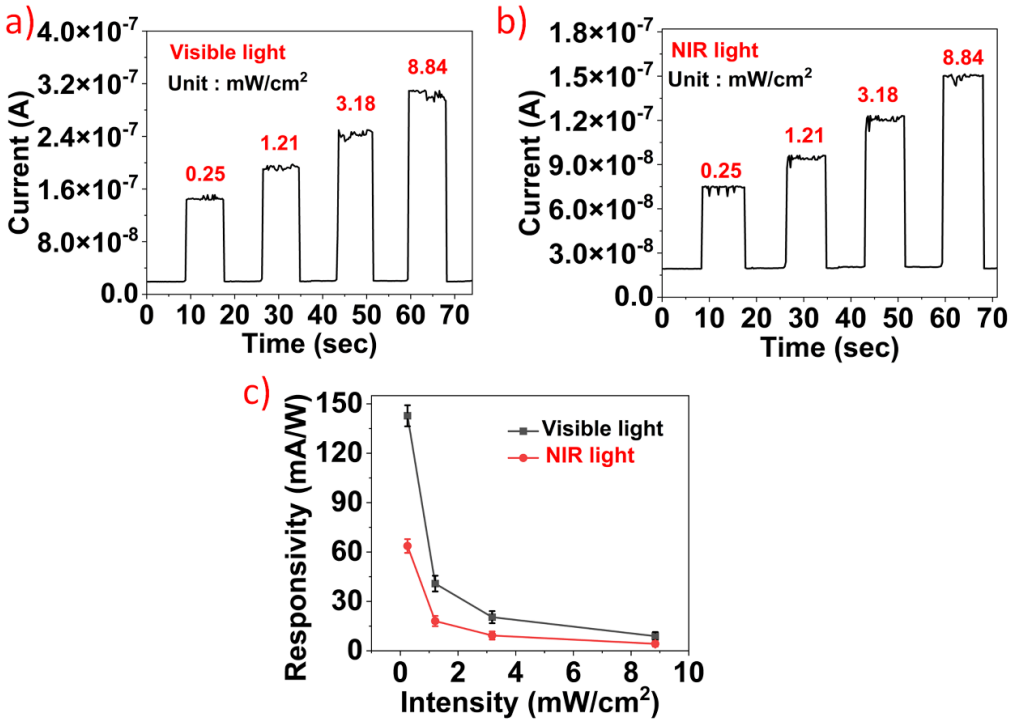

Figure S16: Photodetection measurements of pristine ReS_2: a-b) temporal response of the device under visible and NIR light illuminations, c) Photoresponsivity of the fabricated device under visible and NIR light illuminations.

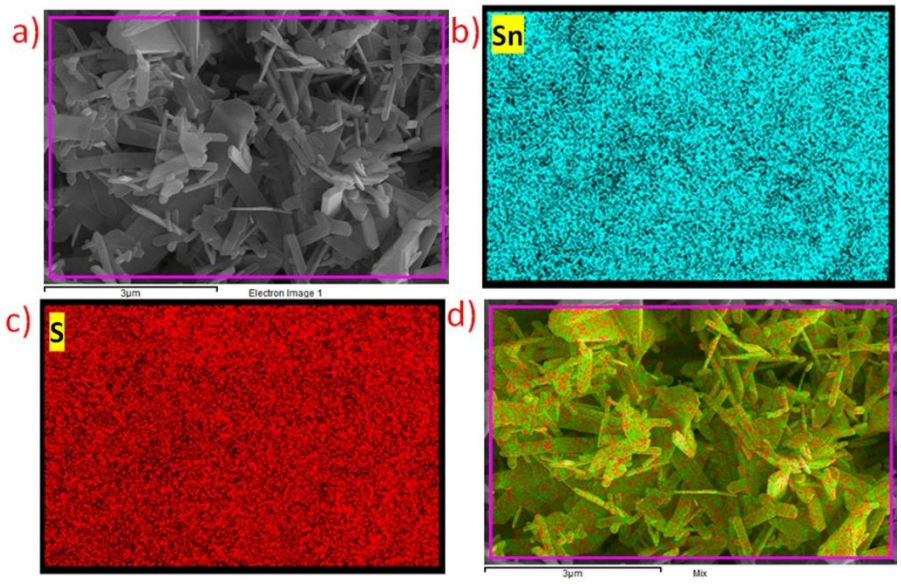

Figure S17: Elemental mapping of SnS deposited on PET substrate, scale bar 3 µm.

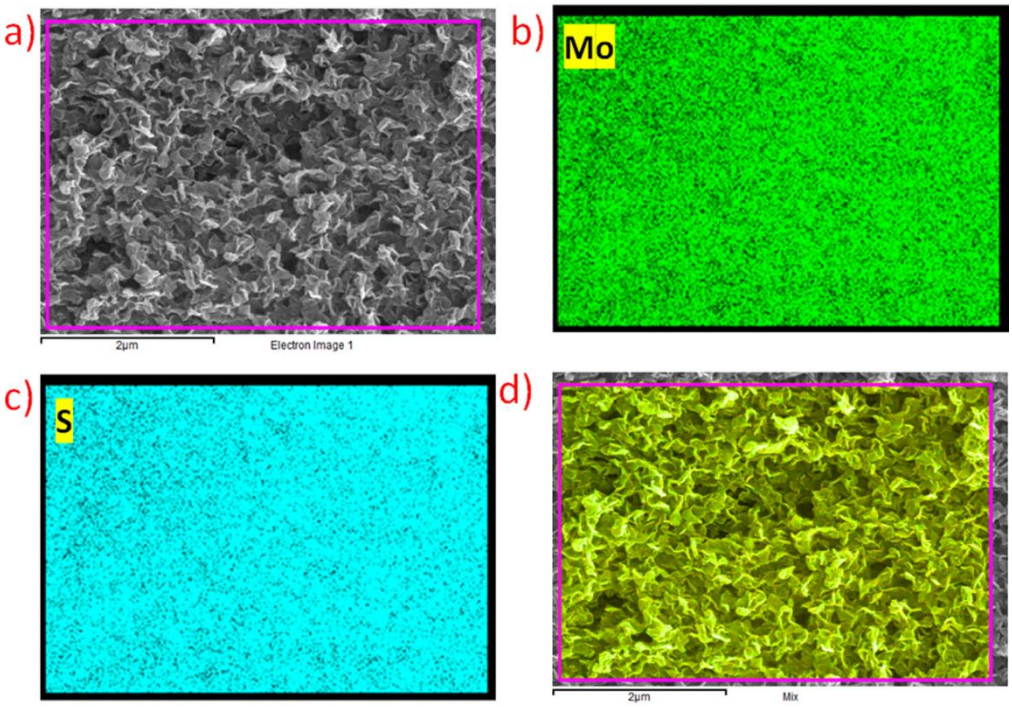

Figure S18: Elemental mapping of MoS_2 deposited on PET substrate, scale bar 2 µm.

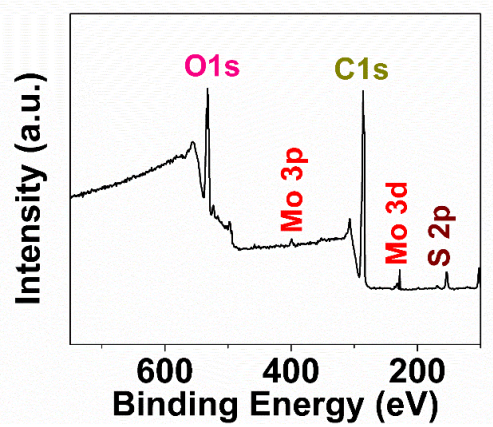

Figure S19: XPS survey spectra of MoS_2.

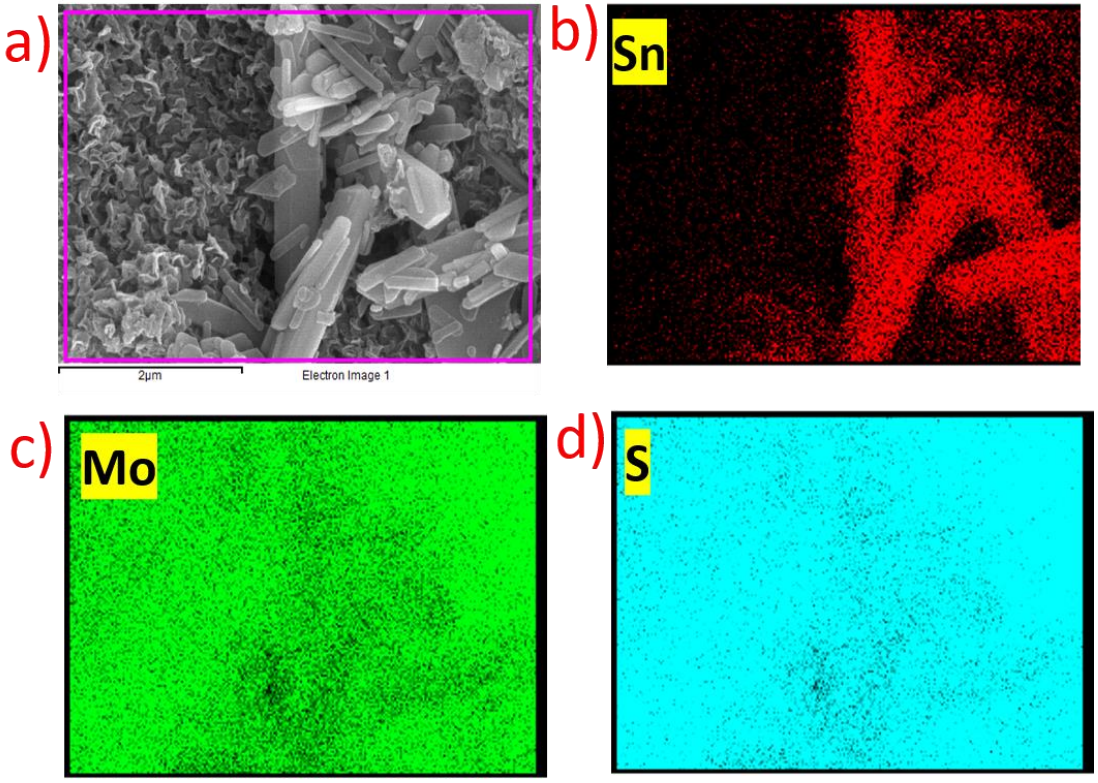

Figure S20: Elemental mapping of SnS/MoS_2 heterojunction on PET substrate, scale bar 2 µm.

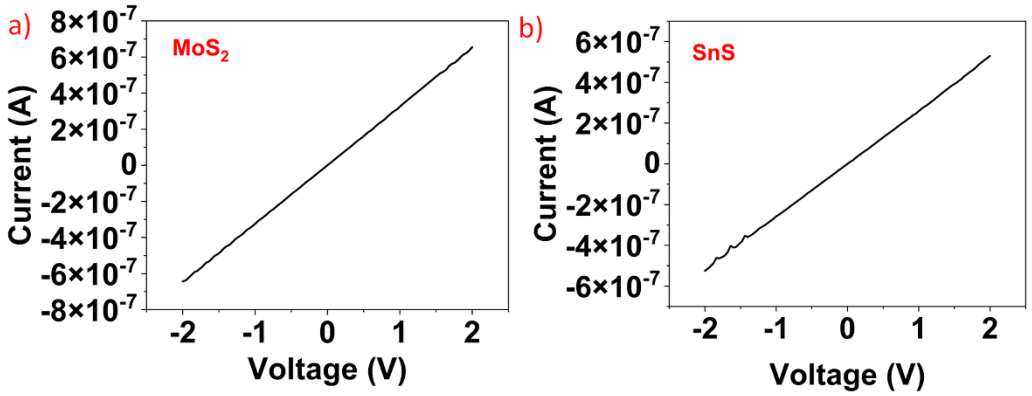

Figure 21: a) current-voltage characteristics of MoS_2 b) current-voltage characteristics of SnS.

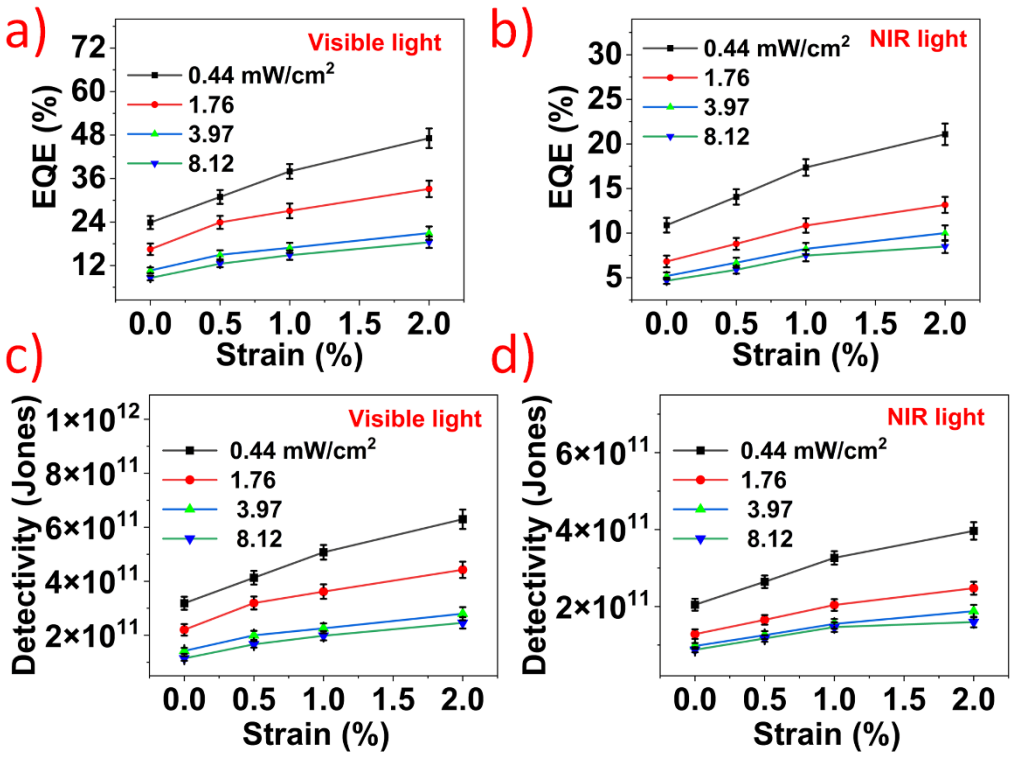

Figure S22: a-b) External quantum efficiency (EQE), c-d) detectivity of the fabricated piezo-phototronic effect based p-SnS/n-MoS_2 photodetector under various strains.

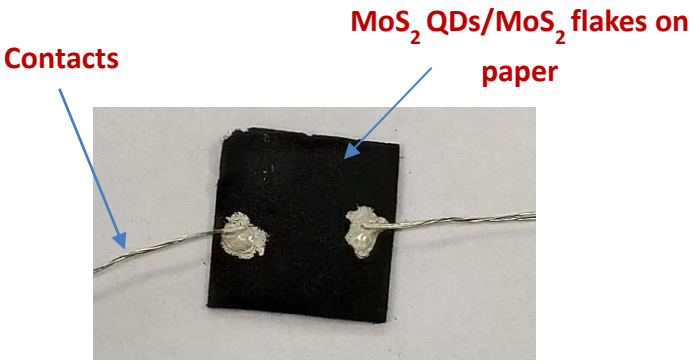

Figure S23: Image of the farbicated device (MoS_2 QDs / MOS_2 flakes on paper) with contaccts.

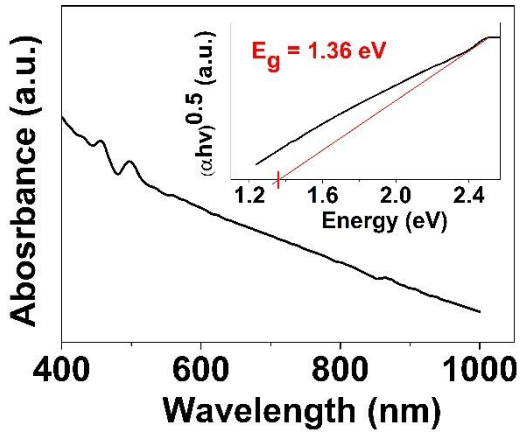

Figure S24: UV-vis absorption spectra of synthesiszed MoS_2 flakes, inset is the Tauc plot of MoS_2, E_g = 1.36 eV.

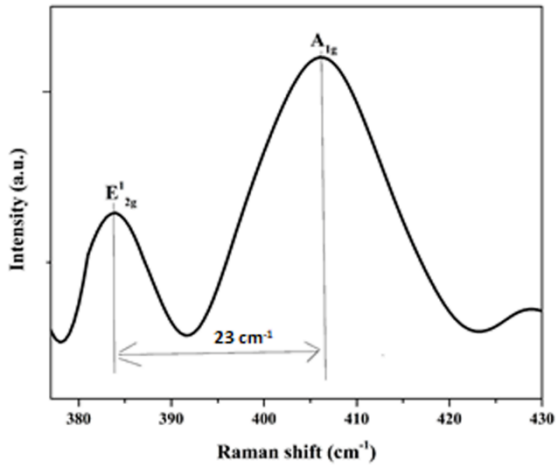

Figure S25: Raman spectra of MoS_2 grown on cellulose paper.

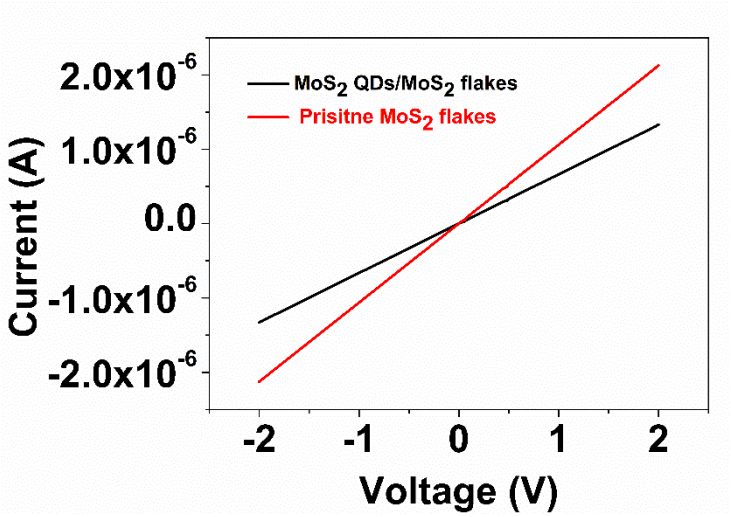

Figure S26: Current –Voltage **(**I-V) curve of MoS_2 QD_S/ MoS_2 flakes and pristine MoS_2 flakes.

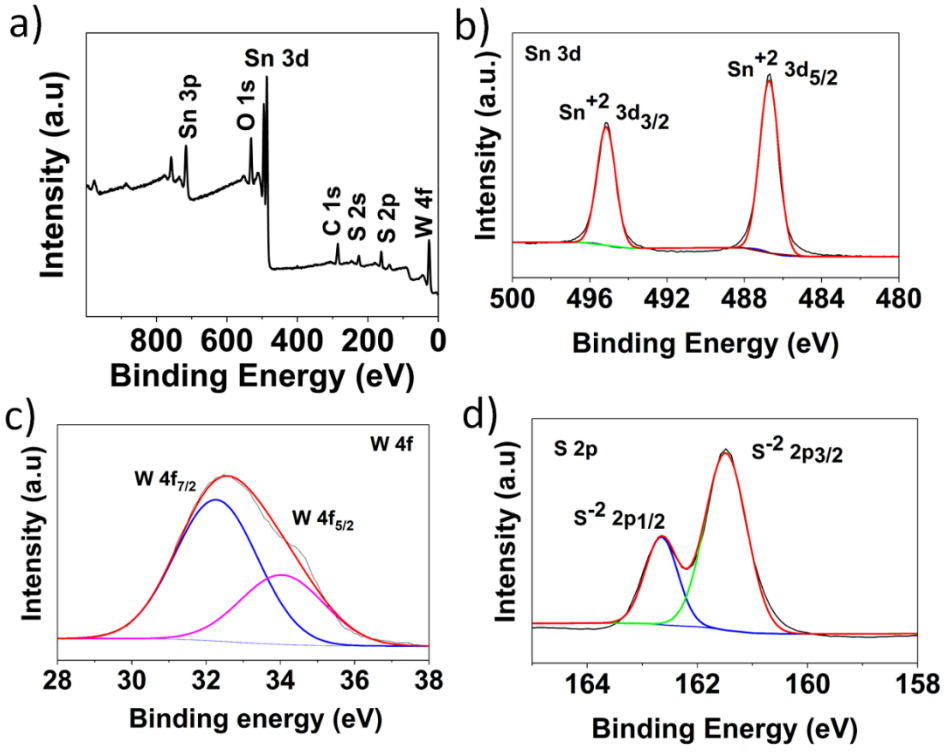

Figure S27: XPS analysis of fabricated WS_2-QDs/SnS device a) Survey spectra b) narrowband spectra of Sn 3d c) narrowband resolution spectra of W 4f d) narrowband spectra of S 2p.

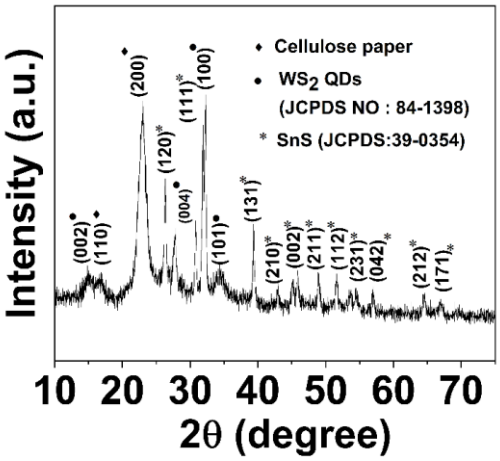

Figure S28: XRD pattern of SnS/paper decorated with WS_2-QDs.

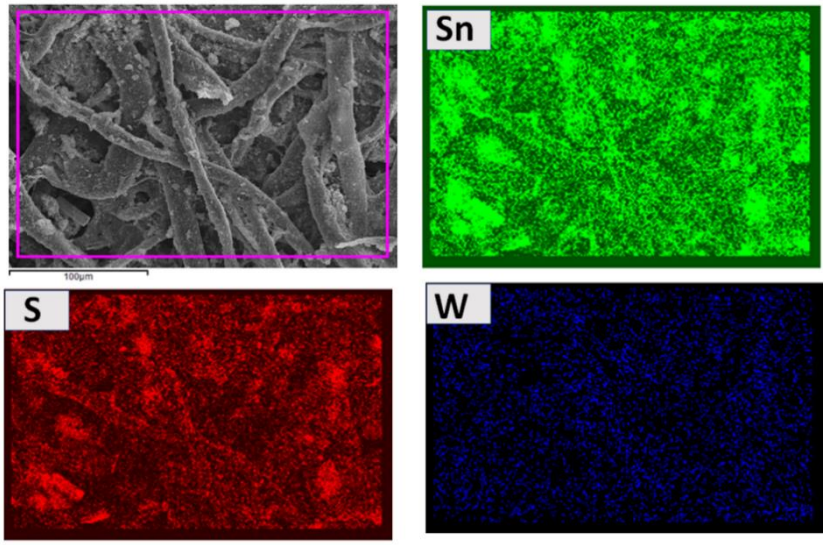

Figure S29: Compositional elemental mapping of SnS decorated with WS_2-QDs.

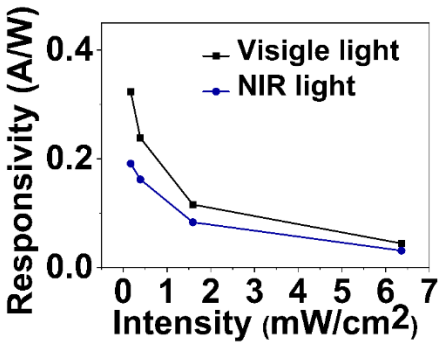

Figure S30: Responsivity of the fabricated pristine SnS device under visible and NIR regions.

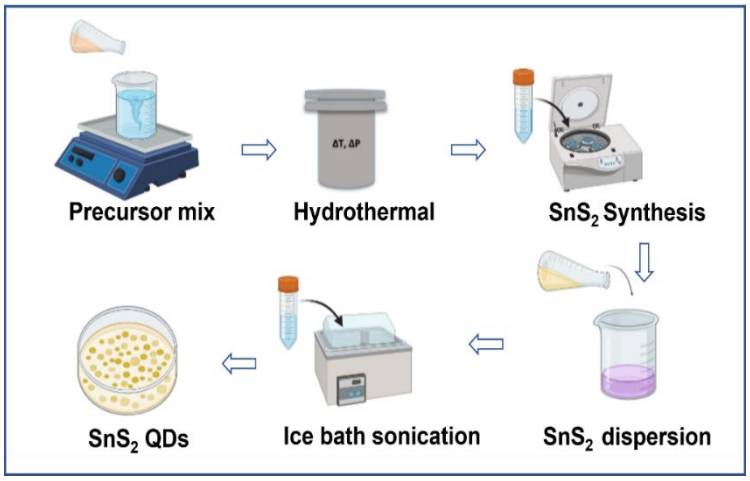

Figure S31: Schematic view of SnS_2 QDs synthesis.

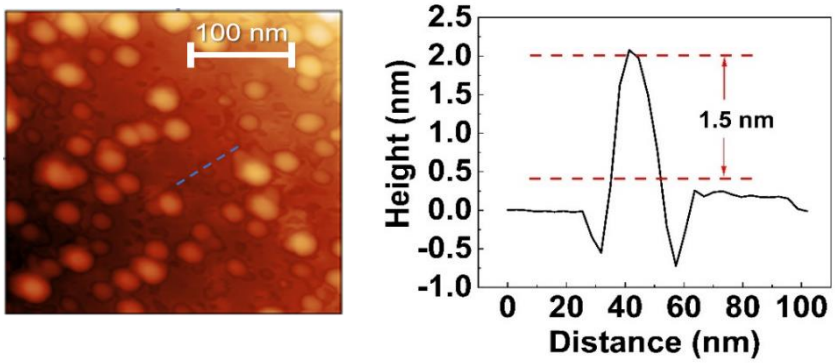

Figure S32: AFM image of the SnS_2-QDs decorated on MoS_2 flake and thickness of the SnS_2-QDs was measured to be around 1.5 nm.

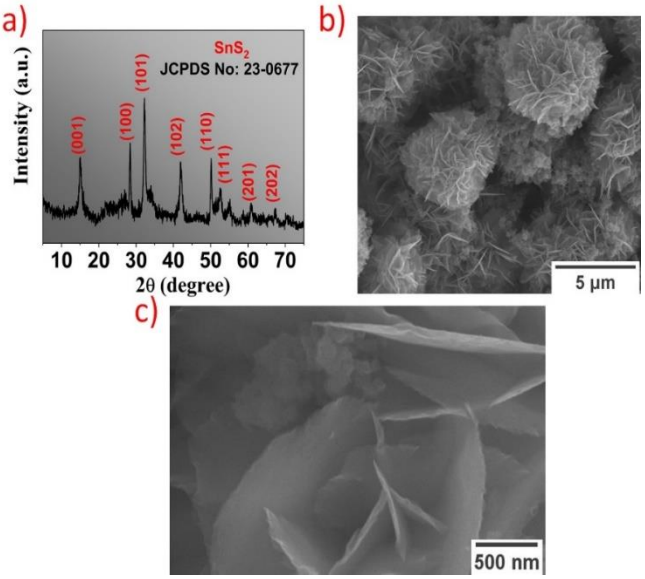

Figure S33: a) XRD pattern of synthesized SnS_2 b, c) FESEM images of synthesized SnS_2.

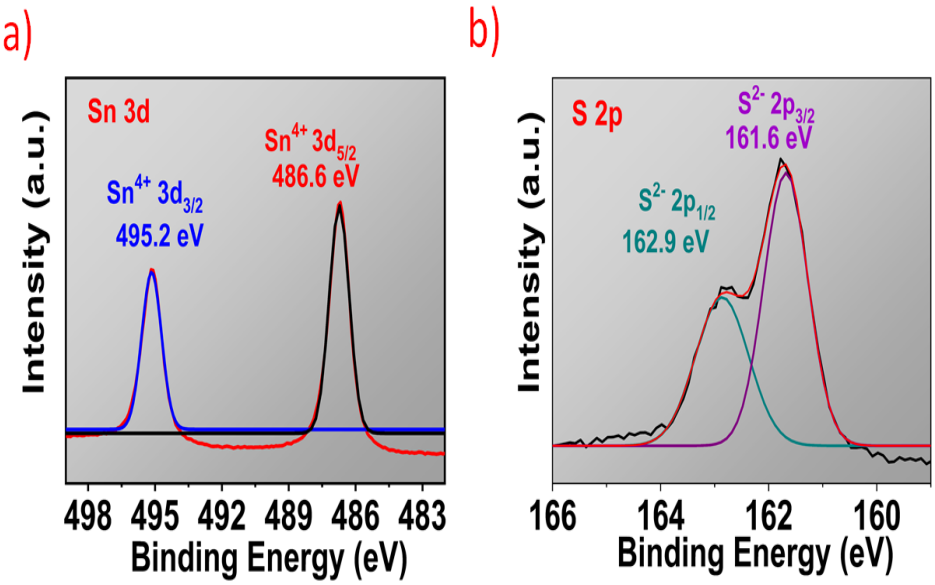

Figure S34: a-b) High resolution XPS spectrum of Sn3d and S 2p.

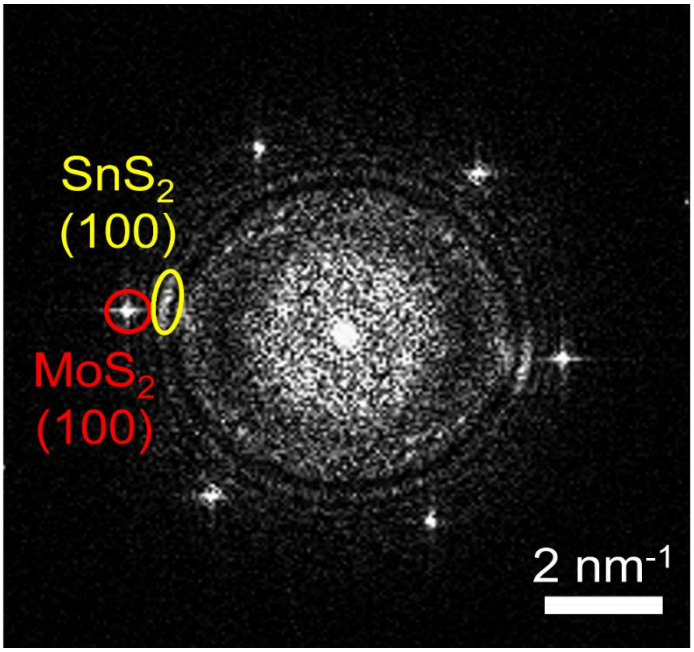

Figure S35: Fast-Fourier Transform (FFT) image of the SnS_2-QDs/MoS_2 HRTEM image.

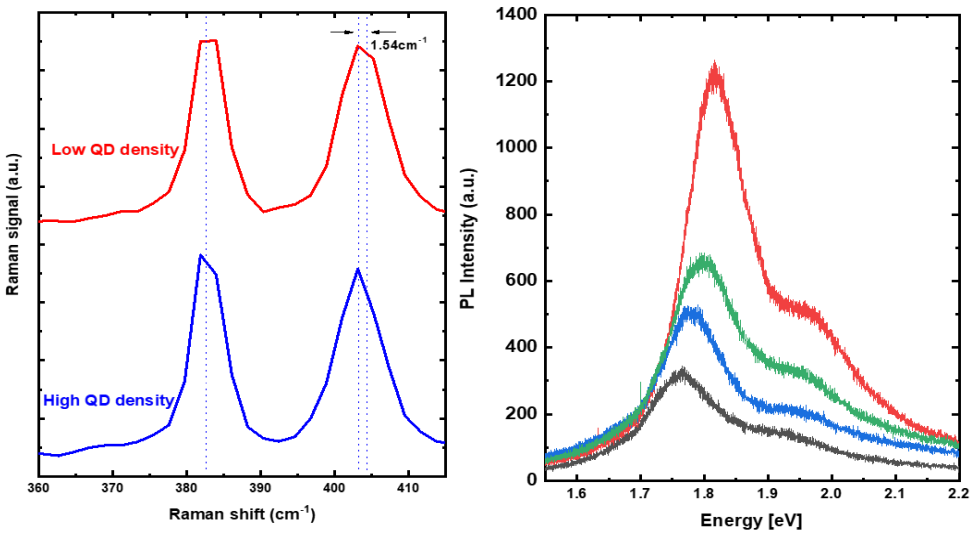

Figure S36: Left. Raman spectra of the MoS_2/SnS_2-QDs heterojunction recorded at low (red) and high (blue) SnS_2 QD concentrations. Right. PL spectra show the emission quenching as the SnS_2 QD increases.

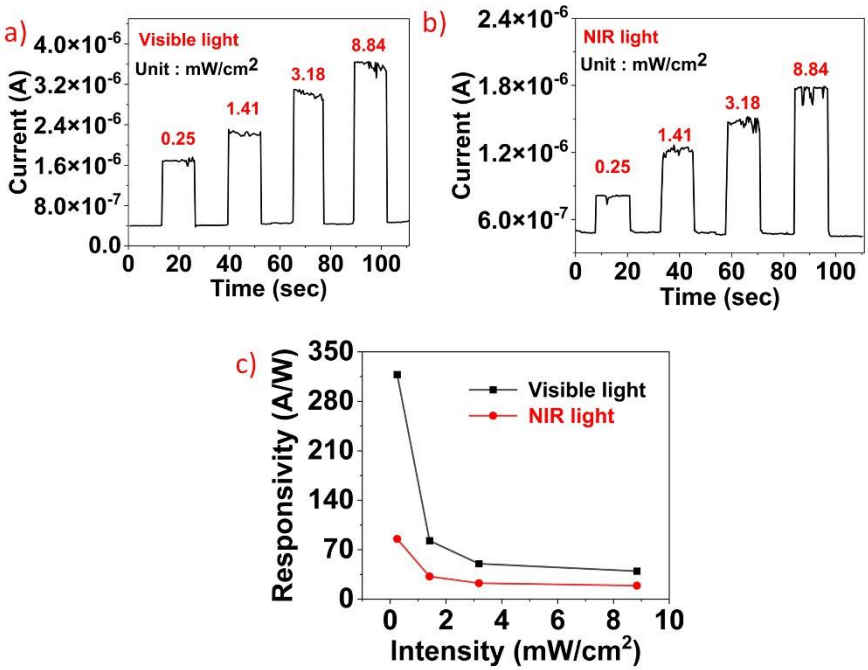

Figure S37: Photodetection measurements of pristine monolayer MoS_2: a-b) Temporal response c) photoresponsivity of MoS_2 under various visible and NIR light illumination.

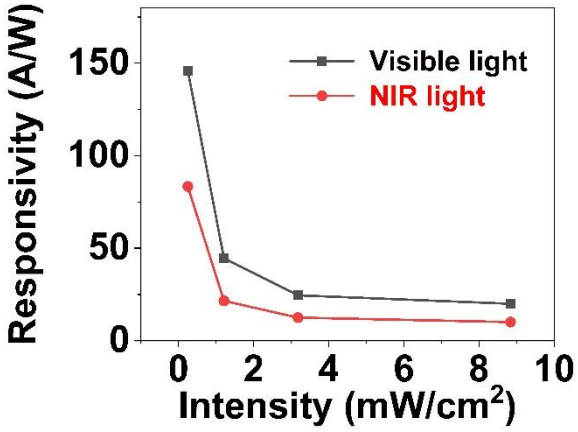

Figure S38: Photoresponsivity of the few layer MoS_2 decorated with SnS_2-QDs under visible and NIR illuminations.

List of Publications

The Thesis is based on following publications:

- **Selamneni, V.,** and Sahatiya, P. Mixed Dimensional Transition Metal Dichalcogenide (TMDs) vdW Heterostructure based Photodetectors: A Review, **Microelectronic Engineering**, 269, 111926, **2022**.
- **Selamneni, V.**, Adepu, V., Raghavan, H., & Sahatiya, P. Ultra-high Responsivity and Enhanced Trap Assisted Charge Transfer by Utilizing $Ti_3C_2T_X$ (MXene) as a Transport Layer for ReS_2 based Flexible Broadband Photodetector: A better Alternative to Graphene. **FlatChem,** 33,100363, **2022**.
- **Selamneni, V.,** Raghavan, H., Hazra, A., & Sahatiya, P. MoS_2/Paper Decorated with Metal Nanoparticles (Au, Pt, and Pd) Based Plasmonic-Enhanced Broadband (Visible-NIR) Flexible Photodetectors. **Advanced Materials Interfaces**, 8(6), 2001988, **2021**.
- **Selamneni, V.,** Mukherjee, A., Raghavan, H., Gomathi, P.T., Kolli, C.S.R., Pal, S., Hazra, A. and Sahatiya, P. Plasmonic Au Nanoparticles Coated on ReS_2 Nanosheets for Visible-Near-Infrared Photodetectors. **ACS Applied Nano Materials**, 5(8), 11381-11390, **2022**.
- **Selamneni, V.,** S. Sukruth, P. Sahatiya, Performance Enhancement of Highly Flexible SnS(p)/MoS_2(n) Heterostructure based Broadband Photodetector by Piezo-Phototronic Effect. **FlatChem**, 33,100379, **2022**.
- **Selamneni, V.,** Anand P, P., Singh, A., & Sahatiya, P. Hybrid 0D–2D WS_2-QDs (n)/SnS (p) as distributed heterojunctions for highly responsive flexible broad-band photodetectors. **ACS Applied Electronic Materials**, 3(9), 4105-4114, **2021**.
- **Selamneni, V.,** Ganeshan, S. K., & Sahatiya, P. All MoS_2 based 2D/0D localized unipolar heterojunctions as flexible broadband (UV-vis-NIR) photodetectors. **Journal of Materials Chemistry C**, 8(33), 11593-11602, **2020**.
- Kolli, C. S. R., **Selamneni, V.**, A. Muñiz Martínez, B., Fest Carreno, A., Emanuel Sanchez, D., Terrones, M., Strupiechonski E, De Luna Bugallo A, & Sahatiya, P. Broadband, Ultra-High-Responsive Monolayer MoS_2/SnS_2 Quantum-Dot-Based Mixed-Dimensional Photodetector. ACS **Applied Materials & Interfaces**, 14, 13, 15415–15425, **2022**. (**Equal Contributed First author**).

Other publications by the candidate:

- Polumati, G., Kolli, C. S. R., **Selamneni, V.,** Salazar, M. F., De Luna Bugallo, A., & Sahatiya, P. Modulation of Schottky Barrier Height by Nitrogen Doping and Its Influence on Responsivity of Monolayer MoS_2 Photodetector. **Advanced Materials Interfaces**, 10(9), 2202108, **2023**.

- Bokka, N., **Selamneni, V.,** Adepu, V., Jajjara, S., & Sahatiya, P. Water soluble flexible and wearable electronic devices: a review. **Flexible and Printed Electronics**, 6, 043006, **2021**.
- **Selamneni, V.,** Akshaya, T., Adepu, V., & Sahatiya, P. Laser-assisted micropyramid patterned PDMS encapsulation of 1D tellurium nanowires on cellulose paper for highly sensitive strain sensor and its photodetection studies. **Nanotechnology**, 32(45), 455201, **2021**.
- Amogh, B. S., **Selamneni, V.,** Bokka, N., & Sahatiya, P. Remarkably Stable Black Phosphorus Quantum Dots-Polyvinyl Alcohol Film as a Water Soluble Breath Sensor. **IEEE Transactions on Electron Devices**, 68(10), 5167-5172, **2021**. (**Equal Contributed First author**).
- Reddy, K. C. S., **Selamneni, V.,** Rao, M. S., Meza-Arroyo, J., Sahatiya, P., & Ramirez-Bon, R. All solution processed flexible p-NiO/n-CdS rectifying junction: Applications towards broadband photodetector and human breath monitoring. Applied Surface Science, 568, 150944, **2021**. (**Equal Contributed First author**).
- Enaganti, P. K., **Selamneni, V.,** Sahatiya, P., & Goel, S. MoS_2/cellulose paper coupled with SnS_2 quantum dots as 2D/0D electrode for high-performance flexible supercapacitor. **New Journal of Chemistry**, 45(19), 8516-8526, **2021**.
- Bokka, N., Adepu, V., **Selamneni, V.,** & Sahatiya, P. Non-contact, controlled and moisture triggered black phosphorus quantum dots/PVA film for transient electronics applications. **Materials Letters**, 290, 129477, **2021**.
- **Selamneni, V.,** Kanungo, S., & Sahatiya, P. Large area growth of SnS_2/graphene on cellulose paper as a flexible broadband photodetector and investigating its band structure through first principles calculations. **Materials Advances**, 2(7), 2373-238, **2021**.
- **Selamneni, V.,** Ganeshan, S. K., Nerurkar, N., Akshaya, T., & Sahatiya, P. Facile fabrication of $MoSe_2$ on paper as an electromechanical piezoresistive pressure–strain sensor. **IEEE Transactions on Instrumentation and Measurement**, 70, 1-8, **2020**.
- **Selamneni, V.,** Dave, A., Mondal, S., Mihailovic, P., & Sahatiya, P. Large area pressure sensor for smart floor sensor applications—An occupancy limiting technology to combat social distancing. **IEEE Consumer Electronics Magazine**, 10(2), 98-103, **2020**.
- **Selamneni, V.,** Kunchur, A., & Sahatiya, P. Large-area, flexible SnS/paper-based piezoresistive pressure sensor for artificial electronic skin application. **IEEE Sensors Journal**, 21(4), 5143-5150, **2020**.
- **Selamneni, V.,** Gohel, K., Bokka, N., Sharma, S., & Sahatiya, P. MoS_2 Based Multifunctional Sensor for Both Chemical and Physical Stimuli and Their Classification Using Machine Learning Algorithms. **IEEE Sensors Journal**, 21(3), 3694-3701, **2020**.

- **Selamneni, V.,** Nerurkar, N., & Sahatiya, P. Large area deposition of $MoSe_2$ on paper as a flexible near-infrared photodetector. **IEEE Sensors Letters**, 4(5), 1-4, **2020**.
- Leelasree, T., **Selamneni, V.,** Akshaya, T., Sahatiya, P., & Aggarwal, H. MOF based flexible, low-cost chemiresistive device as a respiration sensor for sleep apnea diagnosis. **Journal of Materials Chemistry B**, 8(44), 10182-10189, **2020**. (Selected as top 50 articles published in Journal of Materials Chemistry B in 2020)
- Bokka, N., **Selamneni, V.,** & Sahatiya, P. A water destructible SnS_2 QD/PVA film based transient multifunctional sensor and machine learning assisted stimulus identification for non-invasive personal care diagnostics. **Materials Advances**, 1(8), 2818-2830, **2020**.
- Bhardwaj, R., **Selamneni, V.,** Thakur, U. N., Sahatiya, P., & Hazra, A. Detection and discrimination of volatile organic compounds by noble metal nanoparticle functionalized MoS_2 coated biodegradable paper sensors. **New Journal of Chemistry**, 44(38), 16613-16625, **2020**.
- **Selamneni, V.,** BS, Amogh., & Sahatiya, P. Highly air-stabilized black phosphorus on disposable paper substrate as a tunnelling effect-based highly sensitive piezoresistive strain sensor. **Medical Devices & Sensors**, 3(4), e10099, **2020**.
- Ganeshan, S. K., **Selamneni, V.,** & Sahatiya, P. Water dissolvable MoS_2 quantum dots/PVA film as an active material for destructible memristors. **New Journal of Chemistry**, 44(28), 11941-11948, **2020**. **(Cover Article)**
- **Selamneni, V.**, & Sahatiya, P. Bolometric effect enhanced ultrafast graphene based do-it-yourself wearable respiration sensor for personal healthcare monitoring. **IEEE Sensors Journal**, 20(7), 3452-3459, **2019**.
- **Selamneni, V.**, Barya, P., Deshpande, N., & Sahatiya, P. Low-cost, disposable, flexible, and smartphone enabled pressure sensor for monitoring drug dosage in smart medicine applications. **IEEE Sensors Journal**, 19(23), 11255-11261, **2019**.

Conference proceedings:

- **Venkatarao Selamneni**, Chandra Sekhar Reddy Kolli, and Parikshit Sahatiya, "High-performance Broadband Photodetector based on a WS_2-QD/monolayer MoS_2 0D/2D Mixed-dimensional Heterostructure," IEEE Xplore proceedings, **ICEE-IEEE 2022**.
- **V. Selamneni** and P. Sahatiya, "Stacked 1D Tellurium Nanowires/Paper based Pressure Sensor with Laser Assisted Patterned PDMS Encapsulation," 2021 IEEE International Flexible Electronics Technology Conference (**IFETC**), **2021**, pp. 0013-0015.

Conferences participated (without proceedings):

- **Venkatarao Selamneni,** Sandeep Jajjara and Parikshit Sahatiya Complete Wafer analysis for the optimization of operating parameters via Temperature, Flow rate, Mo:S ratio: A strategy for MoS_2 growth, XXI **International Workshop on Physics of Semiconductor Devices (IWPSD),** 14-17 December, **2021**, IIT Delhi, (virtual). (Poster presentation)

- Harini Raghavan, **Venkatarao Selamneni** and Parikshit Sahatiya, Metal Nanoparticles (Au, Pt and Pd) Functionalized MoS_2 Based Plasmonic-Enhanced Broadband (Visible-NIR) Flexible Photodetector, XXI **International Workshop on Physics of Semiconductor Devices (IWPSD),** 14-17 December, **2021**, IIT Delhi, (virtual). (Poster presentation)

- **Venkatarao Selamneni,** Parikshit Sahatiya. Stacked 1D Tellurium Nanowires/Paper based Pressure Sensor with Laser Assisted Patterned PDMS Encapsulation, **IEEE International Flexible Electronics Conference (IFETC) 2021,** Virtual, August 8-11, 2021. (Oral presentation)

- **Venkatarao Selamneni,** Nikita Nerurkar, and Parikshit Sahatiya, Large area, flexible Near Infrared photodetector based on $MoSe_2$ deposited on paper, **International Conference on Nanoscience and Nanotechnology (ICONN) 2021,** SRM University, Virtual, February 01-03, 2021. (Poster presentation)

- **Venkatarao Selamneni,** Sankalp Koduvayur Ganeshan, Parikshit Sahatiya, Flexible Broadband (UV-Vis-NIR) Photodetector based on all MoS_2 0D/2D Mixed Dimensional Unipolar Heterojunctions, **2020 MRS Fall Meeting,** Boston, Virtual, November 27–December 4, 2020. (Poster presentation)

- **Venkatarao Selamneni,** Pranav Anand P, and Parikshit Sahatiya, WS_2 QD (n) decorated on SnS (p) as Localized Heterojunctions for Highly Responsive Flexible Broadband Photodetector, **IEEE ICEE 2020**, IIT Delhi, Virtual, November 26-28, 2020. (Poster presentation, received Best Poster Award)

- **Venkatarao Selamneni,** Sankalp K G, Nikita Nerurkar and Parikshit Sahatiya, Flexible Pressure-Strain Sensor as Wireless keyboard and Human Motion Monitoring Using Facile Fabrication of $MoSe_2$ on Paper **International Conference on Nanoscience and Technology (ICONSAT),** Kolkata, Mar'2020. (Poster presentation)

- Sankalp K G, **Venkatarao Selamneni** and Parikshit Sahatiya, Water Dissolvable Memoristor based on in-situ functionalized MoS_2 Quantum Dots/PVA film, **International Conference on Nanoscience and Technology (ICONSAT),** Kolkata, Mar' 2020. (Poster presentation)

- Amogh B.S, **Venkatarao Selameni** and Parikshit Sahatiya, Highly Sensitive Transient Breath Sensor based on Black Phosphorus Quantum Dots-PVA Composite, **International Conference on Nanoscience and Technology (ICONSAT),** Kolkata, Mar' 2020. (Poster presentation)

- **Venkataro Selamneni** and Parikshit Sahatiya, Flexible Photodetector based on solution processed direct growth of 2D SnS_2/Graphene on cellulose paper, **International Workshop on Physics of Semiconductor Devices (IWPSD),** Kolkata, Dec' 2019. (Poster presentation)

- **Venkatarao Selamneni** and Parikshit Sahatiya, Black phosphorous on paper based strain sensor for human motion monitoring, **IEEE Nanotechnology Materials and Devices Conference (NMDC),** Stockholm, Sweden, Oct' 2019. (Oral presentation)

Book Chapter:

- **Selamneni V**., Bokka N., Adepu V., Sahatiya P. Carbon Nanomaterials for Emerging Electronic Devices and Sensors. In: Hazra A., Goswami R. (eds) Carbon Nanomaterial Electronics: Devices and Applications. Advances in Sustainability Science and Technology. **Springer, Singapore**. **2021**.
- Vivek Adepu, Naveen Bokka, **Venkatarao Selamneni**, Thanga Gomathi Paramasivan, Parikshit Sahatiya, Flexible and Wearable Strain/Pressure Sensors, A.S.M.A. Haseeb (editor), **Encyclopedia of Materials: Electronics, Academic Press**, 180-198, **2023**.

Patent filed:

- Parikshit Sahatiya and **Venkatarao Selamneni** "A Method of Manufacturing a Sensor Mat and A Smart Sensing Door Mat Thereof", Application number: **202211008833** patent number: **IN-PA-2984**.

Biography of the Candidate

Venkatarao Selamneni received the B.Tech. degree in electronics and communication engineering from Gudlavalleru Engineering College affiliated to Jawaharlal Nehru Technological University, Hyderabad, Andhra Pradesh, India, in 2008 and the M.Tech. degree in Microelectronics and VLSI Design from NIT Allahabad, Uttar Pradesh, India, in 2011. He is currently pursuing the Ph.D. degree in electrical and electronics engineering at Birla Institute of Technology and Science, Pilani, Hyderabad, Telangana, India. He has seven years of teaching experience He has published 28 Journals, 2 conference papers, and filed 1 Indian patent. His research interest includes the growth of large-area high-quality 2D materials (TMDs) and their hybrids with low-dimensional nanomaterials for electronic device applications.

Biography of the Supervisor

Dr. Parikshit Sahatiya received his PhD degree from Indian Institute of Technology Hyderabad, India. Post PhD, he joined Redpine Signals Inc. as Research Scientist. Currently, he is an Assistant Professor in the Department of Electrical and Electronics Engineering, Birla Institute of Technology and Science (BITS) Pilani Hyderabad Campus. Dr. Sahatiya's research is very interdisciplinary which include 2D materials based flexible and wearable nanoelectronic devices and sensors. Some of applications which Dr. Sahatiya's lab have demonstrated include artificial skin, human motion monitoring, wireless keypad, sleep apnea diagnostics and posture analysis and smart bed etc. Further, Dr. Sahatiya's lab also focuses on understanding the transport of complex heterostructure (including monolayer 2D vdW vertical heterostructure) which have led to the development of broadband photodetectors. Recently, Dr. Sahatiya has been exploring memristors and trying to understand the physical mechanism of the same. Further, he is also working tow arms the device-circuit interface using memristor by developing data driven models for the memristors. Also, Dr. Sahatiya's lab has also been actively working in the field of Transient electronics and exploring different triggers for the destruction of the devices. Dr. Sahatiya has published more than 100 Journal articles and have delivered talks nationally and internationally. Dr. Sahatiya's lab is currently being funded by Government (SERB), DRDO and Industry grants and have a fully equipped lab for the development of various 2D materials based devices. Dr. Sahatiya serves as an Associate Editor for Nature Scientific Reports, Frontiers in Electronics (for both flexible and wearable electronics specialty) and Frontiers in Chemistry. Dr. Sahatiya is a member of the Royal Society of Chemistry and also Materials Research Society.